Tracing water masses and pollution in the Southern Ocean using neodymium and lead isotopes

by

Alexander Matthew Griffiths

Submitted in fulfilment of the requirements for the degree of

Doctor of Philosophy (Ph.D.) and the Diploma of Imperial College London

Department of Earth Science and Engineering of
Imperial College London

October 2019

Supervisors: Prof. Mark Rehkämper & Prof. Tina van de Flierdt

Declaration of Originality

I, Alexander Matthew Griffiths, hereby declare that this thesis is the product of my own work at Imperial College London under the supervision of Prof. Mark Rehkämper and Prof. Tina van de Flierdt, and the appropriate citations are included to acknowledge the work of others. All other published and unpublished work used in this thesis has been appropriately referenced.

……

Alexander Matthew Griffiths

Copyright Declaration

Abstract

Trace elements and their isotopes play a vital role in the ocean as participants in, and tracers of, processes of interest to climate change and environmental pollution. This thesis focuses on the use of isotopic variations in neodymium (Nd) and lead (Pb) to understand the cycling of these elements in the Southern Ocean.

Neodymium isotopes have been used as a palaeo-proxy to understand changes in Antarctic Bottom Water (AABW) circulation through time. The biogeochemical processes controlling Nd in seawater, however, remain under-constrained due to a paucity of modern observations in the Southern Ocean. In chapter 2, Nd isotope and rare earth element (REE) data are presented for the Wilkes Land continental margin. In this region, AABW exhibits a distinct ε_{Nd} signature that is intermediate between Atlantic and Pacific sector AABW. The REE data confirm that the ε_{Nd} signature is not caused by distinct local continental inputs but by mixing of advected AABW with (modified) Circumpolar Deep Water (CDW).

Anthropogenic emissions from mining, smelting and fossil fuel combustion are important sources of oceanic Pb contamination. Seawater Pb isotope data, however, is currently severely limited by analytical challenges such as sample contamination, time-consuming extraction procedures and insufficient instrumental detection limits. In chapter 3, a novel method is presented for the determination of seawater Pb isotope compositions and concentrations. The method encompasses solid-phase extraction of Pb from seawater with Nobias chelate PA-1 resin followed by multi-collector inductively coupled mass spectrometry (MC-ICP-MS) analyses using a ^{207}Pb-^{204}Pb double-spike to correct for instrumental mass discrimination. When compared to an established double-spike procedure that employs thermal ionisation mass spectrometry (TIMS), the results are unbiased by systematic error and demonstrates improved precision for the $^{206}Pb/^{207}Pb$, $^{208}Pb/^{207}Pb$ ratios and the minor ^{204}Pb ratios (by about a factor of 2).

In chapter 4, the new method is applied to seawater samples from the Australian sector of the Southern Ocean to assess the sources and processes governing the distribution of Pb in this region. Surface waters exhibit a high fraction of anthropogenic Pb (~30–50%). Reversible scavenging and equilibrium exchange are the dominant processes responsible for the vertical transport of this anthropogenic Pb to deeper waters. These processes may account for ~80% of the observed dissolved Pb isotope in the intermediate depth waters at the Polar Front.

Overall, the thesis highlights the essential role that isotope analyses play in deconvolving the processes responsible for the biogeochemical cycling of Nd and Pb in the ocean.

Acknowledgements

I would like to thank all the people who have provided both academic and personal support throughout my Ph.D.

First of all, I want to thank Mark Rehkämper and Tina van der Flierdt for being the best supervisors. They provided me with the support and guidance to complete my thesis and gave me the opportunity to develop as a scientist. It has been a privilege to have worked with them over the past four years.

In addition, this thesis would not have been possible without the efforts of different collaborators: Myriam Lambelet, Kirsty Crocket, Richard Abell, Frank Nitsche, Hollie Packman, Susan Little, Yee Lap Leung, Andrew Bowie and Melanie East.

I would also like to show my gratitude to everyone in the MAGIC research group, in particular Katharina Kressig and Barry Coles for all their support in the labs, and my PhD twin, Naomi Pratt, for her encouragement throughout the four years. A very special thanks also to Myriam Lambelet for showing me the analytical ropes early on (I know that must have been a difficult task requiring a huge amount of patience, so thank you!). And an extremely big thank you to Hollie Packman for her companionship in the lab, support during difficult analytical and write-up times towards the end, and her constant optimism.

I would also like to extend my gratitude to Steve Galer, Yves Plancherel and Cedric John for agreeing to be my examiners. I hope they find the work interesting and I look forward to our discussion.

Finally, a special thanks to all my friends and family for their help throughout the four years, especially to my parents who have supported me throughout my education and enabled me to achieve this feat.

Table of Contents

Chapter 3: High-precision Pb isotope analysis of seawater using Nobias chelate resin and ^{207}Pb-^{204}Pb double-spike MC-ICP-MS

Chapter 4: Pathways and processes controlling the distribution of anthropogenic lead in the interior of the Southern Ocean

Chapter 5: Conclusion and future research

List of Figures

Chapter 1: Introduction

Chapter 2: Neodymium isotope composition and rare earth element distribution of East Antarctic continental shelf and deep water

Chapter 3: High-precision Pb isotope analysis of seawater using Nobias chelate resin and ^{207}Pb-^{204}Pb double-spike MC-ICP-MS

Chapter 4: Pathways and processes controlling the distribution of anthropogenic lead in the interior of the Southern Ocean

List of Tables

Chapter 2: Neodymium isotope composition and rare earth element distribution of East Antarctic continental shelf and deep water

Chapter 3: High-precision Pb isotope analysis of seawater using Nobias chelate resin and ^{207}Pb-^{204}Pb double-spike MC-ICP-MS

Chapter 1

Introduction

The role of trace elements and their isotopes varies significantly in the ocean. While some elements act as important nutrients in biological production (e.g., Fe, Zn, Cd), others can be used as tracers of ocean circulation (e.g., Nd, Pb) or anthropogenic pollution (e.g., Pb, Hg). The focus of this thesis will be on the application of Nd and Pb isotopes to trace water masses and pollution in the ocean.

1.1. Rationale of the GEOTRACES programme

A significant amount of knowledge about past ocean conditions, and consequently the processes governing modern global climate change, has been acquired from trace-element isotope archives in marine sediments. These geochemical archives provide information about past changes in important marine parameters and conditions (e.g., seawater carbonate chemistry, ocean circulation and biological productivity) and are a crucial source of information about the role of the ocean system in past climate change (Henderson, et al., 2007). Accurate reconstructions of marine conditions in the past will provide important insights into the future consequences of global climate change. However, without understanding the modern-day biogeochemical cycling of key trace elements and their isotopes, the ability to apply these as proxies for oceanographic processes is severely limited.

In the modern ocean, the biogeochemical cycles of many trace elements and their isotopes have been significantly perturbed by various anthropogenic activities, including the release of large quantities of toxic and radioactive elements to the ocean. Understanding the pathways and processes that govern the fate of these contaminants is important in order to protect the marine environment. However, this requires specific knowledge about the natural biogeochemical cycling of these contaminants so that the impact of anthropogenic activities can be fully constrained.

Despite the importance of understanding the biogeochemical cycles of trace elements and their isotopes, the sources and sinks of these elements in the ocean, as well as the mechanisms controlling their internal cycling, remain largely unconstrained. Since the mid-2000s, however, there has been a concerted effort to address this problem. The international research programme GEOTRACES was established “to identify processes and quantify fluxes that control the distributions of key trace elements and isotopes in the ocean, and to establish the sensitivity of these distributions to changing environmental conditions” (GEOTRACES plan, 2006). In order to achieve this aim, the programme has three main objectives:

(1) To determine the global ocean distribution of selected trace elements and their isotopes and to evaluate the sources, sinks and internal cycling of these species to characterise more completely the physical, chemical and biological processes regulating their distributions;

(2) To understand the processes involved in marine trace element cycles sufficiently well so that the response of these cycles to global change can be predicted, and their impact on the carbon cycle and climate is understood;

(3) To understand the processes, which control the concentrations and isotope compositions of geochemical species used for proxies of the past environment, both in the water column and in the substrates that reflect the water column.

Several "key parameters" were defined as part of the GEOTRACES programme including Nd isotopes as a tracer of natural sources of trace elements to the ocean and proxy for ocean circulation; and Pb isotopes as a tracer of natural and anthropogenic Pb sources to the ocean. As such, this thesis contributes to the overarching aim of the international GEOTRACES programme and, by extension, the wider understanding of the impact of climate change and anthropogenic activities on the environment.

1.2. Neodymium isotopes in the ocean

1.2.1. Neodymium isotope systematics

Neodymium has seven isotopes (^{142}Nd, ^{143}Nd, ^{144}Nd, ^{145}Nd, ^{146}Nd, ^{148}Nd and ^{150}Nd), with a radiogenic isotope, ^{143}Nd, produced by α-decay of ^{147}Sm (half-life = 1.06 x 10^{11} yrs; $\lambda = 6.54 \times 10^{12}$ yr^{-1}; Dickin, 2005). The natural variability of the ^{143}Nd/^{144}Nd ratio in rocks is small because of the long half-life of ^{147}Sm and the limited natural variability of the parent to daughter (Sm/Nd) ratio. As a consequence, ^{143}Nd/^{144}Nd ratios are commonly expressed in ε_{Nd} notation:

$$\varepsilon_{Nd} = \left(\frac{\frac{143_{Nd}}{144_{Nd}} sample}{\frac{143_{Nd}}{144_{Nd}} CHUR} - 1 \right) 10^4$$

where CHUR (Chondritic Uniform Reservoir) is the mean ^{143}Nd/^{144}Nd value measured for chondritic meteorites which is assumed to be identical to the present-day average for the bulk silicate earth (^{143}Nd/^{144}Nd CHUR = 0.512638; Jacobsen and Wasserburg, 1980).

The use of the Nd isotope system as a geological tool is founded on the variability of the parent (^{147}Sm) and daughter (^{143}Nd) isotope ratio in natural rocks, which is ultimately controlled by the age of the rock and the mineralogical processes during rock formation and breakdown (i.e., crystallisation or weathering). During igneous processes, the parent element Sm is slightly more compatible than the daughter element Nd, meaning it is preferentially retained in the mantle during the melting process. Neodymium is more likely to enter the melt phase, leading to an enrichment of Nd in crustal rocks (Figure 1.1). The elemental fractionation between Sm and Nd is a consequence of the lanthanide contraction: Samarium has a smaller ionic radius, making it more compatible in the mineral assemblage of the mantle compared to the larger Nd ion. Consequently, old rocks of the continental crust have low Sm/Nd ratios and therefore exhibit low $^{143}Nd/^{144}Nd$ ratios (lower than the bulk silicate earth) or an unradiogenic (negative) ε_{Nd} value (Figure 1.1). Conversely, the modern terrestrial mantle and young rocks evolved to have high $^{143}Nd/^{144}Nd$ ratios and radiogenic (more positive) ε_{Nd} values (Figure 1.1), reflecting the evolution of earth's mantle over billions of years (i.e., high Sm/Nd ratios due to continuous depletion during melt extraction).

1.2.2. Sources of neodymium to the ocean

The main sources of the lithogenic element Nd to the ocean were originally thought to be fluvial and aeolian inputs (e.g., Goldstein et al., 1984). Over the past 20 years, however, the exchange of sediments along continental margins with seawater has been shown to act as a major contributor to the global seawater Nd budget (e.g., Lacan and Jeandel, 2005).

The rare earth element (REE) concentrations of rivers are several orders of magnitude higher than seawater concentrations (e.g., Elderfield et al., 1990). The direct supply of dissolved REEs from rivers to the ocean must overcome intense colloidal precipitation within the fresh/brackish regions of an estuary (e.g., Elderfield et al., 1990; Sholkovitz, 1995). Estimates suggest that approximately 70–95% of riverine dissolved light rare earth elements (LREEs, including Nd) are removed in estuaries (Sholkovitz, 1995). Despite the high removal rate, riverine REE particulates deposited as sediments in the high-salinity region of an estuary can become suspended, re-dissolved and eventually released into coastal waters (e.g., Sholkovitz, 1995; Rousseau et al., 2015). Moreover, a recent study found that suspended particles transported by the Amazon River were continuously weathered during estuarine mixing, which ultimately affects the net dissolved Nd flux to the ocean (Rousseau et al., 2015).

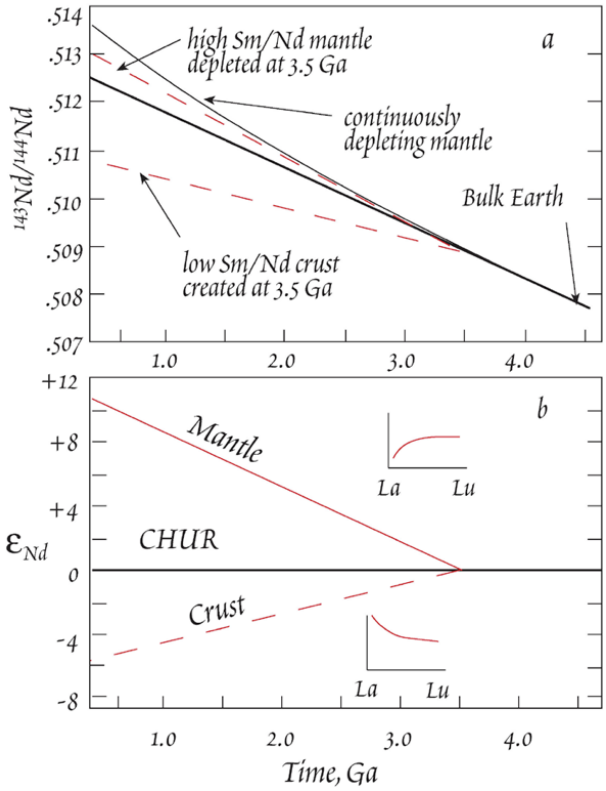

Figure 1.1 (a) The evolution of Nd isotopes over time in the crust and mantle. The bold black line shows the evolution of CHUR while the dotted red lines correspond to the depleted crust formed at 3.5 Ga and the corresponding enriched residual mantle. (b) The evolution of Nd isotopes over time in the crust and mantle converted to ε_{Nd}. The insets display the rare earth element (REE) fractionation of the crust and mantle which produces the isotopic evolution over time (White, 2013).

Another important source of Nd to the ocean comes from atmospheric dust (e.g., Tachikawa et al., 1999) with global atmospheric fluxes estimated to be ~30–130% of global river fluxes (Greaves et al., 1994). However, solubility of Nd from mineral dust is considered to be relatively low (i.e., a few percent; see discussion in van de Flierdt et al., 2004).

Observational and conceptual studies suggest that sediments along continental margins could represent the most important source of dissolved Nd to the ocean (e.g., Jeandel et al., 2007; Lacan and Jeandel, 2005). Models substantiate these observations by quantifying the global Nd flux from continental margins as ~1 x 10^{10} g yr^{-1}, which is approximately two orders of magnitude greater than riverine (~3 x 10^{8} g yr^{-1}) and atmospheric (~1–3 x 10^{8} g yr^{-1}) sources (Arsouze et al., 2009; Rempfer et al., 2011).

Like rivers, hydrothermal fluxes exhibit significantly greater REE concentrations than seawater; but unlike rivers, hydrothermal inputs have a negligible effect on the global budget of dissolved Nd in the ocean as hydrothermal REEs are efficiently scavenged from seawater by localised Fe-Mn oxides near hydrothermal vent sites (e.g., German et al., 1990; Halliday et al., 1992).

1.2.3. Neodymium isotopes as a water mass tracer

Since the 1970's, a series of pioneering studies found that the distinct Nd isotope compositions of different areas of continental crust are responsible for the distinct ε_{Nd} values that are found for different water masses in their respective ocean basins (e.g., Piepgras, et al., 1979; Piepgras and Wasserburg, 1980; Piepgras and Wasserburg, 1982). This is a reflection of the quasi-conservative behaviour of Nd isotopes in the ocean, which implies that the ε_{Nd} value of a water mass is controlled predominantly by inputs from the weathering of continental rocks proximal to the water mass formation site. This signature is subsequently only altered by conservative mixing between water masses. The relatively short residence time of Nd in seawater (~300–1000 years; e.g., Jeandel, et al., 1995; Tachikawa, et al., 2003; Rempfer et al., 2011) compared to the average ocean mixing time (~1500 years; Broecker and Peng, 1982) prevents homogenisation of the distinct water mass ε_{Nd} values between ocean basins and thus produces distinct basin-scale variability in water mass ε_{Nd} values (Lacan, et al., 2012; van de Flierdt et al., 2016). Weathered inputs from older cratonic rocks and sediments in the North Atlantic and younger volcanic rocks and sediments in the North Pacific produced two ε_{Nd} 'endmembers' in the ocean: the unradiogenic North Atlantic Deep Water ($\varepsilon_{Nd} = -13.5$; Piepgras and Wasserburg, 1987) and the radiogenic North Pacific Deep Water ($\varepsilon_{Nd} = -4$; Piepgras and Jacobsen, 1988). Physical mixing of these deep water masses along the thermohaline circulation belt produces intermediate ε_{Nd} values in Southern Ocean deep water masses ($\varepsilon_{Nd} = -8$; Piepgras and Wasserburg, 1982; Bertram and Elderfield, 1992; Jeandel, 1993). These initial findings demonstrated that Nd isotopes may constitute a robust proxy for past ocean circulation.

Since the beginning of the GEOTRACES programme, improved spatial resolution of Nd isotope data has underscored three important caveats when considering Nd isotopes as a water mass tracer. Firstly, many ocean regions do not exhibit strong correlations between Nd isotopes and conservative hydrographic properties because of different circulation regimes. In the western Atlantic, Nd isotopes show strong co-variation with salinity in laterally advected

deep water masses, particularly the cold and fresh Labrador Seawater (von Blanckenburg, 1999; Lambelet et al., 2016). In contrast, Stichel et al., (2015) found that the homogeneity of Nd isotope compositions along the eastern Atlantic makes it difficult to identify the distinct warm and salty Mediterranean Overflow Water. This could be the result of active vertical homogenisation and/or less pronounced lateral advection of water masses, both of which would compromise the ε_{Nd} signal of a water mass.

Secondly, boundary exchange processes can significantly alter the Nd isotope composition of seawater by adsorption and/or desorption mechanisms, particle dissolution and benthic fluxes from continental margins, seamounts and the seafloor with very different ε_{Nd} values (Figure 1.2; Lacan and Jeandel, 2005; Rickli et al., 2014). While some studies concluded that boundary exchange can be locally limited and its effects eventually diluted by surrounding waters (Stichel et al., 2012a), a few studies observed the 'fingerprint' of this non-conservative behaviour of Nd in water masses far from the area of seawater-sediment interaction (Lacan and Jeandel, 2001; Rickli et al., 2014).

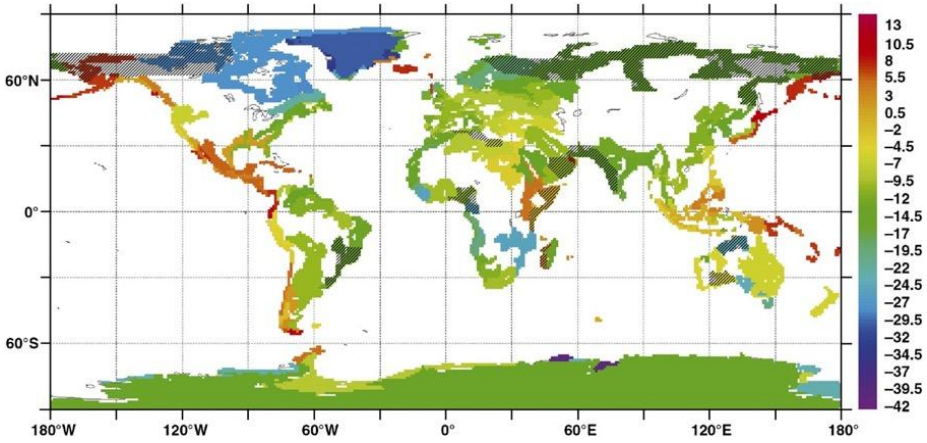

Figure 1.2 Extrapolated map from discrete data points showing the variability of the Nd isotope composition for all continental margins surrounding the ocean (Jeandel et al., 2007).

Finally, Nd concentrations exhibit nutrient-like behaviour and are de-coupled from Nd isotopes, which tend to reflect water mass mixing, a paradigm known as the Nd-paradox (Lacan and Jeandel, 2001; Goldstein and Hemming, 2003). Neodymium concentrations are depleted at the surface and they increase with depth and in deep waters along the ocean conveyor belt (Elderfield and Greaves, 1982; De Baar et al., 1985; Bertram and Elderfield, 1993). This suggests that processes other than external Nd inputs to the ocean and water mass

mixing affect Nd distribution and cycling in the water column. Reversible scavenging, which encompasses both adsorption and desorption between dissolved and particulate Nd in the water column, has been proposed to account for the Nd-paradox (Tachikawa et al., 1997; Siddall et al., 2008; Arsouze et al., 2009; Rempfer et al., 2011).

Despite the recent progress made by the GEOTRACES programme, there are still large gaps in observational data, which makes it difficult to fully constrain the cycling of Nd in the ocean and assess whether Nd isotopes are indeed a robust water mass tracer.

1.3. Lead isotopes in the ocean

1.3.1. Lead isotope systematics

Lead has four naturally occurring stable isotopes: ^{208}Pb, ^{207}Pb, ^{206}Pb and ^{204}Pb. The ^{204}Pb isotope is the lowest abundance isotope (~1%; Dickin, 2005; Komárek et al., 2008) and is a primordial nuclide which can act as a constant reference isotope. In contrast, ^{206}Pb, ^{207}Pb and ^{208}Pb are radiogenic daughters from the decay chains of ^{238}U, ^{235}U and ^{232}Th, respectively. The isotopic composition of Pb in a terrestrial reservoir is a function of three variables: (1) the decay rate of the parent isotopes (half-lives = 4.47 Gyr, 0.704 Gyr and 14.01 Gyr for ^{238}U, ^{235}U and ^{232}Th, respectively; Le Roux and Glendenin, 1963; Jaffey, et al., 1971); (2) the initial abundance of U, Th and Pb isotopes in the source reservoir; and (3) the geological age of the reservoir.

During the formation of a terrestrial reservoir, elemental fractionation will generate a unique chemical fingerprint characterised by distinct U/Pb and Th/Pb ratios. The differences in the initial abundances of the radioactive parents ^{235}U, ^{238}U and ^{232}Th (relative to the inherited Pb already present), coupled with the contrasting half-lives of the decay systems, produce different relative abundances of the radiogenic daughters ^{206}Pb, ^{207}Pb and ^{208}Pb over a period of time. Reservoirs with distinct Pb isotope signatures, furthermore, mix over time to generate a diverse array of terrestrial reservoirs that have unique intermediate Pb isotope compositions (Settle and Patterson, 1980; Bollhöfer and Rosman, 2000). Therefore, the Pb ores that are employed in various anthropogenic activities, and the subsequent anthropogenic emissions from these ores, exhibit unique Pb isotope signatures. The relative mass differences between Pb isotopes are relatively small due to the high atomic weight of Pb. As a consequence, the stable isotope fractionation of Pb isotopes from physical, chemical or biological processes is essentially negligible compared to the observed radiogenic isotope

effects. Therefore, Pb isotopes have been employed as a tool to identify the different sources and pathways of Pb in the environment (e.g., Rosman et al., 1994; Knowlton and Moran, 2010).

1.3.2. Spatiotemporal changes in anthropogenic Pb sources to the North Atlantic

During the 19th and 20th century, anthropogenic emissions from high temperature processes such as fossil fuel combustion, non-ferrous metal smelting and waste incineration have significantly perturbed the global biogeochemical cycles of many trace elements (Nriagu and Pacyna, 1988; Duce et al., 1991). These high temperature processes vaporise and emit volatile elements and pollutants such as Pb to the atmosphere where they eventually condense onto fine atmospheric particles (e.g., Cziczo et al., 2009) before being transported long distances to the marine environment (Duce et al., 1991). The dominance of atmospheric inputs of Pb over riverine fluxes (Duce et al., 1991), coupled with the short residence time of Pb in the surface ocean (1–2 years; Craig et al., 1973; Bacon et al., 1976) and the magnitude of historic anthropogenic Pb emissions, means that the modern ocean is completely overwhelmed by anthropogenic Pb sources (Boyle et al., 2014).

Seawater Pb isotope composition data has provided important information about the spatiotemporal changes of Pb sources to the modern ocean. Since the first seawater Pb measurements in the 1970s (Schaule and Patterson, 1981), most studies have focused on the North Atlantic Ocean, a region surrounded by early-industrialised countries and historically the biggest consumers of leaded petrol (Nriagu, 1990). The Bermuda Atlantic Time Series (BATS) station, in conjunction with regional coral analyses dating back to 1780, has provided an extensive time series of surface Pb concentrations and isotope compositions for the western North Atlantic Ocean (Figure 1.3; Kelly et al., 2009). The surface water trends have followed the fluctuations in emission intensities and alterations in Pb ores used to sustain US and European industrial activities over the course of the last two hundred years (Wu and Boyle, 1997a; Véron et al., 1998; Hurst, 2002; Kelly et al., 2009).

For example, the trend in Pb isotope composition between 1920 and 1980 follows the different Pb ores used for the production of the petrol additive tetraethyllead. Before 1973, Ethyl Corporation (US), the main producer of tetraethyllead, used both Idaho smelter Pb with low $^{206}Pb/^{207}Pb$ ratios (~1.15) and the Mississippi ores with high $^{206}Pb/^{207}Pb$ ratios (~1.22), resulting in a fluctuating intermediate $^{206}Pb/^{207}Pb$ signature in the coral records (Figure 1.3).

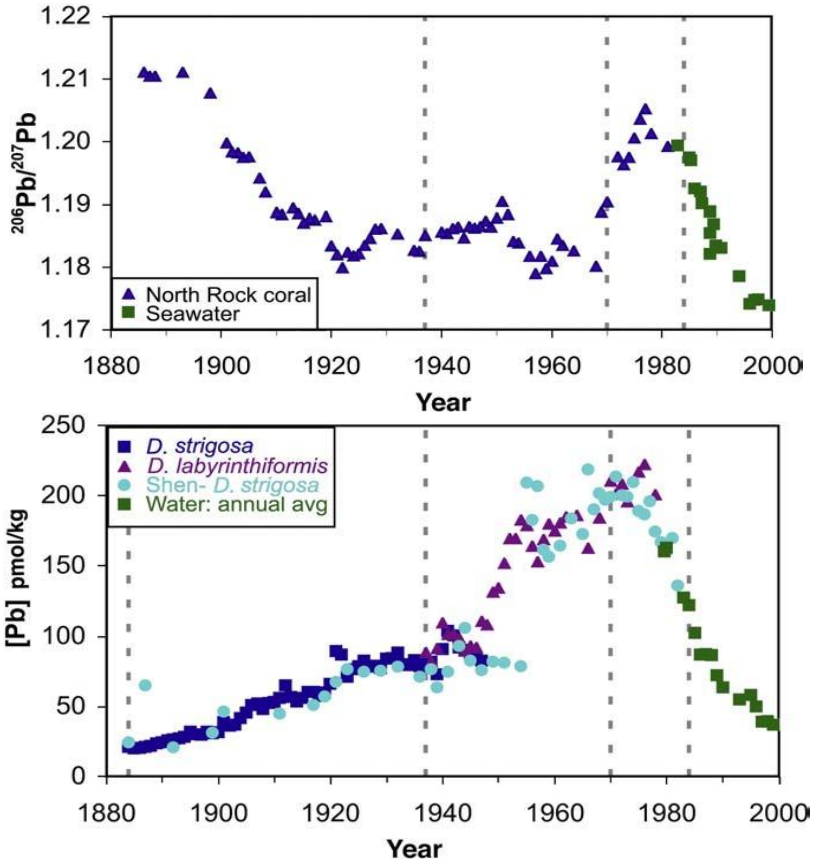

Figure 1.3 Pb concentration (top) and $^{206}Pb/^{207}Pb$ ratio (bottom) of surface water near Bermuda between 1880–2000. The data before 1979 corresponds to analyses from three types of corals. The data between 1979–2000 corresponds to the annual average of direct seawater measurements (Kelly et al., 2009).

After 1973, tetraethyllead production explicitly used Mississippi ores because the Idaho smelter ceased production (Boyle et al., 2014). As a consequence, westerlies shifted to much higher $^{206}Pb/^{207}Pb$ isotope ratios and supplied a distinctly higher $^{206}Pb/^{207}Pb$ signature to BATS surface waters (Figure 1.3; Weiss et al., 2003).

Similarly, the decrease in surface water Pb concentrations and isotope compositions in the 1980s can be attributed to the dominance of Eurafrican emissions as the phase-out of leaded petrol in the US began earlier than in European countries (Véron et al., 1994). The majority of European tetraethyllead was produced by Associated Octel (UK), which used Pb ores with significantly lower $^{206}Pb/^{207}Pb$ ratios from Australia, Morocco and Sweden (1.11–1.16;

Hopper et al., 1991; Grousset et al., 1994). At the same time, during the phase-out of leaded petrol, the US began to source Mexican-Peruvian ores for tetraethyllead production with much lower $^{206}Pb/^{207}Pb$ ratios than Mississippi ores, resulting in prevailing US westerlies with much lower $^{206}Pb/^{207}Pb$ emissions (Weiss et al., 2003). The complete phase-out of leaded petrol across North America and Europe in the 1990s resulted in both Pb concentrations and $^{206}Pb/^{207}Pb$ ratios decreasing and the Pb isotope composition reflecting the low-level industrial emissions from both continents (Boyle et al., 2012; Noble et al., 2015).

Across the entire North Atlantic basin, Pb concentration and isotope composition data from the eastern, subarctic and tropical regions have provided information about natural sources of Pb and the long-distance transport mechanisms of anthropogenic emissions. In the early 1980s, the surface water distribution of Pb isotope compositions in the North Atlantic displayed strong latitudinal sections, which mirrored the prevailing wind belts in the atmosphere (Weiss et al., 2003). As expected, surface seawater Pb isotope compositions were dominated by two anthropogenic end members (Eastern US and European sources), with the Eastern US source dominating the latitudinal section of the prevailing westerlies. However, the presence of a strong Eastern US signature towards Africa within the trade wind zone suggested that lateral advection of surface seawater from the western North Atlantic to the North African Basin must also act as an important mechanism for the transport of Pb emissions (Véron et al., 1994). Moreover, the presence of a different Pb isotope signature in the Iberian Basin provided evidence of a regionalised natural North African Pb source to the North Atlantic (Weiss et al., 2003).

Since the phase-out of leaded petrol in the US and Europe, surface waters have become increasingly homogenous in Pb concentrations and isotope compositions, with no significant bias towards any of the anthropogenic Pb sources (Weiss et al., 2003). Recent high-resolution transects across the North Atlantic have even shown that natural sources are now important sources of Pb to the North Atlantic (Bridgestock et al., 2016; Zurbrick et al., 2018). For example, tropical Atlantic surface waters now exhibit a significant component of North African dust (characterised by high $^{206}Pb/^{207}Pb$ and $^{208}Pb/^{207}Pb$ ratios) that accounts for 30–50% of the total surface water Pb budget (Bridgestock et al., 2016).

1.3.3. Processes controlling the distribution of Pb in the North Atlantic

Since the late 1970s, vertical distributions of Pb concentrations and isotope compositions have been measured at BATS to provide a time series of the transport of anthropogenic Pb to the western North Atlantic deep ocean (Figure 1.4). More recently, high-resolution full depth transects across the North Atlantic have been obtained during several GEOTRACES cruises to help elucidate the processes controlling the distribution of anthropogenic Pb emissions in the water column (Noble et al., 2015; Bridgestock et al., 2016; Zurbrick et al., 2018).

Surface water Pb is exported predominantly by advection and eddy diffusion along isopycnals into the thermocline and deeper waters. Given the residence time of Pb in the deep ocean (50–200 years; e.g., Craig et al., 1973; Bacon et al., 1976; Schaule and Patterson, 1981) and the decadal timescales of thermocline water ventilation (Jenkins, 1980), anthropogenic Pb in surface waters will be exported to the deep ocean on decadal timescales. This is highlighted by the BATS vertical profile time series in the western North Atlantic where thermocline Pb concentrations decrease following a reduction in the surface Pb concentrations on a decadal timescale (Figure 1.4; Boyle et al., 2014; Noble et al., 2015).

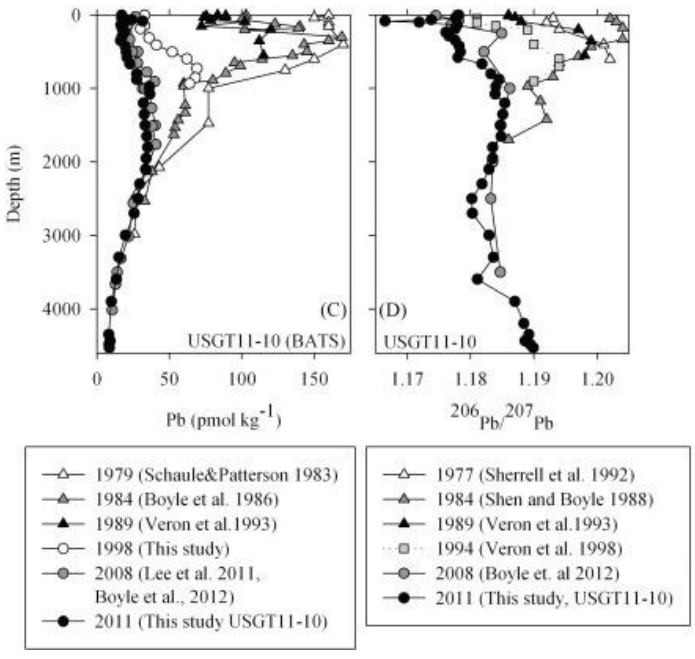

Figure 1.4 Vertical profiles for Pb concentrations (left) and $^{206}Pb/^{207}Pb$ ratios (right) at BATS showing the temporal variability in the water column between 1977 and 2011 (Noble et al., 2015).

The dominance and strength of lateral advection in transporting anthropogenic Pb in the western Atlantic has been shown by a recent high resolution transect across the North Atlantic basin. Peak Pb concentrations reside at the subsurface but become progressively broader as the signal deepens towards the west (Noble et al., 2015). This subsurface anthropogenic Pb distribution reflects the differences in ventilation timescales across the basin where the western North Atlantic deep waters correspond to more recently ventilated waters, which were exposed to peak Pb emissions during the US phase-out of leaded petrol in the early 1980s.

Modelling studies support the conclusion that physical ventilation of the surface mixed layer dominates the transport of surface anthropogenic Pb to the deeper ocean in the western North Atlantic Ocean (Boyle, 1986; Shen and Boyle, 1988). The inability of the models to reproduce the Pb profiles below the subsurface, however, implies that the vertical transport of anthropogenic Pb via scavenging and equilibrium exchange may exert some control on the distribution of Pb in this region. Recent observational discrepancies in Pb concentrations and isotope compositions of intermediate water masses provide empirical evidence that, although physical processes dominate the transport of anthropogenic Pb to intermediate and deep waters of the North Atlantic Ocean, there must be an interplay between advection and scavenging which controls the redistribution of Pb emissions in the region (Bridgestock et al., 2016; Zurbrick et al., 2018).

Although the GEOTRACES programme has increased the number of observational data over the last decade, data coverage across other ocean basins is still limited especially when compared to other trace element isotope systems (e.g., Nd). The lack of observations ultimately reflects the extreme analytical challenges presented by: (1) the necessity of ultraclean protocols for sampling and lab analysis to avoid sample contamination; (2) time-consuming Pb extraction, purification and measurement procedures; (3) inaccurate procedures for the correction of instrumental mass bias; and (4) insufficient instrumental detection limits to measure Pb isotopes in seawater at extremely low concentrations. Improvements in analytical protocols as well as high-resolution sampling transects in hydrographically and biogeochemically complex regions is critical in order to understand the processes that control the biogeochemical cycling of Pb in the ocean and its potential to act as a tracer of ocean processes.

1.4. Importance of the Southern Ocean

1.4.1. Ocean circulation and oceanographic fronts

The continuous zonal flow of atmospheric and oceanic circulation is a unique feature of the Southern Ocean (Figure 1.5). The westerlies, a strong belt of atmospheric flow located between 45°S and 55°S, drives the eastward flowing Antarctic Circumpolar Current (ACC; Figure 1.5; Trenberth et al., 1990; Lumpkin and Speer, 2007). The ACC circulates Antarctica with an annual mean transport of approximately 130 Sv and consists of a number of interlinked currents with multiple branches which produce highly dynamic flow (e.g., Sokolov and Rintoul, 2009). Despite the complexity of current flow, three main fronts can be distinguished: the Subantarctic Front (SAF), the Polar Front (PF) and the Southern ACC Front (SACCF; Orsi et al., 1995). At lower latitudes, the ACC is restricted by the SAF where warm and saline waters are separated from higher latitude cold fresh waters, while farther poleward, the SACCF forms the southern boundary of the ACC (e.g. Orsi et al., 1995). In between these two boundary fronts, the SAF and PF are characterised by strong physical and biogeochemical meridional gradients (Pollard et al 2002).

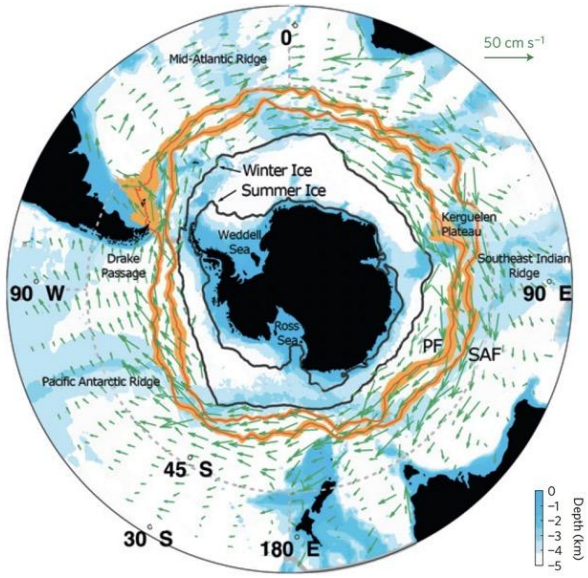

Figure 1.5 Map of the Southern Ocean with green arrows showing the direction and strength of the surface currents, with the largest arrows indicating the location of ACC flow. The orange bands show the mean geographical position of the Polar Front (PF) and Subantarctic Front (SAF) while the black lines denote the mean winter and summer ice extent (Marshall and Speer, 2012).

The meridional gradients between the SAF and PF are a product of steeply rising isopycnals caused by meridional flow in the Southern Ocean (Figure 1.6; Speer et al., 2000; Rintoul and Trull, 2001). The southward transported Circumpolar Deep Water (CDW) upwells south of the PF and supplies nutrient-rich deep waters to the surface. The path of the CDW return flow depends on the density of the deep water. Following upwelling, less dense Upper CDW is transported northward in a wind-driven Ekman flow and subducts north of the PF (Figure 1.6). The denser shoaling Lower CDW water mixes with dense shelf water along the Antarctic continental ice shelf to form Antarctic Bottom Water (AABW; Rintoul, 1998; Orsi et al., 1999). The steep density gradients between the fronts results in a weakly stratified water column that can be destabilised, leading to deep winter mixed layers and large seasonal variations of mixed layer depths (e.g., de Boyer Montegut et al., 2004). The deep winter mixing, and associated formation of subducted Antarctic Intermediate Water (AAIW) and Subantarctic Mode Water (SAMW), is critical in ventilating the intermediate ocean and transferring nutrients to lower latitudes (Rintoul and Trull, 2001).

1.4.2. Southern Ocean biogeochemistry: A High-Nutrient-Low-Chloroyphyll region

The upwelling of deep waters in the Southern Ocean supplies nutrient-rich waters to the surface through isopycnal and diapycnal transport (Figure 1.6; Pollard et al., 2002). Despite the high supply of macronutrients to the surface waters of the Southern Ocean, biological production and phytoplankton growth across the Southern Ocean remains limited (e.g., Sarmiento et al., 2004). The combination of high macronutrient concentrations and low chlorophyll levels means that the Southern Ocean forms the largest High-Nutrient-Low-Chlorophyll (HNLC) region in the world (Martin et al., 1990; Sarmiento and Orr, 1991).

Primary production in the Southern Ocean is controlled predominantly by the availability of light and micronutrients (e.g., Sunda and Huntsman, 1997). The amount of light available for primary production depends on latitude, season, sea ice coverage and the intensity of vertical mixing. When light is not limiting, biological productivity in the Southern Ocean is limited by the supply of iron (Fe), a critical micronutrient in the photosynthetic process of phytoplankton (e.g. Martin et al., 1990; De Baar and De Jong, 2001; Tagliabue et al., 2010). There are very few external sources of Fe to the Southern Ocean: inputs from atmospheric sources are highly regionalised, such as the Kerguelen plateau (Blain et al., 2007); hydrothermal sources have recently been shown to be important in the Southern Ocean, but these sources only trigger local hotspots of enhanced biological

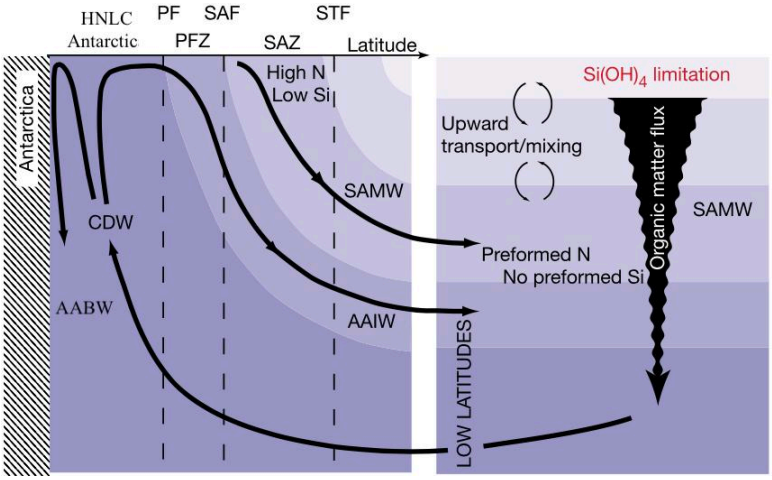

Figure 1.6 Schematic showing the meridional flow and distribution of nutrients (silicate) controlling the biological processes across the Southern Ocean fronts. Upper Circumpolar Deep Water (CDW) upwells to the surface of the Southern Ocean to form the HNLC Antarctic region. This water mass is transported to the north across the Polar Front (PF) into the Polar Front Zone (PFZ), where Antarctic Intermediate Water (AAIW) forms, and then across the Subantarctic Front (SAF) into the Subantarctic Zone (SAZ). The shades of purple correspond to areas of high (deep purple) and low (light purple) silicate concentrations. Silicate is gradually depleted in surface waters in an equatorward direction until silicate limitation is reached at low latitudes (adapted from Sarmiento et al., 2004).

activity and their large-scale effect on Southern Ocean biogeochemistry still remains unconstrained (e.g., Ardyna et al., 2019); and continental riverine inputs of Fe are negligible (De Baar and De Jong, 2001). As is the case for the macronutrients, upwelling is one of the main sources of Fe to surface waters (Figure 1.6; Tagliabue et al., 2010); but unlike macronutrients, Fe is continuously removed down through the water column via scavenging, which converts bioavailable soluble Fe to colloidal or particulate forms through adsorption, precipitation and aggregation (e.g., Wu et al., 2001). As a consequence, Fe to macronutrient ratios of upwelled deep waters are insufficient to sustain biological production in the Southern Ocean resulting in the HNLC Antarctic region (Figure 1.6).

The Southern Ocean PF signifies the biogeochemical divide between the HNLC Antarctic region, where summer inventories of all macronutrients (nitrate, phosphate and silicate) are available in surface waters, and the subantarctic sector, where Fe supplied from sea ice and upwelled silica-rich deep are sufficient to sustain intense diatom blooms and opal production (Figure 1.6; Brzezinski et al., 2002; Sarmiento et al., 2004). Moving northwards, while nitrate and phosphate remain in abundance, silicate concentrations become

progressively depleted and eventually limit opal production (Figure 1.6). The Southern Ocean is therefore characterised by distinct biogeochemical provinces with strong opal gradients across the frontal system (Figure 1.6).

The combination of ACC transport, meridional circulation and biogeochemical regimes is critical in the global transfer of physical (heat and salt) and biogeochemical (carbon, oxygen etc.) properties to other ocean basins and the atmosphere. The Southern Ocean therefore plays an important role in mitigating present and past climate change (e.g., Marshall and Speer, 2012). An understanding of the biogeochemical cycling of Nd and constraints on the present-day Nd isotope compositions of key bottom and deep-water formation sites are essential pre-requisites for the application of Nd isotopes as a palaeo-proxy. Moreover, the dynamic interplay between physical and biogeochemical processes in the Southern Ocean will inevitably play an important role in the global redistribution of both anthropogenic and natural Pb. Despite the importance of the Southern Ocean, the data currently available for seawater Nd isotope composition in this region is spatially limited to results obtained for seawater samples collected in the vicinity of West Antarctica (Figure 1.7 (a)). There is an even greater paucity of Pb isotope data available for seawater samples across the Southern Ocean (Figure 1.7 (b)).

1.5. Research aims, objectives and thesis outline

The aim of this thesis is to understand the processes that control the biogeochemical cycling of Nd and Pb in the Australian Sector of the Southern Ocean proximal to East Antarctica. In order to achieve this aim, the following research objectives were designed and addressed:

Objective 1: Determine the processes that govern the Nd isotope composition of deep and bottom waters (AABW) across the East Antarctic continental shelf.

In chapter 2, Nd isotope composition and dissolved rare earth element (REE) concentration results are presented for seawater samples collected along the Wilkes Land continental margin. The study was conducted to test the hypothesis that AABW at this location reflects the regional weathered inputs of Nd to the Southern Ocean from Antarctica.

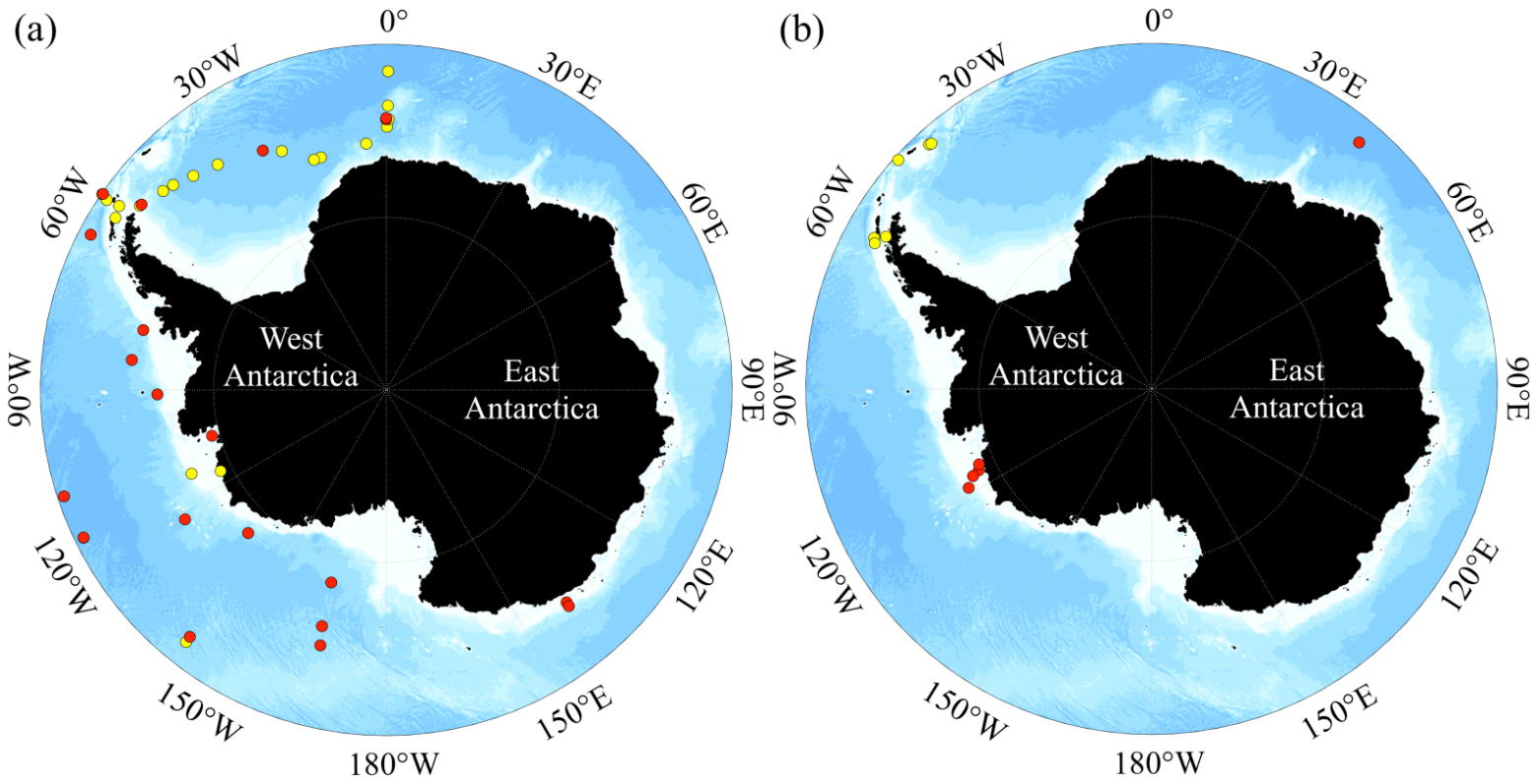

Figure 1.7 Published (a) Nd isotope and (b) Pb isotope seawater measurements for depth profiles (red) and surface water samples (yellow) from across the Southern Ocean (> 50°S). Data for Nd isotopes were taken from a compiled dataset (van de Flierdt et al., 2016), while the Pb isotope data are from Flegal et al. (1993), Lee et al. (2015) and Ndungu et al. (2016).

Objective 2: Develop an analytical procedure to determine the Pb isotope composition of seawater that (1) provides unbiased and precise results and (2) has a greater analytical throughput than established high-precision methods.

Chapter 3 describes a new method that was developed to provide high-precision seawater Pb isotope analyses while simultaneously improving the analytical throughput. The procedure involves solid-phase extraction of Pb from seawater using Nobias chelate PA-1 resin, purification by anion-exchange chromatography, and analyses by MC-ICP-MS using a ^{207}Pb-^{204}Pb double-spike to correct for instrumental mass discrimination.

Objective 3: Determine the relative importance of the different transport mechanisms for the redistribution of anthropogenic Pb into the interior of the Southern Ocean.

In chapter 4, seawater samples were collected along a meridional transect between Australia and Antarctica for analyses of Pb concentrations and isotope compositions. This was conducted to test the hypothesis that particle scavenging is as an important mechanism for the transport of anthropogenic Pb to the deep ocean in this region.

Chapter 2

Neodymium isotope composition and rare earth element distribution of East Antarctic continental shelf and deep water

Abstract

Antarctic Bottom Water (AABW) plays a key role in the Earth's climate system by forming the lower limb of the Meridional Overturning Circulation and, thus, influencing large scale redistribution of heat, nutrients and carbon. The neodymium (Nd) isotope composition of seawater has been used as palaeo-proxy to understand circulation changes in AABW through time. The biogeochemical processes controlling Nd in seawater, however, remain under constrained, and modern observations of Nd isotopes in AABW are still scarce and geographically limited.

To overcome this limitation, samples were collected for Nd isotope and rare earth element (REE) analysis at nine stations along the Wilkes Land continental margin and in the Australian-Antarctic Basin (65°S 125°E). The results show that the different water masses have the following Nd isotope characteristics: Antarctic Surface Water (AASW), ε_{Nd} = −9.0 ± 1.0 (2sd; *n* = 22); Modified Circumpolar Deep Water (MCDW), ε_{Nd} = −8.8 ± 0.8 (2sd; *n* = 22); Antarctic Bottom Water (AABW), ε_{Nd} = −8.3 ± 0.5 (2sd; *n* = 17). MCDW values are within the range of published data for Circumpolar Deep Water in the Southern Ocean. This, coupled with no observable fractionation of REEs, suggests that boundary exchange processes do not modify the Nd isotope composition of MCDW on the continental slope and shelf. AABW observations confirm regional variability around Antarctica: AABW along the Wilkes Land continental margin exhibits a distinct intermediate ε_{Nd} signature lying between that of published data for less radiogenic Atlantic sector AABW (ε_{Nd} = −9.1 ± 0.7) and more radiogenic Pacific sector AABW (ε_{Nd} = −7.4 ± 0.9). REE data suggests, however, that the regional ε_{Nd} signature is not caused by distinct local continental inputs, but instead reflects mixing of advected AABW with local MCDW and CDW.

An algorithm, using a neural network model based on spatial and hydrographic data, has been developed to assess the spatial variability of ε_{Nd} for AABW across the Southern Ocean. The model predicts the Nd isotope composition of AABW with high accuracy (*n* = 67; 2sd = 0.44). When the algorithm is applied to an independent hydrographic dataset (WOA13), the results highlight the difference between radiogenic and unradiogenic AABW in the east and west, respectively, as well as ε_{Nd} extrema in areas of AABW formation. Further studies from different regions around East Antarctica, however, are required to quantify how boundary exchange and local inputs affect deep and bottom water ε_{Nd} signatures.

2.1. Introduction

Since the late 1970's, neodymium (Nd) isotopes, or the radiogenic $^{143}Nd/^{144}Nd$ ratio, commonly expressed as ε_{Nd}, (the parts per 10,000 deviation of any sample from the Chondritic Uniform Reservoir, CHUR; Jacobsen and Wasserburg, 1980), have been identified as an effective 'quasi-conservative' water mass tracer for present and past ocean circulation (e.g., Piepgras et al., 1979; Piepgras and Wasserburg, 1980; Goldstein and Hemming, 2003; Piotrowski et al., 2008). The term quasi-conservative explains how the initial ε_{Nd} value for a water mass is set by the external inputs of weathered rocks with different petrogenetic origins around the formation zone of a water mass (e.g., Piepgras et al., 1979; Elderfield and Greaves, 1982; Jeandel et al., 2007), but how subsequent changes in open ocean ε_{Nd} are controlled by water mass mixing (e.g., Piepgras et al., 1979; Piepgras and Jacobsen, 1988). This quasi-conservative behaviour, coupled with a shorter Nd ocean residence time (300–1000 years; Tachikawa et al., 2003; Rempfer et al., 2011) relative to global ocean mixing timescales (1500 years; Broecker and Peng, 1982), allows Nd isotopes to act as an inter-basin water mass tracer with useful applications in regions of important and complex physical dynamics.

The Southern Ocean plays an important role in present and past climate change through global heat redistribution and carbon cycling (e.g., Deacon, 1937; Deacon, 1984; Gruber et al., 2004; Russell and Dixon, 2006; Lumpkin and Speer, 2007; Morrison and Hogg, 2012). Antarctic Bottom Water (AABW) constitutes an important component of the lower limb of the overturning circulation (Speer et al., 2000; Pardo et al., 2012). Several studies have attempted to understand past changes in formation and northward AABW transport using Nd isotopes on a range of timescales (e.g., Scher and Martin, 2004; Piotrowski et al., 2008; Piotrowski et al., 2009; Lippold et al., 2016; Lang et al., 2016). The success of this approach, however, depends on two key requirements: firstly, a well-established end-member value for AABW as a frame of reference for palaeo-oceanographic studies; and secondly, an understanding of the mechanisms controlling modern Nd biogeochemical cycles. Progress on both issues, however, ultimately depends on the number of observations available. Moreover, improved spatial resolution of Nd isotope data in the Southern Ocean over the last decade has provided direct observations of Nd isotope variability in AABW that could provide clear challenges for palaeo-proxy applications.

Neodymium isotopes in the Southern Ocean not only reflect physical mixing but are also a sensitive tracer for the provenance of weathering inputs from the Antarctic continent

(Carter et al., 2012; Stichel, 2012b; Rickli et al., 2014). AABW has a number of different formation sites, including, but not restricted to, the Weddell Sea, the Ross Sea, Adélie Land and Prydz Bay (Orsi et al., 1999). The observed local differences between Ross Sea Bottom Water (RSBW, $\varepsilon_{Nd} = -7$; Basak et al., 2015), a local precursor of AABW in the Ross Sea, and AABW in the Atlantic sector of the Southern Ocean ($\varepsilon_{Nd} = -8.6$ to -9.6; Stichel et al., 2012b) could reflect localisation of AABW caused by regional varieties of external inputs across the continent at the site of water mass formation.

A further consideration is the influence of 'boundary exchange' on the Nd isotope composition of AABW. Boundary exchange refers to all the potential processes leading to either the net release or removal of Nd at the land-ocean interface which can either set or alter the Nd isotope signature of a water mass (e.g., Lacan and Jeandel, 2005; Jeandel and Oelkers, 2015; Jeandel, 2016). Rousseau et al. (2015) has shown that the Nd isotope composition of waters in the North Atlantic are set by lithogenic inputs around the continental margins of the Amazon estuary. Importantly, boundary exchange processes can significantly alter the Nd isotope composition of seawater by adsorption and/or desorption mechanisms, particle dissolution and benthic fluxes during water mass transit near ocean boundaries (Jeandel and Oelkers, 2015; Jeandel, 2016). For example, Rickli et al. (2014) reported direct observations of changes in the Nd isotope signature of AABW across the Pacific sector of the Southern Ocean that could be related to the range of ε_{Nd} values in the shelf lithology of Antarctica (Roy et al., 2007; van de Flierdt et al., 2007). The coupled effect of regional inputs during water mass formation and 'boundary exchange' reinforces the possibility of very different and localised ε_{Nd} signatures of AABW around the Antarctic continent.

One of the main sources of AABW in the Southern Ocean comes from the Adélie Land coast in East Antarctica (e.g., Orsi et al., 1999; Rintoul, 1998). This form of AABW constitutes the main bottom water exported across the Wilkes Land continental margin and into the eastern Indian Ocean (e.g., Nakano and Suginohara, 2002; Fukamachi et al., 2010). Although recent observations have characterised the Nd isotopic fingerprint of this particular form of AABW near its formation site (Lambelet et al., 2018), there still remains a severe lack of data around East Antarctica (Figure 1.1 (a)). Consequently, the potential influence of regional inputs and 'boundary exchange' on this local AABW as it is exported across the Wilkes Land continental margin has not yet been examined. This study will present 61 new measurements of water column Nd isotope composition and dissolved rare earth element (REE) concentrations from the Wilkes Land continental margin. The integration of REE patterns with Nd isotope composition of seawater will help elucidate how inputs and

biogeochemical processes are affecting the ε_{Nd} signatures of deep and bottom waters masses along East Antarctic margins. The aim, therefore, will be to (1) understand how local varieties of AABW may reflect different regional inputs of Nd to the Southern Ocean from East Antarctica; and (2) examine the extent to which boundary exchange either sets or alters the Nd isotope signature of deep and bottom water masses in East Antarctica.

2.2. Oceanographic setting

2.2.1. Regional circulation in the Australian-Antarctic Basin

The Australian-Antarctic basin is bounded to the south by Wilkes Land and Adélie Land continental margin, to the west by the Kerguelen Plateau and to the north and east by the South-Indian Ridge (Figure 2.1 (a)). The regional circulation patterns show three important features: the Antarctic Circumpolar Current (ACC), a cyclonic gyre and the westward Antarctic Continental Slope Current (Figure 2.1 (a); McCartney and Donohue, 2007).

In the southwest Australian-Antarctic Basin, a western boundary current travels northward along the eastern margin of the Kerguelen Plateau (black arrows; Figure 2.1 (a)). This western boundary current forms from the northward extension of the westward Antarctic Continental Slope Current (blue arrows; Figure 2.1 (a)) and is enhanced by eastward residual flow through the Princess Elizabeth Trough (purple arrows; Figure 2.1 (a)) and the Fawn Trough (green arrows; Figure 2.1 (a)). An eastward flow, a combination of the ACC and warmer waters from the Atlantic, enters the Australian-Antarctic Basin north of the Kerguelen Plateau (red arrows; Figure 2.1 (a)). The Crozet-Kerguelen Confluence forms east of the Kerguelen Plateau where the eastward flowing ACC encounters the western boundary current and its residual currents. This confluence moves eastwards after separating from the western boundary current and extends with the ACC along the Southeast Indian Ridge and continues into the Pacific Ocean. The western boundary current flows along the centre of the basin, eventually recirculating south and then west along the continental slope with the Antarctic Continental Slope Current (black arrows; Figure 2.1 (a)). The western boundary current and the Crozet-Kerguelen Confluence form, respectively, the western and northern limb of this strong cyclonic gyre in the Australian-Antarctic Basin.

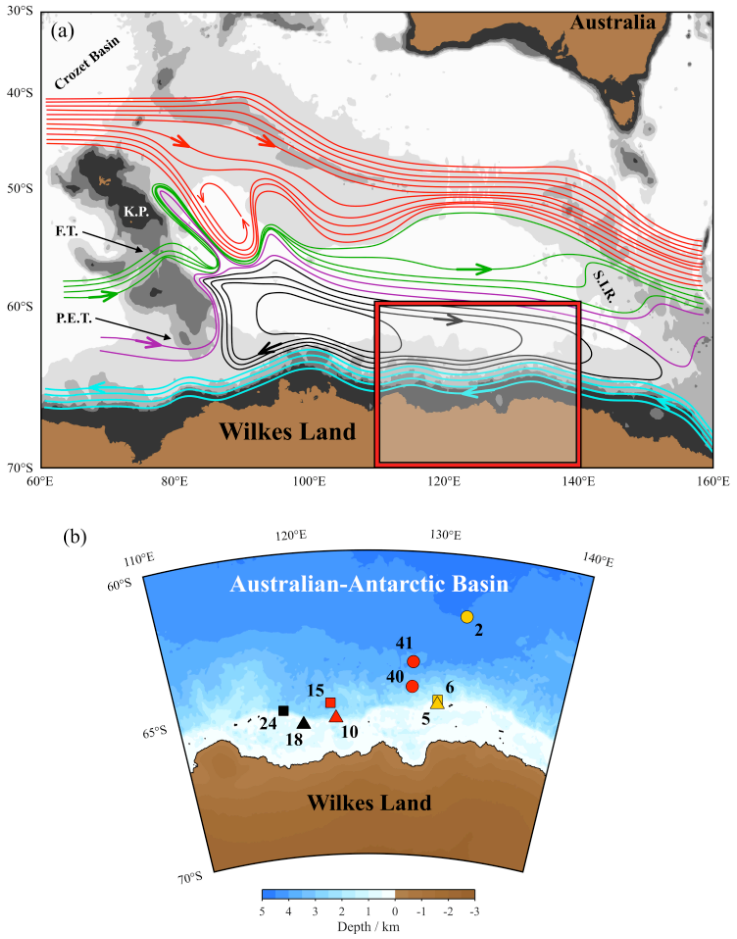

Figure 2.1 Study area of the Wilkes Land continental margin, East Antarctica. Figure 2.1 (a) is a schematic of the regional circulation patterns off the coast of eastern East Antarctica (Wilkes Land) and around the Australian-Antarctic Basin (adapted from McCartney and Donohue, 2007). The following abbreviations are used to label geographical landmarks: Princess Elizabeth Trough (P.E.T.), Fawn Trough (F.T.), Kerguelen Plateau (K.P.), and the Southeast Indian Ridge (S.I.R.). Blue and solid black arrows represent the westward flow of the Antarctic Slope Current and the cyclonic gyre within the Australian-Antarctic Basin, respectively. Part of the cyclonic gyre passes west into the Weddell-Enderby Basin and recirculates back into the Australian-Antarctic Basin as currents through the Princess Elizabeth Trough (purple arrows) and Fawn Trough (green arrows). The red arrows correspond to the Antarctic Circumpolar Current domain. East of Kerguelen Plateau, the three inflows from the west (purple, green and red) and the western boundary current of the Australian-Antarctic Basin cyclonic gyre form the Crozet-Kerguelen Confluence. The red box indicates the area of Figure 2.1 (b), which enlarges the location of nine sampling stations in the area of the Wilkes Land continental margin (NBP1503). The circles (stations 2, 40 and 41) represent the deep offshore stations, the squares (stations 6, 15, and 24) show the slope stations and triangles (stations 5, 10 and 18) denote the shelf stations. The symbol colours denote relative latitudinal position of the stations: yellow (east), black (west) and red (in between).

2.2.2. Study area: Wilkes Land continental margin

There were two main considerations when selecting the sampling location: (1) the formation site of local AABW and (2) the circulation regime of this local AABW precursor. Local AABW forms at the Adélie Depression between 140°E–146°E along the continental margin (Rintoul, 1998). Bindoff et al., (2000) has also associated extrema in local bottom water properties on the continental slope at 139.8°E and 128.4°E with bottom-water-formation processes. Considering the Antarctic Continental Slope Current drives bottom waters westward along the margin, capturing the local AABW would require sampling west of 140°E. On the Wilkes Land continental margin between 120°E and 135°E, nine stations were identified where seawater samples could be collected to cover the features of the continental margin (Figure 2.1 (b)). The stations are categorised depending on their proximity to the Antarctic continent: three deep offshore stations (> 3000 m depth; stations 2, 40 and 41); three continental slope stations (1000–3000 m depth; stations 6, 15 and 24); and three shelf stations (< 1000 m depth; stations 5, 10 and 18). All stations are located along the Antarctic continental margin within the Antarctic Zone and do not cross the major fronts of the Southern Ocean (e.g., Sokolov and Rintoul, 2002). The shelf system is extremely dynamic and affected by seasonal sea ice formation. Here, the hydrographic data (temperature, salinity and oxygen) from the expedition NBP1503 on the R/V Nathaniel B. Palmer during the Austral Autumn (3/04/2015–30/04/2015) is used to define the seasonal hydrographic conditions and water masses at the time of sampling.

2.2.3. Water mass distribution

The major water masses dominating the Australian-Antarctic basin are Antarctic Surface Waters (AASW), Modified Circumpolar Deep Water (MCDW), and Antarctic Bottom Water (AABW; Figure 2.2). These water masses have been identified based on potential temperature (θ, °C), practical salinity (S, psu) and neutral density (γ^n, kg m^{-3}; Jackett and McDougall, 1997).

Antarctic Surface Water is defined as a water mass with a neutral density less than 28.03 kg m^{-3}, potential temperatures ranging from –1.84 °C to 2.0 °C and salinity values greater than 34 (Figure 2.2; Whitworth et al., 1998). The large potential temperature range enables a subdivision of AASW into three classes: cold ($\theta < -1.6$ °C), intermediate ($-1.6 < \theta < 0$ °C) and warm ($\theta > 0$ °C). The coldest class tends to reside over the shelf and continental slope while the two warmer forms of AASW sit more offshore between the

MCDW and shallow temperature-minimum layer (Figure 2.2 (a–c); Bindoff et al., 2000). AASW in the study region has very high AASW temperatures off the continental slope (Figure 2.2 (a)). Station 6, located on the continental shelf, but close to offshore station 41, has very cold AASW (θ = –1.75 °C; Figure 2.2 (b)).

Modified Circumpolar Deep Water is a mixture of offshore Circumpolar Deep Water (CDW) and local shelf water as CDW flows poleward onto the continental margin (Whitworth et al., 1998). This water mass occupies the density range in between the AASW and AABW in the study region, and is significantly colder (θ < 1.8 °C) and less saline (S < 34.7) than normal CDW (Wong et al., 1998). Bindoff et al., (2000) showed that CDW exhibits a distinct spatial structure, with the warmest and most saline CDW (θ ~ 2°C) residing to the west (80°E–100°E), and more modified colder (θ < 1.75 °C) and fresher waters in the east (140°E–150°E) close to the formation areas of bottom waters. Figure 2.2 reinforces this spatial structure: CDW is not present at intermediate and deep water depths in this region and MCDW has a persistent signal off the continental shelf at deep stations (e.g., station 41; Figure 2.2 (a)). Station 2 and 41, however, show very high potential temperature values (θ = ~1.75 °C) across an appropriate salinity range (S = ~34.7) which may signify the presence of a less modified CDW off the continental slope.

AABW is the dominant bottom water of the region with a neutral density greater than 28.27 kg m^{-3}, potential temperatures greater than –1.7°C and a salinities between 34.65 and 34.72 (Whitworth et al., 1998). Figure 2.2 (c) indicates that AABW is not present on the shelf during the austral summer and, therefore, MCDW forms the bottom water mass for stations closest to the continent. Adélie Land Bottom Water (ALBW) constitutes an important local precursor for AABW, but there is no evidence in this region of ALBW with its dense (γ^n > 28.27 kg m^{-3}), warm (θ < –0.5 °C) and less saline (34.66 < S < 34.68) properties.

2.3. Materials and methods

2.3.1. Sampling procedure

A total of 61 seawater samples across nine stations were collected for Nd isotope composition and REE analysis during the expedition NBP1503 on the R/V Nathaniel B. Palmer between 3rd April and 30th April 2015. All samples were collected using 12 L standard Niskin bottles (Ocean Test Equipment Inc.) mounted on a CTD rosette frame. Approximately 10 L of seawater was filtered directly from the Niskin bottles into collapsible 10 L pre-cleaned LDPE containers using 0.2 μm AcroPak500 cartridge filters.

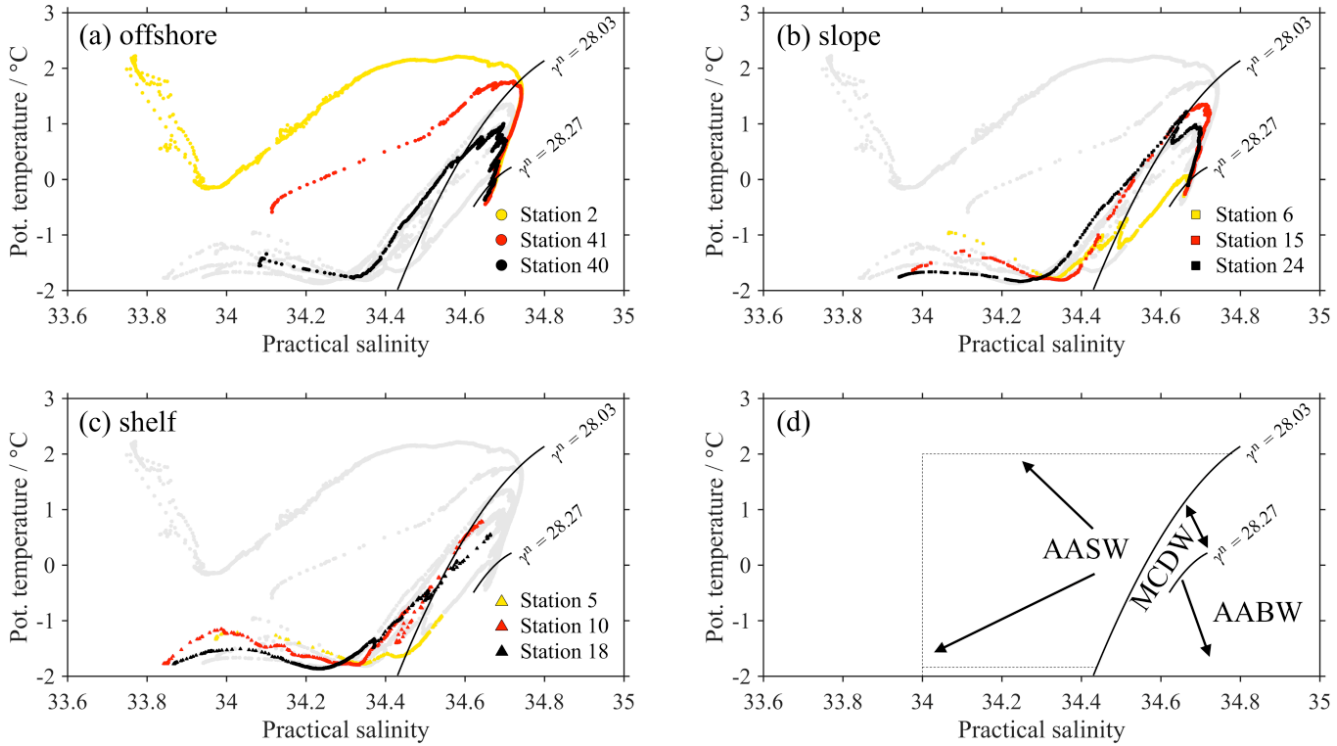

Figure 2.2 Potential temperature vs salinity diagrams for the stations sampled during the NBP1503 cruise along the Wilkes Land continental margin: (a) offshore stations, (b) slope stations and (c) shelf stations. Results for offshore, slope and shelf stations are shown in all three panels in grey for comparison, with colours highlighting the data for the respective area. The solid black lines, labelled with $\gamma^n = 28.03$ and 28.27 kg m^{-3}, are the neutral density surfaces that separate the Antarctic Surface Waters (AASW) from Modified Circumpolar Deep Water (MCDW), and MCDW from Antarctic Bottom Water (AABW), respectively. The dashed lines represent the upper salinity and potential temperature limits of AASW. As neutral density is a function of temperature, salinity and other parameters (pressure, latitude and longitude), the contours are computed by fitting second order polynomials to the entire NBP1503 CTD dataset. A schematic of water mass definitions and distributions for the area is shown in (d).

The samples were then acidified on board to pH ~2 with 6 M HCl (2 mL L-1; Trace Metal Grade, Fisher Scientific). At the MAGIC Laboratories (Imperial College London, UK) in a Class 100 (ISO V) laminar flow hood, ~250 mL aliquots of each seawater sample were taken in pre-cleaned 500 mL LDPE bottles for REE analyses.

2.3.2. Neodymium isotope composition and concentration analysis

The analytical procedure to determine the Nd isotope composition and concentration of seawater was carried out in the MAGIC Laboratories at Imperial College London (UK) and has been described in detail by Crocket et al. (2014) and Lambelet et al. (2016).

Briefly, the 10 L seawater samples were weighed and spiked with a calculated amount of ^{150}Nd (97.8% purity; provided by D. Vance, ETH Zurich) and, after leaving to equilibrate for one week, the pH of the samples was raised to 3.5 using aqueous NH_3. The samples were then pre-concentrated by pumping the seawater through C^{18} cartridges loaded with a REE complexing agent (Shabani et al., 1992; Jeandel et al., 1998). The REEs for each sample were subsequently eluted from the cartridges using 6 M distilled HCl and then refluxed with aqua regia (3:1 ratio of concentrated HCl and concentrated HNO_3) to remove any remaining organics. After the pre-concentration phase, a two-step ion exchange chromatography protocol was required to isolate Nd from the other ions. Firstly, the REEs were extracted from the post-pumping residual sample matrix using Biorad® AG50W-X8 resin (200-400 μm mesh). Then, the Nd was separated from the remaining REEs using Eichrom® Ln spec resin (20–50 μm mesh size, 0.32 mL resin bed). After the column chromatography, samples were dried, then re-dissolved in HCl and loaded with an activator solution, TaF_5, onto degassed single W filaments (0.025 mm thick, 0.51 mm wide, 99.95% pure; sourced from H. Cross Company). Neodymium isotope compositions and concentrations were then measured as Nd oxides (NdO^+) on a Thermo Finnigan Triton thermal ionisation mass spectrometer.

A neodymium oxide reagent, JNdi-1, with a high $^{143}Nd/^{144}Nd$ ratio and low abundance of neighbouring REEs (e.g., Ce and Sm; Tanaka et al., 2000) was used as an external standard to determine measurement precision on the MAGIC Titron TIMS. The average of the $^{143}Nd/^{144}Nd$ ratio of 5–10 ng JNdi-1 loads, typically five measurements per batch of 16 samples, was used to correct sample measurements to the JNdi-1 reference value (0.512115 ± 0.000007; Tanaka et al., 2000). The accuracy of the procedure was monitored using 10 ng loads of column processed USGS rock standard BCR-2 ($^{143}Nd/^{144}Nd$;

ε_{Nd} = 0.06 ± 0.19, 2sd, *n* = 5). Over the course of the 11-month measurement period, the faraday cups for the MAGIC Titron TIMS had to be cleaned and eventually the graphite insets had to be replaced due to natural degradation. Measured $^{143}Nd/^{144}Nd$ ratios for the JNdi-1 standard before and after cleaning the cups, and with the new inlets installed were slightly different but did not affect the reproducibility of the JNdi-1 standards or the correction factor applied to sample measurements/ BCR-2 standards within the same batch. The JNdi-1 $^{143}Nd/^{144}Nd$ ratios measured during sample analysis across an 11-month period were between 0.512047 ± 0.000010 and 0.512112 ± 0.000011, with a long-term external reproducibility of ± 0.000011 (ε_{Nd} = ± 0.23; 2sd; *n* = 35). The external reproducibility of the five standards of a batch was propagated with the internal reproducibility of each sample measurement to assess the overall error of the seawater sample. The procedural blanks (seawater pumping, column chemistry and mass spectrometry) ranged from 131 to 422 pg of total Nd, which corresponds to less than 2% of the total Nd content of the most Nd depleted sample analysed. Following the method outlined by Struve et al., (2016), mixing calculations showed that the blanks did not compromise the Nd isotope composition and therefore no blank correction was required.

2.3.3. Rare earth element concentration analysis

The concentrations of all REEs were analysed at the Scottish Association for Marine Science (SAMS, UK) by ICP-MS (XSeries 2, Thermo Finnigan) following the purification of REE from the seawater matrix by an automated pre-concentration system, the SeaFAST Pico (Elemental Scientific Inc., Nebraska, USA). The method is an adaptation from the online procedure developed by Hathorne et al., (2012) for offline measurement by ICP-MS.

Firstly, 25 mL aliquots of the seawater samples, along with calibration solutions and seawater standards, were doped with indium standard (Aristar®) to act as an internal standard and correct for instrumental drift. Then, the SeaFAST Pico used a double 10 mL sample loop loading and 0.5 mL elution method to pre-concentrate the seawater sample. Finally, the REE concentrations were determined by ICP-MS measurements using external standardisation based on a six-point calibration of REE standards (Aristar®). The accuracy of sample measurements was determined by repeat analysis of GEOTRACES inter-calibration seawater sample (BATS 2000 m; *n* = 10). All elements are in good agreement with inter-calibration results, deviating by < 5% from the consensus values, with La (7.7%) and Tm (5.2%) the only exceptions (Table 2.1). The precision was assessed by repeat measurements of a bulk

Table 2.1 REE concentrations for reference seawater samples (BATS 2000 m and an internal "bulk seawater' standard) measured during the analysis of NBP1503 seawater samples

	Element														
	Y	La	Ce	Pr	Nd	Sm	Eu	Gd	Tb	Dy	Ho	Er	Tm	Yb	Lu
BATS 2000 m															
Consensus values (pmol kg^{-1})[a]		23.6	5.1	4.0	17.1	3.5	0.9	4.9	0.79	5.8	1.52	5.1	0.75	4.8	0.81
2sd (pmol kg^{-1})		2.8	2.3	0.4	1.2	0.4	0.1	0.5	0.08	0.4	0.09	0.3	0.05	0.3	0.04
Relative 2sd (%)		11.8	44.4	8.8	7.0	9.8	10.9	10.9	9.60	6.6	5.98	5.0	6.35	5.2	4.96
BATS 2000 m (this study, 2019)															
average value (pmol kg^{-1}; n = 10)	139.6	22.0	4.9	4.0	17.4	3.6	0.9	4.9	0.8	5.7	1.50	5.1	0.7	4.7	0.82
2sd (pmol kg^{-1})	5.7	2.6	1.6	0.4	1.2	0.8	0.1	0.6	0.1	0.5	0.06	0.4	0.1	0.8	0.08
Consensus deviation (%)[b]		–7.7	–3.9	–1.0	1.5	3.1	–4.7	0.2	–0.2	–0.8	–1.54	–0.2	–5.2	–2.0	1.51
BSW (this study, 2019)[c]															
average value (pmol kg^{-1}; n = 9)	173.8	29.4	4.8	4.5	20.3	3.9	1.0	5.4	0.9	6.6	1.8	6.3	1.0	6.7	1.2
2sd (pmol kg^{-1})	11.7	4.1	0.8	0.4	2.3	0.3	0.2	0.5	0.1	0.7	0.3	0.8	0.1	0.7	0.2
Relative 2sd (%)	6.70	13.8	17.6	8.6	11.3	8.0	15.6	8.5	12.5	10.8	15.2	13.1	10.0	10.9	13.4

[a] Dissolved REE consensus values for the BATS 2000 m seawater sample obtained during the international GEOTRACES inter-calibration exercise (van de Flierdt et al., 2012). Yttrium was not measured/reported during the international inter-calibration exercise.

[b] Calculated percentage deviation of the absolute concentrations measured in this study from the absolute concentrations of the consensus values ($[REE]–[REE]_{consensus}/[REE]$) x 100.

[c] 900 mL aliquot was taken from a sample from the NBP1503 cruise (station 24, niskin bottle 14) to measure as an internal bulk seawater (BSW) standard during the analyses of all the seawater samples.

seawater standard throughout the course of the analyses, yielding an external reproducibility between 6.7 and 17.6% (2sd, n = 9; Table 2.1). The procedural blanks, ≤ 1% of the most depleted sample for all REEs except Ce (3.65%), were monitored throughout a run for each batch of samples and corrected on a batch per batch basis.

2.3.4. Neural network empirical model

2.3.4.1. Structure and function of neural network

The distribution of ε_{Nd} for AABW was modelled using a feedforward backpropagation neural network. This type of neural network operates based on a two-phase learning process: (1) the forward propagation of input variables followed by the backward propagation of the output activations obtained through neural network processes; and (2) the update of input weights and bias levels during every iteration to reduce the residual error (e.g., Bishop, 1995; Jo et al., 2012; Velo et al., 2013).

The structure of the neural network consists of interconnected neurons divided into three distinct layers (Beale et al., 2017). Firstly, the initial 'input layer' has as many neurons as the selected number of input variables and is responsible for receiving and transmitting input arguments. Secondly, the 'hidden layer' contains an optimised number of neurons based on training, with each individual neuron containing a summation function and a tan-sigmoid activation function to produce output activations. Finally, the 'output layer' has the same number of neurons as the number of target variables and uses a summation function with a linear transfer function to process the output activation received from the hidden layer.

In terms of how the model functions, the input variables from the input layer of the neural network are weighted and transferred to a neuron of the hidden layer. Here, the input variables and weights are passed through the summation function with an independent bias term, and then through the activation function to calculate the output activation, y_j, for a neuron of the hidden layer:

$$y_j(x_i) = \tanh\left(\sum_{i=1}^{n} w_{ij}x_i + b_j\right) \quad (2.1)$$

where x_i denotes the inputs entering the neuron from the input layer; w_{ij} are the weights associated with each input for neuron, j; b is the bias term for neuron, j; and n is the total number of inputs. The term tanh represents the tan-sigmoid activation function, which maps

the output activation, y_j, between (1, –1). This hyperbolic tangent function is represented by the following equation:

$$\tanh(x) = \frac{e^x - e^{-x}}{e^x + e^{-x}} \quad (2.2)$$

The output activation, y_j, from each neuron of the hidden layer is weighted and passed with the output layer bias term to the summation and linear function of the output layer neuron(s):

$$f(y_j) = \sum_{j=1}^{m} W_j y_j + B \quad (2.3)$$

where y_j denotes the output activation of a neuron in the hidden layer; W_j are the weights associated with each input from a neuron of the hidden layer; B represents the bias term of the output layer; and m denotes the total number of neurons in the previous hidden layer. After a complete iteration, the network compares the output values to the target variable and calculates the residual network error. This error is then back-propagated to allow the network to adjust the weights and biases associated with each neuron in the network layers to develop a more precise algorithm. This neural network structure is an effective method to solve function approximation problems, such as mapping Nd isotope composition based on hydrographic data, because of two main attributes: (1) the repeated feedforward and backpropagation of the inputs and outputs progressively minimises the model error; and (2) the combined non-linear and linear activation functions in the hidden and output layers, respectively, allow the development of an algorithm that can account for complex correlations between a variety of parameters (Gardner and Dorling, 1995).

3.4.2.2. Neural network selected input variables

The model input variables used to predict the Nd isotope composition of AABW were latitude, longitude, potential temperature (θ), salinity (S) and oxygen (O_2). These variables constrain the natural variability of ε_{Nd} for AABW caused by water mass formation/ventilation (θ, S and O_2) and physical mixing (θ, S), but also the spatial variability caused by continental inputs around the different sites of AABW formation (latitude and longitude). Moreover, these variables are available as metadata for all ε_{Nd} observations across the Southern Ocean (Carter et al., 2012; Stichel et al., 2012b; Garcia-Solsona et al., 2014; Rickli et al., 2014; Basak et al., 2015; Lambelet et al., 2018; this study) and represent key parameters of large

hydrographic datasets, which will be used to map the Nd isotope composition of AABW through the trained neural network algorithm.

3.4.3.3. Neural network configuration and training

The neural network modelling was conducted in MATLAB® using the 'feedforwardnet' function from the Neural Network Toolbox (MathWorks®, USA; Beale et al., 2017). The training of the neural network was performed by the Bayesian regularization backpropagation method ('trainbr' function). Baysian regularisation combines the most effective training method for non-linear function fitting problems, the Levenberg-Marquardt approximation (Hagan and Menhaj, 1994; Velo et al., 2013), with an automated optimal regularisation technique to avoid model overfitting (Beale et al., 2017). This is beneficial for studies with limited observations as internal regularisation provides an alternative to subset data validation, and thus, allows the neural network to use the entire dataset to develop an algorithm. The optimal size of the neural network, i.e., the number of neurons in the hidden layer, can only be determined by trial and error of different network sizes and the evaluation of the output statistical results/errors (Beale et al., 2017). For each neural network structure ranging from 5–25 neurons, the training procedure was run 10 times and the neural network with the highest correlation coefficient and the least RMSE was determined to be the optimal size. For this study, a neural network size of 8 neurons provided the best fitting function, i.e., a compromise between model underestimation and model overfitting.

2.4. Results

2.4.1. Spatial distribution of neodymium isotope composition

The results of Nd isotope composition measurements for all seawater samples are shown as vertical depth profiles of ε_{Nd} in Figure 2.3. Overall, there is little variation in Nd isotope composition in the study area, with ε_{Nd} values ranging from –9.9 (station 18; 248 m depth) to –7.8 (station 40; 2752 m depth). Figure 2.3 shows that there is some vertical variability in the ε_{Nd} values of seawater at all stations. The two offshore stations, Station 2 and 41 exhibit slightly more radiogenic ε_{Nd} values in the top 500 m (ε_{Nd} = –8 to –9) and are about 1 epsilon unit lower at depths of 500–1000 m. Between 1500 m and the bottom depth, both profiles show homogenous values at around ε_{Nd} = –8.7 ± 0.5 (2sd; n = 13; Figure 2.3 (a)). Slope stations 15 and 24 show identical profiles, with a sub-surface minimum of ε_{Nd} = –9.4 and

–9.6, respectively, and homogenous values between 1000–2500 m (ε_{Nd} = –8.3 ± 0.2; 2sd; n = 9). Station 6, the most easterly of the slope stations, shows slightly higher Nd isotope composition (ε_{Nd} = –7.9 to –8.6; Figure 2.3 (b)).

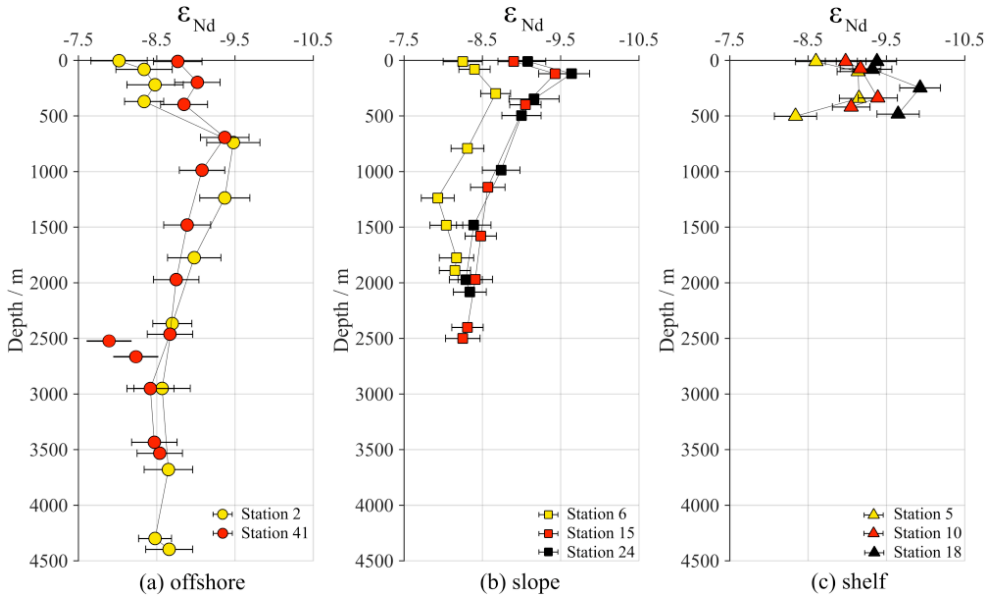

Figure 2.3 Depth profiles of dissolved Nd isotope compositions in the study area. (a) offshore, (b) slope and (c) shelf areas. The colour of the symbols represents the relative longitudinal position of the stations, with yellow denoting the most easterly station and black representing the most westerly station. The error bars denote propagated internal 2 sigma measurement errors and external 2 sigma uncertainties for repeat measurements of the pure Nd JNdi standard. This applies to all figures that feature uncertainties on measured Nd isotope compositions. The two data points in panel (a) with uncapped error bars represent deep water samples taken at station 40.

A similar east versus west gradient can be observed for the shelf stations, where the highest ε_{Nd} values are found at the easternmost station 5 with values of ε_{Nd} = –8.6 and –8.4 in 10 and 500 m water depth (Figure 2.3 (c)). Overall, there seems to be no discernible difference between ε_{Nd} values at offshore stations, slope stations and shelf stations at a comparable longitude for a given depth. There is, however, a clear east-west gradient along the shelf and slope: more radiogenic values are observed to the east and gradually shift, by about one epsilon unit, to less radiogenic values in the west (Figure 2.3 (b–c)).

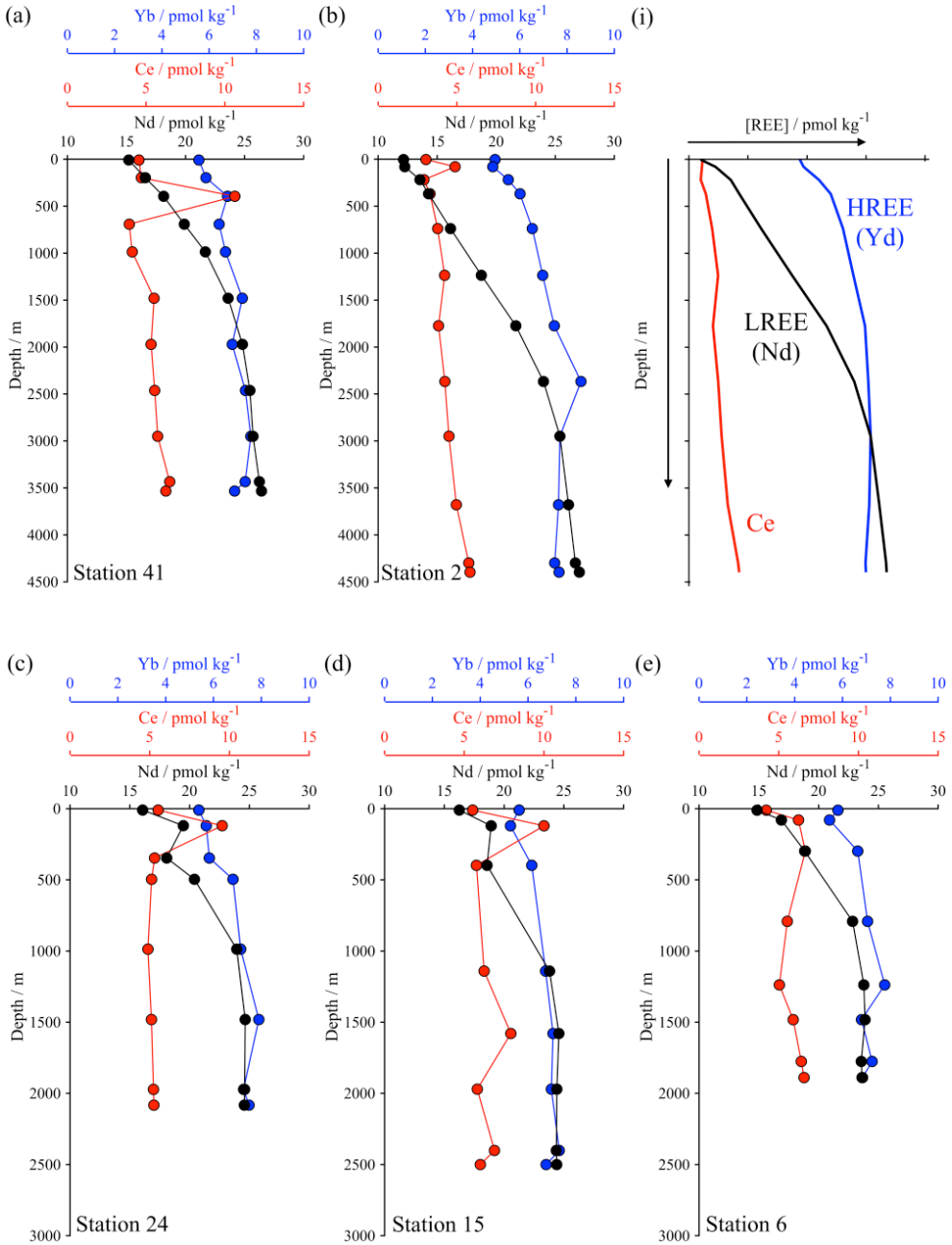
(a)
(b)
(c)
(d)
(e)
(i)
Yb / pmol kg-1
Ce / pmol kg-1
Nd / pmol kg-1
Depth / m
Station 41
Station 2
Station 24
Station 15
Station 6
[REE] / pmol kg-1
HREE
(Yd)
LREE
(Nd)
Ce

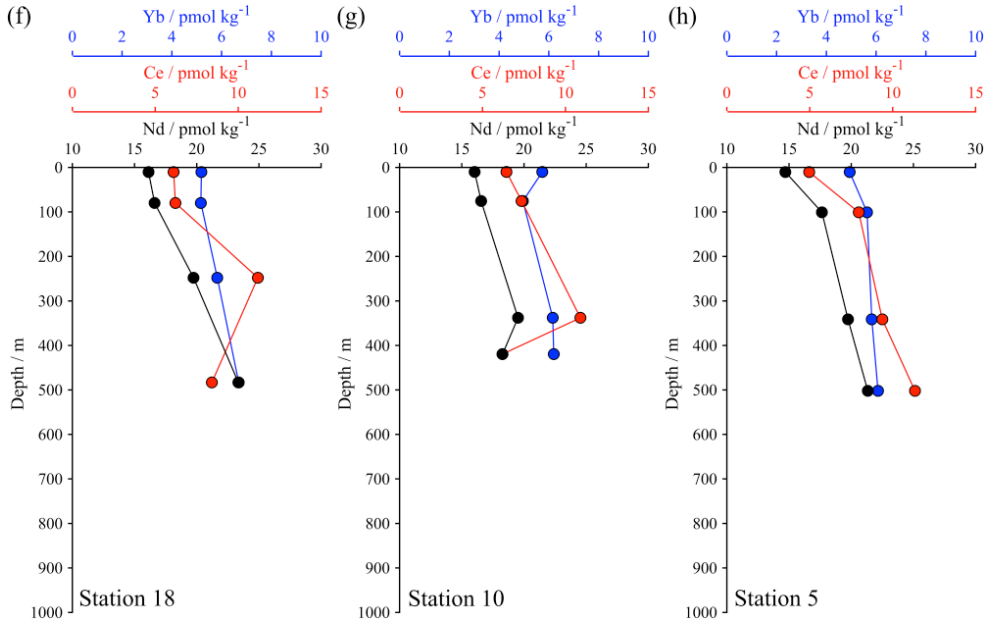

Figure 2.4 Depth profiles of representative dissolved rare earth element concentrations (REEs) in the study area for offshore (a–b), slope (c–e) and shelf (f–h) stations from west (right) to east (left). Light REEs (LREE)—Nd (black), heavy REEs (HREE)—Yb (blue), and Ce (red). The elements selected here were chosen to cover LREE and HREE variation as well as the redox sensitive element Ce. Neodymium concentration data was taken from isotope dilution calculations performed on the spiked isotopic measurements.

2.4.2. Spatial distribution of dissolved rare earth element concentrations

The depth profiles of three dissolved REE concentrations are shown in Figure 2.4 to highlight the range of patterns observed for REEs in the study area. Neodymium is used to denote the light rare earth elements (LREEs; i.e., La to Dy), Yb to represent heavy rare earth elements (HREEs; i.e., Ho to Lu), and Ce concentrations are presented because this element has unique redox properties. Neodymium concentrations increase from ~12–16 pmol kg^{-1} at the surface to ~22–26 pmol kg^{-1} at depth, with a much slower rate of increase beyond the middle of the water column (~500–1000 m) at offshore and slope stations (Figure 2.4 (a–e)). Patterns are broadly characterised by a convex shape or nutrient-like profile (Figure 2.4 (a–e)) with more linear increases observed at the slope stations (Figure 2.4 (f–h)). The overall increase in REE concentrations with depth is less pronounced and more linear for Yb (Figure 2.4). Small but analytically resolvable increases in Yb from ~4–5 pmol kg^{-1} at the surface to ~7–8 pmol kg^{-1} at depth is present across all stations (Table 2.1; Figure 2.4).

Cerium exhibits a very different behaviour compared to the other REEs. The concentration profiles for Ce show uniformity throughout the water column at the offshore and slope stations, with concentrations ranging between 4 and 6 pmol kg^{-1}. At offshore and slope stations 41, 15 and 24, Ce concentrations show a positive excursion to values of ~10 pmol kg^{-1} in the sub-surface (~50 to 500 m water depth). At all three shelf stations Ce concentrations increase from ~17 pmol kg^{-1} to ~20–25 pmol kg^{-1} at 350–500 m water depth.

Schematic trends for LREEs, HREEs, and Ce concentrations for offshore and slope stations are illustrated in Figure 2.4 (i). Key features are a general HREE enrichment over LREE, increasing LREE concentrations throughout the water column, but relatively invariant HREE and Ce concentrations.

2.5. Discussion

In order to assess the processes that govern the distribution of dissolved Nd isotope compositions of seawater around the Wilkes Land continental margin, the results have to be placed in the context of the spatial structure of water masses (i.e., neutral density levels; Figure 2.5). Antarctic Surface Water shows systematic zonal variability in its Nd isotope composition that is independent of neutral density and position on the continental margin (i.e., shelf, slope or offshore; ε_{Nd} = –8.0 to –9.9). The observed zonal gradient on the slope and shelf of increasingly radiogenic ε_{Nd} values to the east (Figure 2.3) is a clear feature of surface waters (Figure 2.5). Conversely, at MCDW neutral density levels ($28.27 > \gamma^n > 28.03$ kg m^{-3}), there is no pronounced east-west gradient and the data shows a strong correlation between Nd isotope composition and neutral density (Figure 2.5; i.e., more radiogenic values in denser waters; range: ε_{Nd} = –7.9 to –9.3 except for one data point from shelf profile at ε_{Nd} = –9.7). At the density level of AABW, both neutral density and ε_{Nd} remain relatively constant (ε_{Nd} = –7.8 to –8.7; n = 17). There is furthermore no discernible relationship between the Nd isotope composition and the location of MCDW and AABW on the continental margin. Deep and bottom waters around the Wilkes land continental margin can hence be characterised as follows: MCDW = –8.8 ± 0.8 (2sd; n = 22) and AABW = –8.3 ± 0.5 (2sd; n = 17), respectively. In the following we will discuss the causes of isotopic variability in ASSW, the processes controlling the Nd isotope composition of MCDW, and the extent of a localised isotopic signature for AABW in this region.

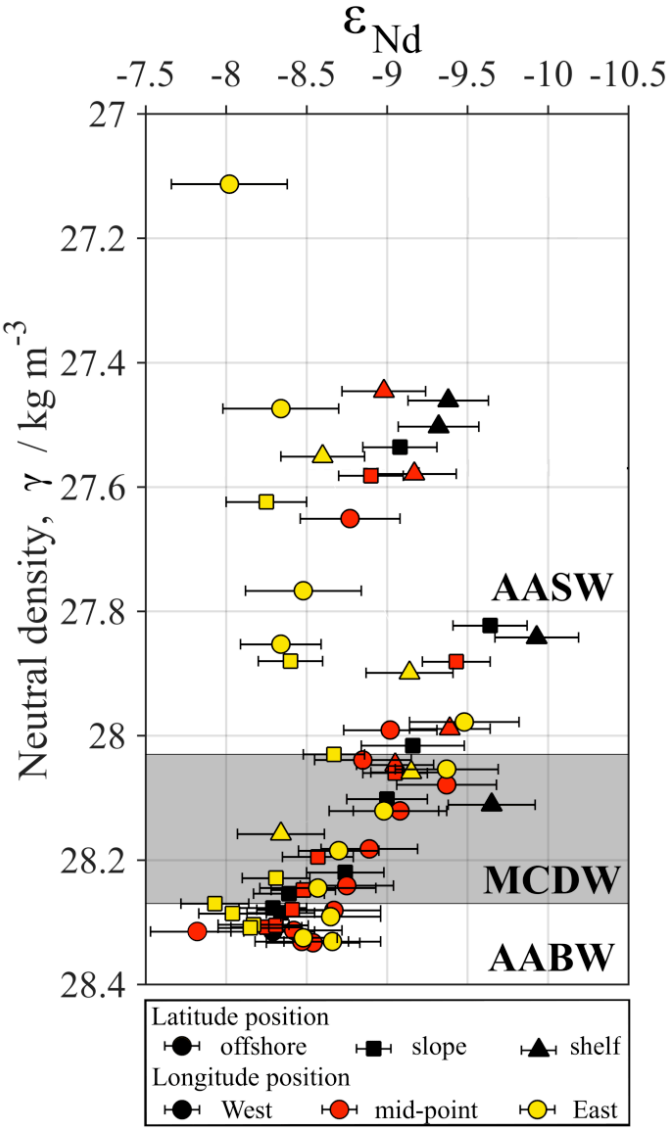

Figure 2.5 Neodymium isotope composition versus neutral density of dissolved seawater from the Wilkes Land margin area, Antarctica. The data are separated according to the position on the margin, i.e., shelf (triangles), slope (squares), and offshore (circles). Colours correspond to the relative latitudinal position of the stations (Figure 2.1 (b)), i.e., east (yellow), west (black), in between (red). Black lines and grey shading delimit the water mass boundaries of Modified Circumpolar Deep Water (MCDW) according to neutral density limits (see section 2.2.3).

2.5.1. Surface current influence on the composition of AASW

The observed variability in Nd isotope compositions in AASW does not correlate with the observed physical properties of AASW (Figure 2.5). The eastern offshore station (station 2) and the eastern slope and shelf stations (station 6 and 5, respectively) have the same Nd isotope composition but different neutral densities as much warmer (~2°C) AASW resides offshore (Figure 2.5). Conversely, the east-west gradient of Nd isotope composition along the slope and shelf does not coincide with a change in the physical parameters of AASW (Figure 2.2 (b–c)) or neutral density (Figure 2.5). Continental inputs and the prevailing surface ocean circulation pattern are the two possible explanations for the east-west variability in Nd isotope composition of AASW.

Firstly, continental inputs to the west or east of the Wilkes Land continental margin could alter the Nd isotope composition of AASW. In general, REEs are supplied to the surface ocean from continental sources predominantly through riverine and atmospheric inputs, but the proximity of the Southern Ocean to an ice-covered continent reduces the relative importance of these inputs in this region. Both model studies and empirical evidence suggest that sediment supply from the Antarctic continental margin constitutes the main source of other continent-derived elements such as iron to the Southern Ocean (Tagliabue et al., 2009; De Jong et al., 2012). Inputs from the resuspension of sediments along the continental margin, however, are more likely to affect the deeper waters along the Antarctic shelf, while more direct inputs from the continent through glacial activity will act as an important source of REEs to the surface waters of the Southern Ocean. For example, Kim et al., (2015) attributed a near two-fold increase in REEs and enrichment of middle REEs (MREE) in the coastal waters of King George Island to glacial meltwater. Similarly, free-drifting icebergs have been identified as a significant source of continental iron to the surface of the Southern Ocean, with iceberg terrigenous inputs 1–3 orders of magnitude greater than estimates of aeolian dust fluxes to the Weddell Sea (Shaw et al., 2011). There remains, however, limited evidence of glacial meltwater as a significant continental source of REEs to the Southern Ocean, as there is no current empirical evidence of REEs released from drifting icebergs in seawater (Hegner et al., 2007; Shaw et al., 2011).

The potential for continental inputs to the AASW along the Wilkes Land continental margin can be assessed by comparing the HREE/LREE ratio ([Tm + Yb + Lu]/[La + Pr + Nd]) to the MREE/MREE* ratio, ([Gd + Tb + Dy] / [Tm + Yb + Lu + La + Pr + Nd]/2), for all AASW samples normalised to Post-Archean Australian Sedimentary rock (PAAS; Freslon

et al., 2014). In this study, AASW shows values on the lower end of the authigenic-pore water array with significantly higher HREE/LREE ratios (4.11–5.91) and lower MREE/MREE* (0.69–0.82) values than the continental source (PAAS = 1; Du et al., 2016). Any continental inputs would reduce and move seawater HREE/LREE ratios towards the lower PAAS values. Moreover, any fluxes from reducing sediments on the shelf (Haley et al., 2004), lithogenic inputs from nearby continental outcrops (Zhang et al., 2008), or continental inputs from glacial meltwater (Kim et al., 2015) would produce a MREE enrichment in AASW, with MREE/MREE* values greater than PAAS. Consequently, the combined HREE/LREE and MREE/ MREE* ratios for AASW indicate that there are no continental sources of REEs to the surface waters of the Wilkes Land continental margin. This is further substantiated by the lack of surface water enrichment of Nd concentrations compared to deeper waters which would indicate continental inputs from Antarctica (Figure 2.4).

A second mechanism to create a zonal (i.e., east versus west) trend in dissolved Nd isotope composition of surface water in the area is the competition between southward flow of warm AASW onto the Wilkes Land shelf and westward flow of the Antarctic slope current (Figure 2.1). Lambelet et al. (2018) reported less radiogenic Nd isotope compositions (ε_{Nd} = –9.32 ± 0.31 to –10.45 ± 0.31) for cold shelf waters near the Adélie Land coast to the east (–1.5 ºC; 66ºS, 140ºE) and more radiogenic Nd isotope compositions (ε_{Nd} = –8.10 ± 0.31) for warmer offshore AASW (~ 4 ºC; 59º S, 160º E). In this study, there is a discernible difference between the Nd isotope composition of cold shelf AASW at the western slope and shelf stations (i.e., stations 24 and 18, respectively), and the offshore warmer AASW (i.e., station 2) to the east (Figures 2.3 and 2.5). The Nd isotope composition of AASW at the eastern shelf and slope stations (station 5 and 6, respectively) resembles the offshore AASW from station 2 and could therefore highlight a junction of surface circulation in the area.

The Antarctic Continental Slope Current transports cold less radiogenic AASW from the Adélie Land coast to the west, while the cyclonic gyre drives warm radiogenic AASW southwards. At the eastern shelf and slope stations (station 5 and 6, respectively), the temperature of AASW has decreased as it approaches higher latitudes (Figure 2.2), but AASW has not successfully mixed with shelf waters from the east, resulting in an unchanged Nd isotope signature at station 5 and 6. This poleward moving AASW eventually mixes with westward flowing surface AASW on the shelf and thus gives rise to the observed zonal gradient. It is suggested, therefore, that the changing Nd isotope composition in AASW across the Wilkes Land continental margin is tracing the southward limb of the cyclonic gyre

onto the shelf (i.e., more radiogenic values in the east) and the change from warm offshore AASW to cold shelf AASW towards the west (i.e., less radiogenic values in the west).

2.5.2. Controls on the Nd isotope composition of MCDW

Circumpolar Deep Water (CDW) represents the most voluminous water mass in the world and constitutes an important component of the ACC (Worthington, 1981; Pardo et al., 2012). Previous studies have reported extreme homogeneity of Nd isotope composition for CDW, reflecting both the well-mixed nature of the large Nd inventory of the CDW in the ACC and the ability of this voluminous water mass, which is fed by deep waters from all ocean basins, to buffer against continental inputs from Antarctica to the Southern Ocean (Carter et al., 2012; Stichel, 2012b; Rickli et al., 2014). Observations across the Atlantic, Pacific and Australian sector of the Southern Ocean show that the Nd isotope composition of UCDW and LCDW are, respectively, ε_{Nd} = –8.2 ± 0.9 (2sd; n = 44) and ε_{Nd} = –8.4 ± 1.6 (2sd; n = 127, Figure 2.6; Jeandel, 1993; Carter et al., 2012; Stichel et al., 2012b; Molina-Kescher et al., 2014; Garcia-Solsona et al., 2014; Rickli et al., 2014; Basak et al., 2015; Lambelet et al., 2018). At the Wilkes Land continental margin, MCDW exhibits a significant range in values from ε_{Nd} = –7.9 ± 0.21 to –9.7 ± 0.27 across the shelf, slope and offshore stations but are within the range of observed Southern Ocean UCDW and LCDW values (Figure 2.6). As MCDW forms from upwelled UCDW and LCDW onto the Antarctic shelves, there are two possible controls on the Nd isotope composition of MCDW: (1) admixture of CDW with surrounding water masses on the continental margin (i.e., AASW and AABW); and (2) boundary exchange with local sediments.

Several studies have reported modification of CDW in various locations across the Southern Ocean through exchange processes with local sediments. In the South Atlantic and Pacific, UCDW exhibits more radiogenic values (as radiogenic as ε_{Nd} = –6.3; Jeandel, 1993; Basak et al., 2015) despite mixing with unradiogenic NADW, which suggests the modification of CDW as it flows past the radiogenic sediments of the Antarctic Peninsula (Roy et al., 2007). Rickli et al., (2014) reported shifts to more radiogenic values in LCDW (ε_{Nd} = –4.9 and –3.1) due to the effects of boundary exchange on the slopes of the Marie Byrd Seamounts in the Pacific sector of the Southern Ocean. More pertinently, there have been observations of shifts towards more radiogenic values for MCDW as it encroaches the coast of the Amundsen Sea Embayment in the Pacific sector of the Southern Ocean (Figure 2.6; Carter et al., 2012; Rickli et al., 2014).

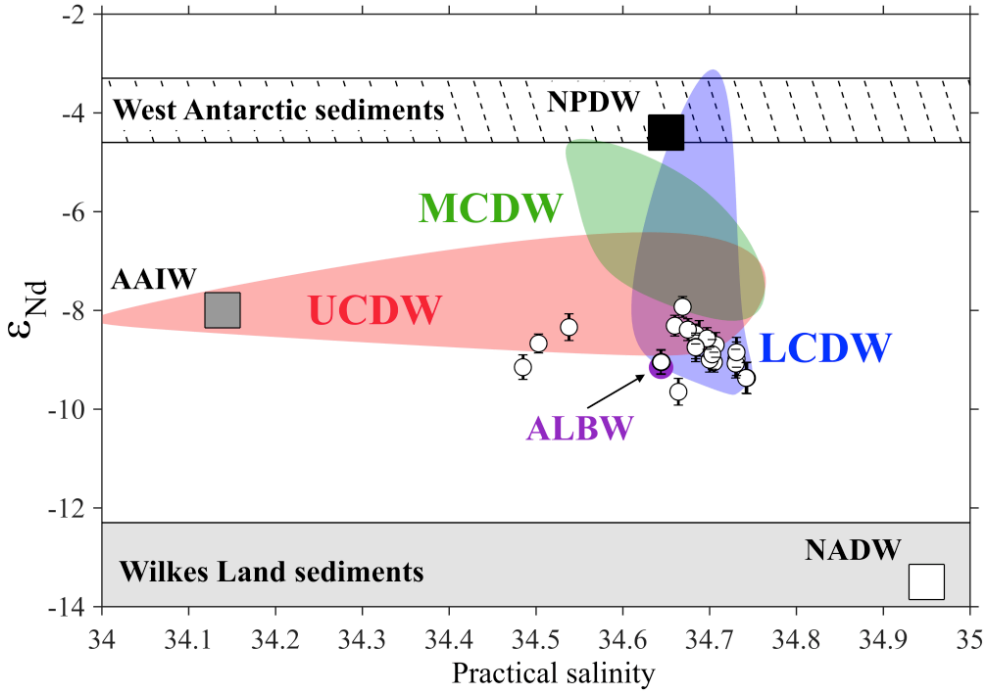

Figure 2.6 Practical salinity vs neodymium isotope composition for MCDW samples (white circles) in the study area. Large black and white squares represent the global endmember values for NPDW (S = 34.65, ε_{Nd} = –4.4; Piepgras and Jacobsen, 1988) and NADW (S = 34.95, ε_{Nd} = –13.5; Piepgras and Wasserburg, 1987), respectively. The grey box corresponds to AAIW (S = 34.14, ε_{Nd} = –8.0; Stichel et al., 2012b). The purple circle represents recently characterised local AABW from the east (i.e., ALBW; S = 34.648; ε_{Nd} = –8.9; Lambelet et al., 2018). The coloured shadings correspond to the observed ranges of CDW varieties in the Southern Ocean: UCDW (red; Carter et al., 2012; Stichel et al., 2012b; Garcia-Solsona et al., 2014, Basak et al., 2015; Lambelet et al., 2018); LCDW (blue; Carter et al., 2012; Stichel et al., 2012b; Garcia-Solsona et al., 2014, Rickli et al., 2014; Basak et al., 2015; Lambelet et al., 2018); and MCDW (green; Carter et al., 2012; Rickli et al., 2014). Any UCDW and LCDW data identified to be affected by boundary exchange processes in original publications have been omitted. For MCDW, all available data was used to assess the observable ε_{Nd} range. The grey box marks the ε_{Nd} range for local sediment on the Wilkes Land continental margin between 120°E and 130°E (Roy et al., 2007; van de Flierdt et al., 2007).

Contrary to MCDW in other sectors of the Southern Ocean, East Antarctic MCDW does not deviate towards the local unradiogenic sediments, indicating an absence of boundary exchange. Moreover, the LCDW-normalised REE patterns for MCDW in the area around the Wilkes Land continental margin suggest a dominant effect of mixing on the Nd isotope composition of MCDW (Figure 2.7 (a)). Rare earth element concentrations for MCDW are within the range of reported results for LCDW (Hathorne et al., 2015), with a distinct absence of any MREE enrichment or HREE depletion, indicating an absence of significant continental inputs from the shelf or slope (Figure 2.7 (a)). The observed fractionation of Ce represents an artefact from the combined analytical uncertainty of Ce from both studies and the extremely low Ce concentrations, which makes an insignificant increase in the absolute concentration appear to be a significant relative increase.

A relevant and interesting question, therefore, is why shelf exchange is not affecting MCDW on the Wilkes Land continental margin? Release of trace metals from sediments to the surrounding water column can be aided by increased bottom turbulence (e.g., high flow speed, significant nepheloid layer), but also depends on the composition of the sediment. Previous dissolution rate experiments confirm that basaltic material is more susceptible to control the Nd isotope composition of surrounding seawater due to the high content of reactive minerals (Pearce et al., 2013). Older continental material typically contains more resistent minerals and hence less reactive silicate and clay minerals (e.g., Dupré et al., 2003; Jeandel and Oelkers, 2015 and references therein). The continental and shelf system across East Antarctica contains sediments derived from the weathering of an old Proterozoic craton with mineralogical compositions dominated by quartz and feldspars with minor clays (e.g., Roy et al., 2007; van de Flierdt et al., 2007; Srivastava et al., 2013). The lack of an elemental imprint from unradiogenic sediments along the Wilkes Land continental margin on seawater chemistry could, therefore, be attributed to the sediment composition.

In the absence of boundary exchange, the Nd isotope composition of MCDW reflects mixing between upwelled CDW and AASW/AABW on the Wilkes Land continental shelf. Figure 2.5 shows that there is a clear correlation between the Nd isotope composition and the neutral density values below 27.8 kg m^{-3}; i.e., a clear mixing line between AASW, MCDW and AABW.

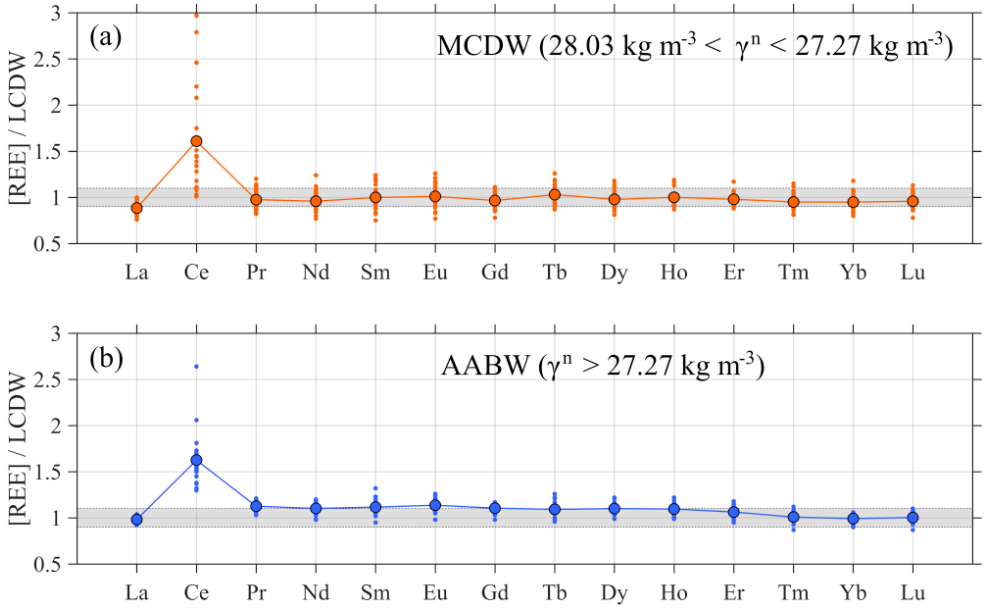

Figure 2.7 Dissolved rare earth element patterns for (a) MCDW and (b) AABW in the study area normalised to average REEs in LCDW as proposed by Hathorne et al., (2015). The smaller circles show all the available data for each element for a given water mass, while the large circles and the connecting line represent the average REE pattern. The grey shading represents the analytical uncertainty of the REE LCDW data and therefore, anything within the grey band is considered to be identical to LCDW.

2.5.3. No local AABW formation around the Wilkes Land margin

Previous studies have shown that bottom waters formed around Antarctica carry a local fingerprint of their formation area (Carter et al., 2012; Stichel et al., 2012b; Garcia-Solsona et al., 2014; Rickli et al., 2014; Basak et al., 2015; Lambelet et al., 2018). For example, the Pacific sector of the Southern Ocean exhibits more radiogenic AABW (ε_{Nd} = −7.4 ± 0.9; Carter et al., 2012; Rickli et al., 2014; Basak et al., 2015) caused by continental inputs of young basaltic bedrock around the formation site of Ross Seas Bottom Water (Figure 2.8). Conversely, the lower Nd isotope values of AABW in the Atlantic sector of the Southern Ocean (ε_{Nd} = −9.1 ± 0.7; Stichel et al., 2012b; Garcia-Solsona et al., 2014) reflects formation of Weddell Sea Bottom Water in areas influenced more by older continental crust around the Weddell Sea (Figure 2.8). On the Wilkes Land continental margin, AABW shows a distinct intermediate ε_{Nd} signature between Pacific and Atlantic AABW (Figure 2.8; ε_{Nd} = −8.3 ± 0.5). It overlaps the radiogenic end of the signature for Adélie Land Bottom Water (ε_{Nd} = –8.6 to –9.5; *n* = 3; Lambelet et al., 2018), which is formed farther east in the Adélie Depression

proximal to some of the oldest continental terrains exposed in Antarctica (offshore sedimentary fingerprint: ε_{Nd} = –14.9 to –20.4; Roy et al., 2007; van de Flierdt et al., 2007; Pierce et al., 2011). Given the prevalence of relatively old (i.e., Proterozoic) continental crust around the Wilkes Land margin (e.g., Pierce et al., 2014), the observed AABW values could be in principle due to a local overprint.

However, two points strongly argue against this line of thinking. Firstly, there is only evidence of active bottom water formation around the Wilkes Land continental margin to the east of the study area (e.g., Foster, 1995). This means that any unradiogenic imprint in bottom waters would have to be a signal derived from exchange with seafloor/margin sediments/benthic inputs. This seems unlikely given the fact that MCDW in the area extends to less radiogenic values than AABW (Figure 2.8). Furthermore, LCDW-normalised REE patterns for AABW, like MCDW REE patterns, lack any deviation from typical LCDW pattern (Figure 2.7 (b)). The local ε_{Nd} signature for AABW must therefore be a product of mixing between advected AABW from the east (i.e., unradiogenic ALBW) and local CDW (more radiogenic) that upwells onto the Wilkes Land continental shelf.

Recent circulation studies of the East Antarctic shelf suggests that the primary regional source of AABW is the Adélie Depression, where brine rejection following sea ice formation produces dense shelf waters that eventually sink to the bottom and are exported through the Adélie Land sill (e.g., Foster and Carmack, 1976; Williams et al., 2010). The Antarctic Continental Slope Current subsequently transports this dense shelf water to the west along the Wilkes Land continental slope while simultaneously entraining a significant amount of encroaching warmer and more saline deep waters from the continental rise (i.e., CDW) to form AABW (Carmack and Killworth, 1978; Foldvik, 1985). Given that the formation process of AABW involves admixture of local shelf waters and upwelled CDW, the properties of AABW depend not only on the cold and saline shelf derived components with a Nd isotope composition influenced by local continental inputs, but also on the amount and characteristics of CDW entrained during the transport and mixing process. The Nd isotope data indicates, therefore, that the dominant fraction of AABW (ε_{Nd} = −8.3 ± 0.5) on the Wilkes Land continental margin must be CDW (ε_{Nd} = –8.2 ± 0.9 to –8.4 ± 1.6; Jeandel, 1993; Carter et al., 2012; Stichel et al., 2012b; Molina-Kescher et al., 2014; Garcia-Solsona et al., 2014; Rickli et al., 2014; Basak et al., 2015; Lambelet et al., 2018).

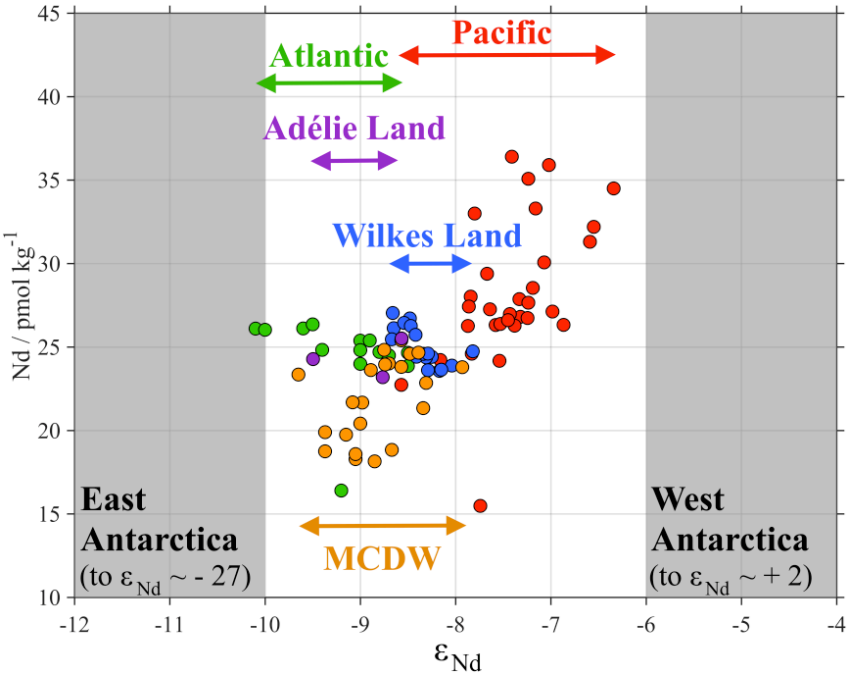

Figure 2.8 Neodymium isotope composition and concentration for AABW across the Southern Ocean (this study and literature values). Different colours refer to specific regions: red—Pacific sector of the Southern Ocean (Carter et al., 2012; Rickli et al., 2014; Basak et al., 2015); green—Atlantic sector of the Southern Ocean (green; Stichel et al., 2012b; Garcia-Solsona et al., 2014); purple—Australian sector of the Southern Ocean (Lambelet et al., 2018); blue—Wilkes Land continental margin (this study). The yellow circles correspond to Modified Circumpolar Deep Water (MCDW) results from the area around the Wilkes Land continental margin (this study).

2.5.4. A new approach to modelling the Nd isotope composition of AABW

The Wilkes Land continental margin dataset has expanded the spatial coverage of ε_{Nd} in the Southern Ocean and increased the total number of AABW observations by a third. Importantly, the dataset corroborates previous global observations of deep water masses exhibiting strong correlations between physical properties and the Nd isotope composition, signifying water mass mixing as the dominant process controlling ε_{Nd} variability in the deep ocean (Figure 2.5; e.g., Goldstein and Hemming, 2003; Lacan et al., 2012; van de Flierdt et al., 2016; Tachikawa et al., 2017 and references therein). While ample studies have focussed on the composition of northern-sourced deep waters (e.g., Lambelet et al., 2016), AABW has for a long time been under sampled and understudied. In terms of its export flux to the global ocean, it is however as important as NADW, and probably was even more important in the

geological past (e.g., Roberts et al., 2010; Piotrowski et al., 2012). Regional variability in the Nd isotope composition of AABW is created in the different AABW formation areas, due to a largely variable geology around the Antarctic continent. This spatial heterogeneity and non-linearity in AABW properties makes it difficult to use traditional empirical models such as multi-linear regressions (MLR; Tachikawa et al., 2017) to predict the Nd isotope composition of AABW. A neural network, however, can account for this non-linear behavoiur by using spatial variables (latitude and longitude) as input parameters and non-linear transfer functions (see section 2.3.4) to map the ε_{Nd} around Antarctica. This approach avoids individual 'regionlised' MLR models for AABW which would reduce the overall statistcal robustness of the model, and, therefore, represents the most effective method to assess ε_{Nd} variabilty of AABW across the Southern Ocean given the limited number of observations.

The neural network model was trained using all available AABW observations ($\gamma > 27.27$ kg m^{-3}; $n = 67$) from Southern Ocean studies (Carter et al., 2012; Stichel et al., 2012b; Garcia-Solsona et al., 2014; Rickli et al., 2014; Basak et al., 2015; Lambelet et al., 2018; this study) and tested using a randomly selected subset ($n = 10$) of the available data. The model output values compared to the target AABW observations show that the trained neural network can predict Nd isotope composition with good accuracy (Figure 2.9 (a); RMSE = 0.05). Moreover, the model residuals (output – observations) show that 95% of all model predicted values are within $\varepsilon_{Nd} = \pm 0.44$ of the target (or observation) values (Figure 2.9 (b)). This represents an improvement compared to the only other attempt to predict ε_{Nd} across separate ocean basins using an empirical model (MLR; 2σ sd $> \pm 2$; Tachikawa et al., 2017). The model input variables (lat, lon, θ, salinity, and O_2) successfully constrain the observational data but there are noticeable output values which diverge from the 1:1 line (Figure 2.9 (a)). For example, the overestimated data point above the 1:1 line (ε_{Nd} output = –7.42, ε_{Nd} observation = –8.57) corresponds to a bottom water sample influenced by an unradiogenic source near the Polar Front in the Eastern Pacifc sector of the Southern Ocean (Carter et al., 2012). The exact source and process controlling this deviation has not been identified, but it is evident that alternative processes (e.g., boundary exchange, benthic flux, etc) will affect the neural network's ability to map ε_{Nd} variability across the Southern Ocean.

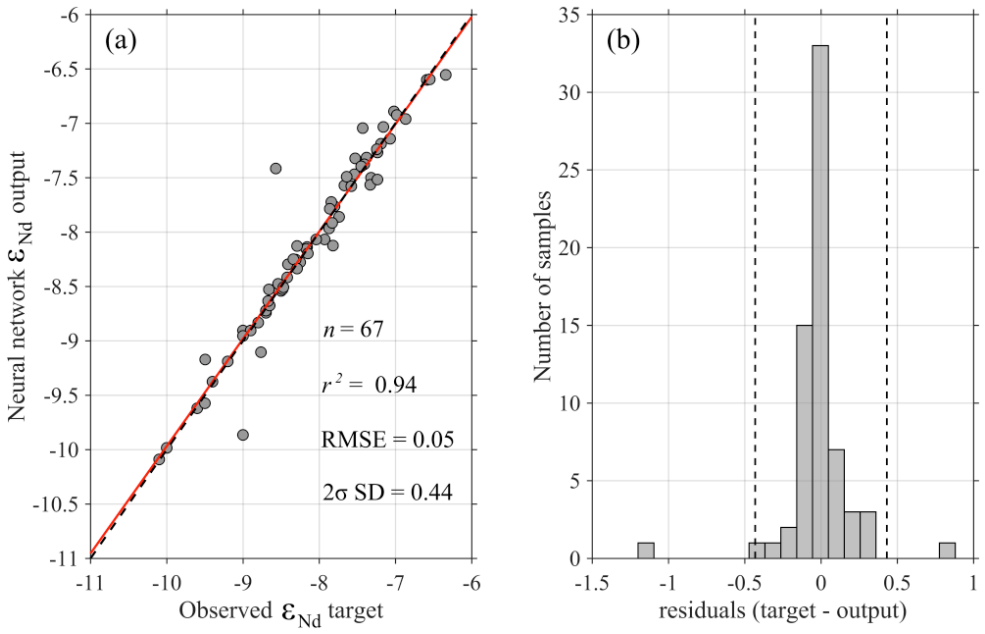

Figure 2.9 Neural network model trained to predict the Nd isotope composition of AABW using available observations across the Southern Ocean (Carter et al., 2012; Stichel et al., 2012b; Rickli et al., 2014; Garcia-Solsona et al., 2014; Basak et al., 2015; Lambelet et al., 2018). Scatter plot (a) shows the results of the trained neural network by comparing the observations to the neural network predicted output values. The broken black line indicates a perfect 1:1 relationship, while the red line represents the line of best fit. The histogram (b) shows the residual (Nd isotope composition of observations – neural network predicted output) frequencies for all AABW observations. The key statistics of the neural network are shown in scatter plot (a). For information about the neural network, see method section 2.3.4.

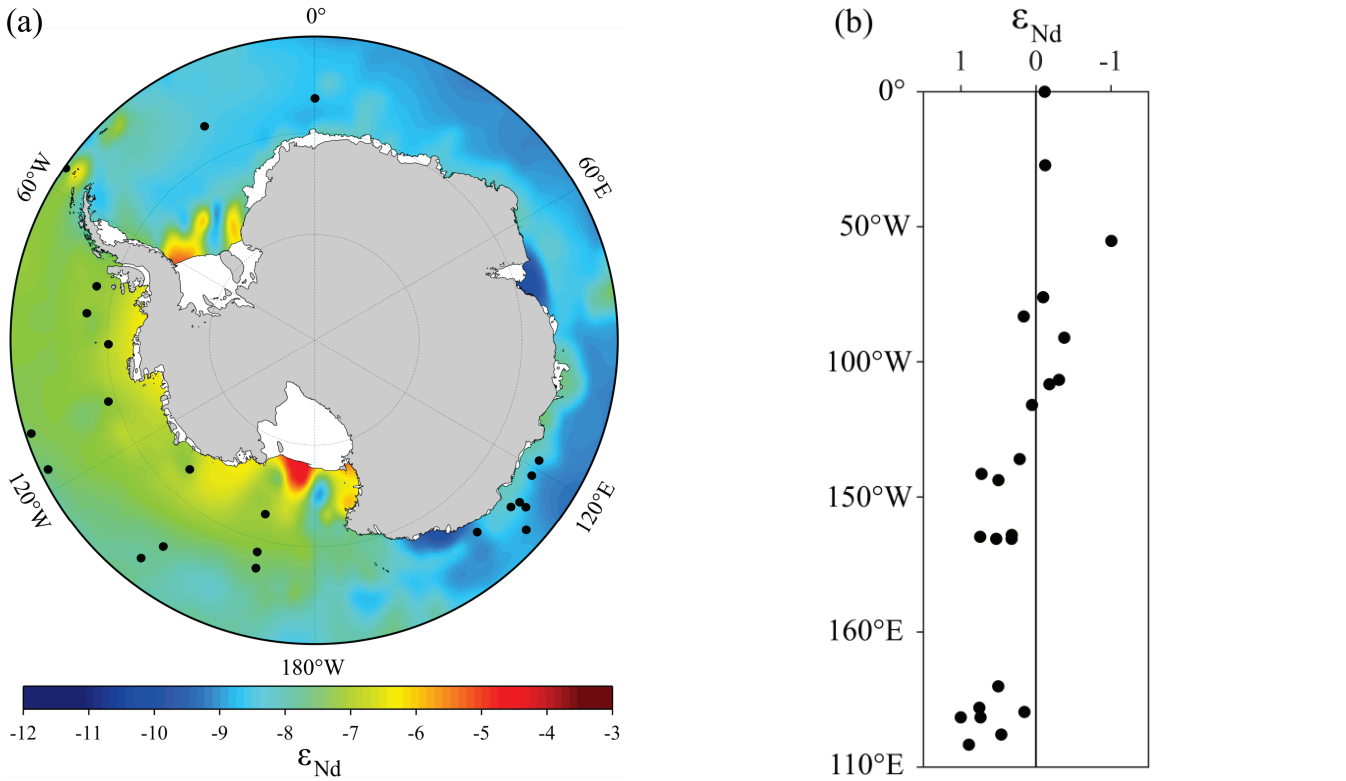

Figure 2.10 The application of the trained neural network to an independent hydrographic dataset (WOA13; Locarnini, et al., 2013; Zweng, et al., 2013; Garcia, et al., 2014) for neutral density values > 28.27 kg m^{-3}. The map (a) shows the depth integrated average of modelled Nd isotope composition to highlight the spatial variability of AABW around the Southern Ocean. The scattered black points represent the location of current observations for Nd isotope composition. The difference between the depth integrated average of the observations and the depth integrated average of the most proximal model output is shown in (b).

The trained network for AABW was applied to an independent hydrographic dataset outside the ε_{Nd} observational domain with the same input variables (WOA13 1°x 1° annual dataset; Locarnini, et al., 2013; Zweng, et al., 2013; Garcia, et al., 2014). The model's predicted distribution of Nd isotope composition for AABW across the Southern Ocean demonstrates the broad difference between eastern unradiogenic and western radiogenic AABW (Figure 2.10 (a)). Moreover, the network characterises the shelf waters associated with bottom water formation (i.e., cold, fresh and ventilated) with extreme ε_{Nd} values based on a linear relationship between observed ε_{Nd} and hydrographic data and spatial information. Eastern unradiogenic AABW source waters (Adelie Land and Prydz Bay; $\varepsilon_{Nd} = \sim -11$) can be easiliy depicted from western radiogenic AABW source waters ($\varepsilon_{Nd} = \sim -5$; Ross Sea and Weddell Sea) but in both areas there are no observations. New samples could easily test the validity of the model in predicting dissolved Nd isotope composition in the Southern Ocean. The absolute difference, however, between available observations and the modelled data show that a neural network can accurately determine the ε_{Nd} varibility of AABW, with more than 70% of the data within the analytical uncertainity typically reported for seawater Nd isotope measurements (Figure 2.10 (b); van de Flierdt et al., 2012). Deviations > 0.6 epsilon are notably observed for the one data point discussed above in the southeastern Pacific Ocean, and for areas off the eastern Ross Sea and in our own study area. While the Ross Sea is very much underconstrained in its modern composition, the Wilkes Land margin, due to the new data presented in this study, is now one of the best characterised areas of Antarctica.

2.6. Conclusion

Observations of dissolved Nd isotope compositions in seawater around the Wilkes Land continental margin in the Australian-Antarctic Basin of the Southern Ocean show that circulation patterns and water mass mixing govern the isotopic fingerprint of waters in the region. The data indicate a limited range in Nd isotope compositions, both in a vertical and lateral sense, but nevertheless allow important conclusions.

Firstly, zonal variability of Nd isotope composition in surface waters across the Wilkes Land continental margin is a reflection of the surface circulation in the region. The Antarctic Continental Slope Current transports cold less radiogenic AASW from the Adélie Land coast to the west, while the cyclonic gyre transports warm radiogenic AASW southwards onto the shelf. REE concentrations show no evidence of continental REE inputs or glacial meltwater to surface waters in the area.

Secondly, mixing of upwelled CDW with AASW and AABW exclusively controls the Nd isotope composition of MCDW (ε_{Nd} = –7.9 to –9.7). MCDW values are identical to published data for CDW across the Southern Ocean which, coupled with no observable fractionation of REEs, suggests that boundary exchange processes do not modify the Nd isotope composition on the slope and shelf. The lack of boundary exchange across the Wilkes Land continental margin is probably due to the unreactive nature of old continental shelf sediments in this region.

Finally, the regional Nd isotope signature for AABW (ε_{Nd} = −8.3 ± 0.5; 2sd; n = 17) is intermediate between published data for less radiogenic Atlantic sector AABW (ε_{Nd} = −9.1 ± 0.7) and more radiogenic Pacific sector AABW (ε_{Nd} = −7.4 ± 0.9). In the absence of active convection, it reflects a mixture of advected AABW from the Adélie Coast with (M)CDW.

The new data constrain dissolved trace metal behaviour in an important area of the Southern Ocean, allowing a first attempt at modelling and predicting Nd isotope compositions in the Southern Ocean. We developed an algorithm using a neural network based on spatial and hydrographic data, in order to assess the Nd isotope composition of AABW in its various formation regions and beyond. The model predicts the Nd isotope composition of AABW with high accuracy (n = 67; RMSE = 0.05; 2sd = 0.44). When applied to an independent hydrographic dataset, the results highlight the difference between radiogenic and unradiogenic AABW in the east and west, respectively, as well as ε_{Nd} extrema in areas of AABW formation. The neural network approach to mapping Nd isotope composition can be a useful tool to predict seawater chemistry in areas of sparse observations.

Acknowledgments and author contributions

Alex Griffiths conducted the sample analyses, with the guidance of Myriam Lambelet. The interpretation and presentation of the data was led by Alex Griffiths with contributions from Myriam Lambelet, Tina van de Flierdt and Mark Rehkämper. REE analysis was carried out with the help of Kirsty Crocket and Richard Abell, and Frank Nistche collected the samples. The authors would like to thank the officers, crew and scientific party of the Nathaniel B. Palmer during the NBP1503 expedition to the East Antarctic shelf, as well as all the members of the MAGIC group, especially Katharina Kreissig and Barry Coles, for their support in the lab. The authors would like to acknowledge studentship funding from the NERC DTP ‘Science and Solutions for a Changing Planet’ at Imperial College London.

Chapter 3

High-precision Pb isotope analysis of seawater using Nobias chelate resin and ^{207}Pb-^{204}Pb double-spike MC-ICP-MS

Abstract

Lead (Pb) isotopes have been used as tracers and chronometers across a wide range of disciplines for many years. Their application to oceanographic research is currently limited by analytical challenges such as sample contamination, time-consuming extraction procedures and insufficient instrumental detection limits.

A new method has been developed to provide high-precision Pb isotope analyses and increase the analytical throughput of seawater samples. The procedure involves solid-phase extraction of Pb from seawater using Nobias chelate PA-1 resin, purification by anion-exchange chromatography, and analyses by MC-ICP-MS using a ^{207}Pb-^{204}Pb double-spike to correct for instrumental mass discrimination.

The procedure was validated and compared to other traditionally used procedures using multiple analyses of internal seawater reference materials. The typical precision of the new procedure for Pb isotope analyses, depending on the seawater concentration, was between ~250–1250 ppm for ratios involving the minor ^{204}Pb isotope (^{208}Pb/^{204}Pb, ^{207}Pb/^{204}Pb, ^{206}Pb/^{204}Pb) and ~100–1200 ppm for ^{206}Pb/^{207}Pb and ^{208}Pb/^{207}Pb ratios.

When compared to an established double-spike TIMS methodology, the results demonstrate improved precision for ^{206}Pb/^{207}Pb and ^{208}Pb/^{207}Pb ratios and a greater reproducibility by at least a factor of two for the ^{204}Pb ratios. Despite higher blank contributions for solid-phase extraction, Nobias and $Mg(OH)_2$ co-precipitation with double-spike correction yield statistically identical results with no discernible difference in the levels of precision. While Nobias coupled with Tl-normalisation produces high-precision Pb isotope ratios comparable to double-spike correction, the reproducibility of all Tl-normalised Pb isotope ratios following $Mg(OH)_2$ co-precipitation are worse. This could be a reflection of the different extraction procedures: $Mg(OH)_2$ co-precipitation is less effective at extracting Pb from the seawater matrix, which could increase the susceptibility of Tl-normalisation to matrix effects during MC-ICP-MS analyses. However, this is difficult to conclude given the limited amount of seawater available for replicate analyses of the reference materials. Finally, instrument and inter-laboratory comparison using GEOTRACES reference samples confirms the trueness of the procedure.

3.1. Introduction

Over the last seventy years, stable naturally-occurring lead isotopes (radiogenic ^{208}Pb, ^{207}Pb, ^{206}Pb and non-radiogenic ^{204}Pb) have been used as isotopic tracers and chronometers for a wide range of disciplines such as geochemistry, forensics and environmental health (Patterson, 1956; Manton, 1973; Buttigieg et al., 2003). The application of Pb isotopes to oceanographic research, however, remains limited due to the significant challenges associated with the analysis of Pb isotopes in seawater. The complex and highly saline seawater matrix (~3.5% of total dissolved solids), coupled with the extremely low concentrations of Pb in seawater (global mean ~10 pmol kg^{-1}; Sohrin and Bruland, 2011) and the high risk of Pb contamination from other environmental sources, make it difficult to extract, pre-concentrate and purify uncontaminated quantities of Pb that can surpass instrument detection limits. While purification procedures have been well-established for many years and produce sufficiently low levels of blank contamination for seawater analysis (Strelow and Toerien, 1966; Strelow, 1978; Reuer et al., 2003; Paul, et al., 2015b) extraction procedures and instrument limitations have hindered the acquisition of high-precision Pb isotope analysis of seawater.

Since the late 1990's, magnesium-hydroxide $Mg(OH)_2$ co-precipitation has provided a simple, rapid and effective extraction procedure (Wu and Boyle, 1997b). The method takes advantage of natural Mg^{2+} in seawater which, after increasing the pH of seawater, forms a precipitate and removes Pb in solution. Major advantages of this method are low levels of blank contamination (0.01–0.12 pmol kg^{-1}; Reuer et al., 2003; Wu et al., 2010; Boyle et al., 2012) compared to traditional organic solvent (28 pmol kg^{-1}; Patterson and Settle, 1976; Munksgaard, Batterham and Parry, 1998) and solid-phase (14–48 pmol kg^{-1}; Reimer and Miyazaki, 1992; Miyazaki and Reimer, 1993; Halicz, Lam and Mclaren, 1994) extraction techniques, as well as high extraction efficiencies (Pb yields 90–100%; Reuer et al., 2003; Wu et al., 2010; Boyle et al., 2012).

Despite the analytical advantages of $Mg(OH)_2$ co-precipitation, most studies have been unable to achieve high-precision Pb isotope analyses because of insufficient quantities of Pb extracted from small volumes of seawater (~250–500 mL; Reuer et al., 2003; Boyle et al., 2012; Lee et al., 2015; Noble et al., 2015). Larger volumes of seawater have been processed to achieve more precise Pb isotope data (~2 L; Paul et al., 2015b), but increasing the volume of seawater with $Mg(OH)_2$ co-precipitation comes with several analytical challenges: (1) the procedure becomes more time-consuming as the precipitate takes longer to form in larger

volumes of seawater; (2) extraction efficiencies are significantly reduced (Pb yields ~40–60%) because large volumes of seawater cannot be centrifuged post-precipitation and fine suspended $Mg(OH)_2$ particles are often discarded with the supernatant; (3) $Mg(OH)_2$ co-precipitation efficiently scavenges $Si(OH)_4$ in seawater which either prevents dissolution of $Mg(OH)_2$ precipitates in column loading solutions or reprecipitates as a thick $Si(OH)_4$ gel during anion-exchange chromatography (Boyle et al., 2012; Lee et al., 2015; Paul et al., 2015b). For larger volumes of seawater with extremely high concentrations of $Si(OH)_4$, even the addition of hydrofluoric acid is not able to prevent $Si(OH)_4$ supersaturation during purification, rendering $Mg(OH)_2$ co-precipitation unsuitable for some seawater samples (e.g., Southern Ocean; Chapter 4).

In recent years, the commercial availability of a new generation of chelating resins has shifted the focus of research back to solid-phase extraction either by columns (Sohrin et al., 2008; Biller and Bruland, 2012; Zurbrick et al., 2013; Minami et al., 2015; Vassileva and Wysocka, 2016; Chien et al., 2017) or batch-extraction (Lee et al., 2011; Conway et al., 2013). For Pb isotope analysis, columns with Toyopearl Chelate-650 or Nobias PA-1 resins have provided a rapid, efficient (Pb yields ~92%) and relatively low blank (0.1 ± 1.3 and 0.33 ± 0.16 pmol kg^{-1}, respectively) extraction procedure which can process larger volumes of seawater (Zurbrick et al., 2013; Chien et al., 2017). Despite solid-phase extraction representing a potential solution to the problems encountered by $Mg(OH)_2$ co-precipitation, accurate Pb isotope analysis of seawater has still been unattainable due to insufficient instrument detection limits and inaccurate procedures to correct for instrumental mass discrimination (Zurbrick et al., 2013; Chien et al., 2017).

Over recent years, Pb isotopes in seawater have been predominantly measured by high resolution inductively coupled plasma mass spectrometry (HR ICP-MS) or multi-collector ICP-MS (MC-ICP-MS) in conjunction with thallium (Tl) normalisation to correct for mass discrimination (Boyle et al., 2012; Zurbrick et al., 2013; Chien et al., 2017; Zurbrick et al., 2017). ICP-source mass spectrometry has several advantages compared to more traditional thermal ionisation mass spectrometry (TIMS): greater speed of analysis, higher analytical throughput of samples, and relatively simple sample preparation. However, older generation ICP-source mass spectrometers are not able to compete with the levels of accuracy produced by TIMS because the transmission efficiency, the ratio of the number of ions detected by the instrument collector to the number of ions entering the mass spectrometer, is significantly inferior (0.5–3.5% versus 2–10%, respectively; Amelin and Davis, 2006; Makishima and Nakamura, 2010; Taylor et al., 2015). This difference in transmission efficiency becomes

critical for seawater analysis when limited quantities of Pb (< 10 ng) have been extracted. The minor ^{204}Pb isotope only accounts for ~1.4% of total Pb and ratios involving this isotope require high-precision analysis.

Another factor limiting the acquisition of high-precision Pb isotope measurements involves the use of Tl-normalisation to correct for instrumental mass discrimination of Pb. Experiments have shown that the assumed mass fractionation relationship between Tl and Pb can be unreliable as matrix element interferences and/or photo-oxidation can induce differential isotope fractionation (Kamenov et al., 2004; Barling and Weis, 2008). Conversely, the double-spike correction technique, a normalisation method combining unspiked and Pb double-spiked analyses of the same sample to deconvolve the extent of Pb fractionation, produces significantly more accurate Pb isotope measurements because the correction is less susceptible to these analytical artefacts (Baker et al., 2004; Taylor et al., 2015). In comparison to Tl-normalisation, however, double-spike correction increases the analytical time, and more importantly, the amount of Pb consumed during measurements. Consequently, given the limited amount of Pb extracted from seawater and the low transmission efficiency of ICP-source mass spectrometry, to date, it has only been possible to combine double-spike correction with TIMS for the precise determination of Pb isotopes in seawater (Paul et al., 2015b).

The aim of this study was to develop a method that improves the precision of Pb isotope measurements in seawater while simultaneously increasing the analytical throughput of seawater samples. The new method combines a rapid batch-extraction technique using a Nobias PA-1 chelating resin with ^{207}Pb-^{204}Pb double-spike mass bias correction on a new generation MC-ICP-MS. The procedure is validated using multiple analyses of internal and international seawater reference materials. The objectives were to: (1) compare solid-phase extraction using Nobias PA-1 chelating resin to $Mg(OH)_2$ co-precipitation; (2) assess the relative merits of double-spike correction versus Tl-normalisation for seawater analyses; and (3) ensure trueness of the results through instrument (TIMS) and interlaboratory calibration.

3.2. Methods and Materials

3.2.1. Seawater reference materials

The performance of the method was assessed by analysing multiple aliquots of filtered and acidified (pH ~2) internal seawater reference materials: Solent seawater 5 (SSW-5), Solent

seawater 9 (SSW-9) and Southern Ocean surface water (SO-145). The performance of the method was also assessed using a GEOTRACES intercalibration sample, GSP, from the Pacific Ocean. The internal seawater reference materials and GSP were selected to cover a wide range of seawater types with varying chemical compositions from polluted coastal water (SSW-5) to pristine open-ocean surface water (SO-145) to validate the method. The trueness of the method was assessed by analysing GSP and two older GEOTRACES seawater reference materials (Atlantic surface water, GSI, and Atlantic deep water, GDI) all of which were specifically collected for interlaboratory calibration of contamination-prone trace metal isotopes. The results were compared to an established high-precision double-spike TIMS method (Paul et al., 2015b).

3.2.2. Reagents and materials

All procedures were carried out on a laboratory bench or in a class 10 laminar flow hood inside a class 1000 clean room laboratory. Purified deionised water (MQ water with a resistivity > 18.2 MΩcm) from a Milli-Q water system (Millipore) was used to clean materials and prepare all reagents. High-purity concentrated HBr (~8.5 M) and HF (~28 M) were purchased from VWR International as optima (distilled) grade acids, while concentrated HNO_3 (15.8 M) and HCl (11.7 M) were obtained from Fisher Scientific as analytical reagent grade acids. All mineral acids were purified in the clean laboratory by sub-boiling distillation using Savillex distillation units. Additional reagents were also purchased from Fisher Scientific and included concentrated optima grade H_2O_2 (~10 M), concentrated optima grade acetic acid (~17 M), and analytical reagent grade aqueous NH_3 solution (18.1 M). The analytical reagent grade aqueous NH_3 was purified by cold vapour phase equilibration using ~700 mL of aqueous NH_3 with ~350 mL of MQ water in a 1 L Savillex Teflon elbow and left for approximately two weeks to obtain purified aqueous NH_3.

All PTFE Teflon vials and PFA Teflon filtration apparatus were purchased from Savillex and cleaned by sequential soaking for one day in 1% Citranox detergent and then two days in heated (~120 °C) 6 M HCl, 8 M HNO_3 and 0.1 M distilled HNO_3 with extensive rinsing using MQ water in between each cleaning step. Low density polyethylene (LDPE) bottles were purchased from Fisher Scientific and cleaned by soaking for two days in heated (~60°C) 1% Citranox detergent, 3 M HCl and ~0.3 M distilled HNO_3 with extensive rinsing using MQ water between each cleaning step. Whatman® membrane filters (Polycarbonate membrane, 47 mm diameter and 0.5 µm pore size) purchased from Fisher Scientific were

cleaned in distilled 6 M HCl for 24–48 hours and stored in MQ water until used during the extraction procedure.

3.2.3. Solid-phase extraction using Nobias chelate resin

Lead was extracted and pre-concentrated from seawater using a batch-extraction technique in combination with Nobias PA-1 chelating resin (Hitachi High Technologies, Japan). Previous studies have demonstrated the ability of this resin—hydrophilic methacrylate polymer beads with ethylenediaminetriacetic (EDTriA) and iminodiacetic (IDA) acid functional groups (Sohrin et al., 2008)—to strongly bind to trace metals in seawater whilst maintaining a low affinity for major seawater cations (e.g., Na, Ca, Mg; Sohrin et al., 2008; Biller and Bruland, 2012; Conway et al., 2013) and producing low blank contamination during extraction procedures (Sohrin et al., 2008; Biller and Bruland, 2012; Chien et al., 2017). The procedure used in this study is based on a previously published method that applies the batch-extraction technique in combination with Nobias PA-1 chelating resin to extract Cd, Zn and Fe isotopes (Conway et al., 2013). Briefly, 0.2–2 L seawater sample aliquots (to provide 2–10 ng of Pb for isotopic measurements depending on seawater concentration) were transferred from the large seawater reference material container to LDPE bottles and treated with 1 mL 0.001 M H_2O_2 (per litre of seawater) to allow oxidation of organics over a 24-hour period. Sample pH was adjusted to 4.8 ± 0.2 by addition of distilled aqueous NH_3 using 2 mL (per L of seawater) of 5 M ammonium acetate as a buffer solution. Ammonium acetate was purified beforehand by passing it through the Nobias PA-1 resin procedure.

Previous studies performed trace metal extraction from seawater with Nobias PA-1 resin using a higher pH value (6.05–6.20; Sohrin et al., 2008; Biller and Bruland, 2012; Conway et al., 2013). For Pb extraction, there were three reasons for adopting a lower pH: (1) Pb yields plateau at 95–100% above pH 3.5, while the yields of major seawater cations continue to increase at a higher pH (Sohrin et al., 2008); (2) the most appropriate pH range for ammonium acetate buffer solution is lower than 6 (3.8–5.8; pKa = 4.8); (3) acidified seawater samples (pH ~2) require less addition of reagent to reach a pH of 4.8, instead of 6.05–6.20, thus reducing potential blank contamination.

After setting the pH, a filtration rig with a vacuum chamber was attached to a vacuum pump. A 0.5 µm PC membrane was attached to a filter unit and approximately 2.5 mL (~0.78 g) of Nobias resin was cleaned with 3 M HNO_3 and MQ water using the filter rig system. The cleaned resin was transferred to the pH-adjusted seawater sample and the

mixture was then shaken vigorously for two hours. The filtration apparatus was used again to separate the resin from the seawater and elute the Pb from the resin with ~30 mL of 3 M HNO_3. Finally, the resin was cleaned using 3 M HNO_3 and stored in a PTFE vial with ~15 mL 3 M HNO_3. Procedural blanks were estimated by processing 1 L of internal seawater reference material (SSW-5) through the full extraction technique five times to remove any Pb and produce a 'blank seawater' sample. The blank seawater sample was then passed through the aforementioned extraction procedure twice with every batch of samples to quantify the maximum blank contribution for a 2 L seawater sample.

3.2.4. Purification by anion-exchange chromatography

After the extraction procedure, samples were evaporated and treated with concentrated distilled HNO_3 and concentrated optima grade H_2O_2 (9:1 ratio) at 140°C for at least 2 hours. After evaporation, samples were refluxed at 140°C in 1 mL 2 M HBr and evaporated to remove any residual traces of nitrates and convert Pb to bromide form. Samples were then re-dissolved in a 5 mL 2 M HBr + 0.01 M HF solution. In this study, the anion-exchange purification procedure for Pb follows an established method that applies Eichrom AG1-X8 resin (100–200 mesh size) and dilute HBr-HNO_3 elution mixtures for the purification of seawater samples (Paul et al., 2015b and references therein). The only modification to the published procedure involves the use of 100 µL AG1-X8 columns instead of 20 µL AG1-X8 columns for the 2nd stage of anion-exchange chromatography.

3.2.5. MC-ICP-MS analyses of Pb isotope compositions

The accurate determination of Pb isotopes with precise correction of instrumental mass discrimination requires separate mass spectrometric analyses of both unspiked and double-spiked aliquots of the same sample. Therefore, after purification, the sample was divided into two unequal aliquots. Two-thirds of the solution remained unspiked while a calibrated ^{207}Pb-^{204}Pb double-spike solution was added to the remaining third (Paul et al., 2015b). The amount of ^{207}Pb-^{204}Pb double-spike added to the aliquot was calculated based on the sample weight, Pb concentration and an estimated extraction yield (~80%) with the intention of creating a mixture which contains a molar ratio of spike (S) Pb to natural (N) Pb that approximates the optimum S/N ≈ 1.226 (S ≈ 55.1% molar proportion; $^{206}Pb/^{204}Pb$ ≈ 0.411 assuming a seawater $^{206}Pb/^{204}Pb$ = 18.4; Rudge, et al., 2009). Following the addition of the double-spike, both the unspiked and double-spiked aliquots were doped with Tl using

Standard Reference Material (SRM) 997 from the National Institute Standards and Technology (NIST) to obtain a total Pb/Tl ratio ≈ 1/3 (Baker et al., 2004). The addition of Tl allowed external normalisation of both the unspiked and spiked measurements. Samples were evaporated, re-dissolved in 1 mL 0.1 M HNO_3 and refluxed to ensure sample-spike homogenisation.

All Pb isotope measurements were performed on a Nu Plasma II double-focusing MC-ICP-MS with an electrostatic analyser. Both unspiked and double-spiked measurements were acquired by static multicollection using a Faraday collector array with ^{205}Tl on the axial cup (^{201}Hg, ^{202}Hg, ^{203}Tl, $^{204}PbHg$, ^{205}Tl, ^{206}Pb, ^{207}Pb and ^{208}Pb on collectors L4, L3, L2 L1, Ax, H1, H2 and H3, respectively). All Faraday collector pre-amplifiers were equipped with 10^{11} Ω resistors except L1 and L3 which were both fitted with 10^{12} Ω resistors to enhance the signal/noise ratio for the corresponding isotopes. The higher resistors assisted in monitoring the low Hg interference levels in the gas background, correcting the isobaric interference on ^{204}Pb based on the known abundance of $^{204}Hg/^{202}Hg$ ratio ($^{204}Hg/^{202}Hg$ = 0.22923; Meija et al., 2010) and amplifying the minor ^{204}Pb isotope signal to improve the precision of the ratios involving the minor ^{204}Pb isotope (henceforth $^{20x}Pb/^{204}Pb$ ratios, where x = 6, 7 and 8). Samples were introduced into the MC-ICP-MS as dilute 0.1 M HNO_3 using a Nu instruments DSN-100 desolvator and a glass micro-flow nebuliser (uptake rate ~140 µL min^{-1}). The instrument parameters (torch position, source lenses, high-voltage lenses and quad lenses) were optimised on a daily basis for maximum intensity of the ^{208}Pb signal using a mixed NIST SRM 981-997 (Pb-Tl) solution (1 ppb Pb/ 3 ppb Tl).

Over a 15-month period, the average instrument sensitivity was ~1500 V ppm^{-1} (total Pb beam). In terms of data collection, an initial sample transfer time (50 seconds) was followed by automatic peak centring, electronic background monitoring (30 seconds) and data analysis as one block of 60 cycles with an integrated measurement time of five seconds. After each sample, the introduction system was washed for 120 seconds with 0.1 M HNO_3. For double-spike runs, a different DSN-100 desolvator and washing station was used to avoid memory effect in the introduction system which could impact any subsequent unspiked Pb measurements. During sample measurements, a set of mixed NIST SRM 981-997 solutions in 0.1 M HNO_3 ranging in Pb concentration from 1 to 10 ppb with a Pb/Tl ratio ≈ 1/3, were measured to monitor the accuracy during every run. For double-spike measurements, mixed NIST SRM 981-997 solutions were prepared by spiking 1/3 of the Pb concentration for the corresponding unspiked standard with ^{207}Pb-^{204}Pb double-spike to achieve the optimum S/N ratio, where N is the Pb of the NIST SRM standard.

All data processing was conducted offline using a programme developed on MATLAB®. The raw isotope beam intensities for both the unspiked and double-spiked measurements were corrected by first removing the electronic background and then any isobaric interferences (i.e., ^{204}Hg). Instrumental mass discrimination for unspiked measurements was corrected by external normalisation using the measured ^{205}Tl/^{203}Tl ratio, the exponential mass fractionation law and an empirically optimised ^{205}Tl/^{203}Tl reference ratio to provide the best fit for the ^{208}Pb/^{206}Pb, ^{207}Pb/^{206}Pb and ^{20x}Pb/^{204}Pb ratios (Rehkamper and Mezger, 2000; Gallon et al., 2008) relative to NIST SRM values (Galer and Abouchami, 1998). Data from the double-spiked measurements were then combined with the Tl-normalised Pb isotope ratios of the unspiked run to iteratively solve a series of non-linear equations and compute the double-spike corrected Pb isotope ratios (Rudge et al., 2009). The MATLAB programme processes the data on a cycle-by-cycle basis to provide accurate propagated instrumental uncertainties (Appendix 1). Lead isotope ratios of measured NIST SRM 981 during every run were normalised to average literature values reported for triple-spike TIMS measurements (Galer and Abouchami, 1998) and the corresponding correction factor applied to seawater sample measurements. Blank corrections were not applied to the Pb isotope data as there was no improvement to the precision of replicate analyses of the seawater reference materials.

3.2.6. Determination of Pb concentration

Lead concentrations were determined by isotope dilution (ID) on a Nu Plasma II MC-ICP-MS after extraction and chemical separation by $Mg(OH)_2$ co-precipitation and anion-exchange chromatography, respectively. The procedure is identical to previous methods measuring Pb concentration in seawater (Boyle et al., 2012; Paul et al., 2015b). Briefly, 50 mL seawater aliquots were spiked with a ^{207}Pb-^{204}Pb double-spike solution based on an estimate of the Pb concentration to achieve an optimal spike-sample ratio ≈ 2.61% (equivalent to ^{206}Pb/^{204}Pb ≈ 0.188; Paul et al., 2015b). Samples were left to equilibrate for ~10 days and then the Pb was extracted by $Mg(OH)_2$ co-precipitation using distilled aqueous NH_3. The seawater supernatant was removed, the precipitate dissolved in a dilute HNO_3-HBr mixture and the sample was subsequently purified by single stage anion-exchange chemistry using 20 µL AG1-X8 columns. The ID MC-ICP-MS analyses for Pb used the same techniques that were applied to the isotopic measurements.

3.3. Results and discussion

3.3.1. Solid-phase extraction vs. $Mg(OH)_2$ co-precipitation

Multiple aliquots of seawater reference materials were analysed by both solid-phase extraction and $Mg(OH)_2$ co-precipitation (following established methods; Paul et al., 2015b) in conjunction with double-spike correction to compare the performance of the extraction procedures (Table 3.1). The mean procedural blank for Nobias was 84 ± 25 pg (1sd, n = 9; excluding one anomalously high blank of 204 pg obtained immediately after cleaning the blank seawater sample) which, when normalised to seawater mass (0.29 ± 0.14 pmol kg^{-1}), is consistent with other solid-phase extraction procedures using Nobias (0.33 ± 0.16 pmol kg^{-1}; Chien et al., 2017) or Toyopearl (0.1 ± 1.3 pmol kg^{-1}; Zurbrick et al., 2013) resins. Blank contamination during solid-phase extraction was three times higher than $Mg(OH)_2$ co-precipitation in this study (27 ± 12 pg; 1sd, n = 6) and a previous study using the same extraction procedure (28 ± 21 pg; 1sd, n = 25; Paul et al., 2015b) On the other hand, Nobias demonstrates a greater efficiency than $Mg(OH)_2$ co-precipitation with significantly higher Pb yields across all seawater reference materials (Table 3.1). Most samples have extraction yields (~90–95%) comparable to other studies using similar procedures (Sohrin et al., 2008; Biller and Bruland, 2012; Conway et al., 2013), with the exception of the low concentration seawater sample (Southern Ocean, SO-145), which exhibits variable extraction efficiencies (60–111%) due to the higher relative error of the Pb concentration measurements. Once blanks contributions to the quantity of Pb measured for each sample were calculated (based on mean procedural blanks, mean measured yields and the same volume of seawater for both extraction methods), they were significantly higher for Nobias (0.9–5.7%) than $Mg(OH)_2$ co-precipitation (0.4–1.9%) across all seawater reference materials. The greater efficiency of solid-phase extraction, therefore, does not compensate for the higher blank contamination.

Despite the different blank contribution levels for the two different extraction methods, all seawater reference materials yielded Pb isotope ratios that were in excellent agreement. Moreover, given a statistically significant number of replicate analyses for each method (e.g., SSW-5, n = 5–7; GSP, n = 7–8), there is no significant difference in the external reproducibility (2sd relative ppm) of the different ratios. The higher blank contributions exhibited by solid-phase extraction, along with any minor fractionation processes during the extraction procedures, have negligible effect on the relative accuracy of the Pb isotope measurements.

Table 3.1 Lead concentration and isotope composition data for seawater reference materials analysed by two extraction methods and measured on a MC-ICP-MS using a ^{207}Pb-^{204}Pb double-spike correction for instrumental mass discrimination.

Sample	*n*-ID[a]	[Pb] ± 1sd (pmol kg^{-1})[b]	Extraction method	*n*-IC[c]	$^{206}Pb/^{204}Pb$ ± 2sd[d]	$^{207}Pb/^{204}Pb$ ± 2sd[d]	$^{208}Pb/^{204}Pb$ ± 2sd[d]	$^{206}Pb/^{207}Pb$ ± 2sd[d]	$^{208}Pb/^{207}Pb$ ± 2sd[d]	Sample size (L)[e]	Total Pb (ng)[f]	Meas. Pb (ng)[g]	Yield (mean) (%)[h]
SSW-9	4	352.9 ± 0.6	Nobias ± 2sd relative (ppm)[d]	3	17.917 ± 11 610	15.593 ± 10 640	37.827 ± 29 760	1.1490 ± 01 60	2.4251 ± 04 150	~ 0.2	11.7	11.0	93–95 (94)
			Co-precipitation ± 2sd relative (ppm)[d]	5	17.914 ± 05 250	15.598 ± 09 560	37.842 ± 30 800	1.1486 ± 03 280	2.4250 ± 02 80	~ 0.2–1.0	15.6	10.3	61–69 (66)
SSW-5	7	248.4 ± 2.0	Nobias ± 2sd relative (ppm)[d]	5	18.095 ± 04 240	15.608 ± 06 370	37.914 ± 17 450	1.1593 ± 02 150	2.4284 ± 02 100	~ 0.2	11.2	10.4	88–95 (93)
			Co-precipitation ± 2sd relative (ppm)[d]	7	18.097 ± 05 270	15.611 ± 04 280	37.919 ± 15 400	1.1592 ± 03 240	2.4284 ± 03 140	~ 0.2	8.3	6.0	63–80 (73)
GSP	6	58.7 ± 0.8	Nobias ± 2sd relative (ppm)[d]	8	18.076 ± 08 430	15.604 ± 07 420	38.194 ± 22 560	1.1584 ± 03 230	2.4468 ± 06 200	~ 0.2–0.7	6.1	5.7	89–96 (92)
			Co-precipitation ± 2sd relative (ppm)[d]	7	18.076 ± 07 360	15.605 ± 05 310	38.194 ± 09 240	1.1584 ± 03 220	2.4469 ± 04 160	~ 0.5	7.1	5.7	75–88 (81)
SO-145	5	7.0 ± 1.2	Nobias ± 2sd relative (ppm)[d]	7	18.521 ± 23 1230	15.646 ± 08 490	38.275 ± 36 930	1.1837 ± 14 1210	2.4447 ± 08 310	~ 2.0–2.1	3.1	2.3	60–111 (76)
			Co-precipitation ± 2sd relative (ppm)[d]	2	18.528 ± 01 65	15.655 ± 06 380	38.282 ± 17 450	1.1835 ± 05 400	2.4449 ± 02 75	~ 2.0	2.8	2.0	72–73 (73)

[a] Number of individual sample aliquots analysed for Pb concentrations using isotope dilution technique.

[b] Pb concentrations were corrected using a mean total procedural blank of 20.8 ± 13.2 pg (1sd; $n = 11$).

[c] Number of individual sample aliquots analysed for Pb isotope compositions.

[d] 2 x standard deviation calculated from results of n sample aliquots over several batches of measurements i.e., long-term reproducibility of a given sample.

[e] Volume of individual aliquots used for Pb isotope composition analyses.

[f] Mean mass of Pb in sample aliquots used for Pb isotope composition analyses calculated using the sample Pb concentration and sample volume.

[g] Mean mass of Pb in individual aliquots used for isotopic analyses following chemical separation (corrected using mean total blank of 83.7 ± 24.7 pg; 1sd; $n = 9$).

[h] Pb extraction efficiency for samples following chemical extraction and purification procedures.

3.3.2. Double-spike correction vs. Tl-normalisation

The procedures used to account for instrumental mass discrimination were validated using multiple measurements of 1 and 10 ppb (~1 and 7 ng of Pb consumed during each measurement, respectively) NIST SRM 981 (Table 3.2). For both concentrations, double-spike corrected Pb isotope ratios are consistent with recent reference values applying double or triple-spike correction to MC-ICP-MS (Thirlwall, 2002; Baker et al., 2004; Makishima et al., 2007; Makishima and Nakamura, 2010; Taylor et al., 2015) or TIMS (Galer and Abouchami, 1998; Thirlwall, 2002; Amelin and Davis, 2006; Taylor et al., 2015; Klaver et al., 2016; Fukami et al., 2017) analyses (Table 3.2; Figure 3.1 (a));. Despite the low level of Pb consumed, the double-spike can effectively and accurately correct for the greater mass fractionation of the plasma ion source relative to TIMS. Double-spike corrected 1 ppb standards were tested to simulate concentration levels appropriate for seawater analyses and exhibit an external reproducibility of ~1000–1400 ppm for $^{20x}Pb/^{204}Pb$ ratios and ~220–280 ppm for $^{206}Pb/^{207}Pb$ and $^{208}Pb/^{207}Pb$ ratios (Table 3.2). Previous studies using MC-ICP-MS coupled with double-spike correction used NIST SRM 981 at much higher concentrations (~50–80 ppb) or exclusively without any real samples and have therefore obtained more precise results (Thirlwall, 2002; Baker et al., 2004; Makishima and Nakamura, 2010; Taylor et al., 2015). The results presented here are comparable to TIMS measurements using 10^{11} Ω resistors for all isotopes and similar quantities of Pb during measurements (~900–1100 ppm for $^{20x}Pb/^{204}Pb$ ratios and ~140–200 ppm for $^{206}Pb/^{207}Pb$ and $^{208}Pb/^{207}Pb$; Bridgestock, 2015; Paul et al., 2015b), but are more than a an order of magnitude worse than TIMS results for ^{204}Pb ratios when using 10^{13} Ω resistors or total evaporation technique (~60–120 ppm for $^{20x}Pb/^{204}Pb$ ratios; $^{206}Pb/^{207}Pb$ and $^{208}Pb/^{207}Pb$ ratios were not reported; Klaver et al., 2016; Fukami et al., 2017).

The external precision of Tl-normalised Pb isotope ratios are ~2 times better than the double-spike correction for all ratios when measuring 10 ppb concentrations, and ~2 times better for the $^{20x}Pb/^{204}Pb$ ratios but only marginally better for $^{206}Pb/^{207}Pb$ and $^{208}Pb/^{207}Pb$ when measuring 1 ppb concentrations (Table 3.2). The high precision of Tl-normalisation is a function of two variables: (1) minimal matrix interferences because of the purity of the standard solutions; and (2) larger double-spike external errors caused by the propagation of measurement errors across the unspiked and double-spiked analyses.

Table 3.2 Lead isotope data for NIST SRM 981 on a MC-ICP-MS using either ^{207}Pb-^{204}Pb double-spike or Tl-normalisation for correction of instrumental mass fractionation.

Standard	Pb (Tl) (ng) [d]	*n*[a]	Mass bias correction	$^{206}Pb/^{204}Pb$ ± 2sd[b]	$^{207}Pb/^{204}Pb$ ± 2sd[b]	$^{208}Pb/^{204}Pb$ ± 2sd[b]	$^{206}Pb/^{207}Pb$ ± 2sd[b]	$^{208}Pb/^{207}Pb$ ± 2sd[b]
SRM 981-997	~1 (3)	53	^{207}Pb-^{204}Pb DS	16.927 ± 17	15.486 ± 18	36.688 ± 50	1.0931 ± 03	2.3691 ± 05
(This study)			± 2sd relative (ppm)[b]	1020	1200	1370	280	220
			± 2se typical run (ppm)[c]	260	290	340		70
			Tl-normalisation	16.935 ± 09	15.497 ± 08	36.723 ± 19	1.0928 ± 03	2.3697 ± 05
			± 2sd relative (ppm)[b]	550	490	530	250	200
			± 2se typical run (ppm)[c]	210	220	220		30
SRM 981-997	~7 (21)	27	^{207}Pb-^{204}Pb DS	16.9338 ± 46	15.4923 ± 57	36.7015 ± 169	1.0930 ± 01	2.3690 ± 03
(This study)			± 2sd relative (ppm)[b]	270	370	460	120	130
			± 2se typical run (ppm)[c]	80	100	120		50
			Tl-normalisation	16.9384 ± 22	15.4985 ± 23	36.7210 ± 54	1.0929 ± 01	2.3693 ± 02
			± 2sd relative (ppm)[b]	130	150	150	55	90
			± 2se typical run (ppm)[c]	60	70	90		20
Galer et al., (1998)	~10		^{207}Pb-^{206}Pb-^{204}Pb TS	16.9405 ± 15	15.4963 ± 16	36.7219 ± 44	1.0932	2.3697
			± 2sd relative (ppm)[b]	90	100	120		

[a] Number of analyses.

[b] 2 x standard deviation calculated from n analyses i.e., long-term external precision of NIST SRM 981 during measurements.

[c] 2 x standard error (2 se) of the mean based on individual results during measurement cycles i.e., internal precision of NIST SRM 981.

[d] Mass of Pb used for a single analysis during measurements.

In contrast to NIST SRM 981 standards, seawater samples and reference materials are subjected to blank contamination, minor isotope fractionation during chemical purification and a greater range of instrumental mass discrimination due to sample matrix effects. Consequently, the external precision of double-spike corrected Pb isotope ratios for NIST SRM 981 standards is better than seawater samples when measuring comparable amounts of Pb. As expected, therefore, the external precisions of Tl-normalised $^{20x}Pb/^{204}Pb$ ratios and $^{206}Pb/^{207}Pb$, $^{208}Pb/^{207}Pb$ ratios for SSW-5 (420–540 and 70–160 ppm), GSP (300–600 and 290–350 ppm) and SO-145 (610–1330 and 440–1160 ppm) are inferior to the external precision of Tl-normalised NIST SRM 981 standards when comparable amounts of Pb are measured.

However, despite the introduction of potential matrix effects and interferences, the results for Tl-normalised seawater data compare extremely well to the precision of corresponding double-spike data (Figure 3.1). The high performance of Tl-normalisation can be explained when examining the difference between the external precisions of both correction procedures following $Mg(OH)_2$ co-precipitation. The external precisions of Tl-normalised $^{20x}Pb/^{204}Pb$ ratios and $^{206}Pb/^{207}Pb$, $^{208}Pb/^{207}Pb$ ratios are worse for SSW-9 (410–965 and 190–380 ppm), SSW-5 (560–790 and 170–230 ppm), and GSP (1080–1720 and 330–440 ppm) than double-spike corrected data (Table 3.1). The superiority of double-spike correction following $Mg(OH)_2$ co-precipitation, and the similarity between double-spike correction and Tl-normalisation after Nobias, indicates that $Mg(OH)_2$ co-precipitation is potentially less effective at extracting high-purity Pb from the seawater matrix, which increases the susceptibility of Tl-normalisation to matrix effects during MC-ICP-MS analyses (Barling and Weis, 2008). However, given the limited amount of seawater available for replicate analyses, it is difficult to state with statistical certainty that the difference in precision between double-spike and Tl-normalised Pb ratios following $Mg(OH)_2$ co-precipitation is a consequence of matrix effects.

The external relative accuracy of Tl-normalisation is demonstrated by the size and coincidence of uncertainty ellipses in $^{206}Pb/^{204}Pb$-$^{206}Pb/^{207}Pb$ isotopic space (Figure 3.1). Overall, Tl-normalised Pb isotope ratios following both extraction procedures are identical to double-spike corrected ratios. There exists, independent of extraction or mass discrimination correction procedures, a co-variation between $^{206}Pb/^{204}Pb$ and $^{206}Pb/^{207}Pb$ (the long axis of the calculated uncertainty ellipse) which does not entirely coincide with the linear mass fractionation vector. This behaviour suggests that the double-spike correction and Tl-normalisation effectively eliminate any significant variation caused by instrumental mass

fractionation, but the deviation (or scatter) must be caused by either mass independent fractionation or analytical uncertainty when analysing low level Pb measurements.

In Figure 3.1, the long-axis of the uncertainty ellipses are not aligned with the mass fractionation vector for both NIST SRM 981 and seawater reference materials, regardless of the amount of Pb measured (NIST = ~1–7 ng, SSW-5 = ~10 ng, GSP = ~6 ng, SO-145 = ~2 ng). The shift of the ellipses away from the mass fractionation line is a consequence of residual uncertainties caused by instrument limitations (e.g., signal-to-noise ratio, increase in blank contribution, electronic baselines and inadequate Hg correction). The alignment of the uncertainty ellipses horizontally across the x-axis signifies that this analytical uncertainty is predominantly controlled by instrument limitations associated with the measurement of the small ^{204}Pb isotope.

Another important observation is that the uncertainty ellipses of the double-spike and Tl-normalised data overlap less with increasing amounts of Pb analysed (Figure 3.1 (d)-(b)). Overall, for low Pb concentration data (~2–10 ng Pb), the mass fractionation relationship between Tl and Pb is not compromised following either extraction method: the distribution of Tl-normalised data is not characterised by extremely large co-variation and overlaps with the ellipses of double-spike data. The oblate nature of the ellipses for both double-spike and Tl-normalisation highlights the analytical limitations (as discussed above) rather than the inability of Tl to accurately correct for mass discrimination. Although there is no observable difference between Tl-normalisation and double-spike correction in this study, for higher amounts of Pb consumed (> 10 ng of Pb) Tl-normalisation may produce less accurate data than double-spiked correction (Figure 3.1 (b)). Within the range of total Pb measured during analyses for seawater measurements, however, provided that the instrument is calibrated with a reference material during each analytical session, solid-phase extraction with Nobias coupled with Tl-normalisation provides an effective method to obtain high-precision Pb isotope measurements of seawater. This approach requires only one mass spectrometric run, thus reducing the analytical time further and increasing the amount of Pb available for measurements.

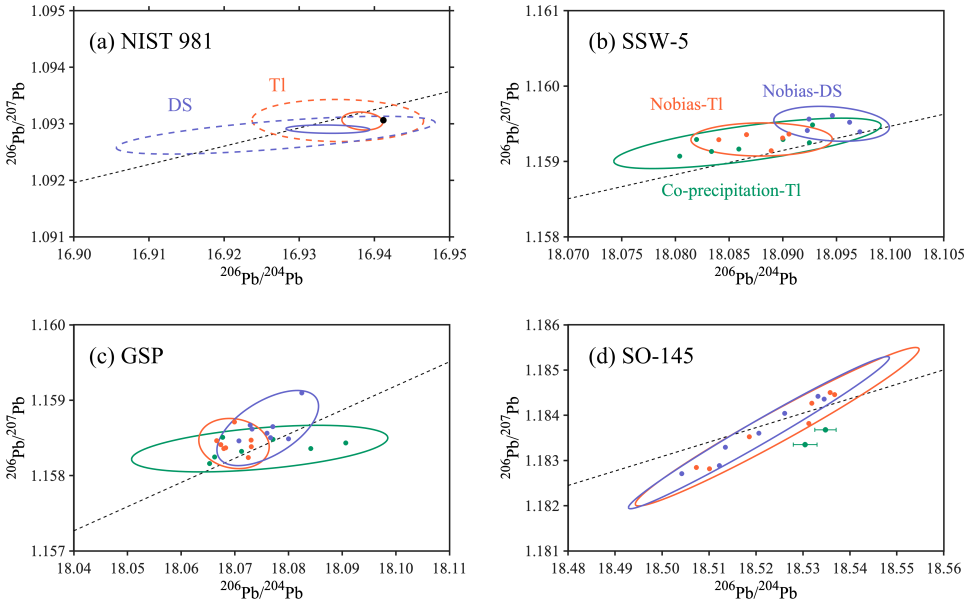

Figure 3.1 $^{206}Pb/^{204}Pb$-$^{206}Pb/^{207}Pb$ isotope plots for (a) NIST SRM 981 (b) SSW-5, (c) GSP and (d) SO-145. Error ellipses represent the eigenvectors and eigenvalues (multiplied by the chi-squared factor to achieve a 95% confidence level) generated from covariation regression analysis of (1) NIST SRM 981 double-spike (purple) and Tl-normalisation (orange) for 1 ppb and 10 ppb solutions (dashed and solid ellipses, respectively); and (2) Nobias with double-spike (purple), Nobias with Tl-normalisation (orange), and $Mg(OH)_2$ co-precipitation with Tl-normalisation (green) for seawater reference materials. The black point in panel (a) represents the NIST SRM 981 poly-spike average taken from the literature (see text section 3.2.2). Every coloured point in (b)-(d) denotes an individual seawater measurement for the respective procedure. The dotted black line represents the linear mass fractionation vector calculated using the mean measured (Nobias) double-spike $^{206}Pb/^{204}Pb$ and $^{206}Pb/^{207}Pb$ ratios and a slope equal to $\delta m_2/\delta m_1$ x R_2/R_1, where δm_1 and δm_2 correspond to the difference in mass for R_1 ($^{206}Pb/^{204}Pb$) and R_2 ($^{206}Pb/^{207}Pb$), respectively. An error ellipse could not be calculated for SO-145 $Mg(OH)_2$ co-precipitation with Tl-normalisation (n = 2; Table 3.1). Here, the points are plotted with the internal errors (2 x standard error of the mean for individual results) for $^{206}Pb/^{204}Pb$ and $^{206}Pb/^{207}Pb$ ratios.

3.3.3. Instrument and interlaboratory calibration

The external reproducibility for multiple analyses of internal seawater reference materials demonstrates furthermore that the new analytical procedure is better than a high-precision $Mg(OH)_2$ co-precipitation double-spike TIMS method previously used in the MAGIC laboratories at Imperial College London (Paul et al., 2015b). For low concentration seawater samples (Pb = ~7 pmol kg^{-1}; n = 7), the typical precision of $^{20x}Pb/^{204}Pb$ ratios and $^{206}Pb/^{207}Pb$, $^{208}Pb/^{207}Pb$ ratios were 490–1230 and 1210, 310 ppm, respectively (Table 3.1). The results represent a significant improvement compared to the established TIMS method for the

Table 3.3 Lead concentration and isotope composition data for three GEOTRACES reference samples in comparison to previous and new TIMS results. For display purposes, only the results for GEOTRACES reference materials analysed by the TIMS method are provided in the table (Paul et al., 2015b). This method has already been shown to produce the same Pb concentration and isotope composition values as those produced by two other laboratories (Boyle et al., 2012).

Sample	Reference	*n*-ID[a]	[Pb] ± 1sd (pmol kg^{-1})[b]	Method[c]	*n*-IC[d]	$^{206}Pb/^{204}Pb$ ± 2sd[e]	$^{207}Pb/^{204}Pb$ ± 2sd[e]	$^{208}Pb/^{204}Pb$ ± 2sd[e]	$^{206}Pb/^{207}Pb$ ± 2sd[e]	$^{208}Pb/^{207}Pb$ ± 2sd[e]	Sample size (L)[f]	Total Pb (ng)[g]	Yield (%)[h]
GSP	This study	6	58.7 ± 0.8	Nobias MC-ICP-MS DS ± 2sd relative (ppm)[d]	8	18.076 ± 08 430	15.604 ± 07 420	38.194 ± 22 560	1.1584 ± 03 230	2.4468 ± 06 200	~ 0.5–0.7	6.1	90–96
	This study	5	56.3 ± 1.7	Co-precipitation TIMS DS ± 2sd relative (ppm)[d]	4	18.072 ± 07 390	15.601 ± 04 270	38.183 ± 10 260	1.1584 ± 01 120	2.4475 ± 03 110	~ 0.5–2.0	13.4	84–97
GSI	This study	1	25.8	Nobias MC-ICP-MS DS ± 2se typical run (ppm)[i]	1	18.365 ± 02	15.634 ± 02	38.260 ± 05	1.1747 ± 01	2.4467 ± 01	~ 1.0	5	86
	Paul et al. (2015)	6	27.9 ± 1.2	Co-precipitation TIMS DS ± 2sd relative (ppm)[d]	3	18.359 ± 26 1430	15.635 ± 07 480	38.246 ± 30 790	1.1741 ± 13 1090	2.4463 ± 09 350	~ 2.0	10	45–60
GDI	This study	1	42.4	Nobias MC-ICP-MS DS ± 2se typical run (ppm)[i]	1	18.477 ± 01	15.626 ± 01	38.278 ± 04	1.1824 ± 01	2.4490 ± 01	~ 1.0	9	85
	Paul et al. (2015)	5	45.7 ± 2.6	Co-precipitation TIMS DS ± 2sd relative (ppm)[d]	2	18.475 ± 41 2240	15.624 ± 10 650	38.276 ± 60 1570	1.1825 ± 19 1600	2.4498 ± 22 900	~ 2.0	17	50–55

[a] Number of individual sample aliquots analysed for Pb concentrations.

[b] Pb concentrations from this study were corrected using a mean total blank of 20.8 ± 13.2 pg (1sd; $n = 11$).

[c] Method conducted to analyse Pb isotopes (extraction, instrument, mass discrimination procedure).

[d] Number of individual sample aliquots analysed for Pb isotope compositions.

[e] 2 x standard deviation (2sd) calculated from results of n sample aliquots over several batches of measurements i.e., long-term reproducibility of a given sample.

[f] Volume of individual aliquots used for Pb isotope composition analyses.

[g] Mean mass of Pb in sample aliquots used for Pb isotope composition analyses calculated using the sample Pb concentration and sample volume.

[h] Pb extraction efficiency for samples across the chemical extraction and purification procedures.

[i] 2 x standard error (2se) of the mean based on individual results during measurement cycles i.e., internal precision of sample *n*.

$^{20x}Pb/^{204}Pb$ ratios (1300–2600 ppm) and $^{206}Pb/^{207}Pb$, $^{208}Pb/^{207}Pb$ ratio (1730 ppm, 920 ppm, respectively; Paul et al., 2015b; Bridgestock, 2015). Importantly, the analytical throughput of the new procedure is significantly higher (~12 samples/month) compared to the previously used $Mg(OH)_2$ co-precipitation double-spike TIMS analyses (~6 samples/month). This improvement in throughput is achieved without compromising the precision of the results or the capability to measure extremely low-level seawater samples. Overall, the method is time-effective, eliminates previous problems associated with $Si(OH)_4$ and provides the desired precision of ~1000 ppm or better for all Pb isotope ratios, even for seawater with Pb concentrations as low as ~7 pmol kg^{-1} (Table 3.1; Boyle et al., 2012).

The trueness of the new method was furthermore confirmed by analysing Pb concentrations and isotope compositions for three GEOTRACES intercalibration samples (GSP, GSI and GDI; Table 3.3). The results are compared to results obtained previously by high-precision TIMS and agree with consensus values for Pb concentrations and reference values from two other laboratories for Pb isotope compositions (Table 3.3; Boyle et al., 2012; Zubrick et al., 2013; Paul et al., 2015b). For Pb concentrations, GSI (25.8 pmol kg^{-1}) and GDI (42.8 pmol kg^{-1}) yielded lower values compared to TIMS values (27.9 and 45.7 pmol kg^{-1}, respectively). The external precision of Pb concentrations for GSI and GDI could not be established because there was not enough sample volume for multiple analyses. Assuming a typical external precision of ~1–2 pmol kg^{-1} for seawater Pb concentrations (Table 3.1), all results are identical within the quoted uncertainties. For Pb isotope compositions, all intercalibration samples were analysed using 0.5–2 L aliquots. Following chemical extraction and purification, ~4–10 ng of Pb were available for isotope analysis. When compared to high-precision TIMS values, both methods produce identical results within quoted uncertainties for all Pb isotope ratios across all intercalibration samples. The excellent agreement of the new method and the established TIMS method is further validated by the mean absolute difference of the external precision for all Pb isotope ratios of GSP (~190–290 ppm for $^{20x}Pb/^{204}Pb$ ratios and ~ < 290 ppm for $^{206}Pb/^{207}Pb$ and $^{208}Pb/^{207}Pb$). The difference in results is approximately half the external precision for $^{20x}Pb/^{204}Pb$ ratios and similar to the external precision of $^{206}Pb/^{207}Pb$ and $^{208}Pb/^{207}Pb$ ratios produced by MC-ICP-MS coupled with double-spike correction (Table 3.1).

3.4. Conclusion

A new analytical procedure was developed to improve the precision and analytical throughput of Pb isotope analysis of seawater. The procedure combines solid-phase extraction of Pb using Nobias PA-1 chelating resin with MC-ICP-MS analyses that employ a ^{207}Pb-^{204}Pb double-spike for correction of mass discrimination. Following multiple analyses of internal and intercalibration seawater reference materials, the typical precision (2sd) of the procedure is ~250–1250 ppm for $^{206}Pb/^{204}Pb$, $^{207}Pb/^{204}Pb$, $^{208}Pb/^{204}Pb$ ratios and ~100–1200 ppm for $^{206}Pb/^{207}Pb$, $^{208}Pb/^{207}Pb$ ratios. Nobias extraction and $Mg(OH)_2$ co-precipitation with double-spike correction produce statistically identical results with no discernible difference in the level of precision. High-precision Pb isotope analyses are attainable using Nobias coupled with Tl-normalisation. Following $Mg(OH)_2$ co-precipitation, Tl-normalisation shows no systematic bias but appears to produce less precise Pb isotope data because of matrix effects during the MC-ICP-MS measurements. Finally, calibration against results obtained for seawater reference materials with an established TIMS double-spike method confirms the trueness of the new procedure.

Acknowledgements and contributions

Alex Griffiths conducted the method development procedure, with the guidance of Mark Rehkämper and Tina van de Flierdt and lead the interpretation and presentation of the data. Additional contributions to the method were received from Hollie Packman, Susan Little, Mark Rehkämper and Tina van de Flierdt. Thanks to the co-authors for providing advice, guidance and insightful comments on the analytical techniques and data interpretation. The author would like to acknowledge all the members of the MAGIC group, especially Katharina Kreissig and Barry Coles, for their support in the lab. The authors would like to acknowledge studentship funding from the NERC DTP ‘Science and Solutions for a Changing Planet’ at Imperial College London. Ed Boyle is thanked for providing additional GSI and GDI reference samples, and James Moffett is thanked for providing GSP samples, sampling for all of which was made possible via NSF support to the GEOTRACES intercalibration phase.

Chapter 4

Pathways and processes controlling the distribution of anthropogenic lead in the interior of the Southern Ocean

Abstract

Anthropogenic lead (Pb) emissions from mining, smelting and fossil fuel combustion are important sources of atmospheric, and thus, oceanic contamination. The interplay between the Antarctic Circumpolar Current and Meridional Overturning Circulation, as well as the different biogeochemical provinces of the Southern Ocean, could play an important role in the global redistribution of these anthropogenic emissions but the sources, fluxes and processes governing the distribution of Pb across this region have not yet been constrained.

Samples were collected for measurements of dissolved Pb concentration and isotope composition at six depth profiles along a meridional transect at 140°E between Australia and Antarctica (GEOTRACES section GS01). The results show that the sources of Pb to the Southern Ocean are (1) anthropogenic emissions from Australia; (2) Australian dust from river plains and deserts; and (3) Antarctic sediments/benthic fluxes influencing deep and bottom water masses as recorded in deep-sea ferromanganese crusts. Surface waters with low $^{206}Pb/^{207}Pb$ and $^{208}Pb/^{207}Pb$ ratios corresponds to a high fraction of anthropogenic Pb (~30–50%). In contrast, the high $^{206}Pb/^{207}Pb$ and $^{208}Pb/^{207}Pb$ of Antarctic Bottom Water record the dominance of natural Pb inputs during bottom water formation (~76–84%).

Despite the strong correlation between Pb isotope signatures and water masses along the section, there is an incongruence between the spatial distribution of sub-surface waters and their location in Pb isotope space. Subantarctic Mode Water in the Subantarctic Zone shows the lowest $^{206}Pb/^{207}Pb$ and $^{208}Pb/^{207}Pb$ ratios and the highest Pb concentrations (~15 pmol kg^{-1}) across the transect despite forming from Antarctic Surface Water with higher $^{206}Pb/^{207}Pb$ and $^{208}Pb/^{207}Pb$ ratios. These observations indicate that the Pb isotope composition of SAMW is tracing the pathway of contaminated Pacific waters laterally advected poleward from east Australia into the Southern Ocean through the Tasman leakage.

Similarly, pre-formed Antarctic Intermediate Water (AAIW) and Upper Circumpolar Deep Water (UCDW) exhibit anonymously low $^{206}Pb/^{207}Pb$ and $^{208}Pb/^{207}Pb$ ratios and high Pb concentrations but the anthropogenic Pb signal in these water masses cannot be reconciled by lateral advection or diapycnal water mass mixing. It is proposed that reversible scavenging and equilibrium exchange are the dominant processes responsible for the vertical transport of anthropogenic Pb to deep waters. The equatorward trend of decreasing $^{206}Pb/^{207}Pb$ and $^{208}Pb/^{207}Pb$ and increasing Pb concentrations in these water masses highlights the spatial variability of reversible scavenging caused by different rates of primary production across the Southern Ocean biogeochemical provinces. In the northern PF region where diatom primary

production and opal levels are higher than HNLC Antarctic region, a particularly strong anthropogenic Pb signal in UCDW indicates that reversible scavenging may be responsible for ~80% of the observed dissolved Pb budget. Nevertheless, it remains difficult to quantitatively resolve the relative contributions of the different processes without well-constrained Southern Ocean scavenging rate constants, particulate settling velocities as well as particle and water mass endmember compositions.

4.1. Introduction

Over the last century, anthropogenic emissions from mining, smelting and fossil fuel combustion have greatly perturbed the lead (Pb) inventory of the modern ocean (e.g., Pacyna and Pacyna, 2001; Kelly et al., 2009; Boyle et al., 2014). These anthropogenic emissions exhibit distinct Pb isotope signatures which reflect the specific Pb ore deposits used to sustain the industrial activity of a particular region (e.g., Bollhöfer and Rosman, 2000; Bollhfer and Rosman, 2001). As a consequence of this regional variability, Pb isotopes can be used to identify sources of contamination and quantify the relative contribution of anthropogenic and natural Pb sources to the surface ocean (e.g., Lee et al., 2015; Bridgestock et al., 2016; Zurbrick et al., 2017).

In conjunction with this spatial variability, the magnitude and isotopic composition of anthropogenic emissions evolve through time because of changes in anthropogenic activities. These temporal variations correspond to a variety of socio-economic developments, from the implementation of environmental regulations (e.g., phase-out of leaded petrol) and changes in the supply of Pb from an particular ore deposit to a given region, to fluctuations in industrial productivity and, therefore, the relative intensity of regional Pb emissions (Shen and Boyle, 1987; Wu and Boyle, 1997a; Veron et al., 1998; Kelly et al., 2009). While the spatiotemporal variability of anthropogenic Pb fluxes to the surface ocean controls the boundary conditions of a water mass during formation, the subsequent distribution of Pb isotopes in the ocean interior is governed by the internal cycling of Pb.

Following atmospheric deposition and dissolution in the ocean, Pb inputs are exported from the surface to deeper waters predominantly by ocean circulation and water mass mixing (Shen and Boyle, 1988; Noble et al., 2015; Bridgestock et al., 2018). The isotopic composition of the Pb source is conserved during water mass transit through the ocean as Pb is not subjected to any significant physical or chemical isotopic fractionation processes in the water column (Sangster, et al., 2000; Komárek, et al., 2008). This conservative behaviour, coupled with the transient nature of Pb inputs to the ocean, allows Pb isotopes to trace the formation sites, circulation pathways and ventilation timescales of water masses across the ocean (e.g., Alleman et al., 1999; Bridgestock et al., 2018).

Recently, however, several studies have shown that Pb isotopes do not necessarily act as conservative tracers of water mass mixing. Within the water column, reversible scavenging and equilibrium exchange between dissolved and adsorbed particulate Pb can act as an important mechanism for transport of anthropogenic Pb to the deep ocean

(Wu et al., 2010; Chen et al., 2016; Zurbrick el al., 2017). Although Pb isotopes have been used successfully to trace oceanographic processes ranging from large-scale ocean circulation to mesoscale eddy phenomena (Veron et al., 1998; Paul et al., 2015a), the interplay between the different processes could affect the ability of Pb isotopes to trace the pathways and ventilation times of water masses in hydrographically dynamic and biologically productive regions.

In the Southern Ocean, the Antarctic Circumpolar Current (ACC) and its interplay with the Meridional Overturning Circulation (MOC) in the different ocean basins could play an important role in the global redistribution of anthropogenic Pb. There are currently, however, only two studies which have used Pb isotopes to examine the origins of Pb in the Southern Ocean. Although recent observations suggest that natural Pb dominates the coastal water column of the Amundsen Sea (60–95%; Ndungu et al., 2016), the presence of anthropogenic Pb has been detected in the open ocean surface waters of the Weddell and Scotia Seas (0–70%; Flegal et al., 1993). Importantly, the pathways and processes controlling the distribution of both anthropogenic and natural Pb in the Southern Ocean could not be constrained in these studies because the observations were restricted either to a specific region or surface water measurements.

In theory, the strong circulation patterns of the ACC and MOC would suggest that, like in the North Atlantic, thermohaline circulation and water mass advection control Pb distribution (e.g., Alleman et al., 1999). Alleman et al. (2001), however, hypothesised that observed differences in the isotopic composition of Southern Ocean sourced water masses in the South Atlantic (Antarctic Intermediate Water and Antarctic Bottom Water) could be due to disparities in either inputs from regional sources near their formation sites, or the magnitude of Pb remineralisation in deeper waters. Observations near the formation sites of intermediate and deep-water masses in the Southern Ocean would allow this hypothesis to be tested.

This study presents Pb isotope composition and concentration data for water column profiles at six locations that form a meridional transect in the Australian sector of the Southern Ocean. The aim is to (1) determine the sources of Pb to the Southern Ocean and quantify the level of anthropogenic Pb contamination in the region; and (2) elucidate the pathways and deconvolve the processes governing the distribution of anthropogenic Pb in the interior of the Southern Ocean.

4.2. Oceanographic setting

4.2.1. Regional circulation and frontal structure

The Australian sector of the Southern Ocean contains two ocean basins separated by the South Indian Ridge (Figure 4.1). The Australian Basin is situated immediately south of Australia and is bounded to the west by Broken Ridge (100°E; not shown in Figure 4.1) and to the east by the Tasman Rise. The second basin, the Australian-Antarctic Basin, lies north of Wilkes and Adélie Land continental margins (East Antarctica) and is bounded to the west by the Kerguelen Plateau (80°E; not shown in Figure 4.1) and to the east by the south-east extension of the South Indian Ridge.

The circulation pattern in this region is dominated by a strong eastward flow, a combination of the Antarctic Circumpolar Current (ACC), warmer waters from the Atlantic and the Agulhas Return Current (black dashed arrows; Figure 4.1), which enters the Australian-Antarctic Basin from the west and extends along the Southeast Indian Ridge into the Pacific Ocean (McCartney and Donohue, 2007). The strong eastward flow forces a western boundary current from the Kerguelen Plateau to extend along the centre of the Australian-Antarctic Basin (dark blue dashed arrows; Figure 4.1; McCartney and Donohue, 2007). This mid-basin flow recirculates at the Southeast Indian Ridge and extends westward along the continental slope with the Antarctic Continental Slope Current (light blue dashed arrows; Figure 4.1; McCartney and Donohue, 2007).

In the Australian Basin, an open anti-cyclonic gyre forms from the eastward flow of South Indian waters which become restricted at the Tasman Rise and recirculate westwards along the centre of the basin back to the Indian ocean (green dashed arrows; Figure 4.1). The Tasman outflow compensates for the limited penetration of this anti-cyclonic gyre by allowing Tasman sea waters, which are partly fed by the East Australian Current, to flow around the Tasman Rise, through the centre of the basin and into the Indian Ocean (orange dashed arrows; Figure 4.1; Rintoul and Bullister, 1999; Speich et al., 2002; McCartney and Donohue, 2007). The surface waters flowing poleward from west of Australia are comprised of three currents: the Leeuwin Current representing flow from North West Cape to the Great Australian Bight; the South Australian Current, between the eastern Great Australian Bight to the north of Tasmania; and the Zeehan Current off western Tasmania (dashed magenta arrow; Figure 4.1; Ridgway and Condie, 2004; Bull and Sebille, 2016).

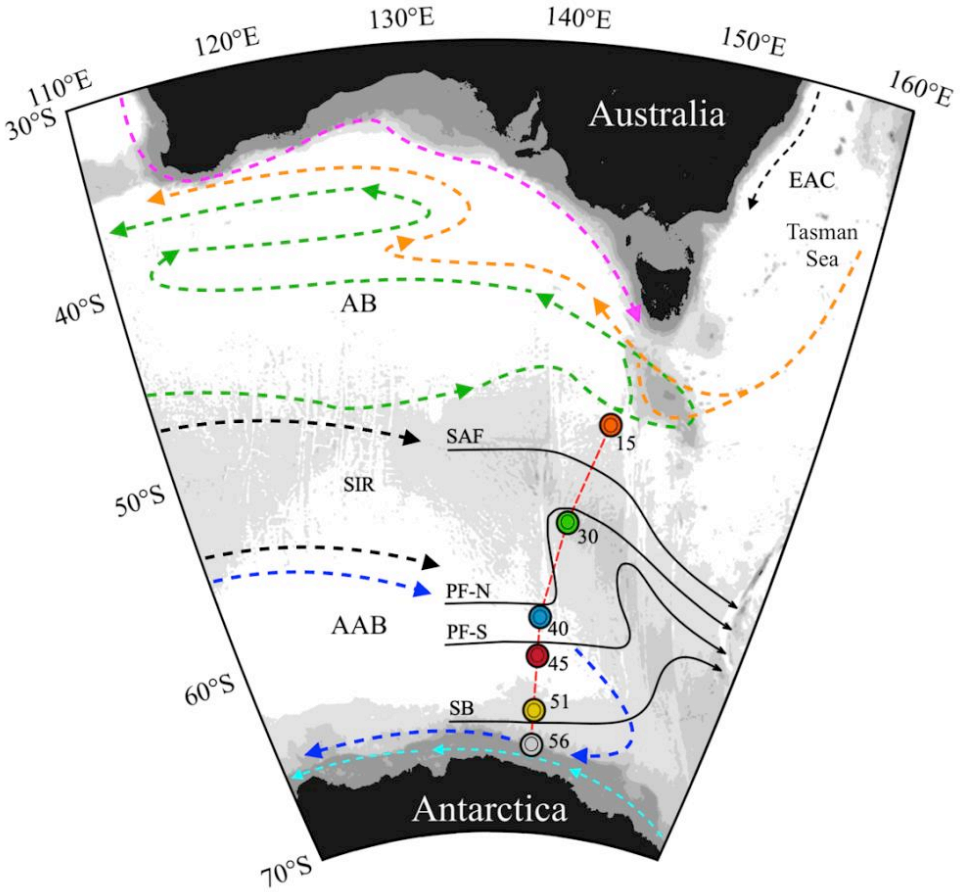

Figure 4.1 Study area in the Australian Basin (AB) and Australian-Antarctic Basin (AAB) which are separated by the South Indian Ridge (SIR) and located between Australia and East Antarctica. The dashed arrows display the regional circulation patterns (the basin-scale total depth-integrated transport field), with the solid black lines depicting the positions of the main Southern Ocean fronts (adapted from McCartney and Donohue, 2007 and Rintoul, 2001). Light blue and dark blue dashed arrows represent the westward (surface) flow of the Antarctic Slope Current and the (deep) cyclonic gyre within the Australian–Antarctic Basin, respectively. The black dashed arrows correspond to the Antarctic Circumpolar Current (ACC) domain. Green and orange dashed arrows represent the anti-cyclonic gyre and Tasman leakage in the Australian Basin, respectively. The magenta dashed arrow displays the combined surface water flow of the Leeuwin Current, South Australia Current and the Zeehan Current. The Southern Ocean fronts along the meridional transect correspond to the Subantarctic Front (SAF), North and South Polar Front (PF-N and PF-S) and the Southern Boundary (SB) of the ACC. The dashed red line and coloured circles denote the location of six sampling stations for dissolved Pb isotopes and concentrations along the GEOTRACES section GS01.

The fronts of the Southern Ocean divide distinct oceanographic regimes caused by the transition between cold, dense Antarctic waters in the south and light subtropical water in the north (section 1.4.2). The Southern Ocean frontal structure between Australia and Antarctica has been evaluated in detail by Sokolov and Rintoul (2002, 2007). In this study, the criteria outlined by Sokolov and Rintoul (2002; Table 6) are used to estimate the positions of the major fronts using hydrographic data collected during sampling on the GEOTRACES section GS01 along the historical SR3 transect between January and February 2018.

The northern limit of the Subantarctic Front (SAF; Figure 4.1; 50.4°S) demarcates the southern limit of the Subantarctic Zone (SAZ) and the northern limit of the ACC. The Polar Frontal Zone (PFZ) extends between the SAF and the northern branch of the Polar Front (PF-N; Figure 4.1). At 140°E, however, the PF-N recirculates several times resulting in an initial eastward crossing at 58.3°S, a westward 56.4°S intersect as it meanders equatorward and another eastward crossing farther north at 53.9°S. The southern branch of the Polar Front (PF-S; Figure 4.1) at 59.9°S indicates the start of the Antarctic Zone (AZ), within which the northern branch of the southern ACC front (SACCF-N) is located at 62.1°S and the southern branch of the SACCF (SACCF-S) at 63.9°S. The AZ extends to the Southern Boundary (SB; Figure 4.1) at 64.3°S which represents the southern limit of ACC waters and the start of the Continental Zone (CZ) at the continental margin.

4.2.2. GEOTRACES section GS01

The seawater samples investigated in this study are from the GEOTRACES section GS01, which follows the SR3 section, a World Ocean Circulation Experiment (WOCE) hydrographic section between Tasmania and Antarctica. During the transect, seawater was collected for a range of trace element, nutrient, contaminant and isotope analyses along with hydrographic data (temperature, salinity and oxygen). The positions of the stations for Pb isotope and concentration measurements were selected to cover the frontal features across the 140°E transect (red markers and dashed line; Figure 4.1). The stations are categorised depending on their location relative to the identified frontal positions: one SAZ station (station 15); two PF stations (station 30 and 40); two AZ stations (station 45 and 51); and one CZ station (stations 56). As the transect crosses the major fronts of the Southern Ocean, seasonal variability will change the position of the fronts (Figure 1.5), but not the position of the water masses across the Australian-Antarctic Basin. Therefore, the hydrographic data

(temperature, salinity and oxygen) from the GEOTRACES GS01 section at the time of sampling is used to define the hydrographic conditions and water masses of the region.

4.2.3. Water mass distribution

Several water masses have been identified at the stations along the SR3 hydrographic section: Antarctic Surface Water (AASW), Subantarctic Surface Water (SASW), Subantarctic Mode Water (SAMW), (preformed) Antarctic Intermediate Water (AAIW), Upper Circumpolar Deep Water (UCDW), Lower Circumpolar Deep Water (LCDW) and Antarctic Bottom Water (AABW). These water masses exhibit spatial variability along the SR3 section and have been identified at individual stations based on potential temperature (θ, °C), practical salinity (S, psu) and neutral density (γ^n, kg m^{-3}; Figure 4.2; Jackett and McDougall, 1997).

Surface waters are classified as either SASW or AASW. Both water masses have neutral density values < 27.13 kg m^{-3} but exhibit different potential temperature and salinity ranges because of their longitudinal positions. SASW is located north of the PF (Orsi et al., 1995) at station 15 and represents a relatively warm (θ = 6–10 °C) and saline (S > 34.0) surface water (Figure 4.2 (a)). Conversely, AASW is much colder and fresher than SASW, with potential temperatures reaching –1.9 °C and salinity values between 33.5–34 (Figure 4.2 (c)). AASW dominates the surface hydrography south of the PF (stations 45, 51 and 56) and becomes increasingly dense towards Antarctica. The two stations closest to the Antarctic continent, station 51 and 56, have surface waters with neutral density values greater than 27.13 kg m^{-3} (Figure 4.2 (c)). This AASW represents the surface water precursor of AAIW which flows northwards and subducts at the SAF to form AAIW. AAIW is therefore only present at station 15 in the SAZ and can be identified by a salinity minimum at intermediate depths within the 27.13–27.55 kg m^{-3} isopycnal range (Figure 4.2 (a); Rintoul and Bullister, 1999; Sokolov and Rintoul, 2002). For the purpose of this study, all samples collected within the 27.13–27.55 kg m^{-3} isopycnal range are referred to as pre-formed AAIW. The other subsurface water mass, SAMW, is only present at station 15 as it forms from deep winter convection north of the SAF around ~50°S (Rintoul and Bullister, 1999). SAMW has a narrow density range (26.9 < γ^n < 27.0 kg m^{-3}) but can be distinguished from surrounding waters by an extreme thermostad (minimum vertical temperature gradient) at subsurface levels (Figure 4.2 (a); Rintoul and Bullister, 1999).

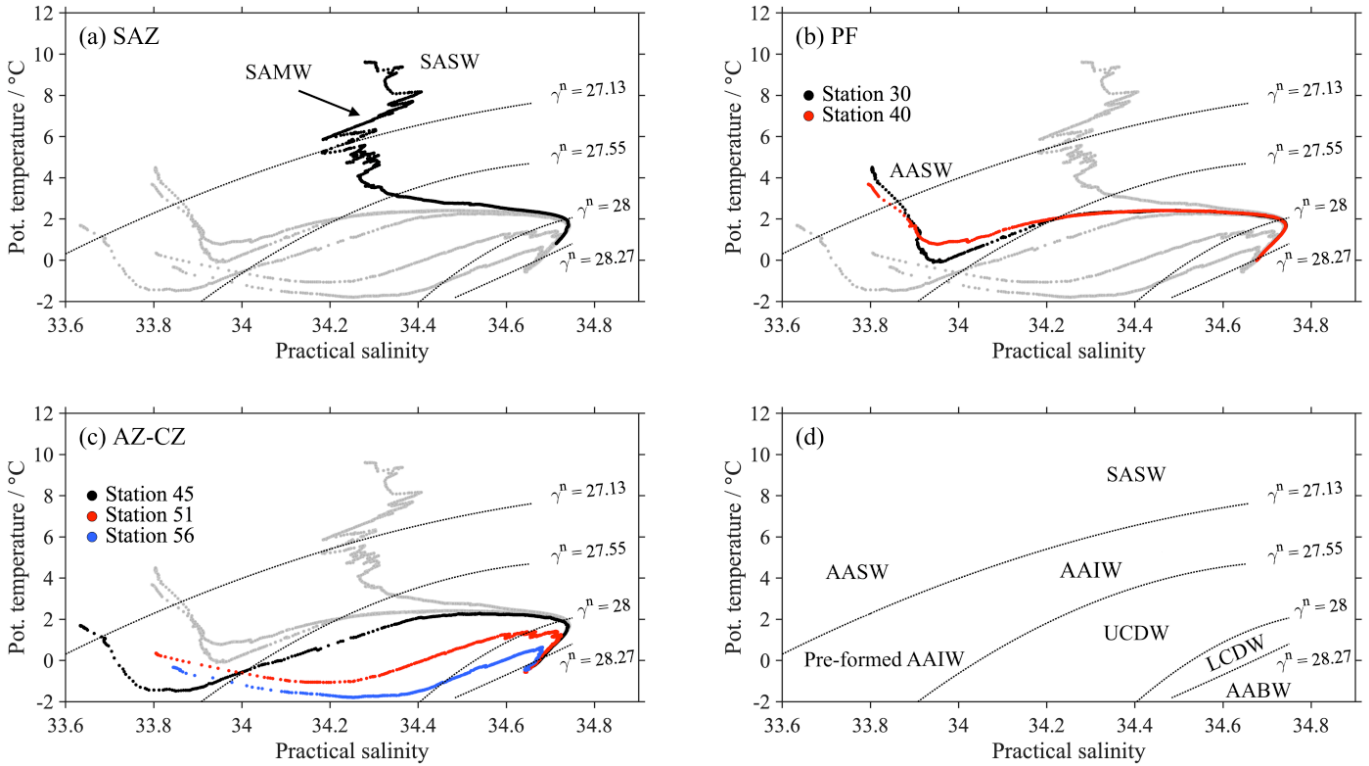

Figure 4.2 Potential temperature versus salinity diagrams for the stations sampled along the SR3 meridional transect. The stations are categorised depending on their position relative to the Southern Ocean Fronts: (a) Subantarctic Zone, (b) Polar Front and (c) Antarctic and Continental Zone. The profiles for each station are shown in all three panels in grey for comparison. The solid black lines, labelled with γ^n = 27.13, 27.55, 28.00 and 28.27 are the neutral density surfaces that separate (sub)surface waters (AASW, SASW and SAMW), pre-formed AAIW, UCDW, LCDW and AABW. A schematic of water mass definitions and distributions for the area is shown in (d). As neutral density is a function of temperature, salinity and other parameters (pressure, latitude and longitude), the contours are computed by fitting second order polynomials to the entire SR3-IN2018_V01 CTD dataset.

The deep waters at all stations along the transect constitute Circumpolar Deep Water (CDW) and can be sub-divided into UCDW and LCDW depending on their hydrography. UCDW is characterised by neutral density values in the range of $27.55 < \gamma^n < 28.0$ kg m^{-3} (Figure 4.2) and an oxygen minimum caused by the flow of old deep waters to the Southern Ocean from the Indian Ocean (Rintoul et al., 2001). LCDW is denser ($28.0 < \gamma^n < 28.27$ kg m^{-3}) and has higher salinities due to the influence of saline North Atlantic Deep Water (Figure 4.2; Orsi et al., 1995; Rintoul et al., 2001). Both UCDW and LCDW eventually outcrop south of the SB and contribute to the formation of northward flowing surface and bottom waters, respectively (Rintoul et al., 2001; Lumpkin and Speer, 2007). At the stations in the study, however, both UCDW and LCDW remain below the surface even at the CZ (station 56; Figure 4.2 (c)).

The densest water in the abyssal ocean, AABW ($\gamma^n > 28.27$ kg m^{-3}), forms at various locations on the continental margins of Antarctica (e.g., Weddell Sea, Ross Sea and Adélie Land Coast; Orsi et al., 1999). The exchange of AABW across ocean basins, however, is restricted by bottom topography (Whitworth et al., 1998; Orsi *et al.*, 1999). This is observed in the Australian Sector of the Southern Ocean where the South Indian Ridge restricts the northward flow of AABW into the Australian Basin (station 15 and 30; Figures 4.1 and 4.2). The lack of exchange produces local varieties of AABW across the Southern Ocean which reflect the properties of the local sources (Orsi et al., 1999). The sources of AABW in the Australian sector of the Southern Ocean are (1) Ross Sea Bottom Water (RSBW) advected from the east; and (2) Adélie Land Bottom Water (ALBW) formed along the Adélie-Wilkes shelf (Rintoul and Bullister, 1999; Williams et al., 2010). The high salinity signature of RSBW has previously not been observed to the west of 140°E because of the dominant influx of ALBW at the Adélie Land coast between 140°E and 148°E (Rintoul, 1998). In this study, there is no hydrographic evidence for RSBW along the SR3 hydrographic section, but the presence of ALBW has been detected at station 51 and 56 with its dense ($\gamma^n > 28.27$ kg m^{-3}), cold ($-0.8 < \theta < -0.5$ °C) and less saline ($34.62 < S < 34.68$) properties. ALBW, constitutes an important local precursor for AABW in the Australian-Antarctic Basin during the time of sample collection in the austral summer.

4.3. Materials and methods

4.3.1. Sampling procedure

A total of 54 seawater samples were collected across six stations for Pb concentration and isotope composition analysis during the expedition SR3-IN2018_V01 (GEOTRACES section cruise GS01) on the RV Investigator from Hobart to Antarctica between the 11th January and the 21st February 2018 (Figure 4.1). Sample collection was conducted using an autonomous trace metal-clean rosette system fitted with 12 trace metal-clean sampling bottles. Following seawater collection, samples were filtered using a 0.2 μm capsule filter (Acropak 200) into acid cleaned 2 x 1 L low density polyethylene (LPDE, Nalgene) bottles inside a clean laboratory container and subsequently acidified to approximately pH 2 using quartz distilled 6 M HCl.

4.3.2. Lead concentration and isotope composition analysis

The analytical procedure to determine the Pb concentration and isotope composition of seawater was carried out in the MAGIC Laboratories at Imperial College London (UK) and has been described in detail in chapter 3, and where appropriate, by Paul et al. (2015b).

Briefly, Pb concentrations were determined by isotope dilution, whereby 50 mL seawater aliquots were spiked with a ^{207}Pb-^{204}Pb double-spike solution and left to equilibrate for ~10 days. The quantity of ^{207}Pb-^{204}Pb double-spike for each sample was calculated based on the mass of the sample aliquot and an estimate of the sample Pb concentration. Following equilibration, Pb was extracted from seawater by $Mg(OH)_2$ co-precipitation, purified using a one-stage anion-exchange chromatography procedure, and then analysed using a Nu Plasma II multi-collector inductively coupled plasma mass spectrometry (MC-ICP-MS; Nu Instruments). Blank corrections were applied to all Pb concentrations using an average procedural blank of 20.8 ± 13.4 pg (1sd; n = 11; Chapter 3). For every batch of analysis (~9 samples), three samples were randomly selected for triplicate analyses to confirm there were no artefacts as a result of spurious blank contamination. Across all samples, only one triplicate measurement was discarded (station 45; 495 m) due to Pb concentrations ~15 pmol kg^{-1} higher than the other replicate analyses of the same sample. The estimated error for Pb concentrations, calculated from the standard deviation of the triplicate mean averaged across all triplicate measurements, was ± 1.4 pmol kg^{-1} (1sd; n = 14) and is consistent with replicate analyses of internal and interlaboratory reference materials (Chapter 3).

For Pb isotope analysis, Pb was separated from the seawater matrix by solid-phase extraction using Nobias PA-1 chelating resin, and then purified by a two-stage anion-exchange chromatography procedure using AG1-X8 resin and dilute HBr-HNO_3 mixtures for matrix and Pb elution. Following extraction and purification, a ^{207}Pb-^{204}Pb double-spike—based on sample weight, measured Pb concentration and estimated analytical yields—was added to a smaller aliquot (~1/3) of the processed sample. Both the unspiked and double-spiked aliquots were then doped with thallium (Tl) using Standard Reference Material (SRM) 997 from the National Institute Standards and Technology (NIST).

All Pb isotope measurements were performed on a Nu Plasma II MC-ICP-MS equipped with 10^{12} Ω resistors to amplify the signal of the minor Pb isotope ^{204}Pb as well as ^{202}Hg, in order to correct for the isobaric ^{204}Hg interference. A set of mixed NIST SRM 981-997 solutions with a Pb:Tl ratio of 1:3 and ranging in Pb concentration between 1–10 ppb were measured to monitor the accuracy during every run. The following steps were taken to correct the raw measured data: (1) removal of the electronic background and the isobaric interference of ^{204}Hg on ^{204}Pb; (2) correction of the instrumental mass discrimination for unspiked measurements using Tl-normalisation based on the exponential mass fractionation law; and (3) application of the double-spike correction to Tl-normalised Pb isotope ratios of the unspiked run using data obtained from the double-spike analyses.

The procedural blanks for the Pb isotope composition procedure ranged from 47–122 pg Pb, which corresponds to 0.7–5.9% of the total Pb content of samples analysed. Blank corrections, however, were not applied to the Pb isotope compositions as this did not improve the precision of replicate analyses of seawater reference materials (Chapter 3). The external reproducibility of both the Pb concentration and isotope composition measurements has been assessed through replicate analyses of seawater reference materials. Moreover, the accuracy of the method has been validated by cross-calibration with a previously established TIMS technique using GEOTRACES intercalibration samples GDI, GSI and GSP (Chapter 3; Boyle et al., 2012; Paul et al., 2015b).

Initial Pb isotope analyses conducted in this study applied $Mg(OH)_2$ co-precipitation instead of the Nobias chelating resin in the first step of sample preparation. However, several studies reported that $Si(OH)_4$ in seawater is efficiently scavenged by $Mg(OH)_2$ and the pre-concentrated $Si(OH)_4$ significantly reduces the solubility of the $Mg(OH)_2$ precipitate (Boyle et al., 2012; Lee et al., 2015). These observations were confirmed by the initial work conducted here: deep waters of the Southern Ocean have extremely high $Si(OH)_4$ concentrations (~60–140 μmol kg^{-1}) and this either prevented dissolution of the $Mg(OH)_2$

precipitate in the 2M HBr-0.01M HF mixture that was used for loading of samples in the subsequent anion-exchange separation of Pb, or led to the precipitation of a thick $Si(OH)_4$ gel during anion-exchange chromatography. Consequently, samples from above 1000 m at station 15 were analysed following $Mg(OH)_2$ co-precipitation (Paul et al., 2015b), while samples from greater depth at this station were lost during the purification procedure. All remaining samples from other stations were subsequently processed using solid-phase extraction (Nobias PA-1) instead of $Mg(OH)_2$ co-precipitation. A comparison between the two methods has shown that they produce statistically identical Pb isotope data (Chapter 3). The results obtained for station 15 can therefore be compared without bias to other results across the meridional section.

4.4. Results

In the Australian sector of the Southern Ocean, seawater measurements exhibit a strong correlation in $^{20x}Pb/^{204}Pb$ versus $^{206}Pb/^{207}Pb$ and $^{206}Pb/^{207}Pb$ versus $^{208}Pb/^{207}Pb$ isotope space (Figure 4.3). The weaker relationship between $^{207}Pb/^{204}Pb$ and $^{206}Pb/^{207}Pb$ corresponds to the significantly smaller variability of the $^{207}Pb/^{204}Pb$ ratio in seawater and therefore the greater effect of analytical uncertainties on the distribution in isotopic space (Figure 4.3 (b)). The strong correlation between high-precision $^{206}Pb/^{204}Pb$ and $^{206}Pb/^{207}Pb$ ratios in seawater has previously been observed in different regions of the Atlantic Ocean (Paul et al., 2015a; Bridgestock et al., 2016; Bridgestock et al., 2018). Furthermore, Bridgestock et al., (2018) evaluated in detail the application of high precision ^{206}Pb, ^{207}Pb and ^{208}Pb $/^{204}Pb$ ratios for assessment of Pb sources and cycling in the ocean. Given the strong correlation between the dissolved Pb isotope ratios along the Southern Ocean GS01 transect, any potential Pb sources to the region can be constrained by combining the $^{206}Pb/^{207}Pb$ and $^{208}Pb/^{207}Pb$. Consequently, the results described here are limited to observed $^{206}Pb/^{207}Pb$ and $^{208}Pb/^{207}Pb$ ratios but the $^{206}Pb/^{207}Pb$ and $^{206}Pb/^{204}Pb$ ratios with Pb concentrations are displayed as depth profiles in Figure 4.4, while the spatial variability of the $^{206}Pb/^{207}Pb$, $^{208}Pb/^{207}Pb$ and Pb concentrations are presented as section plots in Figure 4.5.

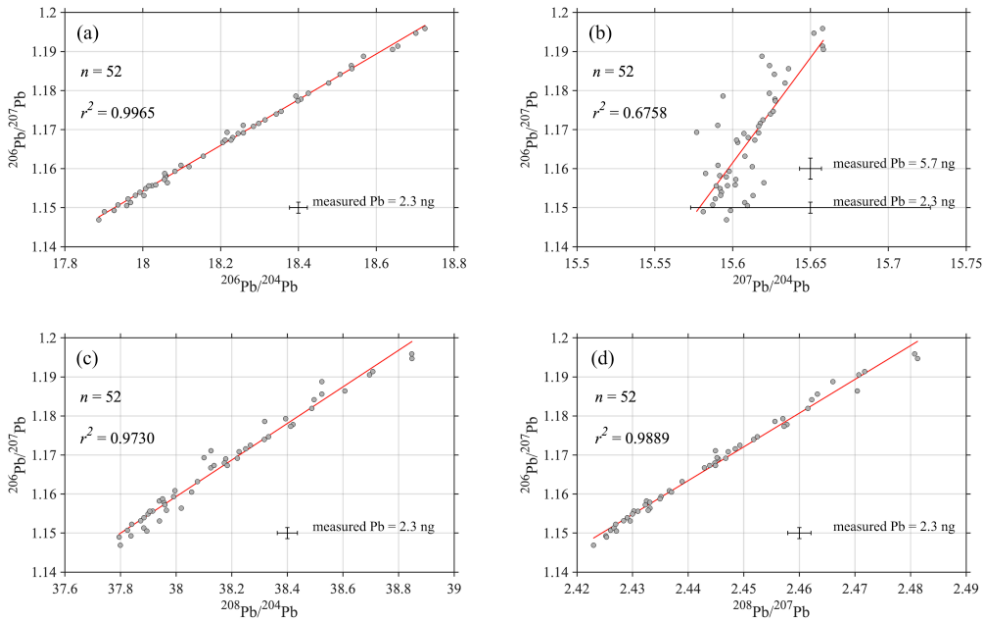

Figure 4.3 Lead isotope plots displaying the relationship between the different Pb ratios for all Southern Ocean seawater samples. Error bars correspond to the 2sd of internal (SO-145; n = 7; 2.3 ng Pb measured) and international (GSP; n = 8; 5.7 ng Pb measured) seawater reference materials (Chapter 3). These error bars represent the largest and smallest possible errors for Southern Ocean measurements.

4.4.1. Spatial distribution of dissolved lead isotopes

The spatial variability of the $^{206}Pb/^{207}Pb$ and $^{208}Pb/^{207}Pb$ ratios is displayed as a section plot with neutral density contours superimposed to delineate the main water masses in the region (Figure 4.5 (a–b)). Overall, there is a large variation in $^{206}Pb/^{207}Pb$ and $^{208}Pb/^{207}Pb$ ratios with values ranging between 1.15–1.12 and 2.42–2.48, respectively (Figure 4.4 and 4.5). The lowest $^{206}Pb/^{207}Pb$ and $^{208}Pb/^{207}Pb$ ratios coincide in the SAZ (station 15) at intermediate depths (320 m) associated with SAMW. The highest $^{206}Pb/^{207}Pb$ and $^{208}Pb/^{207}Pb$ ratios are observed in AABW of station 51 (2950 m) and station 45 (4315 m), respectively. In general, $^{206}Pb/^{207}Pb$ and $^{208}Pb/^{207}Pb$ ratios increase vertically down through the water column and meridionally from north to south. There is, however, a pronounced meridional change in $^{206}Pb/^{207}Pb$ and $^{208}Pb/^{207}Pb$ ratios at surface and intermediate waters towards the Antarctic continent. Surface water Pb isotope ratios are relatively uniform between station 15 in the SAZ and station 51 in the AZ ($1.15 < ^{206}Pb/^{207}Pb < 1.16$; $^{208}Pb/^{207}Pb \approx 2.43$) but markedly different at station 56 in the CZ with much higher $^{206}Pb/^{207}Pb$ (1.17) and $^{208}Pb/^{207}Pb$ (2.44) ratios. The $^{206}Pb/^{207}Pb$ and $^{208}Pb/^{207}Pb$ ratios in subsurface waters and UCDW

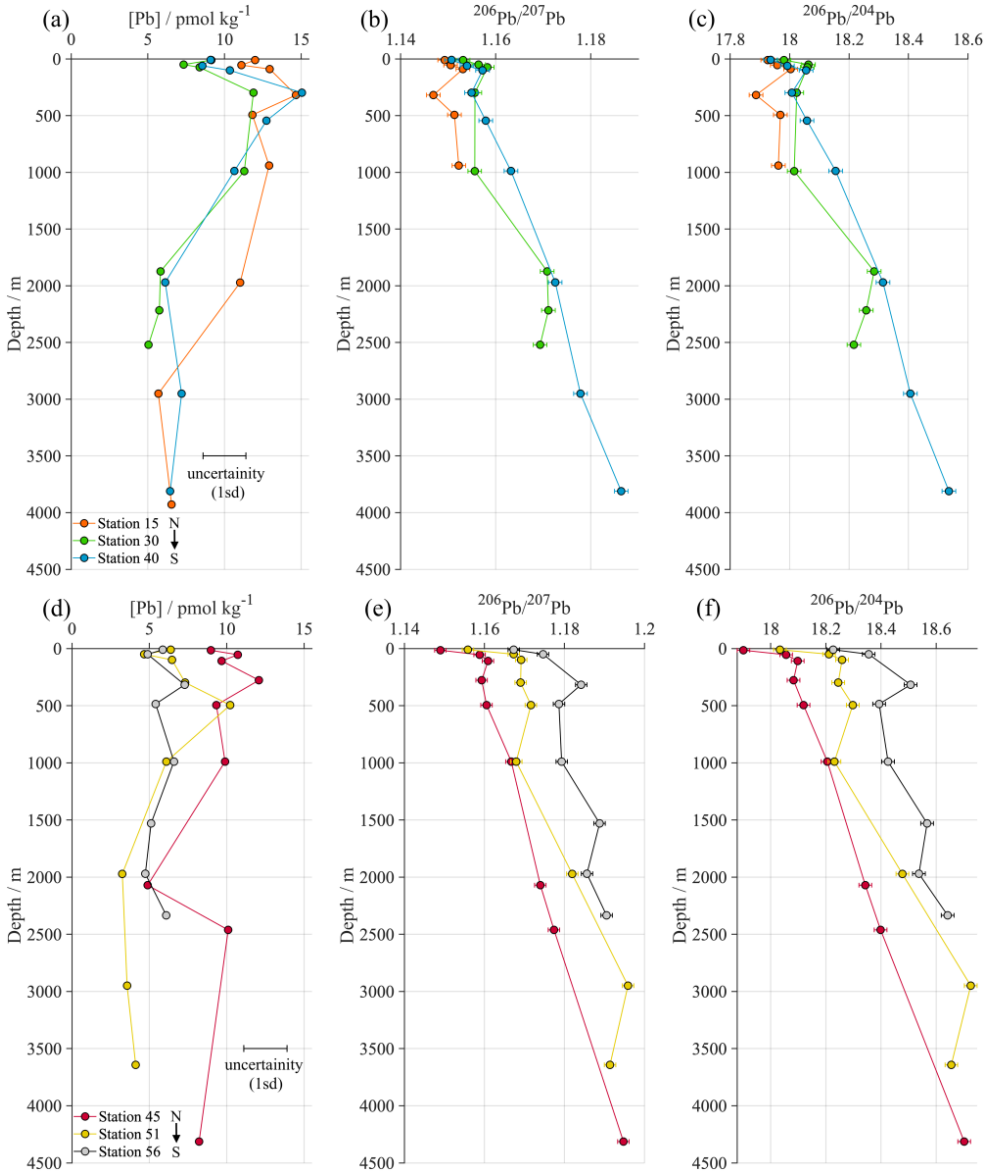

Figure 4.4 Water column depth versus Pb concentration (left), $^{206}Pb/^{207}Pb$ (middle) and $^{206}Pb/^{204}Pb$ (right) for all stations across the GS01 transect. Panel (a)–(c) are the depth profiles for stations north of the PF; panel (d)–(f) are the depth profiles for stations south of the PF. The uncertainty bar for Pb concentrations ((a) and (d)) represents the standard deviation of the triplicate mean averaged across all triplicate measurements (1.4 pmol kg^{-1}; see section 4.3.2.). The error bars for $^{206}Pb/^{207}Pb$ and $^{206}Pb/^{204}Pb$ ratios represent the 2sd of replicate analyses of an in-house Southern Ocean seawater standard (SO-145; see chapter 3).

(~100–1000 m) at stations north of the AZ, are nearly indistinguishable from the surface water $^{206}Pb/^{207}Pb$ and $^{208}Pb/^{207}Pb$ data. The southernmost stations, station 45 in the AZ and station 56 in the CZ, however, show much higher $^{206}Pb/^{207}Pb$ and $^{208}Pb/^{207}Pb$ values in subsurface waters and UCDW. As a consequence of meridionally changing surface and intermediate water Pb isotope signatures, vertical gradients between surface / intermediate waters and bottom waters become less pronounced towards Antarctica.

4.4.2. Spatial distribution of lead concentrations

The spatial distribution of dissolved Pb concentrations are shown in Figure 4.3 and 4.4 (c). Lead concentrations across the region vary between ~3.3 and 15 pmol kg^{-1}. The highest Pb concentrations appear in intermediate waters (~300 m) at station 15 and 40, while the lowest values appear at depth in LCDW and AABW at station 51. Similar to the meridional Pb isotope trend observed at subsurface and UCDW levels (~100 to 1000 m), there appears to be distinctively higher Pb concentrations north of the AZ at stations 15 to 45. This 'tongue' of high Pb concentrations disappears towards Antarctica (stations 51 and 56). This meridional decrease in Pb concentrations from ~13 pmol kg^{-1} in the north to ~5 pmol kg^{-1} in the south between 100–1000 m results in a more homogenous depth profile in the AZ and CZ compared to more northern latitudes (Figure 4.3). In contrast to the Pb isotope distribution, however, Pb concentrations are not uniform along the surface north of the CZ. In detail, at stations 30, 40 and 45 (northernmost AZ to southernmost PFZ; Figure 4.3 (c–e)) there is an initial increase in Pb from ~9–10 pmol kg^{-1} at the surface to ~13–15 pmol kg^{-1} in intermediate waters, followed by a decrease to ~5 pmol kg^{-1} in deep and bottom waters.

4.5. Discussion

4.5.1. Sources of lead to the Southern Ocean

Across the GS01 section between Australia and Antarctica, seawater Pb isotope data define a mixing array between three Pb sources: (1) a high $^{206}Pb/^{207}Pb$-$^{208}Pb/^{207}Pb$ natural source recorded by local deep-sea ferromanganese (Fe-Mn) crusts; (2) a mid-to-high $^{206}Pb/^{207}Pb$-$^{208}Pb/^{207}Pb$ Australian natural dust source; and (3) a low $^{206}Pb/^{207}Pb$-$^{208}Pb/^{207}Pb$ Australian anthropogenic source (Figure 4.6 (a)).

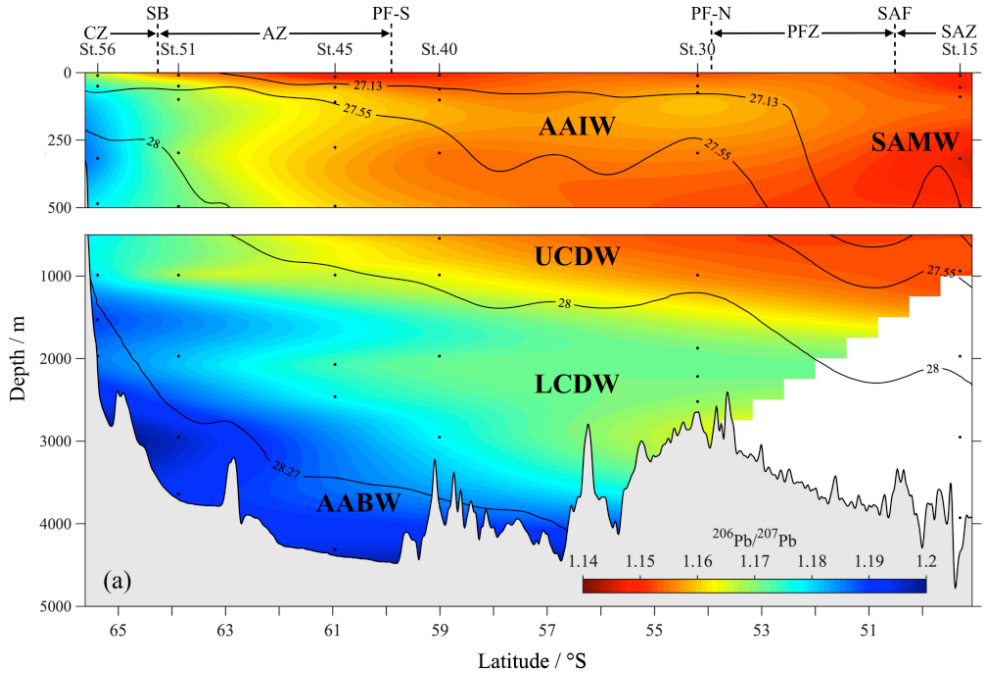
SB
PF-S
PF-N
SAF
CZ
AZ
PFZ
SAZ
St.56
St.51
St.45
St.40
St.30
St.15
AAIW
SAMW
UCDW
LCDW
AABW
27.13
27.55
28
28.27
Depth / m
$^{206}Pb/^{207}Pb$
1.14 1.15 1.16 1.17 1.18 1.19 1.2
(a)
Latitude / °S

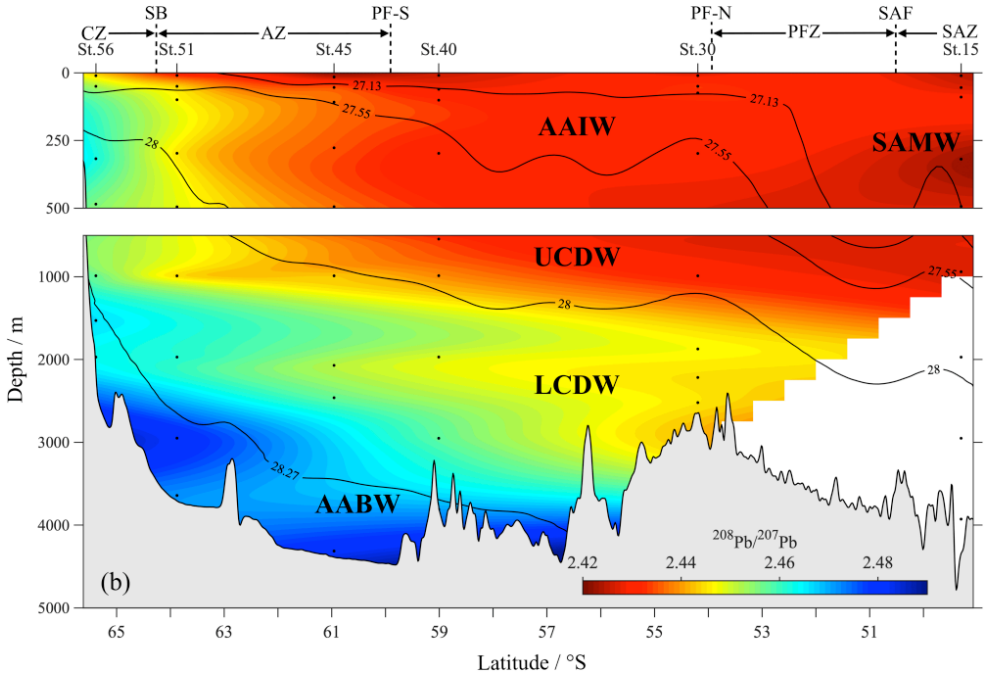
SB
PF-S
PF-N
SAF
CZ
AZ
PFZ
SAZ
St.56
St.51
St.45
St.40
St.30
St.15
AAIW
SAMW
UCDW
LCDW
AABW
27.13
27.55
28
28.27
Depth / m
$^{208}Pb/^{207}Pb$
2.42 2.44 2.46 2.48
(b)
Latitude / °S

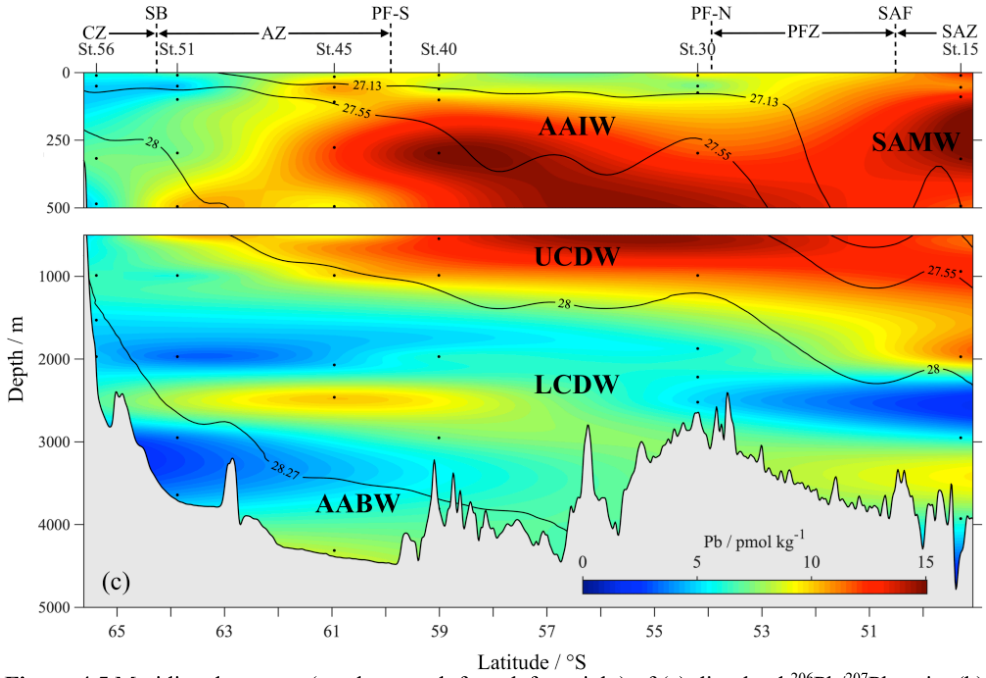

Figure 4.5 Meridional transect (south to north from left to right) of (a) dissolved $^{206}Pb/^{207}Pb$ ratio, (b) $^{206}Pb/^{207}Pb$ ratio and (c) dissolved Pb concentrations in the Southern Ocean. Sample locations are shown by black dots and neutral density contours demarcate the regional water masses. Stations, fronts and zones are shown on the upper x-axis by solid ticks, dashed ticks and black arrows, respectively. The distribution of $^{206}Pb/^{204}Pb$ are identical to the distribution of $^{206}Pb/^{207}Pb$ and $^{208}Pb/^{207}Pb$ ratios.

There are a number of potential natural sources of Pb to the Southern Ocean, particularly from Antarctica: emissions from active volcanoes such as Mount Erebus, sediment transported by coastal polynyas and benthic inputs from the continental margin (Flegal et al., 1993; Ndungu et al., 2016). The Pb isotope composition of Antarctic continental snow reflects a mixture of natural continental sources (e.g., volcanic emissions) and anthropogenic emissions from either South America and Australia (Flegal et al., 1993; Rosman et al., 1994; Barbante et al., 1998). Figure 4.6 (a) shows that seawater Pb isotope data displays distinctly lower $^{206}Pb/^{207}Pb$ and $^{208}Pb/^{207}Pb$ ratios than Antarctic snow from Law Dome and Dome C. However, the Pb isotope composition of local seafloor Fe-Mn crusts, which records the Pb isotope signature of deep and bottom waters in the past, exhibits much lower $^{206}Pb/^{207}Pb$ and $^{208}Pb/^{207}Pb$ ratios than Antarctic snow and follows the seawater array (Figure 4.6 (a)). This indicates that the natural Pb sources controlling deep and bottom water Pb isotope composition are either sediments transported from the continent or benthic fluxes from the continental margin (Figure 4.6 (a) and (b)).

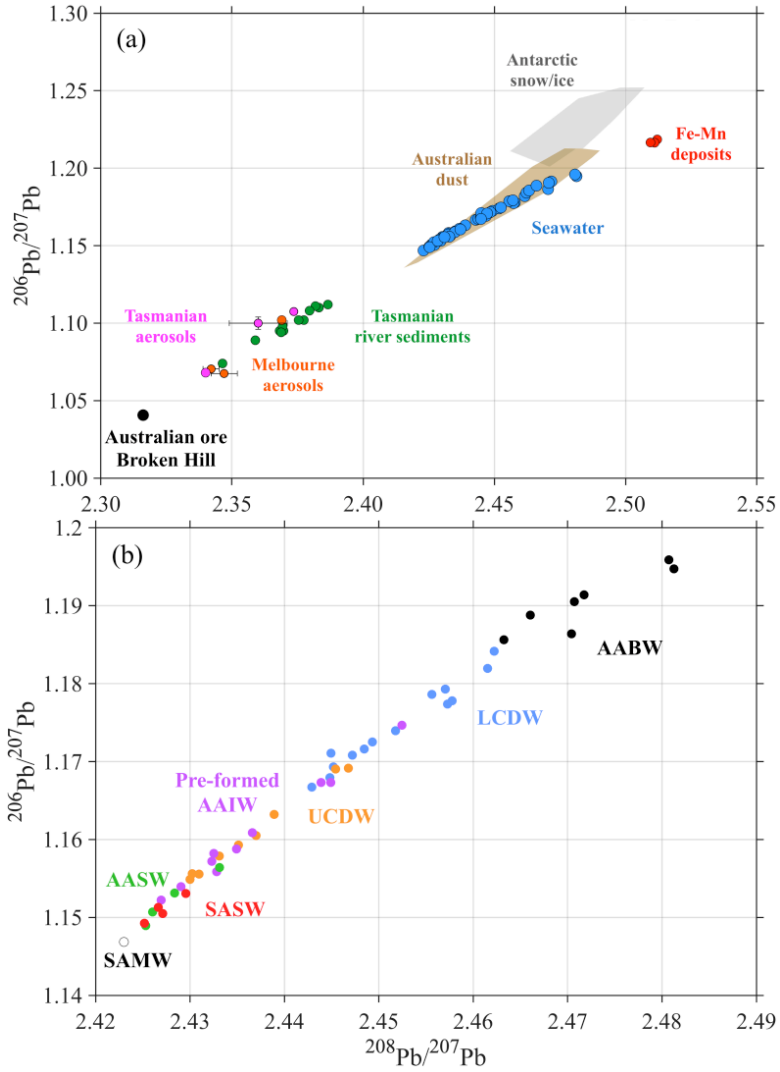

Figure 4.6 Panel (a): A three isotope plot ($^{206}Pb/^{207}Pb$ versus $^{208}Pb/^{207}Pb$) showing the distribution of all seawater samples in the context of Southern Ocean Pb sources. The graph shows seawater (blue circles) in relation to natural Pb sources: grey shaded area denotes snow/ice samples from Dome C and Law Dome (Rosman et al., 1994; Vallelonga et al., 2002); brown shaded area represents Australian aeolian sources (De Decker et al., 2010; Vallelonga et al., 2010, acid digested samples only) and red circles show local deep-sea Fe-Mn deposits from the deep Australian-Antarctic basin (Abouchami and Goldstein, 1995). Melbourne aerosols (orange circles; Bollhöfer and Rosman, 2000), Tasmanian aerosols (magenta circles; Bollhöfer and Rosman, 2000), sediments from the Derwent River, Tasmania (grey circles; Townsend and Seen, 2012) and Australian Pb ore deposits from Broken Hill (black circle; Townsend et al., 1998) are the anthropogenic sources of Pb to the Southern Ocean. Melbourne and Tasmanian aerosol data with error bars represent the mean and range when samples are reported as a range of values from multiple measurements of the same sample. Panel (b): The distribution of all seawater samples shown in panel (a) in the context of Southern Ocean water masses following the water mass identification criteria outlined in section 4.2.3.

Given the importance of bottom water formation near the Adélie-Wilkes shelf (Rintoul and Bullister, 1999; Williams et al., 2010) and previously observed sources of natural Pb from surface sea sediments in the Amundsen Sea of West Antarctica (Ndungu et al., 2016), it is plausible that the control on the Pb isotope composition of deep and bottom waters in this region are sediments and/or benthic fluxes. This inference is substantiated by observations from deep waters farther west in the Indian sector of the Southern Ocean which also indicate that the Pb isotope compositions of Fe-Mn crusts record the natural endmember for deep and bottom waters in the Indian sector of the Southern Ocean (Lee et al., 2015).

The supply of natural Pb to the Southern Ocean through sediment transport and/or benthic fluxes can only account for the Pb isotope composition of deep and bottom waters. Surface waters between Australia and Antarctica are exposed to the atmospheric supply of Pb in the form of natural dust from south-east Australian river plains and deserts, or Australian anthropogenic emissions (Figure 4.6 (a) and (b)). These natural and anthropogenic sources of Pb to the surface waters of the Southern Ocean are important given that Southern Hemisphere dust originates primarily from Australia (120–132 Tg a^{-1}), which is more than double the amount of dust supplied by the South American continent (50 Tg a^{-1}; Luo et al., 2003; Li et al. 2008). On a regional level, the relative contributions of these southern hemispheric sources vary significantly across the Southern Ocean, but dust deposition at 140°E between Tasmania and Antarctica is dominated by Australian sources (80–90%; Li et al., 2008).

A single anthropogenic source (Australian ore, Broken Hill) for seawater in this region reflects the dominance of Australian emissions due to regional isolation from other potential anthropogenic emissions. Surface and intermediate waters and all regional anthropogenic sources (Melbourne and Tasmanian aerosols) fall along a mixing line between Broken Hill Pb ores and Australian dust (Figure 4.6 (a) and (b)). Tasmanian river sediments have clearly been affected by the deposition of anthropogenic emissions but exhibit a higher contribution of natural Pb from Australian dust than Melbourne and Tasmanian aerosols.

4.5.2. Lead isotope and concentration fingerprint of Southern Ocean water masses

4.5.2.1. Surface and Bottom Waters

Regional water masses exhibit distinct Pb isotope fingerprints along the mixing trajectory between natural and anthropogenic regional Pb sources (Figures 4.6 (b)). Despite the relatively low Pb concentrations in surface waters across most of the transect (Figure 4.4 and 4.3 (c)), SASW and AASW are characterised by distinctly low $^{206}Pb/^{207}Pb$ and $^{208}Pb/^{207}Pb$

ratios, indicating significant anthropogenic influence. A mixing calculation that applies the Pb isotope composition of the most natural Pb endmember for surface waters (i.e., Australian dust from the Strzlecki Desert; $^{206}Pb/^{207}Pb$ = 1.2126; Vallelonga et al., 2010) and Melbourne/Tasmanian aerosols (i.e., anthropogenic Pb endmember; average $^{206}Pb/^{207}Pb$ = 1.0844; Bollhöfer and Rosman, 2000) indicates that emissions from Australia constitute at least a third of the surface water Pb inventory along the SR3 transect (~30–50%).

On the other end of the isotopic spectrum of Southern Ocean waters along the SR3 transect lies the Pb isotope composition of AABW (Figures 4.6 (b)). It shows the closest similarity to the natural Pb isotope compositions of Fe-Mn crusts in the region, with elevated $^{206}Pb/^{207}Pb$ and $^{208}Pb/^{207}Pb$ ratios and a significantly smaller contribution of anthropogenic Pb than surface waters (~16–24% anthropogenic Pb using $^{206}Pb/^{207}Pb$ = 1.2172 for the Fe-Mn endmember). Despite forming close to Antarctica and far from any potential anthropogenic emissions, AABW is still significantly perturbed by anthropogenic Pb. The perturbation of AABW could come directly from the wet or dry deposition of Australian Pb emissions, or indirectly from the supply of contaminated continental snow/ice at the site of bottom water mass formation. Given that there is isotopic evidence of significant quantities of anthropogenic Pb in East Antarctic snow and ice (Law Dome/ Dome C data in Figure 4.6), direct deposition and continental supply are both plausible explanations for the observed perturbation of AABW (e.g., Rosman et al., 1994; Vallelonga et al., 2002).

4.5.2.2. Intermediate and deep waters (SAMW, AAIW, UCDW, LCDW)

Another explanation for the admixture of an anthropogenic Pb isotope component in AABW along the southern part of the section relates to the formation process of AABW. The primary source of AABW in this region is the Adélie Depression, where brine rejection following sea ice formation produces dense shelf waters that subduct and are exported through the Adélie Land sill (e.g., Foster and Carmack, 1976; Williams et al., 2010). The Antarctic Continental Slope Current subsequently transports this dense shelf water along the continental slope while simultaneously entraining a significant amount of encroaching warmer and more saline LCDW from the continental rise to form AABW (Carmack and Killworth, 1978; Foldvik, 1985). Given that the formation process of AABW involves admixture of Adélie Land shelf water and LCDW, the properties of AABW depend not only on the cold and saline shelf derived components with initial boundary conditions influenced by local continental inputs, but also on the LCDW entrained during the poleward transport. LCDW in turn is

characterised by lower Pb isotope ratios (Figure 4.6 (b)), making it feasible that AABW signatures are a mixture of natural Pb (as presented by Fe-Mn crust data) and LCDW carrying pre-formed Pb from other parts of the ocean without substantial input of atmospheric Pb.

Although all water masses follow a mixing line between the two identified natural sources and the anthropogenic endmember, there is a clear incongruence between the distribution of water masses in Pb isotopic space and the spatial distribution of water masses in the water column. The two anomalies are: (1) SAMW exhibits a distinctly greater anthropogenic Pb isotope imprint than surface waters; and (2) intermediate water masses (i.e., preformed AAIW and UCDW) are dominated by anthropogenic Pb, which contrasts with more natural LCDW. A combination of lateral and vertical processes certainly controls the pathways and distribution of Pb into the interior of the Southern Ocean and will be discussed below.

4.5.3. Origins of polluted SAMW: the Tasman leakage

The observed subsurface Pb isotope minimum at station 15 in the SAZ corresponds to SAMW (γ^n = 26.96 kg m^{-3}). In the Southern Ocean, SAMW constitutes a homogeneous body of water extending vertically from the subsurface to over 500 m on the equatorward side of the SAF and horizontally across the Indian and Pacific Ocean (McCartney, 1982). Despite the homogeneity of SAMW, Herraiz-Borreguero and Rintoul (2011) have identified several circumpolar classes of SAMW. South of Australia, the 26.9 ≤ γ^n < 27 kg m^{-3} SAMW forms predominately from wind-driven Ekman transport of Antarctic surface waters north of the SAF between 130°E and 160°E, and is exported at depth into the subtropical gyre of the Australian Basin or central Indian Ocean (Herraiz-Borreguero and Rintoul, 2011b; Rintoul and England, 2002).

In the central Indian Ocean, low SAMW ^{206}Pb/^{207}Pb and ^{208}Pb/^{207}Pb ratios (~1.14 and ~2.42, respectively) were observed between 2009–2010, and attributed to the contamination of formation sites in the south Indian Ocean around 8–12 years earlier by leaded gasoline from western Australia (Lee et al., 2015). Along the SR3 transect, however, the lowest Pb isotope ratios are observed proximal to the south Australian SAMW formation site north of the SAF (Figure 4.1 and 4.5). The Pb isotope composition of SAMW should therefore reflect the surface waters around the SAF. The Pb isotope composition of subsurface SAMW at station 15 marks the most extreme (i.e., lowest) ratios of the transect and therefore can't

solely reflect subduction of SAMW north of the SAZ. This suggests that advection of subsurface waters from an area proximal to the anthropogenic source and subsequent mixing with locally formed SAMW is responsible for the extreme Pb isotope signature. This interpretation is plausible given that the Australian Basin acts as an important conduit for south-east and eastward flowing Indian waters as well as south-west Pacific waters from the Tasman Sea (e.g., McCartney and Donohue, 2007; Figure 4.1). Moreover, SAMW at station 15 is denser than the dominant type of SAMW (γ^n < 26.94 kg m^{-3}) south of Tasmania, corroborating the hypothesis that SAMW has been subjected to mixing with denser, most likely subtropical waters (Herraiz-Borreguero and Rintoul, 2011) .

A significant contribution to the eastward flow of the AAC into the Australian Basin comes from warmer waters of the South Atlantic and Agulhas return current near southern Africa. The $^{206}Pb/^{207}Pb$ and $^{208}Pb/^{207}Pb$ ratios of anthropogenic Pb sources from southern Africa are indistinguishable from Australian Pb sources (1.06–1.11 and 2.34–2.37, respectively; Bollhöfer and Rosman, 2000) and the anthropogenic signal in SAMW could therefore reflect inter-ocean basin transport of Pb from the Atlantic to the Australian Basin. Koch-Larrouy et al. (2010), however, have demonstrated using an ocean circulation model that the contribution of the Agulhas return current to SAMW at formation sites along the Indian Ocean becomes progressively less from west to east and eventually negligible at the formation site south west of Tasmania.

It is possible, therefore, to conclude that the contribution of anthropogenic Pb to SAMW in the Australian Basin must come from poleward circulation close to Australia. From the west, the Leeuwin Current could provide a transport pathway for contaminated (sub)surface coastal waters from western and southern Australia into the Australian Basin against the flow of the subtropical gyre (Bull and Sebille, 2016). The extent of this flow, however, is geographically limited to the southern tip of Tasmania at ~44°E (Ridgway and Condie, 2004) and is only estimated to constitute ~10% of transported SAMW from the formation site south west of Tasmania (Koch-Larrouy et al., 2010). A more plausible argument is that the Tasman leakage acts as a transport pathway for contaminated Pacific waters from the east coast of Australia to as far south as 48.5°S (Rintoul and Bullister, 1999). Hydrographic observations showing abrupt changes in the temperature (> 1 °C) of SAMW around Tasmania have been ascribed to the advection of warm and saline subtropical waters from the Tasman Sea (Herraiz-Borreguero and Rintoul, 2011b). Furthermore, models have quantified that one-third of the SAMW transported from the areas of dense SAMW formation in the Australian Basin correspond to the Tasman leakage (Koch-Larrouy et al., 2010).

Based on just one depth profile (station 15), it is difficult to conclude with any certainty that the Tasman leakage is responsible for the SAMW $^{206}Pb/^{207}Pb$ and $^{208}Pb/^{207}Pb$ ratio minima in the SAZ. However, the ability of Pb isotopes to trace mesoscale circulations patterns has previously been demonstrated in the South Atlantic (Paul et al., 2015a), and the Tasman leakage could act as an important transport pathway for contaminants and nutrients to the Southern Ocean.

4.5.4. Controls on the Pb isotope composition of intermediate and deep waters

The only other water masses that show similarly high Pb concentrations like SAMW are preformed AAIW and UCDW (Figures 4.5 (a–b) and 4.6 (b)). They also show a large range of Pb isotope signatures extending to values as high as 47% anthropogenic fraction. In regions of strong hydrodynamic flow, lateral advection is the dominant mechanism transporting anthropogenic Pb into the ocean interior (e.g., Noble et al., 2015; Bridgestock et al., 2018). The combined effect of zonal circulation and meridional water mass transport along and across circumpolar fronts will exert some level of control on the distribution of Pb in the Southern Ocean. Meridional circulation transports Indian Deep Water (IDW) poleward into the Australian Basin while the ACC simultaneously provides an influx of CDW (UCDW and LCDW) from the South Atlantic (e.g., Talley, 2013; Tamsitt et al., 2019). The confluence of meridional and zonal derived deep waters from other ocean basins in the ACC domain contributes to the poleward flow of UCDW and LCDW which, in turn, forms the equatorward flowing AASW (eventually subducting to form AAIW) and AABW, respectively (Rintoul, 2001; Lumpkin and Speer, 2007; Talley, 2013). The amount of control lateral advection has on the distribution of Pb in the Southern Ocean, however, will vary spatially depending on competing vertical processes in the water column.

4.5.4.1. Role of circulation and water mass mixing in the Southern Ocean

The most prominent feature in the Australian sector of the Southern Ocean is the low $^{206}Pb/^{207}Pb$ and $^{208}Pb/^{207}Pb$ ratios and concomitant high Pb concentrations in pre-formed AAIW and UCDW (Figures 4.5 and 4.6 (b)). Given the transport pathways and water mass formation sites in the region, the effect of zonal and meridional water mass transport can be assessed using salinity as a conservative parameter and comparing deep waters in the region to the Pb isotope composition of deep-water masses upstream in the Indian Ocean (Figure 4.7).

Pre-formed AAIW at station 51 in the AZ is exposed at the surface to atmospheric deposition of Australian emissions and therefore exhibits a much lower $^{206}Pb/^{207}Pb$ ratio than underlying waters at the same station (Figure 4.5). The meridional circulation transports this pre-formed AAIW equatorward and subducts past the SAF to form AAIW at station 15 in the SAZ. The exposure of pre-formed AAIW to the atmosphere and subsequent lateral advection to lower latitudes will contribute to the transport of anthropogenic Pb to the ocean interior. There is a clear difference, however, between the higher $^{206}Pb/^{207}Pb$ ratio of pre-formed AAIW at station 51 and the lower $^{206}Pb/^{207}Pb$ ratio of AAIW at station 15. This discrepancy coincides with a south-north meridional increase in Pb concentration along the isopycnal range of pre-formed AAIW and implies an addition of anthropogenic Pb along the meridional pathway of this water mass (Figure 4.5 (c)).

Similarly, there is a clear progression to lower $^{206}Pb/^{207}Pb$ ratios moving in an equatorward direction along the isopycnal range of UCDW. Unlike pre-formed AAIW, the lower $^{206}Pb/^{207}Pb$ ratio could be due to the influx of anthropogenic Pb from meridionally transported deep waters of the North Indian Ocean (i.e., IDW). The deep waters within the same isopycnal range, however, display significantly higher $^{206}Pb/^{207}Pb$ ratios than UCDW at station 30 in the PF (Figure 4.5). Moreover, UCDW transported zonally from the west exhibit much higher $^{206}Pb/^{207}Pb$ ratios than UCDW along the SR3 transect. The lowest $^{206}Pb/^{207}Pb$ ratio for UCDW from the west is 1.165 (Lee et al., 2015; Figure 4.7) while UCDW observations north of station 51 are ~1.160 (Figure 4.7). The return flow along the lower isopycnal limits of UCDW is also unable to account for the low $^{206}Pb/^{207}Pb$ ratios of UCDW. Any equatorward flow would export the higher $^{206}Pb/^{207}Pb$ ratios of surface waters proximal to Antarctica (e.g., station 56) into the intermediate waters of the PF and SAZ. Lateral advection along zonal and meridional circulation pathways does not, therefore, resolve the low $^{206}Pb/^{207}Pb$ ratio and concomitant high Pb concentration observed in both pre-formed AAIW and UCDW.

4.5.4.2. Diapycnal mixing?

The inability of lateral advection to reconcile the distribution of Pb isotopes in pre-formed AAIW and UCDW implies that the observed addition of anthropogenic Pb to these water masses must be transported from the surface by vertical processes. The upwelling and transformation of UCDW to intermediate water densities (i.e., AAIW and SAMW) is compensated by diapycnal mixing south of the SAF (Rintoul, 2001; Rintoul and England,

2002) but vertical mixing of these water masses does not reconcile the observed distribution of Pb concentration and isotope composition in the region. If diapycnal mixing was the mechanism controlling the vertical transport of anthropogenic Pb, the underlying waters would exhibit a gradual increase in $^{206}Pb/^{207}Pb$ ratios and significantly lower Pb concentrations than the surface waters. In contrast, Pb isotopes at stations 30, 40 and 45 are largely homogenous between the subsurface and UCDW (Figures 4.3 and 4.4), while Pb concentrations at the same stations are appreciably higher in pre-formed AAIW and UCDW than the surface waters (Figure 4.3). The distribution of Pb concentrations and isotope compositions in the surrounding waters means that diapycnal mixing is not responsible for the discrepancy.

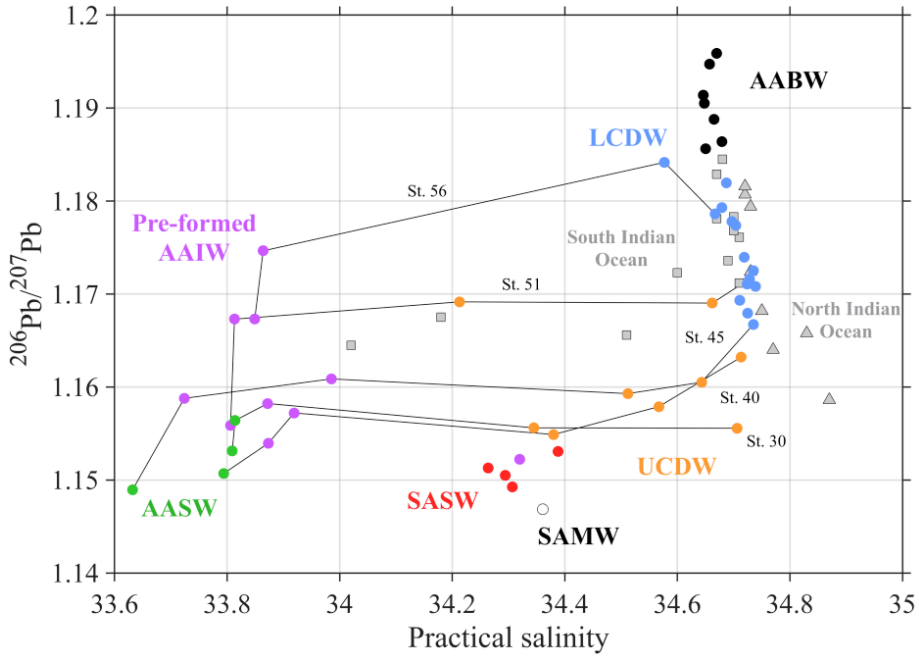

Figure 4.7 $^{206}Pb/^{207}Pb$ versus salinity used to demonstrate the non-conservative behaviour of Pb in pre-formed AAIW and UCDW. The coloured points denote each labelled water mass which corresponds to the same colour code used in Figure 4.6 (b). The black lines connect the surface waters to UCDW for stations 30, 40, 45, 51 and 56. The grey squares and grey triangles represent the $^{206}Pb/^{207}Pb$ ratio of deep water masses (UCDW and LCDW; $27.55 < \gamma^n < 28.27$) in the South Indian (station 14) and North Indian (station 3) Ocean, respectively (Lee et al., 2015).

On the other hand, LCDW exhibits the same $^{206}Pb/^{207}Pb$ isotope signature as IDW from the north and LCDW to the west (Figure 4.7). The inflow of deep waters to the Australian sector of the Southern Ocean must therefore control the Pb isotope composition of LCDW, with any variation caused by diapycnal mixing between more natural Pb in AABW and anthropogenic Pb in UCDW. As discussed previously, diapycnal mixing between UCDW and LCDW may act as a mechanism of transporting some anthropogenic Pb to AABW levels (see section 4.5.2.2.).

4.5.4.3. Role of scavenging in the Southern Ocean

The distribution of Pb concentrations and isotope compositions in pre-formed AAIW and UCDW can be reconciled by attributing the vertical transport mechanism to reversible scavenging and equilibrium exchange processes. The influence of equilibrium exchange on the Pb isotope composition of natural waters has recently been quantified in closed-system exchange experiments (Chen et al., 2016). Simulations of spiked estuarine water have shown that dissolved Pb with low $^{206}Pb/^{207}Pb$ ratios would induce equilibrium exchange with relatively high $^{206}Pb/^{207}Pb$ particulates in the water column, i.e., there is an isotopic shift due to net release of ^{206}Pb from particulates to surrounding water and net adsorption of ^{207}Pb from the water to particulates (Chen et al., 2016).

Observational evidence of coupled reversible scavenging and equilibrium exchange processes have been shown to play an important role in transporting anthropogenic Pb to deep water masses of the Pacific Ocean (Wu et al., 2010). In the Southern Ocean, scavenging during intense periods of primary production has been proposed as the process responsible for the low Pb concentrations of surface waters despite significant contributions of anthropogenic Pb from regional industrial sources (Westerlund and Ohman, 1991; Flegal, et al., 1993). Lai et al. (2008) showed that the dominant phase in subsurface waters along the SR3 meridional transect is particulate Pb and the spatial variability of dissolved Pb is caused by strong scavenging. This is in stark contrast to other regions such as the tropical Atlantic where particulate Pb represents ~7–12% of the total Pb budget in the water column and the dominant process controlling the distribution of anthropogenic Pb is ocean circulation (Bridgestock et al., 2018).

In this study, adsorption of dissolved Pb onto particulates in the water column at the surface (i.e., scavenging) would produce the observed low Pb concentration in surface waters. The adsorption of ^{207}Pb onto particulates at the surface because of the influx of high

anthropogenic $^{206}Pb/^{207}Pb$ ratios, followed by the sinking and remineralisation of these particulates at depth would increase the dissolved Pb concentration, release the adsorbed ^{207}Pb into deep water masses and produce the observed lower $^{206}Pb/^{207}Pb$ ratio. The biogeochemical provinces of the Southern Ocean, however, exhibit spatial variability in this process across the meridional transect.

The meridional trend towards higher $^{206}Pb/^{207}Pb$ ratios and lower Pb concentrations in UCDW from the SAZ (station 15) to the AZ (station 51) reflects reduced scavenging—and subsequently reduced flux of anthropogenic Pb to deeper waters—caused by lower rates of primary production across the different biological regimes of the Southern Ocean fronts (Bender et al., 2016; Rigual-Hernández, et al., 2015). The region south of the PF represents the HNLC Antarctic region where surface water inventories of all macronutrients are sufficient to sustain biological production but other factors such as light availability and Fe concentrations limit phytoplankton growth (e.g., de Baar et al., 2005). Consequently, the distribution of Pb in intermediate waters of the CZ and AZ are controlled more by ocean circulation than vertical transport processes (i.e., scavenging and equilibrium exchange; Figure 4.5). Between the PF and SAF in the summer, light and Fe, coupled with upwelled silicate-rich deep waters, are sufficient to sustain diatom growth and increase, relative to the HNLC region, the amount of biogenic (opal) particulates in the water column. Surface silicate levels are not regenerated by upwelled deeper waters to the north and become progressively depleted at lower latitudes, eventually limiting opal production at the subtropical front (Brzezinski et al., 2002; Sarmiento et al., 2004). Previous studies that cross the HNLC region and the strong opal gradients in the Southern Ocean have demonstrated that the partition coefficient of ^{231}Pa (i.e., the affinity of a dissolved trace element to marine particulates) increases in the PFZ because of high rates of opal production (Walter et al., 1997; Chase et al., 2002). Although the effects of particle composition on the partition coefficient of Pb in seawater have not yet been examined, the increase in anthropogenic Pb in the UCDW around the PF-S suggests that opal production and cycling is an important control on the vertical transport of Pb in the Southern Ocean (Figure 4.4 and 4.5).

In reality, the Pb concentrations and isotope compositions of pre-formed AAIW and UCDW is a function of all of the aforementioned processes. The dominance of reversible scavenging simply overrides the contribution already made by circulation and water mass mixing. The relative contribution of these processes is difficult to quantitatively deconvolve because there are no existing constraints on particulate Pb concentrations and isotope compositions, Pb scavenging rates, or particle settling velocities in the Southern Ocean.

The effects of reversible scavenging can be approximated by removing the maximum possible contribution made by ocean circulation and water mass mixing to the observed Pb isotope signatures of water masses (Figure 4.7). For example, the sample collected at 1000 m within UCDW at station 30 exhibits a relatively high Pb concentration (11.3 pmol kg^{-1}) and low $^{206}Pb/^{207}Pb$ ratio (1.156) compared to underlying LCDW (5.8 pmol kg^{-1} and 1.171, respectively; Figure 4.7). The lowest $^{206}Pb/^{207}Pb$ ratio along an equivalent neutral density isopycnal from the Indian Ocean will correspond to the maximum possible contribution of lateral advection to the observed Pb isotope composition of UCDW at this station. Here, the North Indian Ocean IDW values ($^{206}Pb/^{207}Pb$ ratio = 1.164, Pb concentration = 7.7 pmol kg^{-1} and salinity = 34.77) at γ^n = 27.970 kg m^{-3} are selected as an upstream endmember of the meridional UCDW circulation. The composition of UCDW ($^{206}Pb/^{207}Pb$ ratio = 1.1690, Pb concentration = 7.3 pmol kg^{-1} and salinity = 34.66) at station 51 along a similar isopycnal (γ^n = 27.995 kg m^{-3}) is used as the downstream endmember along the flow path of this water mass. A multi-endmember mixing calculation between the IDW endmember, UCDW endmember and underlying LCDW at station 30 was used to find a $^{206}Pb/^{207}Pb$ ratio of 1.167 at the corresponding salinity value (34.706) for UCDW at station 30 (red square; Figure 4.8). This $^{206}Pb/^{207}Pb$ ratio corresponds to the maximum contribution made by lateral advection along the UCDW pathway taking into account any residual mixing with LCDW. If the surface water $^{206}Pb/^{207}Pb$ ratio at station 30 ($^{206}Pb/^{207}Pb$ = 1.153) is furthermore assumed to represent the maximum possible contribution from reversible scavenging, the difference between the observed Pb isotope composition of UCDW ($^{206}Pb/^{207}Pb$ = 1.156) and the calculated $^{206}Pb/^{207}Pb$ ratio along the lateral advection mixing line ($^{206}Pb/^{207}Pb$ = 1.167) constitutes the change in the $^{206}Pb/^{207}Pb$ ratio effected by reversible scavenging. Based on the above mixing calculation, reversible scavenging is responsible for approximately ~80% of the observed Pb inventory in UCDW at station 30 in the PF.

The mass balance and water mass mixing calculations are not accurate and the interpretation relies on a series of assumptions: (1) both the IDW and UCDW endmembers are in steady state and controlled explicitly by lateral advection and water mass mixing; (2) meridional circulation of UCDW is unidirectional in the southward horizontal plane; and (3) the contribution of downward diapycnal mixing on the Pb isotope composition is negligible. Despite the limitations of these calculations, it is a useful approach to highlight the potential dominance of reversible scavenging relative to the contributions made by lateral advection and water mass mixing.

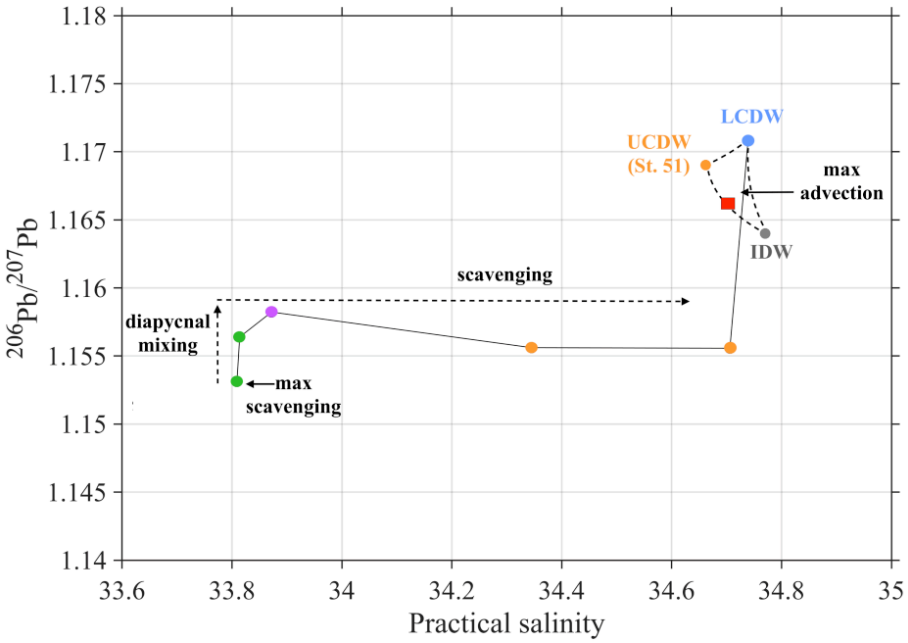

Figure 4.8 Schematic illustrating the effects of reversible scavenging and equilibrium exchange on the distribution of anthropogenic Pb in UCDW. The coloured points denote each of the different water mass corresponding to the same colour code used in Figure 4.6 (b) and 4.7, while the black lines connect the surface waters to LCDW at station 30. UCDW at station 51 and IDW from the North Indian Ocean (station 3; Lee et al., 2015) form the lateral advection endmembers. Multi-endmember mixing between these endmembers and LCDW (black dashed lines) computes the maximum contribution made by lateral advection and upward diapycnal mixing (red square).

4.5.5. Temporal evolution of Pb concentrations along the SR3 transect

Along the SR3 hydrographic transect, Pb concentration data from January–February 2002 (surface and intermediate depths; Lai et al., 2008) and March–April 2008 (full depth profiles; Schlitzer et al., 2018) can be used in conjunction with Pb concentrations from this study to assess the spatiotemporal variability of Pb in the region (Figure 4.9). The spatiotemporal trends show two important features: (1) surface and subsurface water Pb concentrations were significantly higher in 2002, particularly to the north (SAZ and PF-N) and south (CZ) proximal to the surrounding continents; and (2) bottom water Pb concentrations in the AZ and CZ close to the Antarctic continental shelf were significantly higher in 2008.

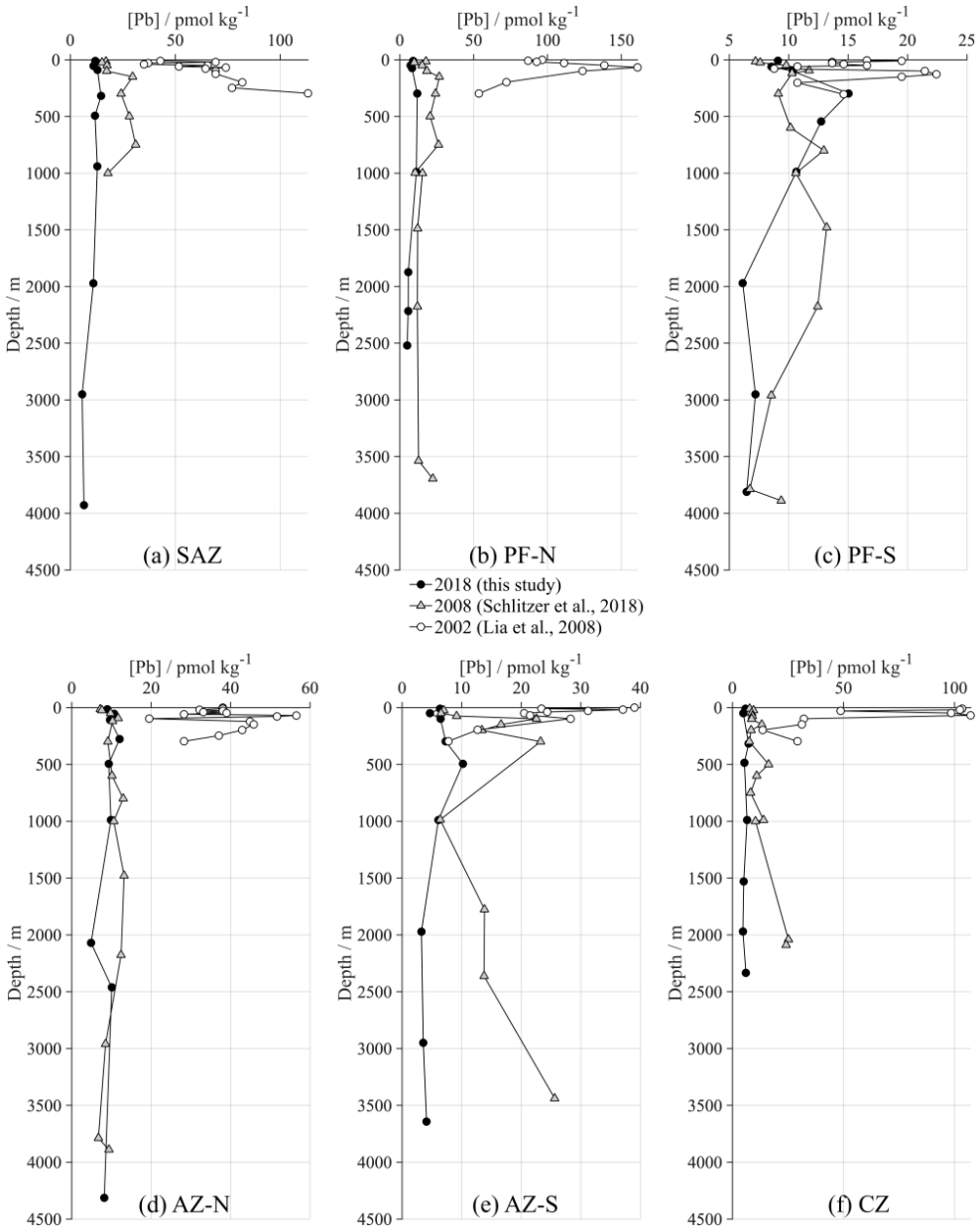

Figure 4.9 Changes in Pb concentration through the water column between 2002 and 2018 along the SR3 transect. Stations are categorised according to the frontal system described in section 4.2.1 from (a) the Subantarctic Zone to (f) the Continental Zone near Antarctica. Black circles correspond to data obtained in this study; grey triangles refer to data obtained between March-April 2008 (Schlitzer et al., 2018); and the white circles correspond to data between January–February 2002 (Lia et al., 2008). Lia et al. (2008) reported Pb concentrations in pmol L^{-1}; a constant density value of ρ =1.025 kg L^{-1} was used to convert from and per volume to per mass units (i.e., pmol kg^{-1}).

Overall, surface and subsurface waters show a significant reduction in Pb concentrations from 2002–2008 and 2008–2018. In 2002, surface and subsurface Pb concentrations between Australia and Antarctica were approximately 5 and 10 times higher (~7–153 pmol kg^{-1}; Lai et al., 2008) than the range observed in 2008 (~7–30 pmol kg^{-1}; Schlitzer et al., 2018) and 2018 (~7–15 pmol kg^{-1}; this study), respectively. The phase-out of leaded petrol in Australia almost two decades ago has significantly reduced the anthropogenic input of 'Broken Hill-type' Pb to the regional atmosphere (O'Brien, 2011). Although Pb isotopes were not measured to confirm the source of Pb in 2002 or 2008, the dominance of Australian emissions in the Pb mixing model of the region (Figure 4.6 (a)) as derived from our 2018 results suggests that the temporal trend from significantly higher to low Pb concentrations is a consequence of the use of leaded petrol in Australia up to the early 2000s. An important geographical trend in seen in the 2002 results that does not exist in 2008 and 2018 is the significant increase in surface and subsurface Pb concentrations from the AZ to the CZ despite being more distal from Australian anthropogenic emissions (Figure 4.9 (e) and (f)). This suggests that meltwaters from East Antarctic glaciers/snow, which were exposed to atmospheric deposition of anthropogenic particles, must be an important mechanism in transporting Antarctic continental Pb to Southern Ocean surface waters (Rosman et al., 1994; Vallelonga et al., 2002).

Another interesting feature across the time period are the higher Pb concentrations (~25 pmol kg^{-1}) of bottom waters at the continental slope in 2008 (Figure 4.9 (e)–(f)). Unlike surface waters, bottom waters will be influenced by both continental meltwater inputs at the site of water mass formation and benthic fluxes/sediment suspension during water mass transit across the continental margin. Following atmospheric deposition on the Antarctic continent, anthropogenic emissions are transported to the Southern Ocean by meltwater but any dissolved Pb is likely to be scavenged onto particles at the freshwater-seawater interface and subsequently transferred to the seafloor (e.g., Bastami et al., 2015). Previous observations of elevated dissolved Pb concentrations at the seawater-sediment interface in both coastal waters (e.g., Chien et al., 2017; Rusiecka et al., 2018) and the deep ocean (Lee et al., 2015; Noble et al., 2015) have been attributed to the resuspension of continental derived sediments and supply of Pb-enriched particles to the overlying water column. In 2009/2010, however, bottom waters to the west in the more isolated Indian sector of the Southern Ocean exhibited very low Pb concentrations (~7 pmol kg^{-1}; Lee et al., 2015). Given the lower Pb concentrations of bottom waters in this region at a similar time period, the elevated concentrations at the CZ and AZ-S in 2008 along the SR3 transect might be a consequence of

larger fluxes of anthropogenic Pb from Antarctica into polynyas near bottom water formation sites and/or coastal benthic supplied "legacy" pollutant Pb from Australian emissions. The lower Pb concentrations of bottom waters in 2018 (~5 pmol kg^{-1}) could highlight the return of natural Antarctic sediment derived Pb in bottom waters with an isotopic signature close to Fe-Mn deposits (Figure 4.6 (a)).

4.6. Conclusion

Observations of Pb concentrations and isotope compositions in seawater along a meridional transect between Australia and Antarctica have allowed, for the first time, a detailed assessment of the processes governing the distribution of Pb across the Southern Ocean.

When combined with existing Pb isotopic records of Antarctic and Australian inputs, the seawater data are consistent with natural Pb from Antarctic sediments/benthic sources, as recorded by deep-sea Fe-Mn crusts, Australian aeolian sources and anthropogenic Pb from Australian emissions. The distribution of water masses in three isotope space reveals a correlation between surface waters with low $^{206}Pb/^{207}Pb$ and $^{208}Pb/^{207}Pb$ ratios, corresponding to a high fraction of anthropogenic Pb (30–50%), and AABW with high $^{206}Pb/^{207}Pb$ and $^{208}Pb/^{207}Pb$ ratios which indicates a dominance of natural Pb inputs during bottom water formation (76–84%). Despite the strong correlation, there is an incongruence between the spatial distribution of SAMW, pre-formed AAIW and UCDW in the water column and their position in Pb isotopic space.

On the one hand, the subsurface $^{206}Pb/^{207}Pb$ and $^{208}Pb/^{207}Pb$ minima associated with SAMW potentially traces the pathway of contaminated Pacific waters laterally advected from the Tasman Sea (East Australia) into the Southern Ocean through the Tasman leakage. On the other hand, lateral advection and diapycnal mixing are not able to reconcile the relatively low $^{206}Pb/^{207}Pb$ and $^{208}Pb/^{207}Pb$ ratios and high Pb concentrations of pre-formed AAIW and UCDW.

In order to reconcile this discrepancy, reversible scavenging and equilibrium exchange must play an important role in the vertical redistribution of anthropogenic Pb from surface waters to UCDW. In the northern PF region where diatom primary production and opal levels are higher than the HNLC Antarctic region (CZ and AZ), reversible scavenging could be responsible for as much as ~80% of the Pb in UCDW. Although the observations qualify the dominance of reversible scavenging in intermediate water masses, it is difficult to fully quantify the effects of reversible scavenging, lateral advection and water mass mixing

without well constrained scavenging rate constants, particle composition, particulate settling velocities and water mass endmember compositions.

Acknowledgements and contributions

Alex Griffiths analysed the Pb concentration and isotope composition of the Southern Ocean samples and lead the interpretation of the results. Additional contributions to the work came from Mark Rehk mper, Tina van de Flierdt, Hollie Packman, Susan Little, Yee Lap Leung and Andrew Bowie. Thanks to Mark Rehk mper and Tina van de Flierdt for their insightful comments throughout the data interpretation process. For the collection of the samples, thanks must go to Andrew Bowie and Melanie East as well as all the participants of the Australian GEOTRACES GS01 section cruise. The authors would like to acknowledge all the members of the MAGIC group, especially Katharina Kreissig and Barry Coles, for their support in the lab. We acknowledge the studentship funding for Alex Griffiths from the NERC DTP 'Science and Solutions for a Changing Planet' at Imperial College London.

Chapter 5

Conclusions and future research

The thesis underscores the importance of isotope analyses for understanding the main processes governing the biogeochemical cycles of trace elements. The development of a new analytical method as well as Nd and Pb isotope analyses of important seawater samples have successfully addressed the overall aim of this study: to understand the processes that control the biogeochemical cycling of Nd and Pb in the Australian Sector of the Southern Ocean. The following section details how the specific objectives of this thesis were fulfilled and suggests possible future research.

Objective 1: Determine the processes that govern the Nd isotope composition of deep and bottom waters (AABW) across the East Antarctic continental shelf.

Observations of dissolved Nd isotope compositions for seawater from the Wilkes Land continental margin in the Australian-Antarctic Basin of the Southern Ocean show that circulation patterns and water mass mixing govern the Nd isotope fingerprint of both deep and bottom waters in the region. Firstly, mixing of upwelled CDW with slope and shelf AASW and AABW exclusively controls the Nd isotope composition of MCDW ($\varepsilon_{Nd} = -8.8 \pm 0.8$). The MCDW values are identical to published data for CDW across the Southern Ocean which, coupled with no observable elemental fractionation of the REEs, suggests that boundary exchange does not modify the Nd isotope composition on the slope and shelf. Secondly, the regional Nd isotope signature for AABW ($\varepsilon_{Nd} = -8.3 \pm 0.5$) is intermediate between published data for less radiogenic Atlantic sector AABW ($\varepsilon_{Nd} = -9.1 \pm 0.7$) and more radiogenic Pacific sector AABW ($\varepsilon_{Nd} = -7.4 \pm 0.9$). In the absence of active convection, it represents a mixture of advected AABW from the Adélie Coast with local CDW. The hypothesis that AABW in this location reflects the regional weathering inputs of Nd to the Southern Ocean from Antarctica can therefore be rejected.

Further studies from different regions around East Antarctica are required to quantify how boundary exchange and local inputs affect deep and bottom water ε_{Nd} signatures. For example, the Prydz Bay to the west of the Wilkes Land continental margin represents another zone of AABW formation. In this location, the conditions may be more conducive to weathering and boundary exchange. This could produce a local highly unradiogenic AABW ε_{Nd} signature, which in turn, could have implications for palaeo-climate studies in the Indian Ocean.

Objective 2: Develop an analytical procedure to determine the Pb isotope composition of seawater that (1) provides unbiased and precise results and (2) has a greater analytical throughput than established high-precision methods.

A novel method to determine the Pb isotope composition of seawater is presented in Chapter 3. The method encompasses extraction of Pb from seawater by solid-phase extraction using Nobias PA-1 resin and a two-stage ion exchange chromatography procedure. The subsequent isotope analyses are conducted by MC-ICP-MS in conjunction with a ^{207}Pb-^{204}Pb double spike for the correction of instrumental mass discrimination. The precision of the method was assessed through replicate analyses of four seawater samples, with typical reproducibilities (± 2sd) of about ±250–1250 ppm for ratios involving the minor ^{204}Pb isotope (^{208}Pb/^{204}Pb, ^{207}Pb/^{204}Pb, ^{206}Pb/^{204}Pb) and about ±150–1200 ppm for ^{207}Pb/^{206}Pb and ^{208}Pb/^{206}Pb. When compared to an established double-spike TIMS methodology (Paul et al., 2015b), the results demonstrate similar precision for ^{208}Pb/^{206}Pb, improved precision for ^{207}Pb/^{206}Pb and greater reproducibility by at least a factor of two for ^{204}Pb ratios. The trueness of the method was confirmed through the analyses of three GEOTRACES intercalibration samples for which reference values, including results produced with the established in-house TIMS method, are available. Importantly, the analytical throughput of the new procedure is significantly higher (~12 samples/month) compared to that of the TIMS method, which employs $Mg(OH)_2$ co-precipitation for the Pb separation (~6 samples/month). This improvement in analytical throughput is achieved without compromising the precision of the results or the capability to measure seawater samples with Pb concentrations as low as ~5 pmol kg^{-1}.

Although the new technique represents a significant improvement, there are several changes that could be made to further streamline the analytical procedure. Firstly, the Nobias resin provides an effective extraction procedure which isolates Pb from a significant proportion of the seawater matrix, especially compared to $Mg(OH)_2$ co-precipitation. Consequently, a one-step anion-exchange chromatography procedure without HF in the loading solution may provide sufficient purification for subsequent Pb isotope analyses following solid-phase extraction with Nobias PA-1 resin. Secondly, the application of a mixed ^{202}Pb–^{205}Pb instead of a ^{207}Pb–^{204}Pb double-spike would allow internal normalisation to correct for instrumental mass discrimination and, importantly for seawater analyses, could additionally provide Pb concentration data with a single analysis per sample. Importantly, such measurements would simultaneously provide fractionation corrected Pb isotope ratios and high quality Pb concentration data using the isotope dilution technique. In theory, this

would streamline the method significantly but highly purified ^{202}Pb and ^{205}Pb spikes are extremely rare and, in practice, may not be suitable for routine analyses with MC-ICP-MS as relatively large quantities of the isotopes would be in need for the measurements, including the preparation of spiked solutions of Pb isotope standards to monitor instrument performance.

Objective 3: Determine the relative importance of the different transport mechanisms for the redistribution of anthropogenic Pb into the interior of the Southern Ocean.

Observations of Pb concentrations and isotope compositions for seawater from a meridional transect between Australia and Antarctica enabled a detailed assessment of the processes governing the distribution of Pb across the Southern Ocean. The results show that both conservative and non-conservative transport mechanisms play an important role in controlling the pathways of anthropogenic Pb into the interior of the Southern Ocean. On the one hand, the subsurface $^{206}Pb/^{207}Pb$ and $^{208}Pb/^{207}Pb$ minima associated with SAMW appear to trace the pathway of contaminated Pacific waters laterally advected from the Tasman Sea (East Australia) into the Southern Ocean through the Tasman leakage. On the other hand, lateral advection and diapycnal mixing are not able to reconcile the relatively low $^{206}Pb/^{207}Pb$ and $^{208}Pb/^{207}Pb$ ratios and high Pb concentrations of pre-formed AAIW and UCDW. Reversible scavenging and equilibrium exchange must hence play an important role in the vertical redistribution of anthropogenic Pb from surface waters to UCDW. In more biologically productive areas such as the northern PF, reversible scavenging may be responsible for as much as ~80% of the Pb in UCDW. This conclusion corroborates the hypothesis that particle scavenging acts as an important transport mechanism for anthropogenic Pb to the deep ocean, although the importance of ocean circulation should not be overlooked.

There are two key questions that could not be answered based on the available observational data in this thesis. Firstly, what is the rate of vertical export of anthropogenic Pb that is generated by reversible scavenging? Secondly, what is the fate of anthropogenic Pb once it has been scavenging and transported into UCDW? The first question can be addressed with a suite of measurements in the Southern Ocean: determination of ^{210}Pb water column inventories to calculate *in situ* Pb residence times; Pb isotope analyses of the particulate phase in the water column to constrain equilibrium exchange processes; and particle composition data to understand the Pb budget of the different types of scavenging material.

Finding answers to the second question will require additional Pb isotope measurements for seawater profiles from farther eastwards along the ACC pathway.

References

Abouchami, W. and Goldstein, S.L., (1995): A lead isotopic study of Circum-Antarctic manganese nodules. Geochimica et Cosmochimica Acta, 59 (9), pp. 1809–1820.

Alleman, L.., Church, T.., Ganguli, P., Véron, A., Hamelin, B. and Flegal, A., (2001): Role of oceanic circulation on contaminant lead distribution in the South Atlantic. Deep Sea Research Part II: Topical Studies in Oceanography, 48 (13), pp. 2855–2876.

Alleman, L., Véron, A., Church, T., Flegal, A. and Hamelin, B., (1999): Invasion of the abyssal North Atlantic by modern anthropogenic lead. Geophysical Research Letters, 26 (10), pp. 1477–1480.

Amelin, Y. and Davis, W.J., (2006): Isotopic analysis of lead in sub-nanogram quantities by TIMS using a ^{202}Pb–^{205}Pb spike. J. Anal. At. Spectrom., 21 (10), pp. 1053–1061.

Ardyna, M., Lacour, L., Sergi, S. et al., (2019): Hydrothermal vents trigger massive phytoplankton blooms in the Southern Ocean. Nature Communications, 10 (1), pp. 1–8.

Arsouze, T., Dutay, J.-C., Lacan, F. and Jeandel, C., (2009): Reconstructing the Nd oceanic cycle using a coupled dynamical – biogeochemical model. Biogeosciences Discussions, 6 (3), pp. 5549–5588.

Bacon, M. P., Spencer, D. W. and Brewer, P. G., (1976): Pb-210-Ra-226 and Po-210-Pb- 210 Disequilibria in Seawater and Suspended Particulate Matter, Earth Planet. Sc. Lett., 32 (2), 277–296.

Baker, J., Peate, D., Waight, T. and Meyzen, C., (2004): Pb isotopic analysis of standards and samples using a ^{207}Pb-^{204}Pb double spike and thallium to correct for mass bias with a double-focusing MC-ICP-MS. Chemical Geology, 211 (3–4), pp. 275–303.

Barbante, C., Turetta, C., Gambaro, A., Capodaglo, G. and Scarponi, G., (1998): Sources and origins of aerosols reaching Antarctica as revealed by lead concentration profiles in shallow snow. Annals of Glaciology, 27, pp. 674–678.

Barling, J. and Weis, D., (2008): Influence of non-spectral matrix effects on the accuracy of Pb isotope ratio measurement by MC-ICP-MS: implications for the external normalization method of instrumental mass bias correction. Journal of Analytical Atomic Spectrometry, 23 (7), pp. 1017–1025.

Basak, C., Pahnke, K., Frank, M., Lamy, F. and Gersonde, R., (2015): Neodymium isotopic characterization of Ross Sea Bottom Water and its advection through the southern South Pacific. Earth and Planetary Science Letters, 419, pp. 211–221.

Bastami, K. D., Neyestani, M. R., Shemirani, F., Soltani, F., Haghparast, S., and Akbari, A. (2015): Heavy metal pollution assessment in relation to sediment properties in the coastal sediments of the southern Caspian Sea. Marine Pollution Bulletin, 92 (1–2), 237– 243.

Beale, M.H., Hagan, M.T. and Demuth, H.B., (2017): Neural Network Toolbox: User's guide. MathWorks, Natick, Mass., pp. 512.

Bender, M.L., Tilbrook, B., Cassar, N., Jonsson, B., Poisson, A. and Trull, T.W., (2016): Ocean productivity south of Australia during spring and summer. Deep-Sea Research Part I: Oceanographic Research Papers, 112, pp. 68–78.

Bertram, C.J. and Elderfield, H., (1993): The geochemical balance of the rare earth elements and neodymium isotopes in the oceans. Geochimica et Cosmochimica Acta, 57, pp. 1957–1986.

Biller, D. V. and Bruland, K.W., (2012): Analysis of Mn, Fe, Co, Ni, Cu, Zn, Cd, and Pb in seawater using the Nobias-chelate PA1 resin and magnetic sector inductively coupled plasma mass spectrometry (ICP-MS). Marine Chemistry, 130–131, pp. 12–20.

Bindoff, N.L., Rosenberg, M.A. and Warner, M.J., (2000): On the circulation of the waters over the Antarctic continental rise and slope between 80 and 150oE. Deep-Sea Research II, 47 (12/13), pp. 2299–2326.

Bishop, C.M., (1995): Neural networks for pattern recognition.

Blain, S., Sarthou, G., Laan, P., (2008): Distribution of dissolved iron during the natural iron fertilisation experiment KEOPS (Kerguelen Plateau, Southern Ocean). Deep-Sea Research. II, 55, pp. 594–605.

Bollhöfer, A. and Rosman, K.J.R., (2000): Isotopic source signatures for atmospheric lead: the Southern Hemisphere. Geochimica et Cosmochimica Acta, 64 (19), pp. 3251–3262.

Bollhfer, A. and Rosman, K.J.R., (2001): Isotopic source signatures for atmospheric lead: The Northern Hemisphere. Geochimica et Cosmochimica Acta, 65 (11), pp. 1727–1740.

Boyle, E.A., Chapnick, S.D., Shen, G.T. and Bacon, M.P., (1986): Temporal variability of lead in the western North Atlantic. Journal of Geophysical Research, 91, pp. 8573–8593.

Boyle, E.A., John, S., Abouchami, W., Adkins, J.F., Echegoyen-Sanz, Y., Ellwood, M., Flegal, A.R., Fornace, K., Gallon, C., Galer, S., Gault-Ringold, M., Lacan, F., Radic, A., Rehkamper, M., Rouxel, O., Sohrin, Y., Stirling, C., Thompson, C., Vance, D., Xue, Z. and Zhao, Y., (2012): GEOTRACES IC1 (BATS) contamination-prone trace element isotopes Cd, Fe, Pb, Zn, Cu, and Mo intercalibration. Limnology and Oceanography: Methods, 10 (1), pp. 653–665.

Boyle, E.A., Lee, J.-M., Echegoyen, Y., Noble, A., Moos, S., Carrasco, G., Zhao, N., Kayser, R., Zhang, J., Gamo, T., Obata, H. and Norisuye, K., (2014): Anthropogenic lead emissions in the ocean: The evolving global experiment. Oceanography, 27 (1), pp. 69–75.

Bridgestock, L., (2015): Tracing the cycling of Pb and Cd from natural and anthropogenic sources through the troposphere and ocean. Thesis, pp. 1–182.

Bridgestock, L., Rehk mper, M., van de Flierdt, T., Paul, M., Milne, A., Lohan, M.C. and Achterberg, E.P., (2018): The distribution of lead concentrations and isotope compositions in the eastern Tropical Atlantic Ocean. Geochimica et Cosmochimica Acta, 225, pp. 36–51.

Bridgestock, L., van de Flierdt, T., Rehk mper, M., Paul, M., Middag, R., Milne, A., Lohan, M.C., Baker, A.R., Chance, R., Khondoker, R., Strekopytov, S., Humphreys-Williams, E., Achterberg, E.P., Rijkenberg, M.J.A., Gerringa, L.J.A. and De Baar, H.J.W., (2016): Return of naturally sourced Pb to Atlantic surface waters. Nature Communications, 7 (1), pp. 1–12.

Broecker, W.S. and Peng, T.H., (1982): Tracers in the Sea. Columbia University Press, Palisades, NY, pp. 690.

Brzezinski, M. A., Dickson, M.-L., Nelson, D. M. and Sambrotto, R., (2003): Ratios of Si, C and N uptake by microplankton in the Southern Ocean. Deep-Sea Research. II 50, pp. 619–633.

Bull, C.Y. Sen and Sebille, E. van, (2016): Sources, fate, and pathways of Leeuwin Current water in the Indian Ocean and Great Australian Bight: A Lagrangian study in an eddy-

resolving ocean model. Journal of Geophysical Research: Oceans, 121, pp. 1626–1639.

Buttigieg, G.A., Baker, M.E., Ruiz, J. and Bonner Denton, M., (2003): Lead isotope ratio determination for the forensic analysis of military small arms projectiles. Analytical Chemistry, 75 (19), pp. 5022–5029.

Carmack, E.C. and Killworth, P.D., (1978): Formation and interleaving of abyssal water masses off Wilkes Land, Antarctica. Deep-Sea Research, 25 (4), pp. 357–369.

Carter, P., Vance, D., Hillenbrand, C.D., Smith, J.A. and Shoosmith, D.R., (2012): The neodymium isotopic composition of waters masses in the eastern Pacific sector of the Southern Ocean. Geochimica et Cosmochimica Acta, 79, pp. 41–59.

Chase, Z., Anderson, R.F., Fleisher, M.Q. and Kubik, P.W., (2002): The influence of particle composition and particle flux on scavenging of Th, Pa and Be in the ocean. Earth and Planetary Science Letters, 204 (1–2), pp. 215–229.

Chen, M., Boyle, E.A., Lee, J.-M., Nurhati, I., Zurbrick, C.M., Switzer, A.D. and Carrasco, G., (2016): Lead isotope exchange between dissolved and fluvial particulate matter: a laboratory study from the Johor River estuary. Philosophical Transactions of the Royal Society A: Mathematical, Physical and Engineering Sciences, 374, pp. 1–20.

Chien, C., Te, Ho, T.Y., Sanborn, M.E., Yin, Q.Z. and Paytan, A., (2017): Lead concentrations and isotopic compositions in the Western Philippine Sea. Marine Chemistry, 189, pp. 10–16.

Chow, T. J., and Earl, J. L., (1972): Lead isotopes in North American coals. Science, 176 (4034), pp. 510–511.

Conway, T.M., Rosenberg, A.D., Adkins, J.F. and John, S.G., (2013): A new method for precise determination of iron, zinc and cadmium stable isotope ratios in seawater by double-spike mass spectrometry. Analytica Chimica Acta, 793, pp. 44–52.

Craig, H., Krishnas, S., and Somayaju, B.l., (1973), Pb-210-Ra-226 - Radioactive Disequilibrium in Deep-Sea, Earth Planet. Science Letters, 17 (2), 295-305.

Crocket, K.C., Lambelet, M., van de Flierdt, T., Rehk mper, M. and Robinson, L.F., (2014): Measurement of fossil deep-sea coral Nd isotopic compositions and concentrations by TIMS as NdO^+, with evaluation of cleaning protocols. Chemical Geology, 374–375, pp. 128–140.

Cziczo, D. J., Stetzer, O., Worringen, A., Ebert, M., Weinbruch, S., Kamphus, M., Lohmann, U., (2009): Inadvertent climate modification due to anthropogenic lead, Nature Geoscience, 2 (5), 333–336.

De Baar, H.J.W., Bacon, M.P., Brewer, P.G. and Bruland, K.W., (1985): Rare earth elements in the Pacific and Atlantic Oceans. Geochimica et Cosmochimica Acta, 49 (9), pp. 1943–1959.

De Baar, H.J.W. and De Jong, J.T.M., (2001): Distributions, sources and sinks of iron in seawater D. Turner, K. Hunter (Eds.), The Biogeochemistry of Iron in Seawater, IUPAC Book Series on Analytical and Physical Chemistry of Environmental Systems, vol. 7, John Wiley and Sons Ltd., Chichester, pp. 123–253

De Boyer Montegut, C., G. Madec, A. S. Fischer, A. Lazar, and D. Iudicone (2004): Mixed layer depth over the global ocean: An examination of profile data and a profile-based climatology. Journal of Geophysical Research. (109) C12003

De Deckker, P., Norman, M., Goodwin, I.D., Wain, A. and Gingele, F.X., (2010): Lead isotopic evidence for an Australian source of aeolian dust to Antarctica at times over the last 170,000 years. Palaeogeography, Palaeoclimatology, Palaeoecology, 285 (3–4), pp. 205–223.

De Jong, J., Schoemann, V., Lannuzel, D., Croot, P., De Baar, H. and Tison, J., (2012): Natural iron fertilization of the Atlantic sector of the Southern Ocean by continental shelf sources of the Antarctic Peninsula. Journal of Geophysical Research, 117 (G1), pp. 1–25.

Dickin, A.P., (2005): Radiogenic Isotope Geology. Cambridge (Second Edition), pp. 492.

Du, J., Haley, B.A. and Mix, A.C., (2016): Neodymium isotopes in authigenic phases, bottom waters and detrital sediments in the Gulf of Alaska and their implications for paleo-circulation reconstruction. Geochimica et Cosmochimica Acta, 193, pp. 14–35.

Duce, R. A. et al., (1991): The atmospheric input of trace species to the world ocean, Global Biogeochemical Cycles, 5 (3), pp. 193–259.

Dupré, B., Dessert, C., Oliva, P., Goddéris, Y., Viers, J., François, L., Millot, R., Gaillardet, J., (2003): Rivers, chemical weathering and Earth's climate. C. R. Geosci., 335, pp. 1141–1160.

Elderfield, H. and Greaves, M.J., (1982): The rare earth elements in seawater. Nature, 296 (5854), pp. 214–219.

Elderfield, H., Upstill-Goddard, R., Sholkovitz, E.R., (1990): The rare earth elements in rivers, estuaries, and coastal seas and their significance to the composition of ocean waters. Geochimica et Cosmochimica Acta, 54, pp. 971–991.

Flegal, A.R., Maring, H. and Niemeyer, S., (1993): Anthropogenic lead in Antarctic sea water. Nature, 365, pp. 242–244.

Foldvik, A., Gammelsrod, T. and Torreson, T., (1985): Circulation and water masses on the southern Weddell Sea shelf. Oceanonology of the Antarctic Continental Shelf, Antarctic Research Series. American Geophysical Union, Washington, pp. 5–20.

Foster, T.D., (1995): Abyssal water mass formation off the eastern Wilkes land cost of Antarctica. Deep-Sea Research Part I, 42 (4), pp. 501–522.

Foster, T.D., Carmack, E.C., (1976): Frontal zone mixing and Antarctic Bottom Water formation in the southern Weddell Sea. Deep-Sea Research, 23, pp. 301–317.

Freslon, N., Bayon, G., Toucanne, S., Bermell, S., Etoubleau, J., Germain, Y., Bollinger, C., Che, S., Khripounoff, A., Ponzevera, E. and Rouget, M., (2014): Rare earth elements and neodymium isotopes in sedimentary organic matter. Geochimica et Cosmochimica Acta, 140, pp. 177–198.

Fukamachi, Y., Rintoul, S.R., Church, J.A., Aoki, S., Sokolov, S., Rosenberg, M.A. and Wakatsuchi, M., (2010): Strong export of Antarctic Bottom Water east of the Kerguelen plateau. Nature Geoscience, 3 (5), pp. 327–331.

Fukami, Y., Tobita, M., Yokoyama, T., Usui, T. and Moriwaki, R., (2017): Precise isotope analysis of sub-nanogram lead by total evaporation thermal ionization mass spectrometry (TE-TIMS) coupled with a ^{204}Pb-^{207}Pb double spike method. Journal of Analytical Atomic Spectrometry, 32 (4), pp. 848–857.

Galer, S.J.G. and Abouchami, W., (1998): Practical application of lead triple spiking for correction of instrumental mass discrimination. Mineralogical Magazine, 62A (1), pp. 491–492.

Gallon, C., Aggarwal, J. and Flegal, A.R., (2008): Comparison of mass discrimination correction methods and sample introduction systems for the determination of lead isotopic composition using a multicollector inductively coupled plasma mass spectrometer. Analytical Chemistry, 80, pp. 8355–8363.

Gallon, C., Ranville, M. A, Conaway, C.H., Landing, W.M., Buck, C.S., Morton, P.L. and Flegal, A.R., (2011): Asian industrial lead inputs to the North Pacific evidenced by lead concentrations and isotopic compositions in surface waters and aerosols. Environmental science and technology, 45 (23), pp. 9874–82.

Garcia-Solsona, E., Jeandel, C., Labatut, M., Lacan, F., Vance, D., Chavagnac, V. and Pradoux, C., (2014): Rare earth elements and Nd isotopes tracing water mass mixing and particle-seawater interactions in the SE Atlantic. Geochimica et Cosmochimica Acta, 125, pp. 351–372.

Garcia, H.E., Boyer, T.P., Locarnini, R.A., Antonov, J.I., Mishonov, A.V., Baranova, O.K., Zweng, M.M., Reagan, J.R., Johnson, D.R. and Levitus, S., (2013): World ocean atlas 2013. Volume 3, Dissolved oxygen, apparent oxygen utilization, and oxygen saturation.

Gardner, M., Dorling, S., (1995): Artificial neural networks (the multilayer perceptron) - a review of applications in the atmospheric sciences. Atmospheric Environment, 32 (14–15), pp. 2627–2636.

GEOTRACES Science Plan, 2006. S.C.O.R.(*). Baltimore: pp. 79.

German, C.R., Klinkhammer, G.P., Edmond, J.M., Mitra, A., and Elderfield, H. (1990): Hydrothermal scavenging of rare-earth elements in the ocean. Nature 345, pp. 516–518.

Goldstein, S.L. and Hemming, S.R., (2003): Long-lived isotopic tracers in oceanography, paleoceanography, and ice-sheet Dynamics. Treatise on Geochemistry, 6, pp. 453–489.

Goldstein, S.L., Onions, R.K., Hamilton, P.J., (1984): A Sm-Nd isotopic study of atmospheric dusts and particulates from major river systems. Earth and Planetary Science Letters 70, pp. 221–236

Greaves, M.J., Statham, P.J., Elderfield, H., (1994): Rare earth element mobilization from marine atmospheric dust into seawater. Marine Chemistry, 46, pp. 255–260.

Grousset, F. E., Quétel, C. R., Thomas, B., Buat-Ménard, P., Donard, O. F. X., and Bucher, A., (1994): Transient Pb isotopic signatures in the Western European atmosphere. Environmental Science and Technology. 28, pp. 1605–1608.

Gruber, N., Gloor, M., Doney, S.C., Follows, M., Gerber, M., Jacobson, A.R., Joos, F., Lindsay, K., Menemenlis, D., Mouchet, A., Sarmiento, J.L. and Takahashi, T., (2004): Oceanic sources and sinks of atmospheric CO_2. Journal of Geophysical Research, pp. 1–13.

Hagan, M.T. and Menhaj, M.B., (1994): Training feedforward networks with the Marquardt algorithm. Neural Networks. IEEE Transactions, 5 (6), pp. 989–993.

Haley, B.A., Klinkhammer, G.P. and McManus, J., (2004): Rare earth elements in pore waters of marine sediments. Geochimica et Cosmochimica Acta, 68 (6), pp. 1265–1279.

Halicz, L., Lam, J.W. and Mclaren, J.W., (1994): Determination of lead and lead isotope ratios in gasoline by inductively coupled plasma mass spectrometry. Journal of Analytical Atomic Spectrometry, 9 (5), pp. 599–603.

Halliday, A.N., Davidson, J.P., Holden, P., Owen, R.M., Olivarez, A.M., (1992): Metalliferous sediments and the scavenging residence time of Nd near hydrothermal vents. Geophysical Research Letters, 19, pp. 761–764.

Hathorne, E.C., Haley, B., Stichel, T., Grasse, P., Zieringer, M. and Frank, M., (2012): Online preconcentration ICP-MS analysis of rare earth elements in seawater. Geochemistry Geophysics Geosystems, 13 (1), pp. 1–12.

Hathorne, E.C., Stichel, T., Brück, B. and Frank, M., (2015): Rare earth element distribution in the Atlantic sector of the Southern Ocean: The balance between particle scavenging and vertical supply. Marine Chemistry, 177, pp. 157–171.

Hegner, E., Dauelsberg, H.J., Rutgers van der Loeff, M., Jeandel, C. and de Baar, H.J.W., (2007): Nd isotopic constraints on the origin of suspended particles in the Atlantic Sector of the Southern Ocean. Geochemistry, Geophysics, Geosystems, 8, pp. 1–18.

Henderson, G.M., Anderson, R.F., Adkins, J., Andersson, P., Boyle, E.A., Cutter, G., de Baar, H., Eisenhauer, A., Frank, M., Francois, R., Orians, K., Gamo, T., German, C., Jenkins, W., Moffett, J., Jeandel, C., Jickells, T., Krishnaswami, S., Mackey, D., J., (2007): GEOTRACES – An international study of the global marine biogeochemical cycles of trace elements and their isotopes. (CdE) Geochemistry, 67 (2), pp. 85–131.

Herraiz-Borreguero, L. and Rintoul, S.R., (2011a): Subantarctic mode water: Distribution and circulation. Ocean Dynamics, 61 (1), pp. 103–126.

Herraiz-Borreguero, L. and Rintoul, S.R., (2011b): Regional circulation and its impact on upper ocean variability south of Tasmania. Deep-Sea Research Part II: Topical Studies in Oceanography, 58 (21–22), pp. 2071–2081.

Hopper, J.F., Ross, H.B., Sturges, W.T. and Barrie, L.A., (1991): Regional source discrimination of atmospheric aerosols in Europe using the isotopic composition of lead. Tellus B, 43 (1), pp. 45–60.

Hurst, R. W. (2002): Lead isotopes as age-sensitive genetic markers in hydrocarbons. 3. Leaded gasoline, 1923-1990 (ALAS model). Environmental Geosciences, 9 (2), pp. 43–50.

Jackett, D.R. and McDougall, T.J., (1997): A neutral density variable for the world's ocean. Journal of. Physical Oceanography, 27 (2), pp. 237–263.

Jacobsen, S.B. and Wasserburg, G.J., (1980): Sm-Nd isotopic evolution of chondrites. Earth and Planetary Science Letters, 50 (1), pp. 139–155.

Jaffey, A. H., Flynn, K. F., Glendenin, L. E., Bentley, W.C. and Essling, A.M., (1971): Precision measurement of half-lives and specific activities of ^{235}U and ^{238}U. Physical Review, C, 4 (5), pp.1889.

Jeandel, C., (1993): Concentration and isotopic composition of Nd in the South Atlantic Ocean. Earth and Planetary Science Letters, 117 (1993), pp. 581–591.

Jeandel, C., (2016): Overview of the mechanisms that could explain the "Boundary Exchange" at the land-ocean contact. Philosophical Transactions of the Royal Society A: Mathematical, Physical and Engineering Sciences, 374 (2081), pp. 20150287.

Jeandel, C. and Oelkers, E.H., (2015): The influence of terrigenous particulate material dissolution on ocean chemistry and global element cycles. Chemical Geology, 395, pp. 50–66.

Jeandel, C., Arsouze, T., Lacan, F., Techine, P. and Dutay, J., (2007): Isotopic Nd compositions and concentrations of the lithogenic inputs into the ocean: A compilation, with an emphasis on the margins. Chemical Geology, 239 (1–2), pp. 156–164.

Jeandel, C., Bishop, J.K. and Zindler, A., (1995): Exchange of neodymium and its isotopes between seawater and small and large particles in the Sargasso Sea. Geochimica et Cosmochimica Acta, 59 (3), pp. 535–547.

Jeandel, C., Thouron, D. and Fieux, M., (1998): Concentrations and isotopic compositions of neodymium in the eastern Indian Ocean and Indonesian straits. Geochimica et Cosmochimica Acta, 62 (15), pp. 2597–2607.

Jenkins, W. J., (1980): Tritium and He-3 in the Sargasso Sea. Journal of Marine Research, 38 (3), pp. 533–569.

Jo, Y.-H., Dai, M., Zhai, W., Yan, X.-H. and Shang, S., (2012): On the variations of sea surface pCO_2 in the northern South China Sea: A remote sensing based neural network approach. Journal of Geophysical Research, 117 (C08022).

Kelly, A.E., Reuer, M.K., Goodkin, N.F. and Boyle, E.A., (2009): Lead concentrations and isotopes in corals and water near Bermuda, 1780–2000. Earth and Planetary Science Letters, 283 (1–4), pp. 93–100.

Kim, I., Kim, G. and Choy, E.J., (2015): The significant inputs of trace elements and rare earth elements from melting glaciers in Antarctic coastal waters. Polar Research, 1, pp. 1–13.

Klaver, M., Smeets, R.J., Koornneef, J.M., Davies, G.R. and Vroon, P.Z., (2016): Pb isotope analysis of ng size samples by TIMS equipped with a 10^{13} Ω resistor using a ^{207}Pb– ^{204}Pb double spike. Journal of Analytical Atomic Spectrometry, 31 (1), pp. 171–178.

Knowlton, S.W. and Moran, S.B., (2010): Stable Pb isotope ratios in aerosols, precipitation, and size-fractionated particulate matter in the Gulf of Maine, Scotian Shelf, and Labrador Sea. Marine pollution bulletin, 60 (7), pp. 984–999.

Koch-Larrouy, A., Morrow, R., Penduff, T. and Juza, M., (2010): Origin and mechanism of Subantarctic Mode Water formation and transformation in the Southern Indian Ocean. Ocean Dynamics, 60 (3), pp. 563–583.

Komárek, M., Ettler, V., Chrastný, V. and Mihaljevič, M., (2008): Lead isotopes in environmental sciences: A review. Environment International, 34 (4), pp. 562–577.

Lacan, F. and Jeandel, C., (2001): Tracing Papua New Guinea imprint on the central Equatorial Pacific Ocean using neodymium isotopic compositions and rare earth element patterns. Earth and Planetary Science Letters, 186 (3–4), pp. 497–512.

Lacan, F. and Jeandel, C., (2005): Neodymium isotopes as a new tool for quantifying exchange fluxes at the continent-ocean interface. Earth and Planetary Science Letters, 232 (3–4), pp. 245–257.

Lacan, F., Tachikawa, K. and Jeandel, C., (2012): Neodymium isotopic composition of the oceans: A compilation of seawater data. Chemical Geology, 300–301, pp. 177–184.

Lai, X., Norisuye, K., Mikata, M., Minami, T., Bowie, A.R. and Sohrin, Y., (2008): Spatial and temporal distribution of Fe, Ni, Cu and Pb along 140°E in the Southern Ocean during austral summer 2001/02. Marine Chemistry, 111 (3–4), pp. 171–183.

Lambelet, M., van de Flierdt, T., Butler, E.C.V., Bowie, A.R., Rintoul, S.R., Watson, R.J., Remenyi, T., Lannuzel, D., Warner, M., Robinson, L.F., Bostock, H.C. and Bradtmiller, L.I., (2018): The neodymium isotope fingerprint of Adélie coast bottom water. Geophysical Research Letters, 45 (20), pp. 11–247.

Lambelet, M., van de Flierdt, T., Crocket, K., Rehk mper, M., Kreissig, K., Coles, B., Rijkenberg, M.J.A., Gerringa, L.J.A., de Baar, H.J.W. and Steinfeldt, R., (2016): Neodymium isotopic composition and concentration in the western North Atlantic Ocean: results from the GEOTRACES GA02 section. Geochimica et Cosmochimica Acta, 177, pp. 1–29.

Lang, D.C., Bailey, I., Wilson, P.A., Chalk, T.B., Foster, G.L. and Gutjahr, M., (2016): Incursions of southern-sourced water into the deep North Atlantic during late Pliocene glacial intensification. Nature Geoscience, 9 (5), pp. 375–379.

Le Roux, L.J. and Glendenin, L.L., (1963): Half-lives of thorium-232. In Proc. of the National Conference on Nuclear Energy, Pretoria, South Africa, pp. 83–94.

Lee, J.M., Boyle, E.A., Echegoyen-Sanz, Y., Fitzsimmons, J.N., Zhang, R. and Kayser, R.A., (2011): Analysis of trace metals (Cu, Cd, Pb, and Fe) in seawater using single batch nitrilotriacetate resin extraction and isotope dilution inductively coupled plasma mass spectrometry. Analytica Chimica Acta, 686 (1–2), pp. 93–101.

Lee, J.M., Boyle, E.A., Gamo, T., Obata, H., Norisuye, K. and Echegoyen, Y., (2015): Impact of anthropogenic Pb and ocean circulation on the recent distribution of Pb isotopes in the Indian Ocean. Geochimica et Cosmochimica Acta, 170, pp. 126–144.

Li, F., Ginoux, P. and Ramaswamy, V., (2008): Distribution, transport, and deposition of mineral dust in the Southern Ocean and Antarctica: Contribution of major sources. Journal of Geophysical Research Atmospheres, 113 (10), pp. 1–15.

Lippold, J., Gutjahr, M., Blaser, P., Christner, E., de Carvalho Ferreira, M.L., Mulitza, S., Christl, M., Wombacher, F., Böhm, E., Antz, B., Cartapanis, O., Vogel, H. and Jaccard, S.L., (2016): Deep water provenance and dynamics of the (de)glacial Atlantic meridional overturning circulation. Earth and Planetary Science Letters, 445, pp. 68–78.

Locarnini, R.A., Mishonov, A.V., Antonov, J.I., Boyer, T.P., Garcia, H.E., Baranova, O.K., Zweng, M.M., Paver, C.R., Reagan, J.R., Johnson, D.R. and Hamilton, M., (2013): World ocean atlas 2013. Volume 1, Temperature.

Lumpkin, R. and Speer, K., (2007): Global ocean meridional overturning. Journal of Physical Oceanography, 37 (10), pp. 2550–2562.

Makishima, A. and Nakamura, E., (2010): Precise isotopic determination of Hf and Pb at sub-nano gram levels by MC-ICP-MS employing a newly designed sample cone and a pre-amplifier with a 10^{12}ohm register. Journal of Analytical Atomic Spectrometry, 25, pp. 1712–1716.

Makishima, A., Nagender Nath, B. and Nakamura, E., (2007): Precise determination of Pb isotope ratios by simple double spike MC-ICP-MS technique without Tl addition. Journal of Analytical Atomic Spectrometry, 22 (4), pp. 407–410.

Manton, W.I., (1973): Significance of lead isotope composition in blood. Nature, 244 (5412), pp. 165–167.

Marshall, J. and Speer, K., (2012): Closure of the meridional overturning circulation through Southern Ocean upwelling. Nature Geoscience. (5) 3, pp. 171–180.

Martin, J. H., Fitzwater, S. E. and Gordon R. M., (1990): Iron deficiency limits phytoplankton growth in Antarctic waters. Global Biogeochemical Cycles. (4) 1, pp. 5–12.

McCartney, M.S., (1982): The subtropical recirculation of mode waters. Journal of Marine Research, 40, pp. 427–464.

McCartney, M.S. and Donohue, K.A., (2007): A deep cyclonic gyre in the Australian-Antarctic Basin. Progress in Oceanography, 75 (4), pp. 675–750.

Meija, J., Yang, L., Sturgeon, R.E. and Mester, Z., (2010): Certification of natural isotopic abundance inorganic mercury reference material NIMS-1 for absolute isotopic composition and atomic weight. Journal of Analytical Atomic Spectrometry, 25 (3), pp. 384–389.

Minami, T., Konagaya, W., Zheng, L., Takano, S., Sasaki, M., Murata, R., Nakaguchi, Y. and Sohrin, Y., (2015): An off-line automated preconcentration system with ethylenediaminetriacetate chelating resin for the determination of trace metals in seawater by high-resolution inductively coupled plasma mass spectrometry. Analytica Chimica

Acta, 854, pp. 183–190.

Miyazaki, A. and Reimer, R.A., (1993): Determination of lead isotope ratios in port wine by inductively coupled plasma mass spectrometry after pre-treatment by UV-irradiation. Journal of Analytical Atomic Spectrometry, 8, pp. 449–442.

Molina-Kescher, M., Frank, M. and Hathorne, E., (2014): South Pacific dissolved Nd isotope compositions and rare earth element distributions: water mass mixing versus biogeochemical cycling. Geochimica et Cosmochimica Acta, 127, pp. 171–189.

Morrison, A. and Hogg, A., (2012): On the relationship between Southern Ocean overturning and ACC transport. Journal of Physical Oceanography, 43, pp. 142–148.

Munksgaard, N.C., Batterham, G.J. and Parry, D.L., (1998): Lead isotope ratios determined by ICP-MS: Investigation of anthropogenic lead in seawater and sediment from the Gulf of Carpentaria, Australia. Marine Pollution Bulletin, 36 (7), pp. 527–534.

Nakano, H. and Suginohara, N., (2002): Importance of the eastern Indian Ocean for the abyssal Pacific. Journal of Geophysical Research, 107 (12), pp. 1–14.

Ndungu, K., Zurbrick, C.M., Stammerjohn, S., Severmann, S., Sherrell, R.M. and Flegal, A.R., (2016): Lead sources to the Amundsen Sea, West Antarctica. Environmental Science and Technology, 50 (12), pp. 6233–6239.

Noble, A.E., Echegoyen-Sanz, Y., Boyle, E.A., Ohnemus, D.C., Lam, P.J., Kayser, R., Reuer, M., Wu, J. and Smethie, W., (2015): Dynamic variability of dissolved Pb and Pb isotope composition from the U.S. North Atlantic GEOTRACES transect. Deep-Sea Research Part II: Topical Studies in Oceanography, 116, pp. 208–225.

Nriagu, J. O., (1990): The rise and fall of leaded gasoline. Science of the total environment, 92, pp. 13–28

Nriagu, J. O., and Pacyna, J. M., (1988): Quantitative assessment of worldwide contamination of air, water and soils by trace-metals. Nature, 333 (6169), pp. 134-139.

O'Brien, E., (2011): Chronology of leaded gasoline / leaded petrol history. The Lead Education and Abatement Design Group, pp. 1–19.

Orsi, A.H., Johnson, G.C. and Bullister, J.L., (1999): Circulation, mixing, and production of Antarctic Bottom Water. Progress in Oceanography, 43 (1), pp. 55–109.

Orsi, A.H., Whitworth III, T. and Nowlin, W., D., (1995): On the extent and frontal structure of the Antarctic Circumpolar Current. 2 (43), pp. 96–97.

Pacyna, J.M. and Pacyna, E.G., (2001): An assessment of global and regional emissions of trace metals to the atmosphere from anthropogenic sources worldwide. Environmental Reviews, 9 (4), pp. 269–298.

Pardo, P.C., Pérez, F.F., Velo, A. and Gilcoto, M., (2012): Water masses distribution in the Southern Ocean: improvement of an extended OMP (eOMP) analysis. Progress in Oceanography, 103, pp. 92–105.

Patterson, C., (1956): Age of meteorites and the Earth. Geochimica et Cosmochimica Acta, 10, pp. 230–237.

Patterson, C.C. and Settle, D.M., (1976): The reduction of orders of magnitude errors in lead analyses of biological materials and natural waters by evaluating and controlling the extent and sources of industrial lead contamination introduced during sample collecting, handling, and analysis. National Bureau of Standards Special Publication, 1 (422), pp. 321–351.

Paul, M., van de Flierdt, T., Rehk mper, M., Khondoker, R., Weiss, D., Lohan, M.C. and Homoky, W.B., (2015a): Tracing the Agulhas leakage with lead isotopes. Geophysical Research Letters, 42 (20), pp. 8515–8521.

Paul, M., Bridgestock, L.J., Rehk mper, M., van de Flierdt, T. and Weiss, D., (2015b): High-precision measurements of seawater Pb isotope compositions by double spike thermal ionization mass spectrometry. Analytica Chimica Acta, 863, pp. 59–69.

Pearce, C.R., Jones, M.T., Oelkers, E.H., Pradoux, C. and Jeandel, C., (2013): The effect of particulate dissolution on the neodymium (Nd) isotope and rare earth element (REE) composition of seawater. Earth and Planetary Science Letters, 369–370, pp. 138–147.

Piepgras, D.J. and Jacobsen, S.B., (1988): The isotopic composition of neodymium in the North Pacific. Geochimica et Cosmochimica Acta, 52 (6), pp. 1373–1381.

Piepgras, D.J. and Wasserburg, G.J., (1980): Neodymium isotopic variations in seawater. Earth and Planetary Science Letters, 50 (1), pp. 128–138.

Piepgras, D.J. and Wasserburg, G.J., (1982): Isotopic composition of neodymium in waters from the Drake Passage. Science, 217 (4556), pp. 207–214.

Piepgras, D.J. and Wasserburg, G.J., (1987): Rare earth element transport in the western North Atlantic inferred from Nd isotopic observations. Geochimica et Cosmochimica Acta, 51 (5), pp. 1257–1271.

Piepgras, D.J., Wasserburg, G.J. and Dasch, E.J., (1979): The isotopic composition of Nd in different ocean masses. Earth and Planetary Science Letters, 45, pp. 223–236.

Pierce, E.L., Hemming, S.R., Williams, T., van de Flierdt, T., Thomson, S.N., Reiners, P.W., Gehrels, G.E., Brachfeld, S.A. and Goldstein, S.L., (2014): A comparison of detrital U-Pb zircon, $^{40}Ar/^{39}Ar$ hornblende, $^{40}Ar/^{39}Ar$ biotite ages in marine sediments off East Antarctica: Implications for the geology of subglacial terrains and provenance studies. Earth-Science Reviews, 138, pp. 156–178.

Pierce, E.L., Williams, T., Flierdt, T. Van De, Hemming, S.R., Goldstein, S.L. and Brachfeld, S.A., (2011): Characterizing the sediment provenance of East Antarctica's weak underbelly: The Aurora and Wilkes sub-glacial basins. Paleoceanography, 26, pp. 1–18.

Piotrowski, A.M., Banakar, V.K., Scrivner, A.E., Elderfield, H., Galy, A. and Dennis, A., (2009): Indian Ocean circulation and productivity during the last glacial cycle. Earth and Planetary Science Letters, 285 (1–2), pp. 179–189.

Piotrowski, A.M., Galy, A., Nicholl, J.A.L., Roberts, N., Wilson, D.J., Clegg, J.A. and Yu, J., (2012): Reconstructing deglacial North and South Atlantic deep water sourcing using foraminiferal Nd isotopes. Earth and Planetary Science Letters, 357–358, pp. 289–297.

Piotrowski, A.M., Goldstein, S.L., Hemming, S.R., Fairbanks, R.G. and Zylberberg, D.R., (2008): Oscillating glacial northern and southern deep water formation from combined neodymium and carbon isotopes. Earth and Planetary Science Letters, 272 (1–2), pp. 394–405.

Pollard, R. T., Lucas, M. I. and Read, J. F., (2002): Physical controls on biogeochemical zonation in the Southern Ocean. Deep Sea Research II (49) 16, pp. 3289–3305.

Rehk mper, M. and Mezger, K., (2000): Investigation of matrix effects for Pb isotope ratio measurements by multiple collector ICP-MS: verification and application of optimized analytical protocols. Journal of. Analytical At. Spectrometry. 15 (11), pp. 1451–1460.

Reimer, R.A. and Miyazaki, A., (1992): Determination of lead in seawater by inductively coupled plasma atomic emission spectrometry combined with chelating resin preconcentration and hydride generation. Journal of Analytical Atomic Spectrometry, 7 (8), pp. 1239–1242.

Rempfer, J., Stocker, T.F., Joos, F., Dutay, J.-C. and Siddall, M., (2011): Modelling Nd isotopes with a coarse resolution ocean circulation model: Sensitivities to model parameters and source/sink distributions. Geochimica et Cosmochimica Acta, 75 (20), pp. 5927–5950.

Reuer, M.K., Boyle, E.A. and Grant, B.C., (2003): Lead isotope analysis of marine carbonates and seawater by multiple collector ICP-MS. Chemical Geology, 200 (1–2), pp. 137–153.

Rickli, J., Gutjahr, M., Vance, D., Fischer-Gödde, M., Hillenbrand, C.-D. and Kuhn, G., (2014): Neodymium and hafnium boundary contributions to seawater along the West Antarctic continental margin. Earth and Planetary Science Letters, 394, pp. 99–110.

Ridgway, K.R. and Condie, S.A., (2004): The 5500-km-long boundary flow off western and southern Australia. Journal of Geophysical Research C: Oceans, 109 (4), pp. 1–18.

Rigual-Hernández, A.S., Trull, T.W., Bray, S.G., Cortina, A. and Armand, L.K., (2015): Latitudinal and temporal distributions of diatom populations in the pelagic waters of the Subantarctic and Polar Frontal Zones of the Southern Ocean and their role in the biological pump. Biogeosciences Discussions, 12 (11), pp. 8615–8690.

Rintoul, S.R., (1998): On the origin and influence of Adelie Land Bottom Water. Jacobs, S., Weiss, R. (Eds.), Ocean, Ice, and Atmosphere: Interactions at the Antarctic Continental Margin, Antarctic Research Series 75. American Geophysical Union, pp. 151–171.

Rintoul, S.R. and Bullister, J.L., (1999): A late winter hydrographic section from Tasmania to Antarctica. Deep-Sea Research Part I: Oceanographic Research Papers, 46 (8), pp. 1417–1454.

Rintoul, S.R. and England, M.H., (2002): Ekman transport dominates local air–sea fluxes in driving variability of Subantarctic Mode Water. Journal of Physical Oceanography, 32 (5), pp. 1308–1321.

Rintoul, S. R. and Trull T. W., (2001): Seasonal evolution of the mixed layer in the Subantarctic Zone south of Australia. Journal of Geophysical Research, (106) C12, pp. 31447–31462.

Rintoul, S., Hughes, C. and Olbers, D., (2001): The Antarctic Circumpolar Current System

Roberts, N.L., Piotrowski, A.M., McManus, J.F. and Keigwin, L.D., (2010): Synchronous deglacial overturning and water mass source changes. Science, 327, pp. 75–78.

Rosman, K., Chisholm, W., Boutron, C., Candelone, J.-P. and Patterson, C.C., (1994): Anthropogenic lead isotopes in Antarctica. Geophysical Research Letters, 21 (24), pp. 2669–2672.

Rousseau, T.C.C., Sonke, J.E., Chmeleff, J., van Beek, P., Souhaut, M., Boaventura, G., Seyler, P. and Jeandel, C., (2015): Rapid neodymium release to marine waters from lithogenic sediments in the Amazon estuary. Nature Communications, 6 (1), pp. 1–8.

Roy, M., van de Flierdt, T., Hemming, S.R. and Goldstein, S.L., (2007): 40Ar/39Ar ages of hornblende grains and bulk Sm/Nd isotopes of circum-Antarctic glacio-marine sediments: Implications for sediment provenance in the Southern Ocean. Chemical Geology, 244 (3–4), pp. 507–519.

Rudge, J.F., Reynolds, B.C. and Bourdon, B., (2009): The double spike toolbox. Chemical Geology, 265 (3–4), pp. 420–431.

Rusiecka, D., Gledhill, M., Milne, A., Achterberg, E.P., Annett, A.L., Atkinson, S., Birchill, A., Karstensen, J., Lohan, M., Mariez, C. and Middag, R., (2018): Anthropogenic signatures of lead in the Northeast Atlantic. Geophysical Research Letters, 45(6), pp. 2734-2743.

Russell, J. and Dixon, K., (2006): The Southern Hemisphere westerlies in a warming world: Propping open the door to the deep ocean. Journal of Climate, 19, pp. 6382–6390.

Sangster, D.F., Outridge, P.M. and Davis, W.J., (2000): Stable lead isotope characteristics of lead ore deposits of environmental significance. Environmental Reviews, 8 (2), pp. 115–147.

Sarmiento, J. L. and Orr, J. C., (1991): Three-dimensional simulations of the impact of Southern Ocean nutrient depletion on atmospheric CO_2 and ocean chemistry. Limnology and. Oceanography. (36) 8, pp. 1928–1950.

Sarmiento, J.L., Gruber, N., Brzezinski, M.A. and Dunne, J.P., (2004): High-latitude controls of thermocline nutrients and low latitude biological productivity. Nature, 427 (6969), pp. 56–60.

Schaule, B. K., and Patterson, C. C. (1981). Lead concentrations in the northeast Pacific: evidence for global anthropogenic perturbations. Earth and Planetary Science Letters. 8, pp. 97–116

Scher, H.D. and Martin, E.E., (2004): Circulation in the Southern Ocean during the Paleogene inferred from neodymium isotopes. Earth and Planetary Science Letters, 228 (3–4), pp. 391–405.

Schlitzer, R., et al., (2018): The GEOTRACES intermediate data product 2017. Chemical Geology, 493, pp. 210–223.

Settle, D.M., and Patterson, C.C., (1980): Lead in Albacore: Guide to lead pollution in Americans. Science, 207 (4436), pp. 1167–1176.

Shabani, M.B., Akagi, T. and Masuda, A., (1992): Preconcentration of trace rare-earth elements in seawater by complexation with bis(2-ethylhexyl) hydrogen phosphate and 2-ethylhexyl dihydrogen phosphate adsorbed on a C18 cartridge and determination by inductively coupled plasma mass spectrometry. Analytical Chemistry, 64 (7), pp. 737–743.

Shaw, T.J., Raiswell, R., Hexel, C.R., Vu, H.P., Moore, W.S., Dudgeon, R. and Smith, K.L., (2011): Input, composition, and potential impact of terrigenous material from free-drifting icebergs in the Weddell Sea. Deep-Sea Research Part II: Topical Studies in Oceanography, 58 (11–12), pp. 1376–1383.

Shen, G.T. and Boyle, E.A., (1987): Lead in Corals: Reconstruction of Historical Industrial Fluxes to the Surface Ocean. Earth and Planetary Science Letters, 82, pp. 289–304.

Shen, G.T. and Boyle, E.A., (1988): Thermocline ventilation of anthropogenic lead in the western North Atlantic. Journal of Geophysical Research: Oceans, 93 (C12), pp. 15715–15732.

Sholkovitz, E.R., (1995): The aquatic chemistry of rare earth elements in rivers and estuaries. Aquatic Geochemistry, 1, pp. 1–34.

Siddall, M., Khatiwala, S., van de Flierdt, T., Jones, K., Goldstein, S.L., Hemming, S. and Anderson, R.F., (2008): Towards explaining the Nd paradox using reversible scavenging in an ocean general circulation model. Earth and Planetary Science Letters, 274 (3–4), pp. 448–461.

Sohrin, Y. and Bruland, K.W., (2011): Global status of trace elements in the ocean. TrAC - Trends in Analytical Chemistry, 30 (8), pp. 1291–1307.

Sohrin, Y., Urushihara, S., Nakatsuka, S., Kono, T., Higo, E., Minami, T., Norisuye, K. and Umetani, S., (2008): Multielemental determination of GEOTRACES key trace metals in seawater by ICPMS after preconcentration using an ethylenediaminetriacetic acid chelating resin. Analytical Chemistry, 80, pp. 6267–6273.

Sokolov, S. and Rintoul, S.R., (2002): Structure of the Southern Ocean fronts at 140°E. Journal of Marine Systems, 37, pp. 151–184.

Sokolov, S. and Rintoul, S.R., (2007): Multiple jets of the Antarctic Circumpolar Current south of Australia. Journal of Physical Oceanography, 37 (5), pp. 1394–1412.

Sokolov, S. and Rintoul S. R., (2009): Circumpolar structure and distribution of the Antarctic Circumpolar Current fronts: Mean circumpolar paths. Journal of Geophysical Research. (114) C11.

Speer, K., Rintoul, S. and Sloyan, B., (2000): The diabatic Deacon cell*. Journal of Physical Oceanography, pp. 3212–3222.

Speich, S., Blanke, B., de Vries, P., Drijfhout, S., Döös, K., Ganachaud, A. and Marsh, R., (2002): Tasman leakage: A new route in the global ocean conveyor belt. Geophysical Research Letters, 29 (10), pp. 1–4.

Srivastava, A.K., Randive, K.R. and Khare, N., (2013): Mineralogical and geochemical studies of glacial sediments from Schirmacher Oasis, East Antarctica. Quaternary International, 292, pp. 205–216.

Stichel, T., Hartman, A.E., Duggan, B., Goldstein, S.L., Scher, H. and Pahnke, K., (2015): Separating biogeochemical cycling of neodymium from water mass mixing in the Eastern North Atlantic. Earth and Planetary Science Letters, 412, pp. 245–260.

Stichel, T., Frank, M., Rickli, J., Hathorne, E.C., Haley, B.A., Jeandel, C. and Pradoux, C., (2012a): Sources and input mechanisms of hafnium and neodymium in surface waters of the Atlantic sector of the Southern Ocean. Geochim. et Cosmochim. Acta, 94, pp. 22–37.

Stichel, T., Frank, M., Rickli, J. and Haley, B.A., (2012b): The hafnium and neodymium isotope composition of seawater in the Atlantic sector of the Southern Ocean. Earth and Planetary Science Letters, 317–318, pp. 282–294.

Strelow, F.W.E., (1978): Distribution coefficients and anion exchange behavior of some elements in hydrobromic-nitric acid mixtures. Analytical Chemistry, 50 (9), pp. 1359–1361.

Strelow, F.W.E. and Toerien, F. von S., (1966): Separation of lead (II) from bismuth (III), thalium (III), cadmium (II), mercury (II), gold (III), platinum (IV), palladium (II), and other elements by anion exchange chromatography. Analytical Chemistry, 38, pp. 545–548.

Struve, T., Van De Flierdt, T., Robinson, L.F., Bradtmiller, L.I., Hines, S.K., Adkins, J.F., Lambelet, M., Crocket, K.C., Kreissig, K., Coles, B. and Auro, M.E., (2016): Neodymium isotope analyses after combined extraction of actinide and lanthanide elements from seawater and deep-sea coral aragonite. Geochemistry, Geophysics, Geosystems, 17 (1), pp. 232–240.

Sunda, W.G., and Huntsman S.A., (1997): Interrelated influence of iron, light and cell size on marine phytoplankton growth. Nature, 390, pp. 389–392.

Tachikawa, K., Arsouze, T., Bayon, G., Bory, A., Colin, C., Dutay, J.C., Frank, N., Giraud, X., Gourlan, A.T., Jeandel, C., Lacan, F., Meynadier, L., Montagna, P., Piotrowski, A.M., Plancherel, Y., Pucéat, E., Roy-Barman, M. and Waelbroeck, C., (2017): The large-scale evolution of neodymium isotopic composition in the global modern and Holocene ocean revealed from seawater and archive data. Chemical Geology, 457, pp. 131–148.

Tachikawa, K., Athias, V. and Jeandel, C., 2003. Neodymium budget in the modern ocean and paleo-oceanographic implications. Journal of Geophysical Research: Oceans, 108(C8).

Tachikawa, K., Jeandel, C. and Dupre, B., (1997): Distribution of rare earth elements and neodymium isotopes in settling particulate material of the tropical Atlantic Ocean (EUMELI site). Deep - Sea Research Part I - Oceanographic Research Papers, 44 (11), pp. 1769–1792.

Tachikawa, K., Jeandel, C., Roy-Barman, M., (1999): A new approach to the Nd residence time in the ocean: the role of atmospheric inputs. Earth and Planetary Science Letters, 170: pp. 433–446.

Tagliabue, A., Bopp, L. and Aumont, O., (2009): Evaluating the importance of atmospheric and sedimentary iron sources to Southern Ocean biogeochemistry, 36, pp. 1–5.

Tagliabue, A., Bopp, L., Dutay, J.-C., Bowie, A.R., Chever, F., Jean-Baptiste, P., Bucciarelli, E., Lannuzel, D., Remenyi, T., Sarthou, G., Aumont, O., Gehlen, M., Jeandel C., (2010): Hydrothermal contribution to the oceanic dissolved iron inventory. Nature Geoscience, 14, pp. 1-5,

Talley, L.D., (2013): Closure of the global overturning circulation through the Indian, Pacific, and southern oceans. Oceanography, 26 (1), pp. 80–97.

Tamsitt, V., Talley, L.D. and Mazloff, M.R., (2019): A deep eastern boundary current carrying Indian Deep Water south of Australia. Journal of Geophysical Research: Oceans, 124 (3), pp. 2218–2238.

Tanaka, T., Togashi, S., Kamioka, H., Amakawa, H., Kagami, H., Hamamoto, T., Yuhara, M., Orihashi, Y., Yoneda, S., Shimizu, H., Kunimaru, T., Takahashi, K., Yanagi, T., Nakano, T., Fujimaki, H., Shinjo, R., Asahara, Y., Tanimizu, M. and Dragusanu, C., (2000): JNdi-1: A neodymium isotopic reference in consistency with LaJolla neodymium. Chemical Geology, 168 (3–4), pp. 279–281.

Taylor, R.N., Ishizuka, O., Michalik, A., Milton, J.A. and Croudace, I.W., (2015): Evaluating the precision of Pb isotope measurement by mass spectrometry. Journal of Analytical Atomic Spectrometry, 30 (1), pp. 198–213.

Thirlwall, M.F., (2002): Multicollector ICP-MS analysis of Pb isotopes using a ^{207}Pb-^{204}Pb double spike demonstrates up to 400 ppm/amu systematic errors in TI-normalization. Chemical Geology, 184 (3–4), pp. 255–279.

Townsend, A.T. and Seen, A.J., (2012): Historical lead isotope record of a sediment core from the Derwent River (Tasmania, Australia): A multiple source environment. Science of the Total Environment, 424, pp. 153–161.

Townsend, A.T., Yu, Z., McGoldrick, P. and Hutton, J.A., (1998): Precise lead isotope ratios in Australian galena samples by high resolution inductively coupled plasma mass spectrometry. Journal of Analytical Atomic Spectrometry, 13 (8), pp. 809–813.

Trenberth, K. E., Large, W. G., and Olson, J. G., (1990): The mean annual cycle in global ocean wind stress. Journal of Physical Oceanography. (20) 11, pp. 1742–1760.

Vallelonga, P., Gabrielli, P., Balliana, E., Wegner, A., Delmonte, B., Turetta, C., Burton, G., Vanhaecke, F., Rosman, K.J.R., Hong, S. and Boutron, C.F., (2010): Lead isotopic compositions in the EPICA Dome C ice core and Southern Hemisphere Potential Source Areas. Quaternary Science Reviews, 29 (1-2), pp. 247–255.

Vallelonga, P., Van de Velde, K., Candelone, J.P., Morgan, V.I., Boutron, C.F. and Rosman, K.J.R., (2002): The lead pollution history of Law Dome, Antarctica, from isotopic measurements on ice cores: 1500 AD to 1989 AD. Earth and Planetary Science Letters, 204 (1–2), pp. 291–306.

van de Flierdt, T., Frank, M., Lee, D.-C., Halliday, A.N., Reynolds, B.C., Hein, J.R. (2004): New constraints on the sources and behavior of neodymium and hafnium in seawater from Pacific Ocean ferromanganese crusts. Geochimica et Cosmochimica Acta, 68(19), pp. 3827–3843.

van de Flierdt, T., Goldstein, S.L., Hemming, S.R., Roy, M., Frank, M. and Halliday, A.N., (2007): Global neodymium–hafnium isotope systematics — revisited. Earth and Planetary Science Letters, 259 (3–4), pp. 432–441.

van de Flierdt, T., Griffiths, A.M., Lambelet, M., Little, S.H., Stichel, T. and Wilson, D.J., (2016): Neodymium in the oceans: a global database, a regional comparison and implications for palaeoceanographic research. Philosophical Transactions of the Royal Society A: Mathematical, Physical and Engineering Sciences, 374 (2081), pp. 20150293.

van de Flierdt, T., Pahnke, K., Amakawa, H., Andersson, P., Basak, C., Coles, B., Colin, C., Crocket, K., Frank, M. and Frank, N., (2012): GEOTRACES intercalibration of neodymium isotopes and rare earth element concentrations in seawater and suspended particles. Part 1: reproducibility of results for the international intercomparison. Limnology and Oceanography: Methods, 10, pp. 234–251.

Vassileva, E. and Wysocka, I., (2016): Development of procedure for measurement of Pb isotope ratios in seawater by application of seaFAST sample pre-treatment system and SF ICP-MS. Spectrochimica Acta - Part B Atomic Spectroscopy, 126, pp. 93–100.

Velo, A., Pérez, F.F., Tanhua, T., Gilcoto, M., Ríos, A.F. and Key, R.M., (2013): Total alkalinity estimation using MLR and neural network techniques. Journal of Marine Systems, 111–112, pp. 11–18.

Véron, A., Church, T.M., and Flegal, A., (1998): Lead isotopes in the western North Atlantic: transient tracers of pollutant lead inputs. Environmental research, 111 (78), pp. 104–111.

Véron, A.J., Church, T.M., Flegal, A.R., Patterson, C.C. and Erel, Y., (1993): Response of lead cycling in the surface Sargasso Sea to changes in tropospheric input. Journal of Geophysical Research: Oceans, 98 (C10), pp. 18269–18276.

Véron, A. J., Church, T. M., Patterson, C. C., and Flegal, A. R., (1994). Use of stable lead isotopes to characterize the sources of anthropogenic lead in North Atlantic surface waters. Geochimica et Cosmochimica Acta, 58 (15), pp. 3199–3206.

von Blanckenburg F., (1999): Tracing past ocean circulation? Science, 286, pp. 1862–1863.

Walter, H.J., Van der Loeff, M.R. and Hoeltzen, H., (1997): Enhanced scavenging of ^{231}Pa relative to ^{230}Th in the South Atlantic south of the Polar Front: Implications for the use of the ^{231}Pa/^{230}Th ratio as a paleoproductivity proxy. Earth and Planetary Science Letters, 149(1-4), pp. 85–100.

Weiss, D., Boyle, E. A., Wu, J., Chavagnac, V., Michel, A., and Reuer, M. K. (2003): Spatial and temporal evolution of lead isotope ratios in the North Atlantic Ocean between 1981 and 1989. Journal of Geophysical Research, 108 (C10), pp. 3306.

Westerlund, S. and Ohman, P., (1991): Cadmium, copper, cobalt, nickel, lead, and zinc in the water column of the Weddell Sea, Antarctica. Geochimica et Cosmochimica Acta, 55, pp. 2127–2146.

White, W.M., (2013): Geochemistry. John Wiley and Sons.

Whitworth III, T., Orsi, A.H., Kim, S.-J., Nowlin Jr., W.D., (1998): Water masses and mixing near the Antarctic Slope Front. In: Jacobs, S.S., Weiss, R.F. (Eds.), Ocean, Ice, and Atmosphere: Interactions at the Antarctic Continental Margin, Antarctic Research Series. American Geophysical Union, Washington, pp. 1–27.

Williams, G.D., Aoki, S., Jacobs, S.S., Rintoul, S.R., Tamura, T. and Bindoff, N.L., (2010): Antarctic Bottom Water from the Adélie and George V Land coast, East Antarctica (140–149°E). Journal of Geophysical Research, 115, pp. 1–29.

Wong, P.S., Bindoff, N.L., Forbes, A., (1998): Ocean-ice shelf interaction and possible bottom water formation in Prydz Bay, Antarctica. In: Jacobs, S., Weiss, R. (Eds.), Ocean, Ice, and Atmosphere: Interactions at the Antarctic Continental Margin, Antarctic Research Series 75. American Geophysical Union, Washington, pp. 173–187.

Worthington, L.V., (1981): The water masses of the world ocean: some results of a fine-scale census. Warren, B.A., Wunsch, C. (Eds.), Evolution of Physical Oceanography: Scientific Surveys in Honor of Henry Stommel. MIT Press, Cambridge, MA, pp. 42–69.

Wu, J., and Boyle, E. A. (1997a): Lead in the western North Atlantic Ocean: Completed response to leaded gasoline phaseout. Geochimica et Cosmochimica Acta, 61(15), pp. 3279–3283.

Wu, J. and Boyle, E.A., (1997b): Low blank preconcentration technique for the determination of lead, copper, and cadmium in small-volume seawater samples by isotope dilution ICPMS. Analytical Chemistry, 69 (13), pp. 2464–2470.

Wu, J., Boyle, E.A., Sunda, W. and Wen, L.-S., (2001): Soluble and colloidal iron in the oligotrophic North Atlantic and North Pacific. Science (293) 5531, pp. 847–849.

Wu, J., Rember, R., Jin, M., Boyle, E. A. and Flegal, A. R., (2010): Isotopic evidence for the source of lead in the North Pacific abyssal water. Geochimica et Cosmochimica Acta, 74 (16), pp. 4629–4638.

Zhang, Y., Lacan, F. and Jeandel, C.Ã., (2008): Dissolved rare earth elements tracing lithogenic inputs over the Kerguelen Plateau (Southern Ocean). Deep Sea Research Part II, 55, pp. 638–652.

Zurbrick, C. M., Boyle, E. A., Kayser, R. J., Reuer, M. K., Wu, J., Planquette, H., Shelley, R., Boutorh, J., Cheize, M., Contreira, L., Menzel Barraqueta, J-L., Lacan, F., and Sarthou, G., (2018). Dissolved Pb and Pb isotopes in the North Atlantic from the GEOVIDE transect (GEOTRACES GA-01) and their decadal evolution. Biogeosciences, 15, pp. 4995–5014.

Zurbrick, C.M., Gallon, C. and Flegal, A.R., (2013): A new method for stable lead isotope extraction from seawater. Analytica Chimica Acta, 800, pp. 29–35.

Zurbrick, C.M., Gallon, C. and Flegal, A.R., (2017): Historic and industrial lead within the Northwest Pacific Ocean evidenced by lead isotopes in seawater. Environmental Science and Technology, 51 (3), pp. 1203–1212.

Zweng, M.M, J.R. Reagan, J.I. Antonov, R.A. Locarnini, A.V. Mishonov, T.P. Boyer, H.E. Garcia, O.K. Baranova, D.R. Johnson, Seidov, M.M.B., (2013): World Ocean Atlas 2013, Volume 2: Salinity. S. Levitus, Ed., A. Mishonov Technical Ed.; NOAA Atlas NESDIS, 74, p. 39 pp.

Appendices

Appendix 1: MATLAB code for Pb double-spike correction on MC-ICP-MS

Appendix 1 details the MATLAB code for the Pb double-spike correction protocol and the appropriate sub-functions that was used in Chapter 3 and 4. The code follows MATLAB syntax with the green lines following the "%" symbol are non-executable code and are notes explaining the process of the code.

----
constants.m

```
function [const] = constants()

% Define constants for ID and IC double spike calculation:
% 1. Isotope masses (mass values taken from: physics.nist.gov);
% 2. Reference isotopic ratios (Gallon et al., 2008; Meija et al., 2010)
% 3. Double Pb spike (207-204) spike (a) ratios; (b) atomic weights; and (c) concentrations
% 4. Natural Pb (arbitrary for ID) (a) ratios and (b) atomic weights
% 5. NIST 981 Pb isotope reference values (Galer et al., 1998)

% 1. Atomic masses
const.masses.M201 = 200.97030284; const.masses.M202 = 201.97064340; % Hg
const.masses.M203 = 202.97234460; const.masses.M205 = 204.97442780; % Tl
const.masses.M204 = 203.9730440; const.masses.M206 = 205.9744657; % Pb
const.masses.M207 = 206.9758973; const.masses.M208 = 207.9766525;
const.masses.Pb = 207.2169080;

% 2. Reference ratios
const.ref_ratios.Hg_41 = 0.51769; const.ref_ratios.Hg_42 = 0.22923; % Hg
const.ref_ratios.Tl_53 = 2.38880; % Tl
const.ref_ratios.Pb_86 = 2.16771; % Pb

% 3. (a) Double spike isotope ratios (Paul et al., 2015; excel macro)
const.spike_ratios.T1 = 0.00239806067622312; % 206Pb/204Pb
const.spike_ratios.T2 = 1.03180795106693; % 207Pb/204Pb
const.spike_ratios.T3 = 0.00820091662229567; % 208Pb/204Pb
const.spike_ratios.P1 = log(const.masses.M206 / const.masses.M204); % 206Pb/204Pb
const.spike_ratios.P2 = log(const.masses.M207 / const.masses.M204); % 207Pb/204Pb
const.spike_ratios.P3 = log(const.masses.M208 / const.masses.M204); % 208Pb/204Pb
```

```
const.spike_ratios.Pb207_Pb206 = const.spike_ratios.T2 / const.spike_ratios.T1;
const.spike_ratios.Pb208_Pb206 = const.spike_ratios.T3 / const.spike_ratios.T1;
const.spike_ratios.Pb204_Pb207 = 1 / const.spike_ratios.T2;
const.spike_ratios.Pb206_Pb207 = 1 / const.spike_ratios.Pb207_Pb206;
const.spike_ratios.Pb208_Pb207 = const.spike_ratios.Pb208_Pb206 * const.spike_ratios.Pb206_Pb207;
const.spike_ratios.tPb_Pb207 = const.spike_ratios.Pb204_Pb207 +...
   const.spike_ratios.Pb206_Pb207 + const.spike_ratios.Pb208_Pb207 + 1;

% 3. (b) Double spike atomic weights
const.spike_wt.fPb207 = 1 / const.spike_ratios.tPb_Pb207;
const.spike_wt.fPb204 = const.spike_wt.fPb207 * const.spike_ratios.Pb204_Pb207;
const.spike_wt.fPb206 = const.spike_wt.fPb207 * const.spike_ratios.Pb206_Pb207;
const.spike_wt.fPb208 = const.spike_wt.fPb207 * const.spike_ratios.Pb208_Pb207;
const.spike_wt.Pb = (const.spike_wt.fPb204 * const.masses.M204) + ...
   (const.spike_wt.fPb206 * const.masses.M206) + (const.spike_wt.fPb207 * const.masses.M207) +...
   (const.spike_wt.fPb208 * const.masses.M208);

% 3. (c) Double spike isotope concs (nmol/g)
const.spike_conc.Pb = 10.4131818612738; % [Pb] ~ 10 ppb
const.spike_conc.tPb = const.spike_conc.Pb / const.spike_wt.Pb;
const.spike_conc.Pb204 = const.spike_conc.tPb * const.spike_wt.fPb204;
const.spike_conc.Pb206 = const.spike_conc.tPb * const.spike_wt.fPb206;
const.spike_conc.Pb207 = const.spike_conc.tPb * const.spike_wt.fPb207;
const.spike_conc.Pb208 = const.spike_conc.tPb * const.spike_wt.fPb208;

% 4. (a) Natural ratios (ID calculation; Paul et al., 2015)
const.nat_ratios.Pb206_Pb204 = 18.5219588141006;
const.nat_ratios.Pb207_Pb204 = 15.6725849700924;
const.nat_ratios.Pb208_Pb204 = 38.7250230036549;
const.nat_ratios.Pb204_Pb207 = 1 / const.nat_ratios.Pb207_Pb204;
const.nat_ratios.Pb206_Pb207 = const.nat_ratios.Pb206_Pb204 / const.nat_ratios.Pb207_Pb204;
const.nat_ratios.Pb208_Pb207 = const.nat_ratios.Pb208_Pb204 / const.nat_ratios.Pb207_Pb204;

% 4. (b) Natural atomic weights
const.nat_wt.tPb_Pb207 = const.nat_ratios.Pb204_Pb207 + const.nat_ratios.Pb206_Pb207 +...
   const.nat_ratios.Pb208_Pb207 + 1;
const.nat_wt.fPb207 = 1 / const.nat_wt.tPb_Pb207;
const.nat_wt.fPb204 = const.nat_wt.fPb207 * const.nat_ratios.Pb204_Pb207;
const.nat_wt.fPb206 = const.nat_wt.fPb207 * const.nat_ratios.Pb206_Pb207;
const.nat_wt.fPb208 = const.nat_wt.fPb207 * const.nat_ratios.Pb208_Pb207;
const.nat_wt.Pb = (const.nat_wt.fPb204 * const.masses.M204) + ...
(const.nat_wt.fPb206 * const.masses.M206) + (const.nat_wt.fPb207 * const.masses.M207) +...
(const.nat_wt.fPb208 * const.masses.M208);

% 5. Reference Pb isotopic values (Galer et al., 1998)
const.galer.Pb207_Pb206 = 0.91475;
const.galer.Pb208_Pb206 = 2.16770;
const.galer.Pb206_Pb204 = 16.9405;
const.galer.Pb207_Pb204 = 15.4963;
const.galer.Pb208_Pb204 = 36.7219;

end
```

---
nonlinear.m

```
function [f] = nonlinear(lamda,alpha,beta,T1,n1...,
          P1,m1,T2,n2,P2,m2,T3,n3,P3,m3)

% System of 3 non-linear equations to solve for lamda, alpha and
% beta variables for 206, 207 and 208 Pb ratios

f1 = lamda * T1 + (1 - lamda) * n1 * exp(- alpha * P1)- m1 * exp(- beta * P1);

f2 = lamda * T2 + (1 - lamda) * n2 * exp(- alpha * P2)- m2 * exp(- beta * P2);

f3 = lamda * T3 + (1 - lamda) * n3 * exp(- alpha * P3)- m3 * exp(- beta * P3);

f = [f1;f2;f3];

end
```

---
jacobian.m

```
function [J] = jacobian(alpha,beta,T1,n1,P1,m1,T2,n2,P2,m2,T3,n3,P3,m3)

% Evaluates the Jacobian of a 3x3 system of non-linear equations to solve
% alpha, beta and lamda for 204Pb ratios

J(1,1) = T1 - n1 * exp(- alpha * P1) * (1 + alpha * P1);
J(1,2) = - n1 * P1 * exp(- alpha * P1);
J(1,3) = m1 * P1 * exp(- beta * P1);

J(2,1) = T2 - n2 * exp(- alpha * P2) * (1 + alpha * P2);
J(2,2) = - n2 * P2 * exp(- alpha * P2);
J(2,3) = m2 * P2 * exp(- beta * P2);

J(3,1) = T3 - n3 * exp(- alpha * P3) * (1 + alpha * P3);
J(3,2) = - n3 * P3 * exp(- alpha * P3);
J(3,3) = m3 * P3 * exp(- beta * P3);

end
```

---

newtonm.m

```
function [xn,yn] = newtonm(x0,J0,y0,T1,n1,P1,m1,T2,n2,P2,m2,T3,n3,P3,m3)

% Newton-Raphson method applied to a system of non-linear equations f(x) = 0,
% given the jacobian function J, with J = del(f1,f2,...,fn)/del(x1,x2,...,xn),
% x = [x1;x2;...;xn], f = [f1;f2;...;fn] and x0 is an initial solution

n = 1000; % set number of iterations n to 1000

while (n > 0)

   xn = x0 - inv(J0) * y0;

   yn(1,1) = xn(1) * T1 + (1 - xn(1)) * n1 * exp(- xn(2) * P1)- m1 * exp(- xn(3) * P1);

   yn(2,1) = xn(1) * T2 + (1 - xn(1)) * n2 * exp(- xn(2) * P2)- m2 * exp(- xn(3) * P2);

   yn(3,1) = xn(1) * T3 + (1 - xn(1)) * n3 * exp(- xn(2) * P3)- m3 * exp(- xn(3) * P3);

    x0 = xn;
    y0 = yn;
    n = n - 1;

end

end
```

Pb_DS.m

```
%% Pb isotope double-spike data reduction for MC-ICP-MS (new generation Nu)

% This script:

% A. reduces the unspike and mix raw .txt files produced by the new generation Nu
% B. performs Tl normalisation and double-spike inversion calculation for Pb isotope composition
% C. corrects data according to published standard values (Galer et al., 1998)
% D. calculates true concentration values using double-spike isotope compositions
% E. calculates total and measured Pb (and analytical yields)
% F. exports results file (.xlsx)

% For the following inputs:

% 1. mix folder containing mix data files (.txt)
% 2. unspike folder containing mix data files (.txt)
% 3. desired results output file name
% 4. standard name
% 5. sample mass, spike mass and [Pb] ID file (.xlsx)
% 6. blank names (IC and ID) or blank average value (ID) for [Pb] blank correction
```

```
% Instructions and notes:

% (1) Five mathematical functions are required to run this script:
% constants.m, Tl_opt.m, nonlinear.m, jacobian.m and newtonm.m - make these accessible
% to MATLAB by adding their folder to the current folder directory
% (2) Set the MATLAB directory (pwd) to the location of the unspike and mix
% folders which contain the raw .csv files - i.e., on the current folder
% window --> right click on the directory (e.g., desktop) > add to path >
% selected folder and subfolders
% (3) Define the unspike and mix folder names to allow MATLAB to identify
% the raw .csv data files - (e.g., mix_folder = ('my folder');)
% (4) Define the file output name - (e.g., results_output = ('my sample');)
% which will be saved in the same directory as the input folders
% (5) Define standards names during run (e.g., standard_name = ('my standard');)
% (6) Define the masses input spreadsheet name (e.g., masses = readtable('my_masses.xlsx');)
% (7) Press the play/run button above under the editor tab

% N.B., the data reduction loops through all the raw data runs (blocks) in
% the folders - there must be an equal number of unspike and mix raw files
% N.B., the data reduction sheet ONLY works when the cup configuration is
% set with 205Tl as the axial mass (204Pb on L1 with the 10^12 bin)

% Written by Alex Griffiths, Mark Rehkamper, Tina van de Flierdt and Barry Coles
% Imperial College London, ESE MAGIC Group
% (10/10/2017)

% ********************************************************************************

% 1-3. INPUT folder names (mix and unspike) and output file name
mix_folder = ('xxx'); % input mix folder name
unspike_folder = ('xxx'); % input unspike folder name
results_output = ('xxx'); % input results file name

% 4. INPUT sample masses, spike masses and Pb ID ratios
masses = readtable('xxx.xlsx'); % input masses file name

% 5. INPUT standard names for identification
standard_name = {'Pb 1 ppb Tl 3 ppb - US' 'Pb 2 ppb Tl 6 ppb - US' 'Pb 3 ppb Tl 9 ppb - US'...
    'Pb 5 ppb Tl 15 ppb - US' 'Pb 10 ppb Tl 30 ppb - US'}; % standard names

% 6. INPUT blank names or blank average value for batch or 'moving average' blank correction
blank_name_IC = {'xxx'};
blank_IC_pg = xx.x;

blank_name_ID = {'xxx'};
blank_ID_pg = xx.x;

% ********************************************************************************

% define constants: load constant variables
[const] = constants();

% Find best 205Tl203Tl ratio to use for Tl normalisation

% direct MATLAB to mix/ spike folders and allow MATLAB to read raw data files
mix_Dir = fullfile(pwd,mix_folder,'*.txt');
mix_files = dir(mix_Dir);
unspike_Dir = fullfile(pwd,unspike_folder,'*.txt');
```

```
unspike_files = dir(unspike_Dir);

% use loop to find NIST standards in unspike folders
for k = 1:length(unspike_files)

    % open raw mass spec txt data files for mix and unspike
    raw_unspikeFile = fopen(unspike_files(k).name);
    sample_IDFile = fopen(unspike_files(k).name);

    % extract data for mix and unspike
    raw_unspike = textscan(raw_unspikeFile,repmat('%s',1,39),'HeaderLines',13,...
    'delimiter',',');
    samplename_ID = textscan(sample_IDFile,repmat('%s',1,39),'HeaderLines',11,...
    'delimiter',',');

    % close raw .csv data files for mix and unspike
    fclose(raw_unspikeFile);
    fclose(sample_IDFile);

    % Extract sample name
    sample_name = erase(cellstr(samplename_ID{1,1}{2,1}),...
        "Sample Name is   ");

    % Use sample name to extract NIST standards only
    if  contains(sample_name,standard_name)

    % unique standard identifier during run
    nist_ID = strcat('NIST',num2str(k));

    % standard structure for names, beams and ratios
    standards.sample_name.(nist_ID) = erase(cellstr(samplename_ID{1,1}{2,1}),...
        "Sample Name is   ");

    % calculate baseline corrected data for unspiked - group in raw_beam struct
    standards.raw_beam.Pb208.(nist_ID) = mean(str2double(raw_unspike{:,25}) -
str2double(raw_unspike{:,8}));
    standards.raw_beam.Pb207.(nist_ID) = mean(str2double(raw_unspike{:,26}) -
str2double(raw_unspike{:,9}));
    standards.raw_beam.Pb206.(nist_ID) = mean(str2double(raw_unspike{:,27}) -
str2double(raw_unspike{:,10}));
    standards.raw_beam.PbHg204.(nist_ID) = mean(str2double(raw_unspike{:,29}) -
str2double(raw_unspike{:,12}));
    standards.raw_beam.Tl205.(nist_ID) = mean(str2double(raw_unspike{:,28}) -
str2double(raw_unspike{:,11}));
    standards.raw_beam.Tl203.(nist_ID) = mean(str2double(raw_unspike{:,30}) -
str2double(raw_unspike{:,13}));
    standards.raw_beam.Hg202.(nist_ID) = mean(str2double(raw_unspike{:,31}) -
str2double(raw_unspike{:,14}));
    standards.raw_beam.Hg201.(nist_ID) = mean(str2double(raw_unspike{:,32}) -
str2double(raw_unspike{:,15}));
    standards.raw_beam.total_Tl_beam.(nist_ID) = standards.raw_beam.Tl205.(nist_ID) +
standards.raw_beam.Tl203.(nist_ID);

    % calculate corrected ratios for 204 unspiked -> 204Pb for 204Hg with 202Hg
    standards.corr_beam.Hg204_2.(nist_ID) = standards.raw_beam.Hg202.(nist_ID) * const.ref_ratios.Hg_42;
    corr_beam.Pb204_2.(nist_ID) = standards.raw_beam.PbHg204.(nist_ID) -
standards.corr_beam.Hg204_2.(nist_ID);
```

```
    % calculate 204Hg/204PbHg from 202Hg
    standards.raw_ratios.Hg204_PbHg204.(nist_ID) = standards.corr_beam.Hg204_2.(nist_ID) ./...
        standards.raw_beam.PbHg204.(nist_ID);

    % calculate Pb raw ratios
    standards.raw_ratios.Pb207_Pb206.(nist_ID) = standards.raw_beam.Pb207.(nist_ID) ./
standards.raw_beam.Pb206.(nist_ID);
    standards.raw_ratios.Pb208_Pb206.(nist_ID) = standards.raw_beam.Pb208.(nist_ID) ./
standards.raw_beam.Pb206.(nist_ID);
    standards.raw_ratios.Pb208_Pb207.(nist_ID) = standards.raw_beam.Pb208.(nist_ID) ./
standards.raw_beam.Pb207.(nist_ID);
    standards.raw_ratios.Pb206_Pb204_2.(nist_ID) = standards.raw_beam.Pb206.(nist_ID) ./
corr_beam.Pb204_2.(nist_ID);
    standards.raw_ratios.Pb207_Pb204_2.(nist_ID) = standards.raw_beam.Pb207.(nist_ID) ./
corr_beam.Pb204_2.(nist_ID);
    standards.raw_ratios.Pb208_Pb204_2.(nist_ID) = standards.raw_beam.Pb208.(nist_ID) ./
corr_beam.Pb204_2.(nist_ID);
    standards.raw_ratios.Pb206_PbHg204.(nist_ID) = standards.raw_beam.Pb206.(nist_ID) ./
standards.raw_beam.PbHg204.(nist_ID);
    standards.raw_ratios.Pb207_PbHg204.(nist_ID) = standards.raw_beam.Pb207.(nist_ID) ./
standards.raw_beam.PbHg204.(nist_ID);
    standards.raw_ratios.Pb208_PbHg204.(nist_ID) = standards.raw_beam.Pb208.(nist_ID) ./
standards.raw_beam.PbHg204.(nist_ID);
    standards.raw_ratios.Hg202_Pb206.(nist_ID) = standards.raw_beam.Hg202.(nist_ID) ./
standards.raw_beam.Pb206.(nist_ID);
    standards.raw_ratios.Tl205_Tl203.(nist_ID) = standards.raw_beam.Tl205.(nist_ID) ./
standards.raw_beam.Tl203.(nist_ID);

    % starting value for 205Tl/203Tl (Gallon et al., (2008))
    standards.Tl205_203_0 = 2.38888;

    % optimisation solver to find best 205Tl/203Tl ratios
    [standards.Tl205_203_opt.(nist_ID),~] = fsolve(@(z) Tl_opt(standards.raw_ratios.Pb207_Pb206.(nist_ID),...
        standards.raw_ratios.Pb208_Pb206.(nist_ID), standards.raw_ratios.Pb206_Pb204_2.(nist_ID),...
        standards.raw_ratios.Pb207_Pb204_2.(nist_ID), standards.raw_ratios.Pb208_Pb204_2.(nist_ID),...
        standards.raw_ratios.Tl205_Tl203.(nist_ID), z), standards.Tl205_203_0);

    end

end

% create standards summary table with calculated 205/203 Tl ratio

% extract standards into specific arrays
standards.ID = struct2array(standards.sample_name)';
standards.Tl_opt = struct2array(standards.Tl205_203_opt)';
standards.Tl_beam = struct2array(standards.raw_beam.total_Tl_beam)';

% find unique standard names
NIST_names = unique(standards.ID);

Tl_summary = table();

for i = 1:length(NIST_names)

index = contains(standards.ID, NIST_names(i));
Tl_summary(i,1) = cell2table(NIST_names(i,1));
Tl_summary(i,2) = array2table(mean(standards.Tl_opt(index,1)));
```

```
Tl_summary(i,3) = array2table(mean(standards.Tl_beam(index,1)));

Tl_summary.Properties.VariableNames = {'NIST','Tl205_203','Tl_beam_V'};

end

clc
clear k NIST_names nist_ID

% A. Extract data and process for Tl normalisation

% pre-allocate sample name for structure
Date = cell(length(mix_files),1);
Sample_Name = cell(length(mix_files),1);

% use loop to open raw data files sequentially in mix and unspike folders
for k = 1:length(mix_files)

    % open raw mass spec txt data files for mix and unspike
    raw_mixFile = fopen(mix_files(k).name);
    raw_unspikeFile = fopen(unspike_files(k).name);
    sample_IDFile = fopen(unspike_files(k).name);

    % extract data for mix and unspike
    raw_mix = textscan(raw_mixFile,repmat('%s',1,39),'HeaderLines',13,...
    'delimiter',',');
    raw_unspike = textscan(raw_unspikeFile,repmat('%s',1,39),'HeaderLines',13,...
    'delimiter',',');
    samplename_ID = textscan(sample_IDFile,repmat('%s',1,39),'HeaderLines',11,...
    'delimiter',',');

    % close raw .csv data files for mix and unspike
    fclose(raw_mixFile);
    fclose(raw_unspikeFile);
    fclose(sample_IDFile);

    % calculate baseline corrected data for mix - group in raw_beam structure
    raw_beam.mix.Pb208 = str2double(raw_mix{:,25}) - str2double(raw_mix{:,8});
    raw_beam.mix.Pb207 = str2double(raw_mix{:,26}) - str2double(raw_mix{:,9});
    raw_beam.mix.Pb206 = str2double(raw_mix{:,27}) - str2double(raw_mix{:,10});
    raw_beam.mix.PbHg204 = str2double(raw_mix{:,29}) - str2double(raw_mix{:,12});
    raw_beam.mix.Tl205 = str2double(raw_mix{:,28}) - str2double(raw_mix{:,11});
    raw_beam.mix.Tl203 = str2double(raw_mix{:,30}) - str2double(raw_mix{:,13});
    raw_beam.mix.Hg202 = str2double(raw_mix{:,31}) - str2double(raw_mix{:,14});
    raw_beam.mix.Hg201 = str2double(raw_mix{:,32}) - str2double(raw_mix{:,15});

    % calculate baseline corrected data for unspiked - group in raw_beam struct
    raw_beam.unspike.Pb208 = str2double(raw_unspike{:,25}) - str2double(raw_unspike{:,8});
    raw_beam.unspike.Pb207 = str2double(raw_unspike{:,26}) - str2double(raw_unspike{:,9});
    raw_beam.unspike.Pb206 = str2double(raw_unspike{:,27}) - str2double(raw_unspike{:,10});
    raw_beam.unspike.PbHg204 = str2double(raw_unspike{:,29}) - str2double(raw_unspike{:,12});
    raw_beam.unspike.Tl205 = str2double(raw_unspike{:,28}) - str2double(raw_unspike{:,11});
    raw_beam.unspike.Tl203 = str2double(raw_unspike{:,30}) - str2double(raw_unspike{:,13});
    raw_beam.unspike.Hg202 = str2double(raw_unspike{:,31}) - str2double(raw_unspike{:,14});
    raw_beam.unspike.Hg201 = str2double(raw_unspike{:,32}) - str2double(raw_unspike{:,15});
```

```
% A. calculate ratios for mix

% 1. calculate corrected ratios for 204 mix -> 204Pb for 204Hg with 202Hg
corr_beam.mix.Hg204_2 = raw_beam.mix.Hg202 * const.ref_ratios.Hg_42;
corr_beam.mix.Pb204_2 = raw_beam.mix.PbHg204 - corr_beam.mix.Hg204_2;

% 2. calculate 204Hg/204PbHg from 202Hg
raw_ratios.mix.Hg204_PbHg204 = corr_beam.mix.Hg204_2 ./ raw_beam.mix.PbHg204;

% 3. calculate Pb raw ratios
raw_ratios.mix.Pb207_Pb206 = raw_beam.mix.Pb207 ./ raw_beam.mix.Pb206;
raw_ratios.mix.Pb208_Pb206 = raw_beam.mix.Pb208 ./ raw_beam.mix.Pb206;
raw_ratios.mix.Pb208_Pb207 = raw_beam.mix.Pb208 ./ raw_beam.mix.Pb207;
raw_ratios.mix.Pb206_PbHg204 = raw_beam.mix.Pb206 ./ raw_beam.mix.PbHg204;
raw_ratios.mix.Pb207_PbHg204 = raw_beam.mix.Pb207 ./ raw_beam.mix.PbHg204;
raw_ratios.mix.Pb208_PbHg204 = raw_beam.mix.Pb208 ./ raw_beam.mix.PbHg204;
raw_ratios.mix.Tl205_Tl203 = raw_beam.mix.Tl205 ./ raw_beam.mix.Tl203;

% 4. calculate beta_mix_Tl_53 and beta_mix_Pb_86 - put into const. struct
const.beta_mix.Tl_53 = log(const.ref_ratios.Tl_53 ./...
   raw_ratios.mix.Tl205_Tl203) ./ log(const.masses.M205 / const.masses.M203);
const.beta_mix.Pb_86 = log(const.ref_ratios.Pb_86 ./...
   raw_ratios.mix.Pb208_Pb206) ./ log(const.masses.M208 / const.masses.M206);

% 5. calculate mass bias corrected ratios

% 207Pb/206Pb ratio corrected using Pb 8/6 exp
corr_ratios.mix.Pb207_Pb206_86exp = raw_ratios.mix.Pb207_Pb206 .*...
   (const.masses.M207 / const.masses.M206) .^ const.beta_mix.Pb_86;

% 204Pb ratios corrected using Tl 5/3 exp
corr_ratios.mix.Pb207_Pb206_53exp = raw_ratios.mix.Pb207_Pb206 .*...
   (const.masses.M207 / const.masses.M206) .^ const.beta_mix.Tl_53;
corr_ratios.mix.Pb208_Pb206_53exp = raw_ratios.mix.Pb208_Pb206 .*...
   (const.masses.M208 / const.masses.M206) .^ const.beta_mix.Tl_53;
corr_ratios.mix.Pb208_Pb207_53exp = raw_ratios.mix.Pb208_Pb207 .*...
   (const.masses.M208 / const.masses.M207) .^ const.beta_mix.Tl_53;
corr_ratios.mix.Pb206_PbHg204_53exp = raw_ratios.mix.Pb206_PbHg204 .*...
   (const.masses.M206 / const.masses.M204) .^ const.beta_mix.Tl_53;
corr_ratios.mix.Pb207_PbHg204_53exp = raw_ratios.mix.Pb207_PbHg204 .*...
   (const.masses.M207 / const.masses.M204) .^ const.beta_mix.Tl_53;
corr_ratios.mix.Pb208_PbHg204_53exp = raw_ratios.mix.Pb208_PbHg204 .*...
   (const.masses.M208 / const.masses.M204) .^ const.beta_mix.Tl_53;

% 6 (a) correct Pb ratios using 201Hg

% calculate 201Hg/206Pb raw
raw_ratios.mix.Hg201_Pb206 = raw_beam.mix.Hg201 ./ raw_beam.mix.Pb206;

% calculate 201Hg/206Pb 5/3 exp
corr_ratios.mix.Hg201_Pb206_53exp = raw_ratios.mix.Hg201_Pb206 .*...
   (const.masses.M201 / const.masses.M204) .^ const.beta_mix.Tl_53;


% calculate 204Hg/206Pb 5/3 exp
corr_ratios.mix.Hg204_Pb206_53exp_1 = corr_ratios.mix.Hg201_Pb206_53exp...
   .* const.ref_ratios.Hg_41;
```

```
% calculate 204Pb/206Pb 5/3 exp 201Hg corrected
corr_ratios.mix.Pb204_Pb206_53exp_1 = (1 ./ corr_ratios.mix.Pb206_PbHg204_53exp)...
   - corr_ratios.mix.Hg204_Pb206_53exp_1;

% calculate 206 207 208Pb/ 204Pb ratios using 201Hg correction
corr_ratios.mix.Pb206_Pb204_53exp_1 = (1 ./corr_ratios.mix.Pb204_Pb206_53exp_1);
corr_ratios.mix.Pb207_Pb204_53exp_1 =...
   corr_ratios.mix.Pb207_Pb206_53exp ./ corr_ratios.mix.Pb204_Pb206_53exp_1;
corr_ratios.mix.Pb208_Pb204_53exp_1 =...
   corr_ratios.mix.Pb208_Pb206_53exp ./ corr_ratios.mix.Pb204_Pb206_53exp_1;

% 6 (b) correct Pb ratios using 202Hg

% calculate 201Hg/206Pb raw
raw_ratios.mix.Hg202_Pb206 = raw_beam.mix.Hg202 ./ raw_beam.mix.Pb206;

% calculate 202Hg/206Pb 5/3 exp
corr_ratios.mix.Hg202_Pb206_53exp = raw_ratios.mix.Hg202_Pb206 .*...
   (const.masses.M202 / const.masses.M204) .^ const.beta_mix.Tl_53;
% calculate 204Hg/206Pb 5/3 exp
corr_ratios.mix.Hg204_Pb206_53exp_2 = corr_ratios.mix.Hg202_Pb206_53exp...
   .* const.ref_ratios.Hg_42;

% calculate 204Pb/206Pb 5/3 exp 202Hg corrected
corr_ratios.mix.Pb204_Pb206_53exp_2 = (1 ./ corr_ratios.mix.Pb206_PbHg204_53exp)...
   - corr_ratios.mix.Hg204_Pb206_53exp_2;

% calculate 206 207 208Pb/ 204Pb ratios using 202Hg correction
corr_ratios.mix.Pb206_Pb204_53exp_2 = (1 ./corr_ratios.mix.Pb204_Pb206_53exp_2);
corr_ratios.mix.Pb207_Pb204_53exp_2 =...
   corr_ratios.mix.Pb207_Pb206_53exp ./ corr_ratios.mix.Pb204_Pb206_53exp_2;
corr_ratios.mix.Pb208_Pb204_53exp_2 =...
   corr_ratios.mix.Pb208_Pb206_53exp ./ corr_ratios.mix.Pb204_Pb206_53exp_2;

% B. calculate ratios for unspike

% 1. calculate corrected ratios for 204 unspiked -> 204Pb for 204Hg with 202Hg
corr_beam.unspike.Hg204_2 = raw_beam.unspike.Hg202 * const.ref_ratios.Hg_42;
corr_beam.unspike.Pb204_2 = raw_beam.unspike.PbHg204 - corr_beam.unspike.Hg204_2;

% 2. calculate 204Hg/204PbHg from 202Hg
raw_ratios.unspike.Hg204_PbHg204 = corr_beam.unspike.Hg204_2 ./...
   raw_beam.unspike.PbHg204;

% 3. calculate Pb raw ratios
raw_ratios.unspike.Pb207_Pb206 = raw_beam.unspike.Pb207 ./ raw_beam.unspike.Pb206;
raw_ratios.unspike.Pb208_Pb206 = raw_beam.unspike.Pb208 ./ raw_beam.unspike.Pb206;
raw_ratios.unspike.Pb208_Pb207 = raw_beam.unspike.Pb208 ./ raw_beam.unspike.Pb207;
raw_ratios.unspike.Pb206_PbHg204 = raw_beam.unspike.Pb206 ./ raw_beam.unspike.PbHg204;
raw_ratios.unspike.Pb207_PbHg204 = raw_beam.unspike.Pb207 ./ raw_beam.unspike.PbHg204;
raw_ratios.unspike.Pb208_PbHg204 = raw_beam.unspike.Pb208 ./ raw_beam.unspike.PbHg204;
raw_ratios.unspike.Tl205_Tl203 = raw_beam.unspike.Tl205 ./ raw_beam.unspike.Tl203;

% match Tl ion beam to sample to extract the appropriate 205Tl/203Tl
[~,I] = min(abs(mean(raw_beam.unspike.total_Tl_beam) - Tl_summary.Tl_beam_V));
const.ref_ratios.Tl_53 = Tl_summary.Tl205_203(I);
```

```
% 4. calculate beta_unspike_Tl_53 and beta_unspike_Pb_86  - put into const structure
   const.beta_unspike.Tl_53 = log(const.ref_ratios.Tl_53 ./ raw_ratios.unspike.Tl205_Tl203)...
      ./ log(const.masses.M205 / const.masses.M203);
   const.beta_unspike.Pb_86 = log(const.ref_ratios.Pb_86 ./ raw_ratios.unspike.Pb208_Pb206)...
      ./ log(const.masses.M208 / const.masses.M206);

   % 5. calculate mass bias corrected ratios 207Pb/206Pb 8/6 exp
   corr_ratios.unspike.Pb207_Pb206_86exp = raw_ratios.unspike.Pb207_Pb206 .*...
      (const.masses.M207 / const.masses.M206) .^ const.beta_unspike.Pb_86;

   % correct Pb ratios corrected using Tl 5/3exp
   corr_ratios.unspike.Pb207_Pb206_53exp = raw_ratios.unspike.Pb207_Pb206 .*...
      (const.masses.M207 / const.masses.M206) .^ const.beta_unspike.Tl_53;
   corr_ratios.unspike.Pb208_Pb206_53exp = raw_ratios.unspike.Pb208_Pb206 .*...
      (const.masses.M208 / const.masses.M206) .^ const.beta_unspike.Tl_53;
   corr_ratios.unspike.Pb208_Pb207_53exp = raw_ratios.unspike.Pb208_Pb207 .*...
      (const.masses.M208 / const.masses.M207) .^ const.beta_unspike.Tl_53;
   corr_ratios.unspike.Pb206_PbHg204_53exp = raw_ratios.unspike.Pb206_PbHg204 .*...
      (const.masses.M206 / const.masses.M204) .^ const.beta_unspike.Tl_53;
   corr_ratios.unspike.Pb207_PbHg204_53exp = raw_ratios.unspike.Pb207_PbHg204 .*...
      (const.masses.M207 / const.masses.M204) .^ const.beta_unspike.Tl_53;
   corr_ratios.unspike.Pb208_PbHg204_53exp = raw_ratios.unspike.Pb208_PbHg204 .*...
      (const.masses.M208 / const.masses.M204) .^ const.beta_unspike.Tl_53;

   % 6 (a) correct Pb ratios using 201Hg

   % calculate 201Hg/206Pb raw
   raw_ratios.unspike.Hg201_Pb206 = raw_beam.unspike.Hg201 ./ raw_beam.unspike.Pb206;

   % calculate 201Hg/206Pb 5/3 exp
   corr_ratios.unspike.Hg201_Pb206_53exp = raw_ratios.unspike.Hg201_Pb206 .*...
      (const.masses.M201 / const.masses.M204) .^ const.beta_unspike.Tl_53;

   % calculate 204Hg/206Pb 5/3 exp
   corr_ratios.unspike.Hg204_Pb206_53exp_1 = corr_ratios.unspike.Hg201_Pb206_53exp...
      .* const.ref_ratios.Hg_41;

   % calculate 204Pb/206Pb 5/3 exp 201Hg corrected
   corr_ratios.unspike.Pb204_Pb206_53exp_1 = (1 ./ corr_ratios.unspike.Pb206_PbHg204_53exp)...
      - corr_ratios.unspike.Hg204_Pb206_53exp_1;

   % calculate 206 207 208Pb/ 204Pb ratios using 201Hg correction
   corr_ratios.unspike.Pb206_Pb204_53exp_1 = (1 ./corr_ratios.unspike.Pb204_Pb206_53exp_1);
   corr_ratios.unspike.Pb207_Pb204_53exp_1 =...
      corr_ratios.unspike.Pb207_Pb206_53exp ./ corr_ratios.unspike.Pb204_Pb206_53exp_1;
   corr_ratios.unspike.Pb208_Pb204_53exp_1 =...
      corr_ratios.unspike.Pb208_Pb206_53exp ./ corr_ratios.unspike.Pb204_Pb206_53exp_1;

   % 6 (b) correct Pb ratios using 202Hg

   % calculate 201Hg/206Pb raw
   raw_ratios.unspike.Hg202_Pb206 = raw_beam.unspike.Hg202 ./ raw_beam.unspike.Pb206;

   % calculate 202Hg/206Pb 5/3 exp
   corr_ratios.unspike.Hg202_Pb206_53exp = raw_ratios.unspike.Hg202_Pb206 .*...
      (const.masses.M202 / const.masses.M204) .^ const.beta_unspike.Tl_53;
```

```
% calculate 204Hg/206Pb 5/3 exp
corr_ratios.unspike.Hg204_Pb206_53exp_2 = corr_ratios.unspike.Hg202_Pb206_53exp...
   .* const.ref_ratios.Hg_42;

% calculate 204Pb/206Pb 5/3 exp 202Hg corrected
corr_ratios.unspike.Pb204_Pb206_53exp_2 =...
   (1 ./ corr_ratios.unspike.Pb206_PbHg204_53exp) - corr_ratios.unspike.Hg204_Pb206_53exp_2;

% calculate 206 7 8Pb/ 204Pb ratios using 202Hg correction
corr_ratios.unspike.Pb206_Pb204_53exp_2 = (1 ./corr_ratios.unspike.Pb204_Pb206_53exp_2);
corr_ratios.unspike.Pb207_Pb204_53exp_2 =...
   corr_ratios.unspike.Pb207_Pb206_53exp ./ corr_ratios.unspike.Pb204_Pb206_53exp_2;
corr_ratios.unspike.Pb208_Pb204_53exp_2 =...
   corr_ratios.unspike.Pb208_Pb206_53exp ./ corr_ratios.unspike.Pb204_Pb206_53exp_2;

% calculate 205Tl/203Tl 8/6 exp
corr_ratios.unspike.Tl205_Tl203_86exp = raw_ratios.unspike.Tl205_Tl203...
   .* (const.masses.M205 / const.masses.M203) .^ const.beta_unspike.Pb_86;

% B. Correct data using double-spike inversion calculation
% get mix ratios (mi) using 202Hg and Tl_53 corrected 204 ratios
double_spike.m1 = corr_ratios.mix.Pb206_Pb204_53exp_2;
double_spike.m2 = corr_ratios.mix.Pb207_Pb204_53exp_2;
double_spike.m3 = corr_ratios.mix.Pb208_Pb204_53exp_2;

% get unspike ratios (ni) using 202Hg and Tl_53 corrected 204 ratios
double_spike.n1 = corr_ratios.unspike.Pb206_Pb204_53exp_2;
double_spike.n2 = corr_ratios.unspike.Pb207_Pb204_53exp_2;
double_spike.n3 = corr_ratios.unspike.Pb208_Pb204_53exp_2;

% before starting the loop, define Vn, Vm and Vt for mass bias error propagation
% calculate covariance for 204Pb ratios for unspike and place into Vn matrix with variance
x = cov(corr_ratios.unspike.Pb206_Pb204_53exp_2, corr_ratios.unspike.Pb207_Pb204_53exp_2,1);
y = cov(corr_ratios.unspike.Pb206_Pb204_53exp_2, corr_ratios.unspike.Pb208_Pb204_53exp_2,1);
z = cov(corr_ratios.unspike.Pb207_Pb204_53exp_2, corr_ratios.unspike.Pb208_Pb204_53exp_2,1);

double_spike.error.Vn = [var(corr_ratios.unspike.Pb206_Pb204_53exp_2)...
   x(1,2) y(1,2); x(1,2) var(corr_ratios.unspike.Pb207_Pb204_53exp_2) z(1,2);...
   y(1,2) z(1,2) var(corr_ratios.unspike.Pb208_Pb204_53exp_2)];

% repeat process for mix 204Pb ratios and and place into Vm matrix with variance
x = cov(corr_ratios.mix.Pb206_Pb204_53exp_2, corr_ratios.mix.Pb207_Pb204_53exp_2,1);
y = cov(corr_ratios.mix.Pb206_Pb204_53exp_2, corr_ratios.mix.Pb208_Pb204_53exp_2,1);
z = cov(corr_ratios.mix.Pb207_Pb204_53exp_2, corr_ratios.mix.Pb208_Pb204_53exp_2,1);

double_spike.error.Vm = [var(corr_ratios.mix.Pb206_Pb204_53exp_2)...
   x(1,2) y(1,2); x(1,2) var(corr_ratios.mix.Pb207_Pb204_53exp_2) z(1,2);...
   y(1,2) z(1,2) var(corr_ratios.mix.Pb208_Pb204_53exp_2)];

% create Vt
double_spike.error.Vt = [0 0 0; 0 0 0; 0 0 0];

% clear x, y, z variables to tidy workspace
clear x y z
```

```
% solve the non-liner equation iteratively to find the alpha and beta values
for i = 1:length(double_spike.m1)
   for j = length(double_spike.n1)

   % create starting point for non-linear iteration in the linear form:
   % F(x,n,m,T) = 0 = b + Ax -> x = b * A^-1;

   % calculate A matrix
   double_spike.A = [const.spike_ratios.T1 - double_spike.n1(j,1)...
      -(double_spike.n1(j,1) .* const.spike_ratios.P1)...
      (double_spike.m1(i,1) .* const.spike_ratios.P1);...
      const.spike_ratios.T2 - double_spike.n2(j,1)...
      -(double_spike.n2(j,1) .* const.spike_ratios.P2)...
      double_spike.m2(i,1) .* const.spike_ratios.P2;...
      const.spike_ratios.T3 - double_spike.n3(j,1)...
      -(double_spike.n3(j,1) .* const.spike_ratios.P3)...
      double_spike.m3(i,1) .* const.spike_ratios.P3];

   % invert A to calculate x
   double_spike.A_prime = double_spike.A^(-1);

   % get b matrix
   double_spike.b = [double_spike.m1(i,1) - double_spike.n1(j,1);...
      double_spike.m2(i,1) - double_spike.n2(j,1);
      double_spike.m3(i,1) - double_spike.n3(j,1)];

   % calculate x and extract/calculate linear solution for lamda, alpha and beta
   double_spike.x0 = double_spike.A_prime * double_spike.b;
   double_spike.lamda0 = double_spike.x0(1,1);
   double_spike.alpha0 = double_spike.x0(2,1)/(1-double_spike.lamda0);
   double_spike.beta0 = double_spike.x0(3,1);
   double_spike.x0 = [double_spike.lamda0; double_spike.alpha0; double_spike.beta0];

   % calculate solution to non-linear double-spike equation using initial
   % estimates from linear solution -> use nonlinear function
   [double_spike.y0] = nonlinear(double_spike.x0(1),double_spike.x0(2),...
      double_spike.x0(3),const.spike_ratios.T1,double_spike.n1(j,1),...
      const.spike_ratios.P1,double_spike.m1(i,1),const.spike_ratios.T2,...
      double_spike.n2(j,1),const.spike_ratios.P2,double_spike.m2(i,1),...
      const.spike_ratios.T3,double_spike.n3(j,1),const.spike_ratios.P3,...
      double_spike.m3(i,1));

   % calculate jacobian to force non-linear double-spike equation -> use
   % jacobian function
   [double_spike.J0] = jacobian(double_spike.x0(2),double_spike.x0(3),...
      const.spike_ratios.T1,double_spike.n1(j,1),const.spike_ratios.P1,...
      double_spike.m1(i,1),const.spike_ratios.T2,double_spike.n2(j,1),...
      const.spike_ratios.P2,double_spike.m2(i,1),const.spike_ratios.T3,...
      double_spike.n3(j,1),const.spike_ratios.P3,double_spike.m3(i,1));

   % calculate iteratively the non-linear solution of the double-spike
   % equation -> use newtonm function
   [double_spike.xn,double_spike.yn] = newtonm(...
      double_spike.x0,double_spike.J0,double_spike.y0,...
      const.spike_ratios.T1,double_spike.n1(j,1),...
      const.spike_ratios.P1,double_spike.m1(i,1),const.spike_ratios.T2,...
      double_spike.n2(j,1),const.spike_ratios.P2,double_spike.m2(i,1),...
      const.spike_ratios.T3,double_spike.n3(j,1),const.spike_ratios.P3,...
      double_spike.m3(i,1));
```

```
% index lamda, alpha and beta values for yn --> 0
double_spike.lamda(i,1) = double_spike.xn(1);
double_spike.alpha(i,1) = double_spike.xn(2);
double_spike.beta(i,1) = double_spike.xn(3);

% calculate 204Pb ratios using exponential law
double_spike.Pb206_Pb204(i,1) = corr_ratios.unspike.Pb206_Pb204_53exp_2(i,1) ...
   .* exp(- double_spike.alpha(i,1) * const.spike_ratios.P1);
double_spike.Pb207_Pb204(i,1) = corr_ratios.unspike.Pb207_Pb204_53exp_2(i,1) ...
   .* exp(- double_spike.alpha(i,1) * const.spike_ratios.P2);
double_spike.Pb208_Pb204(i,1) = corr_ratios.unspike.Pb208_Pb204_53exp_2(i,1) ...
   .* exp(- double_spike.alpha(i,1) * const.spike_ratios.P3);

% calculate other Pb ratios using 204Pb double-spike ratios
double_spike.Pb207_Pb206(i,1) = double_spike.Pb207_Pb204(i,1) ./ ...
   double_spike.Pb206_Pb204(i,1);
double_spike.Pb208_Pb206(i,1) = double_spike.Pb208_Pb204(i,1) ./ ...
   double_spike.Pb206_Pb204(i,1);
double_spike.Pb208_Pb207(i,1) = double_spike.Pb208_Pb204(i,1) ./ ...
   double_spike.Pb207_Pb204(i,1);

% calculate errors in x (lamda, alpha and beta) by propgating n,m and T
% calculate dF/dx using the determined lamda, alpha, beta values and invert matrix
[double_spike.error.JdF_dx_prime] = jacobian(double_spike.alpha(i,1),double_spike.beta(i,1),...
   const.spike_ratios.T1,double_spike.n1(j,1),const.spike_ratios.P1,...
   double_spike.m1(i,1),const.spike_ratios.T2,double_spike.n2(j,1),...
   const.spike_ratios.P2,double_spike.m2(i,1),const.spike_ratios.T3,...
   double_spike.n3(j,1),const.spike_ratios.P3,double_spike.m3(i,1))^(-1);

% calculate dF/dn, dF/dm and dF/dT
double_spike.error.dF_dn = [1 - double_spike.lamda(i,1) * exp(- double_spike.alpha(i,1)...
   * const.spike_ratios.P1), 0, 0; 0, 1 - double_spike.lamda(i,1) * exp(- ...
   double_spike.alpha(i,1) * const.spike_ratios.P2), 0; 0, 0, 1 - ...
   double_spike.lamda(i,1) * exp(- double_spike.alpha(i,1) * const.spike_ratios.P3)];

double_spike.error.dF_dm = [- exp(- double_spike.beta(i,1)...
   * const.spike_ratios.P1), 0, 0; 0, - exp(- double_spike.beta(i,1)...
   * const.spike_ratios.P2) 0; 0, 0, - exp(- double_spike.beta(i,1)*...
   const.spike_ratios.P3)];

double_spike.error.dF_dT = [double_spike.lamda(i,1), 0, 0; 0, double_spike.lamda(i,1),...
   0; 0, 0, double_spike.lamda(i,1)];

% calculate dx/dn, dx/dm, dx/dT
double_spike.error.dx_dn = (double_spike.error.JdF_dx_prime * double_spike.error.dF_dn);
double_spike.error.dx_dm = (double_spike.error.JdF_dx_prime * double_spike.error.dF_dm);
double_spike.error.dx_dT = (double_spike.error.JdF_dx_prime * double_spike.error.dF_dT);

% calculate n, m and t and sum the corresponding matrices to give Vx
n = (double_spike.error.dx_dn * double_spike.error.Vn * double_spike.error.dx_dn');
m = (double_spike.error.dx_dm * double_spike.error.Vm * double_spike.error.dx_dm');
t = (double_spike.error.dx_dT * double_spike.error.Vt * double_spike.error.dx_dT');

double_spike.error.Vx = n + m + t;
clear n m t
```

```
% calulate dy/dx and calculate Vy using dy/dx'
double_spike.error.dy_dx = [1, 0, 0; double_spike.alpha(i,1) /...
   (1 - double_spike.lamda(i,1)), 1 / (1 - double_spike.lamda(i,1)), 0;...
   0, 0, 1];

double_spike.error.Vy = (double_spike.error.Vx * double_spike.error.dy_dx * ...
   double_spike.error.dy_dx');

% place respective errors in lamda, alpha and beta structures
double_spike.error.lamda(i,1) = sqrt(double_spike.error.Vy(1,1));
double_spike.error.alpha(i,1) = sqrt(double_spike.error.Vy(2,2));
double_spike.error.beta(i,1) = sqrt(double_spike.error.Vy(3,3));

% calculate errors in N (VN)
% define dy/dn, dy/dm and dy/dT
double_spike.error.dy_dn = (double_spike.error.dx_dn * double_spike.error.dy_dx);
double_spike.error.dy_dm = (double_spike.error.dx_dm * double_spike.error.dy_dx);
double_spike.error.dy_dT = (double_spike.error.dx_dT * double_spike.error.dy_dx);

% calculate dN/dn, dN/dm and dN/dT
% dN/dn 3 x 3 matrix
double_spike.error.dN_dn(1,1) = exp(- double_spike.alpha(i,1) * const.spike_ratios.P1)...
   - const.spike_ratios.P1 * double_spike.Pb206_Pb204(i,1) * exp(- ...
   double_spike.alpha(i,1) * const.spike_ratios.P1) * double_spike.error.dy_dn(2,1);
double_spike.error.dN_dn(1,2) = - const.spike_ratios.P1 * double_spike.Pb206_Pb204(i,1) * exp(- ...
   double_spike.alpha(i,1) * const.spike_ratios.P1) * double_spike.error.dy_dn(2,2);
double_spike.error.dN_dn(1,3) = - const.spike_ratios.P1 * double_spike.Pb206_Pb204(i,1) * exp(- ...
   double_spike.alpha(i,1) * const.spike_ratios.P1) * double_spike.error.dy_dn(2,3);
double_spike.error.dN_dn(2,1) = - const.spike_ratios.P2 * double_spike.Pb207_Pb204(i,1) * exp(- ...
   double_spike.alpha(i,1) * const.spike_ratios.P2) * double_spike.error.dy_dn(2,1);
double_spike.error.dN_dn(2,2) = exp(- double_spike.alpha(i,1) * const.spike_ratios.P2)...
   - const.spike_ratios.P2 * double_spike.Pb207_Pb204(i,1) * exp(- ...
   double_spike.alpha(i,1) * const.spike_ratios.P2) * double_spike.error.dy_dn(2,2);
double_spike.error.dN_dn(2,3) = - const.spike_ratios.P2 * double_spike.Pb207_Pb204(i,1) * exp(- ...
   double_spike.alpha(i,1) * const.spike_ratios.P2) * double_spike.error.dy_dn(2,3);
double_spike.error.dN_dn(3,1) = - const.spike_ratios.P3 * double_spike.Pb208_Pb204(i,1) * exp(- ...
   double_spike.alpha(i,1) * const.spike_ratios.P3) * double_spike.error.dy_dn(2,1);
double_spike.error.dN_dn(3,2) = - const.spike_ratios.P3 * double_spike.Pb208_Pb204(i,1) * exp(- ...
   double_spike.alpha(i,1) * const.spike_ratios.P3) * double_spike.error.dy_dn(2,2);
double_spike.error.dN_dn(3,3) = exp(- double_spike.alpha(i,1) * const.spike_ratios.P3)...
   - const.spike_ratios.P3 * double_spike.Pb208_Pb204(i,1) * exp(- ...
   double_spike.alpha(i,1) * const.spike_ratios.P3) * double_spike.error.dy_dn(2,3);

% dN/dm 3 x 3 matrix
double_spike.error.dN_dm(1,1) = - const.spike_ratios.P1 * double_spike.Pb206_Pb204(i,1) * exp(- ...
   double_spike.alpha(i,1) * const.spike_ratios.P1) * double_spike.error.dy_dm(2,1);
double_spike.error.dN_dm(1,2) = - const.spike_ratios.P1 * double_spike.Pb206_Pb204(i,1) * exp(- ...
   double_spike.alpha(i,1) * const.spike_ratios.P1) * double_spike.error.dy_dm(2,2);
double_spike.error.dN_dm(1,3) = - const.spike_ratios.P1 * double_spike.Pb206_Pb204(i,1) * exp(- ...
   double_spike.alpha(i,1) * const.spike_ratios.P1) * double_spike.error.dy_dm(2,3);
double_spike.error.dN_dm(2,1) = - const.spike_ratios.P2 * double_spike.Pb207_Pb204(i,1) * exp(- ...
   double_spike.alpha(i,1) * const.spike_ratios.P2) * double_spike.error.dy_dm(2,1);
double_spike.error.dN_dm(2,2) = - const.spike_ratios.P2 * double_spike.Pb207_Pb204(i,1) * exp(- ...
   double_spike.alpha(i,1) * const.spike_ratios.P2) * double_spike.error.dy_dm(2,2);
double_spike.error.dN_dm(2,3) = - const.spike_ratios.P2 * double_spike.Pb207_Pb204(i,1) * exp(- ...
   double_spike.alpha(i,1) * const.spike_ratios.P2) * double_spike.error.dy_dm(2,3);
double_spike.error.dN_dm(3,1) = - const.spike_ratios.P3 * double_spike.Pb208_Pb204(i,1) * exp(- ...
   double_spike.alpha(i,1) * const.spike_ratios.P3) * double_spike.error.dy_dm(2,1);
double_spike.error.dN_dm(3,2) = - const.spike_ratios.P3 * double_spike.Pb208_Pb204(i,1) * exp(- ...
```

```
        double_spike.alpha(i,1) * const.spike_ratios.P3) * double_spike.error.dy_dm(2,2);
    double_spike.error.dN_dm(3,3) = - const.spike_ratios.P3 * double_spike.Pb208_Pb204(i,1) * exp(- ...
        double_spike.alpha(i,1) * const.spike_ratios.P3) * double_spike.error.dy_dm(2,3);

    % dN/dT 3 x 3 matrix
    double_spike.error.dN_dT(1,1) = - const.spike_ratios.P1 * double_spike.Pb206_Pb204(i,1) * exp(- ...
        double_spike.alpha(i,1) * const.spike_ratios.P1) * double_spike.error.dy_dT(2,1);
    double_spike.error.dN_dT(1,2) = - const.spike_ratios.P1 * double_spike.Pb206_Pb204(i,1) * exp(- ...
        double_spike.alpha(i,1) * const.spike_ratios.P1) * double_spike.error.dy_dT(2,2);
    double_spike.error.dN_dT(1,3) = - const.spike_ratios.P1 * double_spike.Pb206_Pb204(i,1) * exp(- ...
        double_spike.alpha(i,1) * const.spike_ratios.P1) * double_spike.error.dy_dT(2,3);
    double_spike.error.dN_dT(2,1) = - const.spike_ratios.P2 * double_spike.Pb207_Pb204(i,1) * exp(- ...
        double_spike.alpha(i,1) * const.spike_ratios.P2) * double_spike.error.dy_dT(2,1);
    double_spike.error.dN_dT(2,2) = - const.spike_ratios.P2 * double_spike.Pb207_Pb204(i,1) * exp(- ...
        double_spike.alpha(i,1) * const.spike_ratios.P2) * double_spike.error.dy_dT(2,2);
    double_spike.error.dN_dT(2,3) = - const.spike_ratios.P2 * double_spike.Pb207_Pb204(i,1) * exp(- ...
        double_spike.alpha(i,1) * const.spike_ratios.P2) * double_spike.error.dy_dT(2,3);
    double_spike.error.dN_dT(3,1) = - const.spike_ratios.P3 * double_spike.Pb208_Pb204(i,1) * exp(- ...
        double_spike.alpha(i,1) * const.spike_ratios.P3) * double_spike.error.dy_dT(2,1);
    double_spike.error.dN_dT(3,2) = - const.spike_ratios.P3 * double_spike.Pb208_Pb204(i,1) * exp(- ...
        double_spike.alpha(i,1) * const.spike_ratios.P3) * double_spike.error.dy_dT(2,2);
    double_spike.error.dN_dT(3,3) = - const.spike_ratios.P3 * double_spike.Pb208_Pb204(i,1) * exp(- ...
        double_spike.alpha(i,1) * const.spike_ratios.P3) * double_spike.error.dy_dT(2,3);

    % calculate n, m and t and sum the corresponding matrices to give Vx
    n = (double_spike.error.dN_dn * double_spike.error.Vn * double_spike.error.dN_dn');
    m = (double_spike.error.dN_dm * double_spike.error.Vm * double_spike.error.dN_dm');
    t = (double_spike.error.dN_dT * double_spike.error.Vt * double_spike.error.dN_dT');

    double_spike.error.VN = n + m + t;
    clear n m t

    end
  end % completes loop for double-spike inversion calculation

  % put final average Pb corrected ratios with std error into 'final' structure

  % create structure with sample names
  string = cellfun(@(x) x(1:29),cellstr(samplename_ID{1,1}{1,1}),'un',0);
  Date(k,1) = cellstr(datestr(erase(cellstr(samplename_ID{1,1}{1,1}),...
    string)));

  Sample_Name(k,1) = erase(cellstr(samplename_ID{1,1}{2,1}),...
    "Sample Name is   ");

  % beta values for 5/3 and 8/6
  ratios.beta_Tl_53(k,1) = mean(const.beta_unspike.Tl_53...
    (abs(const.beta_unspike.Tl_53 - mean(const.beta_unspike.Tl_53))...
  < 2 * std(const.beta_unspike.Tl_53)));
  ratios.beta_Tl_53(k,2) = 2 * std(const.beta_unspike.Tl_53...
    (abs(const.beta_unspike.Tl_53 - mean(const.beta_unspike.Tl_53))...
  < 2 * std(const.beta_unspike.Tl_53))) / sqrt(sum((abs(const.beta_unspike.Tl_53 -
mean(const.beta_unspike.Tl_53))...
  < 2 * std(const.beta_unspike.Tl_53))));

  ratios.beta_Pb_86(k,1) = mean(const.beta_unspike.Pb_86...
    (abs(const.beta_unspike.Pb_86 - mean(const.beta_unspike.Pb_86))...
  < 2 * std(const.beta_unspike.Pb_86)));
```

```
    ratios.beta_Pb_86(k,2) = 2 * std(const.beta_unspike.Pb_86...
        (abs(const.beta_unspike.Pb_86 - mean(const.beta_unspike.Pb_86))...
    < 2 * std(const.beta_unspike.Pb_86))) / sqrt(sum((abs(const.beta_unspike.Pb_86 -
mean(const.beta_unspike.Pb_86))...
    < 2 * std(const.beta_unspike.Pb_86))));

    % Pb corrected ratio (207Pb/206Pb)
    ratios.Pb207_Pb206_86exp(k,1) = mean(corr_ratios.unspike.Pb207_Pb206_86exp...
            (abs(corr_ratios.unspike.Pb207_Pb206_86exp - mean(corr_ratios.unspike.Pb207_Pb206_86exp))...
    < 2 * std(corr_ratios.unspike.Pb207_Pb206_86exp)));
    ratios.Pb207_Pb206_86exp(k,2) = 2 * std(corr_ratios.unspike.Pb207_Pb206_86exp...
        (abs(corr_ratios.unspike.Pb207_Pb206_86exp - mean(corr_ratios.unspike.Pb207_Pb206_86exp))...
    < 2 * std(corr_ratios.unspike.Pb207_Pb206_86exp))) /
sqrt(sum((abs(corr_ratios.unspike.Pb207_Pb206_86exp...
    - mean(corr_ratios.unspike.Pb207_Pb206_86exp))...
    < 2 * std(corr_ratios.unspike.Pb207_Pb206_86exp))));

    % Tl and DS corrected ratio (207Pb/206Pb)
    ratios.Pb207_Pb206_53exp(k,1) = mean(corr_ratios.unspike.Pb207_Pb206_53exp...
        (abs(corr_ratios.unspike.Pb207_Pb206_53exp - mean(corr_ratios.unspike.Pb207_Pb206_53exp))...
    < 2 * std(corr_ratios.unspike.Pb207_Pb206_53exp)));
    ratios.Pb207_Pb206_53exp(k,2) = 2 * std(corr_ratios.unspike.Pb207_Pb206_53exp...
        (abs(corr_ratios.unspike.Pb207_Pb206_53exp - mean(corr_ratios.unspike.Pb207_Pb206_53exp))...
    < 2 * std(corr_ratios.unspike.Pb207_Pb206_53exp))) /
sqrt(sum((abs(corr_ratios.unspike.Pb207_Pb206_53exp...
    - mean(corr_ratios.unspike.Pb207_Pb206_53exp))...
    < 2 * std(corr_ratios.unspike.Pb207_Pb206_53exp))));

    ratios.Pb207_Pb206_DS(k,1) = mean(double_spike.Pb207_Pb206...
        (abs(double_spike.Pb207_Pb206 - mean(double_spike.Pb207_Pb206))...
    < 2 * std(double_spike.Pb207_Pb206)));
    ratios.Pb207_Pb206_DS(k,2) = 2 * std(double_spike.Pb207_Pb206...
        (abs(double_spike.Pb207_Pb206 - mean(double_spike.Pb207_Pb206))...
    < 2 * std(double_spike.Pb207_Pb206))) / sqrt(sum((abs(double_spike.Pb207_Pb206...
    - mean(double_spike.Pb207_Pb206))...
    < 2 * std(double_spike.Pb207_Pb206))));

    % Tl and ds corrected ratio (208Pb/206Pb)
    ratios.Pb208_Pb206_53exp(k,1) = mean(corr_ratios.unspike.Pb208_Pb206_53exp...
        (abs(corr_ratios.unspike.Pb208_Pb206_53exp - mean(corr_ratios.unspike.Pb208_Pb206_53exp))...
    < 2 * std(corr_ratios.unspike.Pb208_Pb206_53exp)));
    ratios.Pb208_Pb206_53exp(k,2) = 2 * std(corr_ratios.unspike.Pb208_Pb206_53exp...
        (abs(corr_ratios.unspike.Pb208_Pb206_53exp - mean(corr_ratios.unspike.Pb208_Pb206_53exp))...
    < 2 * std(corr_ratios.unspike.Pb208_Pb206_53exp))) /
sqrt(sum((abs(corr_ratios.unspike.Pb208_Pb206_53exp...
    - mean(corr_ratios.unspike.Pb208_Pb206_53exp))...
    < 2 * std(corr_ratios.unspike.Pb208_Pb206_53exp))));

    ratios.Pb208_Pb206_DS(k,1) = mean(double_spike.Pb208_Pb206...
        (abs(double_spike.Pb208_Pb206 - mean(double_spike.Pb208_Pb206))...
    < 2 * std(double_spike.Pb208_Pb206)));
    ratios.Pb208_Pb206_DS(k,2) = 2 * std(double_spike.Pb208_Pb206...
        (abs(double_spike.Pb208_Pb206 - mean(double_spike.Pb208_Pb206))...
    < 2 * std(double_spike.Pb208_Pb206))) / sqrt(sum((abs(double_spike.Pb208_Pb206...
    - mean(double_spike.Pb208_Pb206))...
    < 2 * std(double_spike.Pb208_Pb206))));
```

```
    % Tl and ds corrected ratio (208Pb/207Pb)
    ratios.Pb208_Pb207_53exp(k,1) = mean(corr_ratios.unspike.Pb208_Pb207_53exp...
        (abs(corr_ratios.unspike.Pb208_Pb207_53exp - mean(corr_ratios.unspike.Pb208_Pb207_53exp))...
    < 2 * std(corr_ratios.unspike.Pb208_Pb207_53exp)));
    ratios.Pb208_Pb207_53exp(k,2) = 2 * std(corr_ratios.unspike.Pb208_Pb207_53exp...
        (abs(corr_ratios.unspike.Pb208_Pb207_53exp - mean(corr_ratios.unspike.Pb208_Pb207_53exp))...
    < 2 * std(corr_ratios.unspike.Pb208_Pb207_53exp))) /
sqrt(sum((abs(corr_ratios.unspike.Pb208_Pb207_53exp...
    - mean(corr_ratios.unspike.Pb208_Pb207_53exp))...
    < 2 * std(corr_ratios.unspike.Pb208_Pb207_53exp))));

    ratios.Pb208_Pb207_DS(k,1) = mean(double_spike.Pb208_Pb207...
        (abs(double_spike.Pb208_Pb207 - mean(double_spike.Pb208_Pb207))...
    < 2 * std(double_spike.Pb208_Pb207)));
    ratios.Pb208_Pb207_DS(k,2) = 2 * std(double_spike.Pb208_Pb207...
        (abs(double_spike.Pb208_Pb207 - mean(double_spike.Pb208_Pb207))...
    < 2 * std(double_spike.Pb208_Pb207))) / sqrt(sum((abs(double_spike.Pb208_Pb207...
    - mean(double_spike.Pb208_Pb207))...
    < 2 * std(double_spike.Pb208_Pb207))));

    % Tl and ds corrected 204Pb ratios
    ratios.Pb206_Pb204_53exp_1(k,1) = mean(corr_ratios.unspike.Pb206_Pb204_53exp_1...
        (abs(corr_ratios.unspike.Pb206_Pb204_53exp_1 - mean(corr_ratios.unspike.Pb206_Pb204_53exp_1))...
    < 2 * std(corr_ratios.unspike.Pb206_Pb204_53exp_1)));
    ratios.Pb206_Pb204_53exp_1(k,2) = 2 * std(corr_ratios.unspike.Pb206_Pb204_53exp_1...
        (abs(corr_ratios.unspike.Pb206_Pb204_53exp_1 - mean(corr_ratios.unspike.Pb206_Pb204_53exp_1))...
    < 2 * std(corr_ratios.unspike.Pb206_Pb204_53exp_1))) /
sqrt(sum((abs(corr_ratios.unspike.Pb206_Pb204_53exp_1...
    - mean(corr_ratios.unspike.Pb206_Pb204_53exp_1))...
    < 2 * std(corr_ratios.unspike.Pb206_Pb204_53exp_1))));

    ratios.Pb206_Pb204_53exp_2(k,1) = mean(corr_ratios.unspike.Pb206_Pb204_53exp_2...
         (abs(corr_ratios.unspike.Pb206_Pb204_53exp_2 - mean(corr_ratios.unspike.Pb206_Pb204_53exp_2))...
    < 2 * std(corr_ratios.unspike.Pb206_Pb204_53exp_2)));
    ratios.Pb206_Pb204_53exp_2(k,2) = 2 * std(corr_ratios.unspike.Pb206_Pb204_53exp_2...
        (abs(corr_ratios.unspike.Pb206_Pb204_53exp_2 - mean(corr_ratios.unspike.Pb206_Pb204_53exp_2))...
    < 2 * std(corr_ratios.unspike.Pb206_Pb204_53exp_2))) /
sqrt(sum((abs(corr_ratios.unspike.Pb206_Pb204_53exp_2...
    - mean(corr_ratios.unspike.Pb206_Pb204_53exp_2))...
    < 2 * std(corr_ratios.unspike.Pb206_Pb204_53exp_2))));

    ratios.Pb206_Pb204_DS(k,1) = mean(double_spike.Pb206_Pb204...
        (abs(double_spike.Pb206_Pb204 - mean(double_spike.Pb206_Pb204))...
    < 2 * std(double_spike.Pb206_Pb204)));
    ratios.Pb206_Pb204_DS(k,2) = 2 * std(double_spike.Pb206_Pb204...
        (abs(double_spike.Pb206_Pb204 - mean(double_spike.Pb206_Pb204))...
    < 2 * std(double_spike.Pb206_Pb204))) / sqrt(sum((abs(double_spike.Pb206_Pb204...
    - mean(double_spike.Pb206_Pb204))...
    < 2 * std(double_spike.Pb206_Pb204))));

    ratios.Pb207_Pb204_53exp_1(k,1) = mean(corr_ratios.unspike.Pb207_Pb204_53exp_1...
        (abs(corr_ratios.unspike.Pb207_Pb204_53exp_1 - mean(corr_ratios.unspike.Pb207_Pb204_53exp_1))...
    < 2 * std(corr_ratios.unspike.Pb207_Pb204_53exp_1)));
    ratios.Pb207_Pb204_53exp_1(k,2) = 2 * std(corr_ratios.unspike.Pb207_Pb204_53exp_1...
        (abs(corr_ratios.unspike.Pb207_Pb204_53exp_1 - mean(corr_ratios.unspike.Pb207_Pb204_53exp_1))...
    < 2 * std(corr_ratios.unspike.Pb207_Pb204_53exp_1))) /
sqrt(sum((abs(corr_ratios.unspike.Pb207_Pb204_53exp_1...
    - mean(corr_ratios.unspike.Pb207_Pb204_53exp_1))...
    < 2 * std(corr_ratios.unspike.Pb207_Pb204_53exp_1))));
```

```
    ratios.Pb207_Pb204_53exp_2(k,1) = mean(corr_ratios.unspike.Pb207_Pb204_53exp_2...
       (abs(corr_ratios.unspike.Pb207_Pb204_53exp_1 - mean(corr_ratios.unspike.Pb207_Pb204_53exp_1))...
    < 2 * std(corr_ratios.unspike.Pb207_Pb204_53exp_1)));
    ratios.Pb207_Pb204_53exp_2(k,2) = 2 * std(corr_ratios.unspike.Pb207_Pb204_53exp_2...
       (abs(corr_ratios.unspike.Pb207_Pb204_53exp_2 - mean(corr_ratios.unspike.Pb207_Pb204_53exp_2))...
    < 2 * std(corr_ratios.unspike.Pb207_Pb204_53exp_2))) /
sqrt(sum((abs(corr_ratios.unspike.Pb207_Pb204_53exp_2...
    - mean(corr_ratios.unspike.Pb207_Pb204_53exp_2))...
    < 2 * std(corr_ratios.unspike.Pb207_Pb204_53exp_2))));

    ratios.Pb207_Pb204_DS(k,1) = mean(double_spike.Pb207_Pb204...
       (abs(double_spike.Pb207_Pb204 - mean(double_spike.Pb207_Pb204))...
    < 2 * std(double_spike.Pb207_Pb204)));
    ratios.Pb207_Pb204_DS(k,2) = 2 * std(double_spike.Pb207_Pb204...
       (abs(double_spike.Pb207_Pb204 - mean(double_spike.Pb207_Pb204))...
    < 2 * std(double_spike.Pb207_Pb204))) / sqrt(sum((abs(double_spike.Pb207_Pb204...
    - mean(double_spike.Pb207_Pb204))...
    < 2 * std(double_spike.Pb207_Pb204))));

    ratios.Pb208_Pb204_53exp_1(k,1) = mean(corr_ratios.unspike.Pb208_Pb204_53exp_1...
       (abs(corr_ratios.unspike.Pb208_Pb204_53exp_1 - mean(corr_ratios.unspike.Pb208_Pb204_53exp_1))...
    < 2 * std(corr_ratios.unspike.Pb208_Pb204_53exp_1)));
    ratios.Pb208_Pb204_53exp_1(k,2) = 2 * std(corr_ratios.unspike.Pb208_Pb204_53exp_1...
       (abs(corr_ratios.unspike.Pb208_Pb204_53exp_1 - mean(corr_ratios.unspike.Pb208_Pb204_53exp_1))...
    < 2 * std(corr_ratios.unspike.Pb208_Pb204_53exp_1))) /
sqrt(sum((abs(corr_ratios.unspike.Pb208_Pb204_53exp_1...
    - mean(corr_ratios.unspike.Pb208_Pb204_53exp_1))...
    < 2 * std(corr_ratios.unspike.Pb208_Pb204_53exp_1))));

    ratios.Pb208_Pb204_53exp_2(k,1) = mean(corr_ratios.unspike.Pb208_Pb204_53exp_2...
       (abs(corr_ratios.unspike.Pb208_Pb204_53exp_2 - mean(corr_ratios.unspike.Pb208_Pb204_53exp_2))...
    < 2 * std(corr_ratios.unspike.Pb208_Pb204_53exp_2)));
    ratios.Pb208_Pb204_53exp_2(k,2) = 2 * std(corr_ratios.unspike.Pb208_Pb204_53exp_2...
       (abs(corr_ratios.unspike.Pb208_Pb204_53exp_2 - mean(corr_ratios.unspike.Pb208_Pb204_53exp_2))...
    < 2 * std(corr_ratios.unspike.Pb208_Pb204_53exp_2))) /
sqrt(sum((abs(corr_ratios.unspike.Pb208_Pb204_53exp_2...
    - mean(corr_ratios.unspike.Pb208_Pb204_53exp_2))...
    < 2 * std(corr_ratios.unspike.Pb208_Pb204_53exp_2))));

    ratios.Pb208_Pb204_DS(k,1) = mean(double_spike.Pb208_Pb204...
       (abs(double_spike.Pb208_Pb204 - mean(double_spike.Pb208_Pb204))...
    < 2 * std(double_spike.Pb208_Pb204)));
    ratios.Pb208_Pb204_DS(k,2) = 2 * std(double_spike.Pb208_Pb204...
       (abs(double_spike.Pb208_Pb204 - mean(double_spike.Pb208_Pb204))...
    < 2 * std(double_spike.Pb208_Pb204))) / sqrt(sum((abs(double_spike.Pb208_Pb204...
    - mean(double_spike.Pb208_Pb204))...
    < 2 * std(double_spike.Pb208_Pb204))));

    % Tl 205/203 corrected using 208/206Pb exp
    ratios.Tl205_Tl203_86exp(k,1) = mean(corr_ratios.unspike.Tl205_Tl203_86exp...
       (abs(corr_ratios.unspike.Tl205_Tl203_86exp - mean(corr_ratios.unspike.Tl205_Tl203_86exp))...
    < 2 * std(corr_ratios.unspike.Tl205_Tl203_86exp)));
    ratios.Tl205_Tl203_86exp(k,2) = 2 * std(corr_ratios.unspike.Tl205_Tl203_86exp...
       (abs(corr_ratios.unspike.Tl205_Tl203_86exp - mean(corr_ratios.unspike.Tl205_Tl203_86exp))...
    < 2 * std(corr_ratios.unspike.Tl205_Tl203_86exp))) /
sqrt(sum((abs(corr_ratios.unspike.Tl205_Tl203_86exp...
    - mean(corr_ratios.unspike.Tl205_Tl203_86exp))...
    < 2 * std(corr_ratios.unspike.Tl205_Tl203_86exp))));
```

```
    % Pb and Tl total beams
    total_Pb_beam = raw_beam.unspike.Pb208 + raw_beam.unspike.Pb207...
       + raw_beam.unspike.Pb206 + corr_beam.unspike.Pb204_2;
    ratios.total_Pb_beam(k,1) = mean(total_Pb_beam...
       (abs(total_Pb_beam - mean(total_Pb_beam)) < 2 * std(total_Pb_beam)));
    ratios.total_Pb_beam(k,2) = 2 * std(total_Pb_beam...
       (abs(total_Pb_beam - mean(total_Pb_beam))...
    < 2 * std(total_Pb_beam))) / sqrt(sum((abs(total_Pb_beam...
    - mean(total_Pb_beam)) < 2 * std(total_Pb_beam))));

    total_Tl_beam = raw_beam.unspike.Tl205 + raw_beam.unspike.Tl203;
    ratios.total_Tl_beam(k,1) = mean(total_Tl_beam...
       (abs(total_Tl_beam - mean(total_Tl_beam)) < 2 * std(total_Tl_beam)));
    ratios.total_Tl_beam(k,2) = 2 * std(total_Tl_beam...
       (abs(total_Tl_beam - mean(total_Tl_beam))...
    < 2 * std(total_Tl_beam))) / sqrt(sum((abs(total_Tl_beam...
    - mean(total_Tl_beam)) < 2 * std(total_Tl_beam))));

    % create structure for Pb DS IC fraction (mix) for Pb yield calculation
    mix_concs.Sample_Name = Sample_Name;

    % calculate specific ratios for yield calculations
    mix_concs.ratios.Pb208_Pb206_53exp(k,1) = mean(corr_ratios.mix.Pb208_Pb206_53exp...
       (abs(corr_ratios.mix.Pb208_Pb206_53exp - mean(corr_ratios.mix.Pb208_Pb206_53exp))...
    < 2 * std(corr_ratios.mix.Pb208_Pb206_53exp)));
    mix_concs.ratios.Pb208_Pb206_53exp(k,2) = 2 * std(corr_ratios.mix.Pb208_Pb206_53exp...
       (abs(corr_ratios.mix.Pb208_Pb206_53exp - mean(corr_ratios.mix.Pb208_Pb206_53exp))...
    < 2 * std(corr_ratios.mix.Pb208_Pb206_53exp))) / sqrt(sum((abs(corr_ratios.mix.Pb208_Pb206_53exp...
    - mean(corr_ratios.mix.Pb208_Pb206_53exp))...
    < 2 * std(corr_ratios.mix.Pb208_Pb206_53exp))));

    mix_concs.ratios.Pb207_Pb206_53exp(k,1) = mean(corr_ratios.mix.Pb207_Pb206_53exp...
       (abs(corr_ratios.mix.Pb207_Pb206_53exp - mean(corr_ratios.mix.Pb207_Pb206_53exp))...
    < 2 * std(corr_ratios.mix.Pb207_Pb206_53exp)));
    mix_concs.ratios.Pb207_Pb206_53exp(k,2) = 2 * std(corr_ratios.mix.Pb207_Pb206_53exp...
       (abs(corr_ratios.mix.Pb207_Pb206_53exp - mean(corr_ratios.mix.Pb207_Pb206_53exp))...
    < 2 * std(corr_ratios.mix.Pb207_Pb206_53exp))) / sqrt(sum((abs(corr_ratios.mix.Pb207_Pb206_53exp...
    - mean(corr_ratios.mix.Pb207_Pb206_53exp))...
    < 2 * std(corr_ratios.mix.Pb207_Pb206_53exp))));

end % finishes the loop for importing and processing raw data

% clear indices used in loops and variables created when importing mass spec data files
clear ans k i j mix_Dir mix_files unspike_Dir unspike_files raw_mixFile raw_unspikeFile...
   raw_mix raw_unspike mix_folder unspike_folder sample_IDFile samplename_ID string vars...
   total_Pb_beam total_Tl_beam

% C. Correct Pb isotope compositions to reference values

% extract standards into structure
index = contains(Sample_Name,standard_name);

standards.name = Sample_Name(contains(Sample_Name,standard_name));
standards.Pb207_Pb206_53exp = ratios.Pb207_Pb206_53exp(index,1);
standards.Pb207_Pb206_DS = ratios.Pb207_Pb206_DS(index,1);
standards.Pb208_Pb206_53exp = ratios.Pb208_Pb206_53exp(index,1);
standards.Pb208_Pb206_DS = ratios.Pb208_Pb206_DS(index,1);
```

```
standards.Pb208_Pb207_53exp = ratios.Pb208_Pb207_53exp(index,1);
standards.Pb208_Pb207_DS = ratios.Pb208_Pb207_DS(index,1);
standards.Pb206_Pb204_53exp_1 = ratios.Pb206_Pb204_53exp_1(index,1);
standards.Pb206_Pb204_53exp_2 = ratios.Pb206_Pb204_53exp_2(index,1);
standards.Pb206_Pb204_DS = ratios.Pb206_Pb204_DS(index,1);
standards.Pb207_Pb204_53exp_1 = ratios.Pb207_Pb204_53exp_1(index,1);
standards.Pb207_Pb204_53exp_2 = ratios.Pb207_Pb204_53exp_2(index,1);
standards.Pb207_Pb204_DS = ratios.Pb207_Pb204_DS(index,1);
standards.Pb208_Pb204_53exp_1 = ratios.Pb208_Pb204_53exp_1(index,1);
standards.Pb208_Pb204_53exp_2 = ratios.Pb208_Pb204_53exp_2(index,1);
standards.Pb208_Pb204_DS = ratios.Pb208_Pb204_DS(index,1);
standards.total_Pb_beam = ratios.total_Pb_beam(index,1);

% calculate the average for each standard and the correction factor

for i = 1:length(standard_name)

    index = contains(standards.name,standard_name(1,i));

    standards.k.name(i,1) = standard_name(1,i);
    standards.k.Pb207_Pb206_53exp(i,1) = const.galer.Pb207_Pb206 /
mean(standards.Pb207_Pb206_53exp(index,1));
    standards.k.Pb207_Pb206_DS(i,1) = const.galer.Pb207_Pb206 / mean(standards.Pb207_Pb206_DS(index,1));
    standards.k.Pb208_Pb206_53exp(i,1) = const.galer.Pb208_Pb206 /
mean(standards.Pb208_Pb206_53exp(index,1));
    standards.k.Pb208_Pb206_DS(i,1) = const.galer.Pb208_Pb206 / mean(standards.Pb208_Pb206_DS(index,1));
    standards.k.Pb206_Pb204_53exp_1(i,1) = const.galer.Pb206_Pb204 /
mean(standards.Pb206_Pb204_53exp_1(index,1));
    standards.k.Pb206_Pb204_53exp_2(i,1) = const.galer.Pb206_Pb204 /
mean(standards.Pb206_Pb204_53exp_2(index,1));
    standards.k.Pb206_Pb204_DS(i,1) = const.galer.Pb206_Pb204 / mean(standards.Pb206_Pb204_DS(index,1));
    standards.k.Pb207_Pb204_53exp_1(i,1) = const.galer.Pb207_Pb204 /
mean(standards.Pb207_Pb204_53exp_1(index,1));
    standards.k.Pb207_Pb204_53exp_2(i,1) = const.galer.Pb207_Pb204 /
mean(standards.Pb207_Pb204_53exp_2(index,1));
    standards.k.Pb207_Pb204_DS(i,1) = const.galer.Pb207_Pb204 / mean(standards.Pb207_Pb204_DS(index,1));
    standards.k.Pb208_Pb204_53exp_1(i,1) = const.galer.Pb208_Pb204 /
mean(standards.Pb208_Pb204_53exp_1(index,1));
    standards.k.Pb208_Pb204_53exp_2(i,1) = const.galer.Pb208_Pb204 /
mean(standards.Pb208_Pb204_53exp_2(index,1));
    standards.k.Pb208_Pb204_DS(i,1) = const.galer.Pb208_Pb204 / mean(standards.Pb208_Pb204_DS(index,1));
    standards.k.total_Pb_beam(i,1) = mean(standards.total_Pb_beam(index,1));

end

% Apply correction factor, k, to final ratios of samples using a standard of a similar Pb ion beam

% create final ratio structure to apply correction
final_ratios = ratios;

for m = 1:length(ratios.Pb207_Pb206_86exp)

    % Condition to omit standards correcting themselves to Galer values
    if ~contains(Sample_Name(m,1),standard_name)

    % Find the closest standard Pb ion beam to correct individual samples
    [ion_beam_diff,standard_index] = min(abs(standards.k.total_Pb_beam - final_ratios.total_Pb_beam(m,1)));
```

```
    % Apply correction factor, k, to each ratio
    final_ratios.Pb207_Pb206_53exp(m,1) = ratios.Pb207_Pb206_53exp(m,1) *
standards.k.Pb207_Pb206_53exp(standard_index,1);
    final_ratios.Pb207_Pb206_DS(m,1) = ratios.Pb207_Pb206_DS(m,1) *
standards.k.Pb207_Pb206_DS(standard_index,1);
    final_ratios.Pb208_Pb206_53exp(m,1) = ratios.Pb208_Pb206_53exp(m,1) *
standards.k.Pb208_Pb206_53exp(standard_index,1);
    final_ratios.Pb208_Pb206_DS(m,1) = ratios.Pb208_Pb206_DS(m,1) *
standards.k.Pb208_Pb206_DS(standard_index,1);
    final_ratios.Pb206_Pb204_53exp_1(m,1) = ratios.Pb206_Pb204_53exp_1(m,1) *
standards.k.Pb206_Pb204_53exp_1(standard_index,1);
    final_ratios.Pb206_Pb204_53exp_2(m,1) = ratios.Pb206_Pb204_53exp_2(m,1) *
standards.k.Pb206_Pb204_53exp_2(standard_index,1);
    final_ratios.Pb206_Pb204_DS(m,1) = ratios.Pb206_Pb204_DS(m,1) *
standards.k.Pb206_Pb204_DS(standard_index,1);
    final_ratios.Pb207_Pb204_53exp_1(m,1) = ratios.Pb207_Pb204_53exp_1(m,1) *
standards.k.Pb207_Pb204_53exp_1(standard_index,1);
    final_ratios.Pb207_Pb204_53exp_2(m,1) = ratios.Pb207_Pb204_53exp_2(m,1) *
standards.k.Pb207_Pb204_53exp_2(standard_index,1);
    final_ratios.Pb207_Pb204_DS(m,1) = ratios.Pb207_Pb204_DS(m,1) *
standards.k.Pb207_Pb204_DS(standard_index,1);
    final_ratios.Pb208_Pb204_53exp_1(m,1) = ratios.Pb208_Pb204_53exp_1(m,1) *
standards.k.Pb208_Pb204_53exp_1(standard_index,1);
    final_ratios.Pb208_Pb204_53exp_2(m,1) = ratios.Pb208_Pb204_53exp_2(m,1) *
standards.k.Pb208_Pb204_53exp_2(standard_index,1);
    final_ratios.Pb208_Pb204_DS(m,1) = ratios.Pb208_Pb204_DS(m,1) *
standards.k.Pb208_Pb204_DS(standard_index,1);

    ratios.ion_beam_smpl_std_diff(m,1) = ion_beam_diff;

    end

end

clear i m ion_beam_diff index standard_index standard_name

% D. Calculate Pb concentration using Pb IC ratios

% create structure for concentration calculation
final_concs.Sample_Name = Sample_Name;

% extract sample and spike masses from 'masses.csv'
for j = 1:length(final_concs.Sample_Name)

    % index samples
    name = final_concs.Sample_Name(j,1);

    % extract masses (g) and calculate spike used (nmol)
    final_concs.sample_mass_ID(j,1) = table2array(masses(ismember(masses.SampleNameIC,name),2));
    final_concs.spike_mass_ID(j,1) = table2array(masses(ismember(masses.SampleNameIC,name),3));
    final_concs.sample_mass_IC(j,1) = table2array(masses(ismember(masses.SampleNameIC,name),5));
    final_concs.spike_mass_IC(j,1) = table2array(masses(ismember(masses.SampleNameIC,name),6));
    final_concs.Pb207_208_ID(j,1) = table2array(masses(ismember(masses.SampleNameIC,name),7));
    final_concs.Pb206_208_ID(j,1) = table2array(masses(ismember(masses.SampleNameIC,name),8));

end
```

```
% calculate the natural atomic weights for samples
final_concs.nat_wt.tPb_Pb207 = 1 ./ final_ratios.Pb207_Pb204_DS(:,1) + 1 ./
final_ratios.Pb207_Pb206_DS(:,1) +...
   final_ratios.Pb208_Pb207_DS(:,1) + 1;
final_concs.nat_wt.fPb207 = 1 ./ final_concs.nat_wt.tPb_Pb207;
final_concs.nat_wt.fPb204 = final_concs.nat_wt.fPb207 * 1 ./ final_ratios.Pb207_Pb204_DS(:,1);
final_concs.nat_wt.fPb206 = final_concs.nat_wt.fPb207 * 1 ./ final_ratios.Pb207_Pb206_DS(:,1);
final_concs.nat_wt.fPb208 = final_concs.nat_wt.fPb207 .* final_ratios.Pb208_Pb207_DS(:,1);
final_concs.nat_wt.Pb = (final_concs.nat_wt.fPb204 * const.masses.M204) + ...
(final_concs.nat_wt.fPb206 * const.masses.M206) + (final_concs.nat_wt.fPb207 * const.masses.M207) +...
(final_concs.nat_wt.fPb208 * const.masses.M208);



% calculate amount of spike used for each isotope (pmol) (const.spike_conc = nmol/g)
final_concs.spike_used.Pb204 = final_concs.spike_mass_ID * (const.spike_conc.Pb204 * 1000);
final_concs.spike_used.Pb206 = final_concs.spike_mass_ID * (const.spike_conc.Pb206 * 1000);
final_concs.spike_used.Pb207 = final_concs.spike_mass_ID * (const.spike_conc.Pb207 * 1000);
final_concs.spike_used.Pb208 = final_concs.spike_mass_ID * (const.spike_conc.Pb208 * 1000);

% calculate residual fractionation correction (uses linear law) using
% sample 207/206 and 208/207 ratios for IC
final_concs.k1 = ((1 ./ final_ratios.Pb207_Pb206_DS(:,1) ./ 1 ./ final_ratios.Pb208_Pb207_DS(:,1) ...
   .* 1 / const.spike_ratios.Pb208_Pb207 - 1 ./ final_ratios.Pb208_Pb207_DS(:,1) ...
   .* const.spike_ratios.Pb206_Pb207 ./ const.spike_ratios.Pb208_Pb207) ./ ...
   (1 / const.spike_ratios.Pb208_Pb207 - 1 ./ final_ratios.Pb208_Pb207_DS(:,1)));

final_concs.k2 = ((1 ./ final_ratios.Pb207_Pb206_DS(:,1) ./ final_ratios.Pb208_Pb207_DS(:,1) - ...
   const.spike_ratios.Pb206_Pb207 / const.spike_ratios.Pb208_Pb207) ./ ...
   (1 / const.spike_ratios.Pb208_Pb207 - 1 ./ final_ratios.Pb208_Pb207_DS(:,1)));

% calculate Pb during ID run
final_concs.id.f = (final_concs.k1 - final_concs.Pb207_208_ID .* final_concs.k2 -
final_concs.Pb206_208_ID)...
   ./ ((const.masses.M206 - const.masses.M208) .* final_concs.Pb206_208_ID - ...
   (const.masses.M208 - const.masses.M207) .* final_concs.Pb207_208_ID .* final_concs.k2);

% calculate 207/208 and 206/208 ratio true-mix values
final_concs.id.Pb207_Pb208 = final_concs.Pb207_208_ID .* (1 - (const.masses.M208 - const.masses.M207)
*...
   final_concs.id.f);
final_concs.id.Pb206_Pb208 = final_concs.Pb206_208_ID .* (1 - (const.masses.M208 - const.masses.M206)
*...
   final_concs.id.f);

% calculate ID unmix for 207Pb (pmol)
final_concs.Pb_207 = (final_concs.spike_used.Pb206 - (final_concs.id.Pb207_Pb208).^-1 .* ...
   final_concs.spike_used.Pb207) ./ ((final_concs.id.Pb207_Pb208).^-1 - (final_ratios.Pb208_Pb207_DS(:,1)));

% calculate total Pb (pmol) using 207Pb (pmol) and sample 207Pb fraction
final_concs.total_Pb = final_concs.Pb_207 ./ final_concs.nat_wt.fPb207;

% calculate concentration (pmol/g) using sample mass (g)
final_concs.Pb_pmol_g = final_concs.total_Pb ./ final_concs.sample_mass_ID;

% calculate Pb concentation (ppt) using sample natural Pb abundance
final_concs.Pb_ppt = final_concs.Pb_pmol_g .* final_concs.nat_wt.Pb;
final_concs.Pb_pmol_kg = final_concs.Pb_pmol_g * 1000;
```

```
% index blanks and calculate average total Pb blank (pmol)

   if isempty(blank_ID_pg)

      blank_ID_pmol = mean(masses.Pb_ppt_ID(contains(masses.SampleNameID,blank_name_ID)))...
         / const.nat_wt.Pb;

   elseif isnan(blank_ID_pg)

      blank_ID_pmol = mean(masses.Pb_ppt_ID(contains(masses.SampleNameID,blank_name_ID)))...
         / const.nat_wt.Pb;

   else

      blank_ID_pmol = blank_ID_pg / const.nat_wt.Pb;

   end

% blank correction - correct the Pb concentrations using the blank value
for m = 1:length(final_concs.Pb_pmol_kg)

      if contains(final_concs.Sample_Name(m,1),blank_name_IC)

      % calculate total Pb (pmol) using 207Pb (pmol) and sample 207Pb fraction
      final_concs.total_Pb_blank_corr(m,1) = final_concs.total_Pb(m,1);
      % calculate concentration (pmol/g) using sample mass (g)
      final_concs.Pb_pmol_g_blank_corr(m,1) = final_concs.total_Pb_blank_corr(m,1) /
final_concs.sample_mass_ID(m,1);

      % calculate Pb concentation (ppt and pmol/kg) using sample natural Pb abundance
      final_concs.Pb_ppt_blank_corr(m,1) = final_concs.Pb_pmol_g_blank_corr(m,1) *
final_concs.nat_wt.Pb(m,1);
      final_concs.Pb_pmol_kg_blank_corr(m,1) = final_concs.Pb_pmol_g_blank_corr(m,1) * 1000;

      else

      % calculate total Pb (pmol) using 207Pb (pmol) and sample 207Pb fraction
      final_concs.total_Pb_blank_corr(m,1) = final_concs.total_Pb(m,1) - blank_ID_pmol;
      % calculate concentration (pmol/g) using sample mass (g)
      final_concs.Pb_pmol_g_blank_corr(m,1) = final_concs.total_Pb_blank_corr(m,1) /
final_concs.sample_mass_ID(m,1);

      % calculate Pb concentation (ppt and pmol/kg) using estimated natural Pb abundance
      final_concs.Pb_ppt_blank_corr(m,1) = final_concs.Pb_pmol_g_blank_corr(m,1) *
final_concs.nat_wt.Pb(m,1);
      final_concs.Pb_pmol_kg_blank_corr(m,1) = final_concs.Pb_pmol_g_blank_corr(m,1) * 1000;

      end
end

% clear indices and variables used in loop for concentration calculation
clear j m name blank_name_ID blank_ID_pg
```

```
% E. Calculate measured [Pb] and yields using Pb mix ratios

% calculate amount of DS used for each isotope (pmol) (const.spike_conc = nmol/g)
mix_concs.spike_used.Pb204 = final_concs.spike_mass_IC .* (const.spike_conc.Pb204 * 1000);
mix_concs.spike_used.Pb206 = final_concs.spike_mass_IC .* (const.spike_conc.Pb206 * 1000);
mix_concs.spike_used.Pb207 = final_concs.spike_mass_IC .* (const.spike_conc.Pb207 * 1000);
mix_concs.spike_used.Pb208 = final_concs.spike_mass_IC .* (const.spike_conc.Pb208 * 1000);

% calculate Pb during ID run using sample residual fractionation k1 and k2
mix_concs.id.f = (final_concs.k1 - (mix_concs.ratios.Pb207_Pb206_53exp(:,1) ./ ...
   mix_concs.ratios.Pb208_Pb206_53exp(:,1)) .* final_concs.k2 - 1 ./
mix_concs.ratios.Pb208_Pb206_53exp(:,1))...
   ./ ((const.masses.M206 - const.masses.M208) .* 1 ./ mix_concs.ratios.Pb208_Pb206_53exp(:,1) - ...
   (const.masses.M208 - const.masses.M207) .* (mix_concs.ratios.Pb207_Pb206_53exp(:,1) ./ ...
   mix_concs.ratios.Pb208_Pb206_53exp(:,1)) .* final_concs.k2);


% calculate 207/208 and 206/208 ratio true-mix values
mix_concs.id.Pb207_Pb208 = mix_concs.ratios.Pb207_Pb206_53exp(:,1) ./ ...
   mix_concs.ratios.Pb208_Pb206_53exp(:,1) .* (1 - (const.masses.M208 - const.masses.M207) .*...
   mix_concs.id.f(:,1));
mix_concs.id.Pb206_Pb208 = 1 ./ mix_concs.ratios.Pb208_Pb206_53exp(:,1) .* (1 - (const.masses.M208 -
const.masses.M206) .*...
   mix_concs.id.f(:,1));

% calculate ID unmix for 207Pb (pmol)
mix_concs.Pb_207 = (mix_concs.spike_used.Pb206 - (mix_concs.id.Pb207_Pb208(:,1)).^-1 .* ...
   mix_concs.spike_used.Pb207) ./ ((mix_concs.id.Pb207_Pb208(:,1)).^-1 -
(final_ratios.Pb208_Pb207_DS(:,1)));

% calculate total Pb (pmol) using 207Pb (pmol) and sample 207Pb fraction
mix_concs.total_Pb = mix_concs.Pb_207 ./ final_concs.nat_wt.fPb207;

% calculate concentration (pmol/g) using sample mass (g)
mix_concs.Pb_pmol_g = mix_concs.total_Pb ./ (final_concs.sample_mass_IC ./ 3);
% calculate Pb concentation (ppt) using sample natural Pb abundance
mix_concs.Pb_ppt = mix_concs.Pb_pmol_g .* final_concs.nat_wt.Pb;

% calculate total amount of Pb (ng) in sample and total Pb (ng) analysed
mix_concs.meas_Pb_ng = (mix_concs.Pb_ppt .* final_concs.sample_mass_IC) ./ 1000;
mix_concs.total_Pb_ng = (final_concs.Pb_ppt .* final_concs.sample_mass_IC) ./ 1000;

% index blanks and calculate average total Pb blank (pmol)
  if isempty(blank_IC_pg)

      blank_IC_pmol = ((mean(mix_concs.meas_Pb_ng(contains(mix_concs.Sample_Name,blank_name_IC)))...
         * 1000) / const.nat_wt.Pb) / 3;

   elseif isnan(blank_IC_pg)

      blank_IC_pmol = ((mean(mix_concs.meas_Pb_ng(contains(mix_concs.Sample_Name,blank_name_IC)))...
         * 1000) / const.nat_wt.Pb) / 3;

   else

      blank_IC_pmol = blank_IC_pg / const.nat_wt.Pb;
end
```

```
% blank correction - correct the Pb measured mixed concentrations using the blank value
for m = 1:length(mix_concs.meas_Pb_ng)

    if contains(mix_concs.Sample_Name(m,1),blank_name_IC)

    % calculate total Pb (pmol) using 207Pb (pmol) and sample 207Pb fraction
    mix_concs.total_Pb_blank_corr(m,1) = mix_concs.total_Pb(m,1);
    % calculate concentration (pmol/g) using sample mass (g)
    mix_concs.Pb_pmol_g_blank_corr(m,1) = mix_concs.total_Pb_blank_corr(m,1) /
(final_concs.sample_mass_IC(m,1) / 3);



    % Calculate Pb concentation (ppt and pmol/kg) using estimated natural Pb abundance
    mix_concs.Pb_ppt_blank_corr(m,1) = mix_concs.Pb_pmol_g_blank_corr(m,1) *
final_concs.nat_wt.Pb(m,1);
    mix_concs.Pb_pmol_kg_blank_corr(m,1) = mix_concs.Pb_pmol_g_blank_corr(m,1) * 1000;

    else

    % calculate total Pb (pmol) using 207Pb (pmol) and sample 207Pb fraction
    mix_concs.total_Pb_blank_corr(m,1) = mix_concs.total_Pb(m,1) - blank_IC_pmol;
    % calculate concentration (pmol/g) using sample mass (g)
    mix_concs.Pb_pmol_g_blank_corr(m,1) = mix_concs.total_Pb_blank_corr(m,1) /
(final_concs.sample_mass_IC(m,1) / 3);

    % Calculate Pb concentation (ppt and pmol/kg) using estimated natural Pb abundance
    mix_concs.Pb_ppt_blank_corr(m,1) = mix_concs.Pb_pmol_g_blank_corr(m,1) *
final_concs.nat_wt.Pb(m,1);
    mix_concs.Pb_pmol_kg_blank_corr(m,1) = mix_concs.Pb_pmol_g_blank_corr(m,1) * 1000;

    end
end

% calculate yield using double-spike Pb_ppt and final Pb blank corrected ppt
mix_concs.yield = (mix_concs.Pb_ppt_blank_corr ./ final_concs.Pb_ppt_blank_corr) .* 100;

% clear indices and variables used in loop for concentration calculation
clear m blank_name_IC blank_IC_pg

% F. Export results as csv file

% Add concentration and yield to final_ratios structure ready for export
final_ratios.Pb_ppt = final_concs.Pb_ppt_blank_corr;
final_ratios.Pb_pmol_kg = final_concs.Pb_pmol_kg_blank_corr;
final_ratios.blank_contribution_ID = (blank_ID_pmol ./ final_concs.total_Pb) .* 100;
final_ratios.total_Pb_ng = (final_concs.sample_mass_IC .* final_concs.Pb_ppt_blank_corr)...
   ./ 1000;
final_ratios.meas_Pb_ng = (mix_concs.Pb_ppt_blank_corr .* final_concs.sample_mass_IC) ./ 1000;
final_ratios.blank_contribution_IC = (blank_IC_pmol ./ (mix_concs.total_Pb .* 3)) .* 100;
final_ratios.sample_mass_g = final_concs.sample_mass_IC;
final_ratios.yield = mix_concs.yield;
```

```
% Declare header lable for sample name
header1 = {'Date' 'Sample Name'};

% Loop through to concatenate header with sample names

name = cell(length(Sample_Name) + 1,2);

for j = 1:length(Sample_Name)

    name{1,1} = header1{1,1};
    name{j+1,1} = Date{j,1};

    name{1,2} = header1{1,2};
    name{j+1,2} = Sample_Name{j,1};

end

% Convert to table
sample = cell2table(name);

% Declare list of variable names
header2 = {'beta Tl 5/3' '2SE' 'beta Pb 8/6' '2SE'...
    '207Pb/206Pb 86 exp' '2SE' '207Pb/206Pb 53 exp' '2SE' '207Pb/206Pb DS' '2SE' ...
    '208Pb/206Pb 53 exp' '2SE' '208Pb/206Pb DS' '2SE' '208Pb/207Pb 53 exp' '2SE' ...
    '208Pb/207Pb DS' '2SE' '206Pb/204Pb 53 exp 1' '2SE' '206Pb/204Pb 53 exp 2' '2SE' ...
    '206Pb/204Pb DS' '2SE' '207Pb/204Pb 53 exp 1' '2SE' '207Pb/204Pb 53 exp 2' '2SE' ...
    '207Pb/204Pb DS' '2SE' '208Pb/204Pb 53 exp 1' '2SE' '208Pb/204Pb 53 exp 2' '2SE' ...
    '208Pb/204Pb DS' '2SE' '205Tl/203Tl 86 exp' '2SE' 'Total Pb ion beam' '2SE' ...
    'Total Tl ion beam' '2SE' '[Pb] (ppt)' '[Pb] (pmol/kg)' 'Blank contribution ID (%)'...
    'Total Pb (ng)' 'Measured Pb (ng)' 'Blank contribution IC (%)' 'Sample mass (g)' 'Yield (%)'};

% Convert final_ratios structure to cell array
data = struct2array(final_ratios);
data = num2cell(data);

% Loop through to concatenate header of variables with data

all_data = cell(size(data,1) + 1,size(header2,2));

for k = 1:size(header2,2)
    for i = 1:size(data,1)

    all_data{1,k} = header2{1,k};
    all_data{i+1,k} = data{i,k};

    end
end

% Convert to table
final_data = cell2table(all_data);

% Concatenate two tables for sample name and variables with headers in 1st row
output = [sample final_data];

% Export the concatenated table
writetable(output, results_output, 'WriteVariableNames', 0);
```

```
% Add sample names to final ratios structure for reference
final_ratios.Sample_Name = Sample_Name;

% Clear unwanted variables
clear i j k l header1 header2 name sample data all_data final_data ...
    Date Sample_Name results_output list sample_mass_IC...
    spike_mass_IC sample_conc_ID

% end of Pb isotope double-spike data reduction
```

Appendices

Appendix 2: Result tables for NBP15 cruise neodymium isotope and rare earth element data, and GS01 section Pb isotope and concentration data.

Appendix 2 presents the data tables for Nd isotope, rare earth element concentration and Pb isotope data presented in chapters 2 and 4 with corresponding hydrographic data.

Table A.1. Seawater neodymium isotope measurements from NBP15 cruise across the Wilkes Land continental margin. The sample name is composed of the cruise code, CTD station and niskin bottle number (cruise_station-niskin). The asterisk next to the sample name corresponds to a duplicate analysis of the previous sample. The ε_{Nd} 2sd error was calculated by propagating the internal 2se error for each sample with the external 2sd error for JNdi-1 standard measurements during the same batch of measurements. For information on Nd concentration errors and hydrographic data, see section 2.3.3 and 2.2.3, respectively.

Sample	Depth (m)	Nd (pmol kg^{-1})	$^{143}Nd/^{144}Nd$	ε_{Nd}	2sd	Pot. temp (°C)	Salinity	Neutral Density (kg m^{-3})	Water mass
Station 2 (-62.014°N, 131.966°E)									
NBP1503_002-23	4	12.16	0.512227	-8.02	0.36	2.219	33.770	27.113	AASW
NBP1503_002-21	81	12.26	0.512210	-8.34	0.36	-0.156	33.953	27.474	AASW
NBP1503_002-19	219	13.55	0.512203	-8.48	0.36	2.152	34.467	27.767	AASW
NBP1503_002-17	369	14.28	0.512210	-8.34	0.25	2.213	34.584	27.853	AASW
NBP1503_002-15	739	16.13	0.512152	-9.48	0.34	2.041	34.710	27.978	AASW
NBP1503_002-13	1237	18.75	0.512157	-9.37	0.32	1.635	34.743	28.054	MCDW
NBP1503_002-11	1774	21.67	0.512178	-8.98	0.34	1.144	34.731	28.121	MCDW
NBP1503_002-09	2367	24.01	0.512192	-8.70	0.25	0.660	34.707	28.185	MCDW
NBP1503_002-07	2950	25.40	0.512199	-8.57	0.36	0.234	34.688	28.245	MCDW
NBP1503_002-05	3679	26.13	0.512195	-8.65	0.31	-0.085	34.674	28.291	AABW
NBP1503_002-03	4299	26.71	0.512203	-8.48	0.21	-0.350	34.659	28.325	AABW
NBP1503_002-01	4397	27.04	0.512194	-8.66	0.30	-0.412	34.653	28.331	AABW
Station 5 (-64.993°N, 130.406°E)									
NBP1503_005-08	10	14.71	0.512197	-8.60	0.26	-1.316	33.975	27.551	AASW
NBP1503_005-06	101	17.65	0.512170	-9.14	0.27	-1.782	34.340	27.899	AASW
NBP1503_005-04	341	19.75	0.512169	-9.15	0.25	-1.423	34.485	28.059	MCDW
NBP1503_005-02	502	21.34	0.512210	-8.34	0.27	-0.944	34.538	28.158	MCDW

Station 6 (-64.845°N, 130.400°E)									
NBP1503_006-16	10	14.85	0.512215	-8.25	0.25	-0.977	34.066	27.624	AASW
NBP1503_006-14	80	16.89	0.512207	-8.40	0.20	-1.785	34.319	27.880	AASW
NBP1503_006-12	298	18.84	0.512193	-8.67	0.19	-0.853	34.503	28.030	MCDW
NBP1503_006-10	792	22.85	0.512212	-8.31	0.21	0.048	34.660	28.229	MCDW
NBP1503_006-08	1238	23.79	0.512232	-7.93	0.21	-0.050	34.669	28.270	MCDW
NBP1503_006-06	1482	23.89	0.512226	-8.04	0.21	-0.142	34.666	28.286	AABW
NBP1503_006-04	1776	23.57	0.512219	-8.17	0.22	-0.271	34.659	28.304	AABW
NBP1503_006-04*	1776	23.44	0.512228	-7.99	0.22	-0.271	34.659	28.304	AABW
NBP1503_006-02	1889	23.64	0.512220	-8.15	0.20	-0.304	34.657	28.309	AABW
Station 10 (-65.509°N, 122.404°E)									
NBP1503_010-17	10	16.04	0.512178	-8.98	0.26	-1.779	33.851	27.446	AASW
NBP1503_010-14	75	16.56	0.512168	-9.17	0.26	-1.194	34.010	27.579	AASW
NBP1503_010-06	338	19.53	0.512156	-9.39	0.25	-1.467	34.431	27.989	AASW
NBP1503_010-02	419	18.28	0.512174	-9.05	0.24	0.776	34.644	28.047	MCDW
Station 15 (-65.001°N, 122.007°E)									
NBP1503_015-24	10	16.26	0.512182	-8.90	0.20	-1.551	34.000	27.582	AASW
NBP1503_015-21	120	18.92	0.512154	-9.43	0.21	-1.785	34.318	27.881	AASW
NBP1503_015-18	398	18.58	0.512174	-9.05	0.20	1.274	34.705	28.060	MCDW
NBP1503_015-15	1141	23.81	0.512199	-8.57	0.22	0.519	34.697	28.195	MCDW
NBP1503_015-12	1579	24.59	0.512203	-8.48	0.20	0.170	34.684	28.248	MCDW
NBP1503_015-08	1970	24.42	0.512207	-8.41	0.22	-0.076	34.671	28.280	AABW
NBP1503_015-05	2401	24.38	0.512212	-8.31	0.20	-0.249	34.662	28.305	AABW
NBP1503_015-05*	2401	24.32	0.512219	-8.17	0.23	-0.249	34.662	28.305	AABW
NBP1503_015-02	2500	24.41	0.512215	-8.25	0.22	-0.269	34.661	28.308	AABW

Station 18 (-65.659°N, 119.781°E)									
NBP1503_018-14	10	16.13	0.512157	-9.38	0.25	-1.778	33.867	27.461	AASW
NBP1503_018-11	80	16.62	0.512160	-9.32	0.25	-1.665	33.911	27.503	AASW
NBP1503_018-08	247	19.75	0.512129	-9.93	0.26	-1.828	34.266	27.842	AASW
NBP1503_018-02	483	23.35	0.512144	-9.65	0.27	0.549	34.664	28.111	MCDW
Station 24 (-65.149°N, 118.283°E)									
NBP1503_024-23	9	16.08	0.512173	-9.08	0.23	-1.748	33.946	27.536	AASW
NBP1503_024-21	119	19.48	0.512144	-9.64	0.23	-1.840	34.249	27.823	AASW
NBP1503_024-18	346	18.09	0.512168	-9.16	0.32	0.828	34.619	28.016	AASW
NBP1503_024-14	496	20.41	0.512176	-9.00	0.25	0.952	34.700	28.102	MCDW
NBP1503_024-11	987	23.95	0.512190	-8.74	0.24	0.290	34.684	28.220	MCDW
NBP1503_024-11*	987	23.92	0.512206	-8.42	0.23	0.290	34.684	28.220	MCDW
NBP1503_024-08	1481	24.66	0.512208	-8.39	0.22	0.069	34.675	28.254	MCDW
NBP1503_024-06	1972	24.61	0.512213	-8.29	0.21	-0.064	34.670	28.277	AABW
NBP1503_024-02	2083	24.59	0.512210	-8.34	0.21	-0.114	34.668	28.285	AABW
Station 40 (-64.450°N, 128.366°E)									
NBP1503_040-06	2571	24.74	0.512237	-7.82	0.29	-0.366	34.650	28.315	AABW
NBP1503_040-02	2669	23.61	0.512213	-8.29	0.26	-0.367	34.650	28.315	AABW
Station 41 (-63.634°N, 128.365°E)									
NBP1503_041-24	10	15.20	0.512188	-8.77	0.31	-0.596	34.114	27.651	AASW
NBP1503_041-22	198	16.60	0.512176	-9.02	0.29	1.610	34.670	27.991	AASW
NBP1503_041-20	396	18.15	0.512184	-8.85	0.30	1.689	34.731	28.039	MCDW
NBP1503_041-18	693	19.90	0.512157	-9.37	0.31	1.450	34.742	28.079	MCDW
NBP1503_041-16	987	21.69	0.512172	-9.08	0.29	1.127	34.730	28.121	MCDW

NBP1503_041-14	1480	23.62	0.512182	-8.89	0.30	0.631	34.703	28.182	MCDW
NBP1503_041-12	1972	24.83	0.512190	-8.75	0.29	0.213	34.684	28.241	MCDW
NBP1503_041-10	2462	25.46	0.512193	-8.67	0.29	-0.036	34.676	28.281	AABW
NBP1503_041-06	2950	25.73	0.512206	-8.42	0.30	-0.264	34.665	28.313	AABW
NBP1503_041-04	3434	26.26	0.512204	-8.47	0.29	-0.431	34.653	28.331	AABW
NBP1503_041-02	3533	26.44	0.512200	-8.54	0.29	-0.447	34.651	28.333	AABW

Table A.2. Seawater rare earth element concentration measurements from NBP15 cruise across the Wilkes Land continental margin. The sample name is composed of the cruise code, CTD station and niskin bottle number (cruise_station-niskin). For information on the analytical methods and estimated concentration errors for each element, see section 2.3.3 and Table 2.1.

Sample	Depth (m)	La	Ce	Pr	Nd	Sm	Eu	Gd	Tb	Dy	Ho	Er	Tm	Yb	Lu
		(pmol kg^{-1})													
Station 2 (-62.014°N, 131.966°E)															
NBP1503_002-23	4	18.95	3.04	2.56	11.61	2.30	0.59	3.51	0.57	4.13	1.32	4.95	0.67	4.95	0.85
NBP1503_002-21	81	19.52	4.89	2.97	13.11	2.34	0.76	4.26	0.62	4.88	1.36	4.68	0.75	4.86	0.88
NBP1503_002-19	219	21.56	2.91	3.11	12.95	2.48	0.76	4.23	0.64	5.28	1.41	5.65	0.79	5.51	1.06
NBP1503_002-17	369	22.28	3.30	3.05	13.75	2.55	0.70	3.64	0.67	5.54	1.46	5.81	0.84	6.01	1.02
NBP1503_002-15	739	24.48	3.78	3.47	16.58	3.05	0.78	4.76	0.76	5.91	1.61	6.00	0.87	6.53	1.05
NBP1503_002-13	1237	29.30	4.23	4.26	17.61	3.47	1.00	5.17	0.82	6.01	1.77	6.01	0.88	6.97	1.17
NBP1503_002-11	1774	32.10	3.84	4.94	21.87	4.01	1.15	6.01	0.92	6.41	1.88	6.63	1.00	7.46	1.32
NBP1503_002-09	2367	36.51	4.24	5.37	23.73	4.46	1.31	5.86	1.18	7.41	2.00	6.91	1.11	8.59	1.29
NBP1503_002-07	2950	36.21	4.50	5.64	24.61	4.45	1.26	6.28	1.00	7.22	2.03	7.18	0.96	7.70	1.29
NBP1503_002-05	3679	37.68	4.97	5.86	25.06	5.10	1.18	6.87	1.01	7.68	2.10	7.16	0.96	7.64	1.25
NBP1503_002-03	4299	36.83	5.76	6.04	26.96	4.74	1.21	6.80	1.02	7.46	2.07	6.94	1.05	7.48	1.37
NBP1503_002-01	4397	37.50	5.84	6.23	26.73	5.05	1.31	6.75	1.14	8.12	2.15	7.28	1.15	7.66	1.31

Station 5 (-64.993°N, 130.406°E)															
NBP1503_005-08	10	23.28	4.97	3.37	15.72	2.94	0.79	4.36	0.75	5.65	1.67	5.77	0.88	4.94	0.97
NBP1503_005-06	101	28.19	7.96	4.02	17.84	3.12	0.87	4.65	0.80	6.39	1.86	6.54	0.87	5.64	1.06
NBP1503_005-04	341	31.21	9.38	4.65	20.64	3.98	0.86	5.05	0.89	6.32	1.85	6.11	1.05	5.83	1.30
NBP1503_005-02	502	32.56	11.35	4.93	22.29	3.88	1.08	5.53	0.99	7.20	1.92	6.34	0.90	6.08	1.25
Station 6 (-64.845°N, 130.400°E)															
NBP1503_006-16	10	21.72	4.22	3.30	14.73	2.54	0.72	4.07	0.70	4.92	1.41	5.43	0.80	5.81	0.94
NBP1503_006-14	80	25.48	6.24	3.98	16.29	3.09	0.76	4.55	0.67	5.46	1.51	5.33	0.80	5.46	0.91
NBP1503_006-12	298	28.26	6.67	4.23	18.30	3.85	0.81	5.35	0.85	5.78	1.69	6.03	0.83	6.64	1.03
NBP1503_006-10	792	33.49	5.54	5.21	21.13	4.34	0.93	5.53	0.99	7.11	1.91	6.23	0.91	7.05	1.22
NBP1503_006-08	1238	34.48	5.04	5.39	23.65	4.35	1.26	6.68	0.94	7.29	2.00	6.65	1.06	7.77	1.25
NBP1503_006-06	1482	34.26	5.91	5.65	23.71	4.48	1.01	6.30	0.91	7.37	1.92	6.86	0.89	6.80	1.14
NBP1503_006-04	1776	35.69	6.42	5.47	24.27	4.22	1.15	6.21	0.93	8.02	2.22	7.34	1.02	7.24	1.41
NBP1503_006-02	1889	36.66	6.59	5.58	25.11	4.25	1.14	6.63	1.04	7.93	2.24	7.19	1.05	6.84	1.31
Station 10 (-65.509°N, 122.404°E)															
NBP1503_010-17	10.30	25.30	6.45	3.86	17.05	3.01	0.68	4.50	0.75	5.69	1.66	5.84	0.86	5.74	0.99
NBP1503_010-14	75.63	25.74	7.36	4.20	17.21	2.80	0.73	4.49	0.66	6.14	1.70	6.02	0.84	4.96	1.04
NBP1503_010-06	338.09	31.59	10.91	5.07	21.81	3.34	1.01	5.23	0.99	6.63	1.89	6.52	0.93	6.16	1.08
NBP1503_010-02	419.72	29.01	6.20	4.41	19.35	3.09	0.93	5.63	0.86	6.64	1.90	6.44	0.96	6.20	1.16
Station 15 (-65.001°N, 122.007°E)															
NBP1503_015-24	10	24.17	5.53	3.85	15.93	2.82	0.77	4.76	0.64	5.00	1.42	5.33	0.79	5.63	0.90
NBP1503_015-21	120	29.36	10.01	4.75	20.11	3.78	0.81	4.59	0.82	6.59	1.83	5.93	0.94	5.27	1.10
NBP1503_015-18	398	29.82	5.77	4.50	19.46	3.39	0.87	5.29	0.90	6.93	1.89	6.65	0.93	6.16	1.29
NBP1503_015-15	1141	37.09	6.25	5.59	24.61	4.48	1.20	6.55	1.02	7.90	2.20	7.89	1.08	6.74	1.37
NBP1503_015-12	1579	37.57	7.93	6.20	28.39	4.90	1.05	6.33	1.12	7.58	2.28	7.20	1.15	7.05	1.40

NBP1503_015-08	1970	36.86	5.82	5.92	25.43	4.71	1.24	5.80	0.99	7.83	2.07	7.49	1.04	6.98	1.43
NBP1503_015-05	2401	36.93	6.90	6.03	25.34	4.74	1.13	6.95	1.06	8.16	2.23	6.93	1.02	7.31	1.43
NBP1503_015-02	2500	35.42	6.01	5.33	22.63	4.83	1.12	6.31	0.99	7.03	1.96	6.43	1.04	6.76	1.22
Station 18 (-65.659°N, 119.781°E)															
NBP1503_018-14	10	24.96	6.11	3.79	16.75	3.44	0.79	4.19	0.71	5.51	1.59	5.53	0.78	5.19	1.06
NBP1503_018-11	80	25.63	6.22	3.74	17.14	2.91	0.83	3.70	0.76	5.66	1.66	5.98	0.89	5.17	1.06
NBP1503_018-08	247	32.42	11.19	5.04	20.19	3.60	0.89	5.13	0.82	6.80	1.91	6.41	0.86	5.83	1.26
NBP1503_018-02	483	35.19	8.42	5.82	24.32	3.77	1.13	5.85	0.99	7.13	1.99	6.90	0.94	6.69	1.32
Station 24 (-65.149°N, 118.283°E)															
NBP1503_024-23	9	23.57	5.53	3.77	16.40	3.42	0.80	4.42	0.68	5.46	1.44	5.34	0.82	5.39	0.97
NBP1503_024-21	119	29.85	9.55	4.48	19.08	3.79	0.80	4.96	0.77	5.80	1.65	5.45	0.86	5.70	1.13
NBP1503_024-18	346	26.58	5.31	3.91	17.71	3.69	0.85	4.84	0.77	5.43	1.69	5.84	0.85	5.83	1.06
NBP1503_024-14	496	30.27	5.12	4.59	20.68	3.63	1.02	5.29	0.94	6.43	1.77	6.16	1.00	6.82	1.20
NBP1503_024-11	987	33.64	4.89	5.26	23.23	5.00	1.09	6.17	1.05	7.33	1.93	6.63	0.96	7.14	1.18
NBP1503_024-08	1481	35.39	5.11	5.47	23.11	4.38	1.16	6.57	1.04	6.97	2.01	6.80	1.02	7.90	1.30
NBP1503_024-06	1972	35.50	5.24	5.58	22.38	4.56	1.10	6.47	0.90	7.39	2.03	7.26	0.96	7.26	1.28
NBP1503_024-02	2083	36.76	5.26	5.47	24.61	4.28	1.13	6.11	1.00	7.58	1.95	6.94	1.03	7.49	1.28
Station 40 (-64.450°N, 128.366°E)															
NBP1503_040-06	2571	36.63	10.08	5.82	25.49	3.95	1.23	6.51	1.10	7.71	2.13	7.29	1.00	6.54	1.34
NBP1503_040-02	2669	37.22	7.88	5.97	26.64	4.37	1.29	6.54	1.08	8.30	2.36	7.75	1.13	6.66	1.37
Station 41 (-63.634°N, 128.365°E)															
NBP1503_041-24	10	23.75	4.55	3.50	14.97	3.09	0.80	4.21	0.63	5.25	1.49	5.13	0.75	5.57	0.91
NBP1503_041-22	198	26.81	4.70	4.04	17.11	3.30	0.87	4.60	0.82	6.39	1.80	6.09	0.90	5.87	1.07
NBP1503_041-20	396	31.86	10.64	4.75	19.99	3.74	0.98	5.25	0.91	6.29	1.79	5.96	0.84	6.78	1.17

NBP1503_041-18	693	29.38	3.93	4.38	17.56	3.94	0.93	4.60	0.83	6.38	1.75	6.21	0.90	6.43	1.13
NBP1503_041-16	987	31.59	4.12	4.67	20.07	4.19	0.95	5.63	0.87	6.67	1.76	6.57	0.90	6.70	1.24
NBP1503_041-14	1480	36.35	5.51	5.55	24.77	5.12	1.21	5.73	1.07	8.13	2.30	7.27	1.18	7.41	1.49
NBP1503_041-12	1972	37.29	5.32	5.93	25.69	4.72	1.17	6.54	1.11	8.40	2.19	7.22	1.04	6.98	1.44
NBP1503_041-10	2462	37.82	5.55	6.15	27.52	4.62	1.29	6.63	1.04	8.69	2.23	7.99	1.08	7.54	1.45
NBP1503_041-06	2950	37.43	5.74	6.19	24.46	4.95	1.10	6.86	0.98	7.69	1.93	7.04	1.10	7.77	1.31
NBP1503_041-04	3434	38.74	6.50	6.28	27.15	5.46	1.12	6.50	1.19	8.00	2.36	7.70	1.03	7.53	1.34
NBP1503_041-02	3533	38.76	6.26	6.27	27.11	4.59	1.25	6.94	1.14	8.61	2.31	7.39	1.09	7.08	1.35

Table A.3. Seawater Pb isotope and concentration measurements from the GS01 section between Australia and East Antarctica. Based on repeat analyses of low concentration Southern Ocean surface water (~7 pmol kg^{-1}), the external errors (2sd) for $^{208}Pb/^{207}Pb$, $^{206}Pb/^{207}Pb$, and $^{206}Pb/^{204}Pb$ ratios are approximately 0.0008, 0.0014 and 0.023, respectively (see section 3.3.1 and Table 3.1). The estimated error for Pb concentrations, calculated from the standard deviation of the triplicate mean averaged across all triplicate measurements, is 1.4 pmol kg^{-1} (1sd; n = 14). For information on the analytical methods and errors for Pb, see section 3.2 and 3.3.

Sample	Depth (m)	$^{208}Pb/^{207}Pb$	$^{206}Pb/^{207}Pb$	$^{206}Pb/^{204}Pb$	[Pb] (pmol/kg)	Pot. Temp (°C)	Salinity	Neutral density (kg m^{-3})
Station 15 (-49.278°N, 144.123°E)								
GS01-09-12	11	2.4252	1.1493	17.926	12.0	9.67	34.31	26.52
GS01-09-10	55	2.4271	1.1505	17.959	11.1	9.60	34.29	26.53
GS01-09-09	90	2.4296	1.1531	18.003	12.9	9.45	34.39	26.63
GS01-09-06	319	2.4230	1.1469	17.887	14.7	7.37	34.36	26.97
GS01-09-05	494	2.4266	1.1513	17.969	11.8	6.01	34.26	27.10
GS01-10-12	941	2.4269	1.1522	17.962	12.9	3.47	34.32	27.49
GS01-10-10	1972				11.0	2.19	34.71	27.95
GS01-10-07	2952				5.7	1.22	34.73	28.11
GS01-10-03	3928				6.5	0.81	34.71	28.16

Station 30 (-54.070°N, 141.599°E)								
GS01-17-12	11	2.4284	1.1531	17.981	9.1	4.48	33.81	26.89
GS01-17-10	50	2.4331	1.1564	18.063	7.3	4.10	33.81	26.94
GS01-17-09	75	2.4325	1.1582	18.059	8.4	2.05	33.87	27.23
GS01-17-06	298	2.4302	1.1556	18.024	11.9	2.33	34.35	27.64
GS01-18-12	990	2.4310	1.1556	18.015	11.3	2.11	34.71	27.96
GS01-18-09	1873	2.4472	1.1708	18.285	5.8	1.34	34.74	28.09
GS01-18-05	2217	2.4449	1.1711	18.258	5.8	1.00	34.72	28.14
GS01-18-01	2521	2.4452	1.1693	18.216	5.0	0.71	34.71	28.18
Station 40 (-58.851°N, 139.838°E)								
GS01-23-12	9	2.4260	1.1507	17.936	9.1	3.63	33.79	26.98
GS01-23-10	61	2.4290	1.1539	17.993	8.6	2.24	33.87	27.21
GS01-23-09	101	2.4323	1.1572	18.055	10.3	1.06	33.92	27.36
GS01-23-06	298	2.4300	1.1549	18.008	15.0	2.34	34.38	27.67
GS01-23-05	545	2.4331	1.1579	18.058	12.7	2.37	34.57	27.82
GS01-24-12	988	2.4389	1.1632	18.155	10.6	2.12	34.71	27.97
GS01-24-10	1970	2.4493	1.1725	18.314	6.1	1.23	34.74	28.11
GS01-24-06	2952	2.4578	1.1778	18.406	7.2	0.42	34.70	28.22
GS01-24-01	3810	2.4704	1.1864	18.536	6.5	0.01	34.68	28.28
Station 45 (-60.852°N, 139.856°E)								
GS01-26-12	16	2.4253	1.1490	17.901	9.0	1.71	33.63	27.03
GS01-26-10	54	2.4349	1.1588	18.056	10.7	0.43	33.72	27.22
GS01-26-09	109	2.4366	1.1609	18.098	9.7	-0.84	33.99	27.54
GS01-26-06	277	2.4351	1.1593	18.083	12.1	2.26	34.51	27.80
GS01-27-12	495	2.4370	1.1605	18.119	9.3	2.20	34.64	27.90
GS01-27-11	989	2.4429	1.1667	18.206	9.9	1.87	34.74	28.02
GS01-27-08	2071	2.4518	1.1740	18.343	4.9	0.91	34.72	28.15
GS01-27-06	2462	2.4573	1.1774	18.399	10.1	0.60	34.70	28.19

GS01-27-01	4314	2.4813	1.1947	18.702	8.2	-0.35	34.66	28.32
Station 51 (-63.853°N, 139.882°E)								
GS01-30-12	10	2.4328	1.1559	18.033	6.4	0.44	33.81	27.29
GS01-30-10	50	2.4439	1.1673	18.212	4.7	0.30	33.81	27.31
GS01-30-09	100	2.4468	1.1692	18.259	6.5	-1.07	34.21	27.77
GS01-30-06	297	2.4454	1.1690	18.245	7.3	1.46	34.66	28.00
GS01-30-05	495	2.4485	1.1716	18.298	10.2	1.16	34.73	28.11
GS01-31-12	990	2.4448	1.1680	18.231	6.1	1.16	34.73	28.10
GS01-31-09	1971	2.4615	1.1820	18.477	3.3	0.33	34.69	28.22
GS01-31-05	2950	2.4807	1.1959	18.725	3.6	-0.14	34.67	28.29
GS01-31-01	3642	2.4718	1.1914	18.655	4.1	-0.57	34.65	28.35
Station 56 (-65.398°N, 139.854°E)								
GS01-33-12	11	2.4449	1.1673	18.227	5.9	-0.32	33.85	27.38
GS01-33-10	50	2.4524	1.1747	18.355	4.9	-0.43	33.86	27.40
GS01-33-06	317				7.3	-0.17	34.58	28.06
GS01-33-05	485				5.4	0.51	34.67	28.13
GS01-34-12	989	2.4570	1.1793	18.425	6.6	0.26	34.68	28.22
GS01-34-09	1529	2.4660	1.1888	18.567	5.1	-0.14	34.67	28.28
GS01-34-05	1971	2.4633	1.1856	18.537	4.7	-0.42	34.65	28.32
GS01-34-01	2334	2.4707	1.1905	18.642	6.1	-0.46	34.65	28.33

Appendices

Appendix 3: Publication 'Neodymium in the ocean: a global database, a regional comparison and implications for palaeoceanographic research'

Appendix 3 presents a paper published in 2016 based on the compilation of global neodymium isotope and hydrographic data.

PHILOSOPHICAL TRANSACTIONS A

rsta.royalsocietypublishing.org

Discussion

Cite this artide: van de Flierdt T, Griffiths AM, Lambelet M, Little SH, Stichel T, Wilson DJ. 2016 Neodymium in the oceans: a global database, a regional comparison and implications for palaeoceanographic research. *Phil. Trans. R. Soc. A* **374**: 20150293. http://dx.doi.org/10.1098/rsta.2015.0293

Accepted: 10 August 2016

One contribution of 20 to a discussion meeting issue 'Biological and climatic impacts of ocean trace element chemistry'.

Subject Areas:
biogeochemistry

Keywords:
dissolved neodymium isotopes, dissolved neodymium concentrations, dissolved aluminium concentrations, seawater, geotraces, palaeoceanography

Author for correspondence:
Tina van de Flierdt
e-mail: tina.vandeflierdt@imperial.ac.uk

Electronic supplementary material is available online at https://dx.doi.org/10.6084/m9.figshare.c.3491598.

THE ROYAL SOCIETY PUBLISHING

Neodymium in the oceans: a global database, a regional comparison and implications for palaeoceanographic research

Tina van de Flierdt[1], Alexander M. Griffiths[1], Myriam Lambelet[1], Susan H. Little[1], Torben Stichel[2] and David J. Wilson[1]

[1]Department of Earth Science and Engineering, Imperial College London, South Kensington Campus, London SW7 2AZ, UK
[2]Ocean and Earth Science, National Oceanography Centre Southampton, University of Southampton, Southampton SO14 3ZH, UK

TvdF, 0000-0001-7176-9755

The neodymium (Nd) isotopic composition of seawater has been used extensively to reconstruct ocean circulation on a variety of time scales. However, dissolved neodymium concentrations and isotopes do not always behave conservatively, and quantitative deconvolution of this non-conservative component can be used to detect trace metal inputs and isotopic exchange at ocean–sediment interfaces. In order to facilitate such comparisons for historical datasets, we here provide an extended global database for Nd isotopes and concentrations in the context of hydrography and nutrients. Since 2010, combined datasets for a large range of trace elements and isotopes are collected on international GEOTRACES section cruises, alongside classical nutrient and hydrography measurements. Here, we take a first step towards exploiting these datasets by comparing high-resolution Nd sections for the western and eastern North Atlantic in the context of hydrography, nutrients and aluminium (Al) concentrations. Evaluating those data in tracer–tracer space reveals that North Atlantic seawater

Nd isotopes and concentrations generally follow the patterns of advection, as do Al concentrations. Deviations from water mass mixing are observed locally, associated with the addition or removal of trace metals in benthic nepheloid layers, exchange with ocean margins (i.e. boundary exchange) and/or exchange with particulate phases (i.e. reversible scavenging). We emphasize that the complexity of some of the new datasets cautions against a quantitative interpretation of individual palaeo Nd isotope records, and indicates the importance of spatial reconstructions for a more balanced approach to deciphering past ocean changes.

This article is part of the themed issue 'Biological and climatic impacts of ocean trace element chemistry'.

1. Introduction

Long-lived radiogenic isotope systems are characterized by slow decay of the parent isotope compared with the age of the Solar System. In the samarium–neodymium (Sm–Nd) system, radioactive ^{147}Sm decays to the radiogenic daughter ^{143}Nd with a half-life of 106 billion years. Ingrowth of ^{143}Nd, together with differentiation of Sm and Nd during melting, has led to characteristic ^{143}Nd/^{144}Nd fingerprints in rocks, which vary as a function of age and lithology. Early applications of this decay system focused on geochronology, high-temperature geochemistry and cosmochemistry. The Nd isotopic composition is typically expressed in the epsilon notation (ε_{Nd}), which denotes the deviation of a measured ^{143}Nd/^{144}Nd ratio from the bulk Earth/chondritic uniform reservoir (CHUR) ratio of 0.512638 in parts per 10 000 [1]. (We acknowledge that there is an ongoing discussion as to whether the bulk Earth actually has a chondritic composition for Sm/Nd (see Huang *et al.* [2] and references therein).)

In the late 1970s, the first direct measurements of Nd isotopes in seawater were accomplished [3,4]. Taken together with indirect seawater measurements, using ferromanganese crusts as archives [4–6], the picture soon emerged that seawater ^{143}Nd/^{144}Nd ratios show a clear provinciality between the different ocean basins [7]. The lowest ^{143}Nd/^{144}Nd ratios were observed in newly formed North Atlantic Deep Water (NADW, $\varepsilon_{Nd} \sim -13.5$), the highest ratios occurred in North Pacific Deep Water (PDW, $\varepsilon_{Nd} \sim -4$), and intermediate values were found in the deep Indian and Southern Oceans ($\varepsilon_{Nd} \sim -7$ to -9). These observations pointed to a residence time of Nd in the deep ocean that is shorter than the deep water transit time between the North Atlantic and the North Pacific, giving rise to the promise of using Nd isotopes as a tracer for water mass sourcing and global ocean circulation ([8]; see also summaries by Goldstein & Hemming [9] and Frank [10]).

Reconstructions of authigenic (seawater-derived) Nd isotope records have been performed for a wide range of time scales and resolutions, from the Archaean to the present day. In particular, a growing number of Late Pleistocene records lend strong support to the notion that Nd isotopes may serve as a tracer for past water mass provenance and ocean circulation, particularly in the Atlantic Ocean [11–19]. However, quantitative use of the tracer is difficult at best, and simplifications have been necessary in order to derive (qualitative) interpretations of past changes. For example, it has often been assumed that the Nd isotopic composition of NADW is uniform and constant [8,9] and that mixing between water masses is largely conservative within an ocean basin. In contrast, recent studies have questioned the constancy of global endmembers through time [20–22] or pointed to non-conservative behaviour [23].

One important question is that of exactly *how* seawater acquires its Nd isotopic composition. This fundamental question is not yet fully resolved, although the general relationship with continental lithology is clear [24]. While early work suggested that the predominant inputs of Nd were via the dissolved riverine load and atmospheric dust [25,26], it has since emerged that the dissolved fluxes from rivers and dust alone are insufficient to close the mass balance of Nd in the ocean ([27,28], see also [29]). Interaction between sediments and seawater along continental margins (i.e. 'boundary exchange' [23,24]) is now thought to dominate the

oceanic Nd budget [30–32]. In detail, both addition and removal of dissolved Nd can be observed during particulate–seawater exchange in marginal settings, involving processes such as adsorption/desorption, isotopic exchange or dissolution/precipitation [33]. One recent example from observational data is the dissolution of riverine particulate matter from the Amazon in the Atlantic Ocean [33,34]. Further suggestions for Nd additions to the ocean have included submarine groundwater discharge [35] and benthic fluxes from porewaters [36,37].

A further puzzle in the marine biogeochemical cycle of Nd and its isotopes is the partial decoupling between concentrations and isotopes, commonly referred to as the Nd paradox [9]. Away from ocean margins and areas of sluggish circulation, Nd isotopes in deep waters typically behave conservatively (i.e. they are only modified by mixing with other water masses). In contrast, Nd concentrations often show a (linear) increase with water depth, an observation that has been explained through the process of reversible scavenging [38,39]. However, recent results on dissolved rare-earth elements (REEs) from the CoFeMUG cruise in the South Atlantic [40], in conjunction with quantitative deconvolution of water masses, demonstrated that a large fraction (greater than 75%) of dissolved light REEs in deep waters are preformed. High bottom water concentrations in that region were explained by remineralization of particles, either *in situ* or along the flow path of Antarctic Bottom Water (AABW) [40].

In order to advance understanding of the interplay of biogeochemical and physical processes affecting dissolved Nd (and other REEs), and in order to provide a more grounded modern-day understanding for palaeo applications of Nd isotopes, Nd isotopes were designated as one of the key parameters in the international GEOTRACES programme (www.geotraces.org). GEOTRACES is a global study to understand the marine biogeochemical cycles of trace elements and their isotopes, and the sea-going phase of the programme was launched in 2010 [41]. Here, we present three different approaches to reflect on the status of pre-GEOTRACES and initial GEOTRACES work on dissolved Nd isotopes and concentrations in seawater, including their significance for palaeoceanographic reconstructions. We begin by presenting a new global database for seawater Nd isotopes and concentrations in the context of hydrography and macronutrients, via the GEOTRACES International Data Assembly Centre (and as electronic supplementary material). In the second part, we carry out a comparison of recently published Nd isotope and concentration data, hydrography, nutrients and Al concentration data from two of the first GEOTRACES transect cruises, in the northwest and northeast Atlantic Ocean. Finally, we reflect on the significance of our observations for the use of Nd isotopes as a palaeoceanographic tracer.

2. An updated global database for neodymium isotopes and concentrations

(a) Rationale

Lacan *et al.* [42] published a global compilation of seawater Nd isotopes and concentrations, which included all published data up to 1 September 2011. It consisted of 880 Nd isotope data points, which were the primary selection criteria for the database (i.e. seawater stations where only REE or Nd concentrations were measured were not included) [42]. Here, we present a similar database, compiled independently and enlarged to contain all data published by 1 January 2016 (i.e. an additional approx. 1000 data points published between 2011 and 2015, which were collected outside the GEOTRACES programme and hence are not always contained in dedicated national and international data centres). Furthermore, and for the first time, to the best of our knowledge, we provide historical Nd isotope and concentration data alongside hydrography data extracted and calculated from the original publications (i.e. temperature, salinity, potential/neutral density and nutrient contents) to facilitate comparison of Nd isotopes and concentrations with basic hydrography.

The rationale for compiling and presenting this database follows from the GEOTRACES-driven shift in the way chemical oceanographic data are collected and archived. International GEOTRACES cruises are only approved as such if they facilitate the collection of a range of

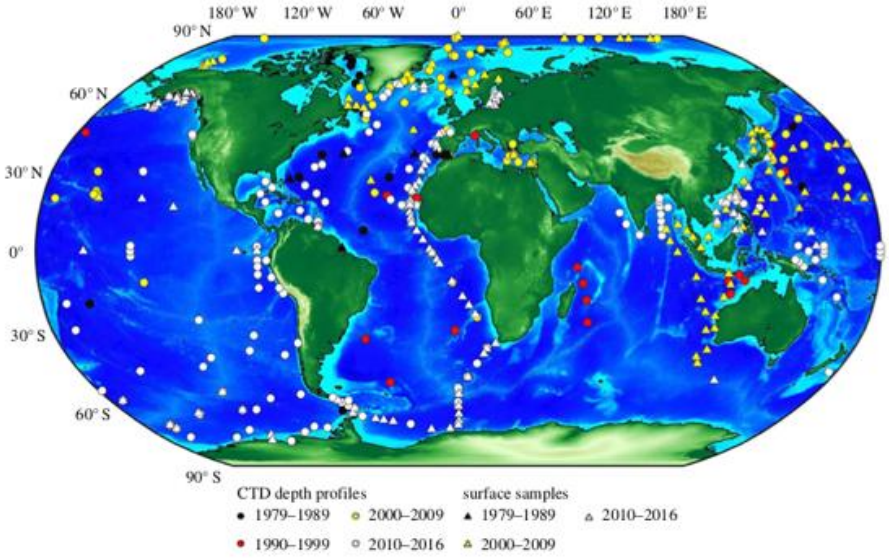

Figure 1. Map of global locations analysed for seawater Nd isotopes and concentrations (CTD = conductivity, temperature and depth). Circles correspond to depth profiles (i.e. three or more samples at one station) and triangles show surface samples only. Colour coding denotes the time period of data publication (see legend). Database compiled from [3,4,27,36,43–96].

key trace element and isotope data (TEIs) [41]. Alongside these key TEIs, classical hydrography and nutrient measurements are routinely carried out. All data are subsequently archived and made publicly available through the GEOTRACES International Data Assembly Centre, hosted at the British Oceanographic Data Centre (www.bodc.ac.uk/geotraces/data). However, such a streamlined documenting and archiving process is a relatively new development for TEIs. Our compilation effort aims to close the gap between historical datasets and new GEOTRACES datasets, and thereby benefit the global community of chemical oceanographers, palaeoceanographers and modellers. A similar database for the full suite of dissolved REEs has been compiled by X. Zheng, Y. Plancherel and P. Scott (http://www.bodc.ac.uk/geotraces/data/historical/). While clearly beneficial towards understanding global Nd cycling, a full evaluation of combined seawater REE and Nd isotope data is beyond the scope of this study.

(b) Observations

The new database is available under the following link: http://www.bodc.ac.uk/geotraces/data/historical/. We encourage the community to make us aware of any potential mistakes or oversights in the database.

As of January 2016, a total of approximately 2200 data points have been published for the Nd isotopic composition of seawater, which is more than double the amount of data available in 2011. In detail, figure 1 (and the online database) reveals that efforts in the 1980s and 1990s each contributed approximately 150 published data points, accomplished by a small number of laboratories. This number almost quadrupled in the 2000s (approx. 570 new data points) and more than doubled again in the last 5 years (approx. 1350 new data points). More seawater measurements have been carried out in the past 5 years than in the preceding 30 years. This major increase in data coverage since the 2000s can be partially attributed to the advance of multicollector inductively coupled plasma mass spectrometry (MC–ICP–MS), facilitating more rapid data generation, coupled to an increase in sea-going efforts and higher sampling resolution at each station. Together with the rising number of laboratories involved in the analysis of seawater Nd isotopic compositions and concentrations, this progress reflects the momentum

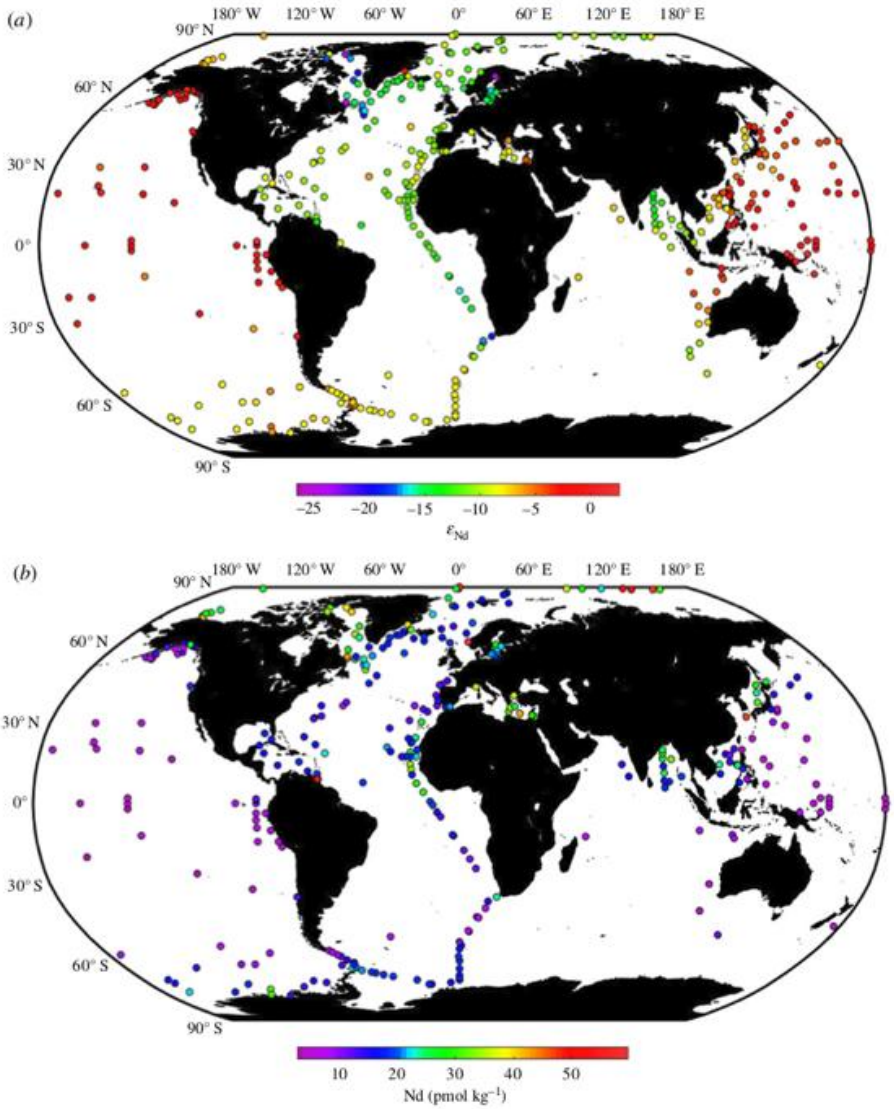

Figure 2. Map of surface (or shallow subsurface) seawater (*a*) Nd isotopic compositions and (*b*) Nd concentrations. Locations shown are restricted to those that yielded data within the top 100 m of the water column. Where measurements were made at multiple depths in one location, only the shallowest data are shown. In order to visualize the main features of the Nd distribution in the open ocean, stations with Nd concentrations greater than 60 pmol kg^{-1} are not shown. For references, see figure 1 and database.

generated by the launch of the GEOTRACES programme in 2006 [43,97]. Given that more than 50 GEOTRACES cruises (section cruises, process studies and international polar year cruises) have already taken place, with only partial Nd data from a handful of these cruises published so far, another pronounced increase in data coverage over the next 5–10 years is to be expected.

The database contains both filtered and unfiltered seawater samples. For operational reasons, many of the older data were generated from unfiltered seawater, whereas most of the newer data are being obtained from filtered seawater (typically 0.2–0.45 µm pore size filters). Given that

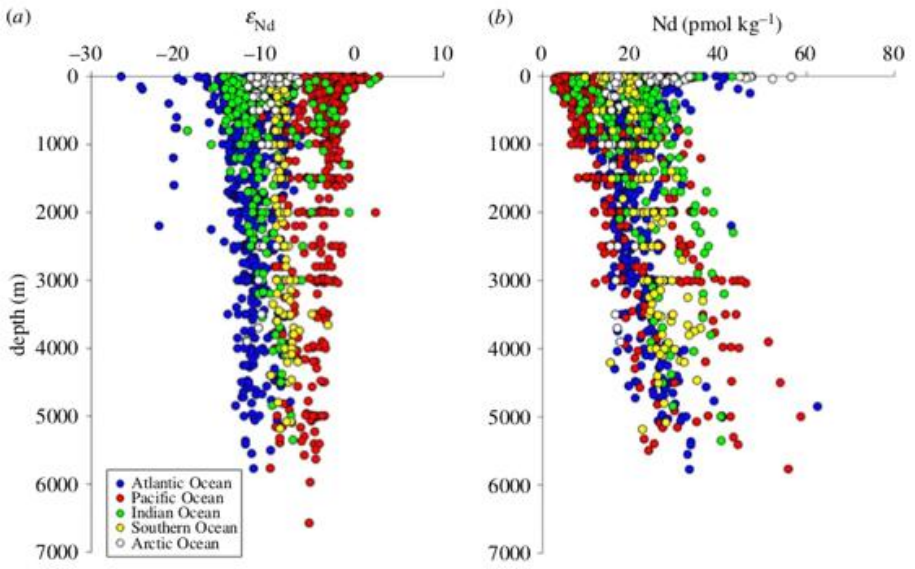

Figure 3. Global depth profiles for seawater (*a*) Nd isotopic compositions and (*b*) Nd concentrations. Colour coding corresponds to different geographical regions. For simplicity, the Arctic Ocean was defined as the area north of 78°N in the Atlantic realm, and north of 71°N in the Pacific realm. The Southern Ocean was defined as latitudes south of 60°S. Data from the marginal seas (i.e. Caribbean, Mediterranean, Baltic and South China seas) are not shown. For better visualization, six data points below 7000 m from the northwest Pacific Ocean [54] are not shown. For references, see figure 1 and global database.

particulate Nd only constitutes approximately 5% of the total seawater Nd budget [28,98,99], we would expect open ocean seawater to yield the same Nd isotopic composition in filtered and unfiltered samples [43]. However, this assumption may not be valid in areas with pronounced benthic nepheloid layers (BNLs), turbulent flow, high continental inputs and/or drastic differences between particulate and dissolved Nd isotopic compositions.

Surface ocean Nd concentrations range from approximately 3 to approximately 60 pmol kg^{-1} (omitting three data points) and Nd isotopic compositions cover a range of 30 epsilon units from $\varepsilon_{Nd} \sim -27$ to approximately +3 (excluding measurements directly at river mouths or in fjords). The lowest (i.e. least radiogenic) ε_{Nd} values are observed in the area of Baffin Bay (Labrador Sea, northwest Atlantic) and the highest (i.e. most radiogenic) ε_{Nd} values are found in the Pacific Ocean. When considering Nd concentrations, higher values ([Nd] > 20 pmol kg^{-1}) are observed in surface waters proximal to continental input sources (e.g. Baffin Bay, Bay of Bengal, Mediterranean Sea). Surface waters in many areas of the Pacific Ocean show lower Nd concentrations ([Nd] < 10 pmol kg^{-1}; figure 2), reflecting a lack of significant surface inputs to remote parts of this large ocean basin, as well as the efficient removal by particle scavenging in some marginal areas [44].

Neodymium concentration profiles increase with water depth in most regions of the global ocean (figure 3*b*), with the exception of marginal seas and areas of strong convection and/or modified particle–seawater dynamics, which instead show invariant vertical concentration profiles (e.g. Arctic Ocean, Nordic Seas, Labrador Sea, Atlantic subpolar gyre, Caribbean, Mediterranean). The often-quoted statement that deep water Nd is generally lower in the North Atlantic and higher in the Pacific and correlates with silicate (see [9] and references therein) does seem to exclude data from the South Atlantic, Southern Ocean and Indian Ocean (figure 4). Zheng *et al.* [40] concluded that linear correlations of dissolved REEs and Si in Atlantic deep waters are due to predominantly conservative behaviour of both elements rather than similar chemical behaviour. This point is further supported by the data compiled in figure 4*b*. In fact, Atlantic deep

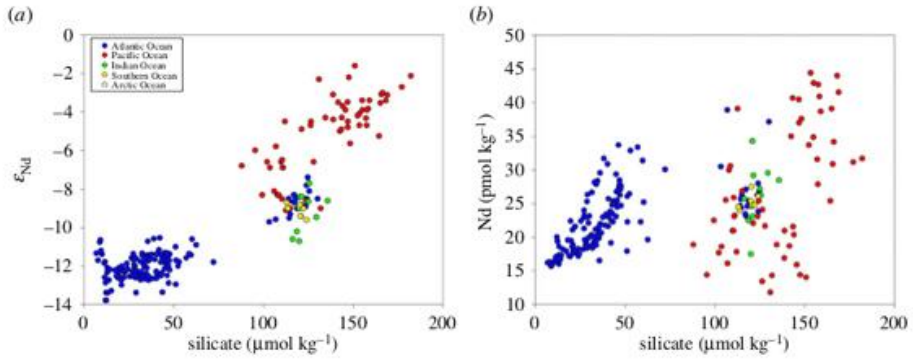

Figure 4. Published samples for which dissolved Si concentrations were available alongside (*a*) Nd isotopic compositions and (*b*) Nd concentrations from water depths below 2000 m. Note that high Nd concentrations are a persistent feature of bottom water layers around the world, and are not observed at all locations in the Pacific Ocean. For references, see figure 1 and global database.

waters describe different slopes in Si versus Nd space, with increasing Si and Nd concentrations with water depth. However, data from the Southern Ocean, Indian Ocean and Pacific Ocean do not continue the same trend and are rather scattered, particularly in areas where biogeochemical processes dominate over physical water mass advection (e.g. [44]; see also [39] and [100]).

3. Western and eastern North Atlantic GEOTRACES sections GA02 and GA03: neodymium, hydrography and nutrients

(a) Study area

To take a closer look at the impact of vertical and lateral processes on the distribution of seawater Nd concentrations and isotopic compositions, we compare the more detailed results of two of the first full GEOTRACES section cruises, which sailed in the North Atlantic between 2010 and 2012 (figure 5). The meridional Dutch GEOTRACES section GA02 covers the full length of the Atlantic Ocean from east of Greenland to the southern Argentinian shelf. Sixty stations were sampled on four cruises between 2010 and 2012, and seawater Nd isotopes and concentrations were determined and published from 12 of the northernmost stations by Lambelet *et al.* [45] (figure 5). The US GEOTRACES section GA03 is located in the subtropical eastern North Atlantic and sailed in two legs in 2010 and 2011. The first leg sampled along a quasi-meridional section extending from Portugal to the coast of Mauritania and a short zonal section to the Cape Verde Islands. The second leg extended sampling from Woods Hole to the Cape Verde Islands in a zonal section across the subtropical North Atlantic. In total, 36 stations were sampled, and seawater from nine stations from the first leg in the eastern North Atlantic has been analysed for Nd isotopes and concentrations and published by Stichel *et al.* [46] (figure 5).

(b) Hydrography

Detailed descriptions of section hydrographies are available from Jenkins *et al.* [102], Lambelet *et al.* [45] and references therein. Key features are highlighted in figures 5 and 6 and are summarized below.

Surface waters in both sections are influenced by the clockwise circulation in the subtropical gyre (approx. 10–40°N), and the anticlockwise flow of the subpolar gyre (north of approx. 50°N). Thermocline waters in the subtropical area are North Atlantic central waters (NACW; approx. 50–750 m depth), in their western and eastern varieties, including Subtropical Mode Water (STMW).

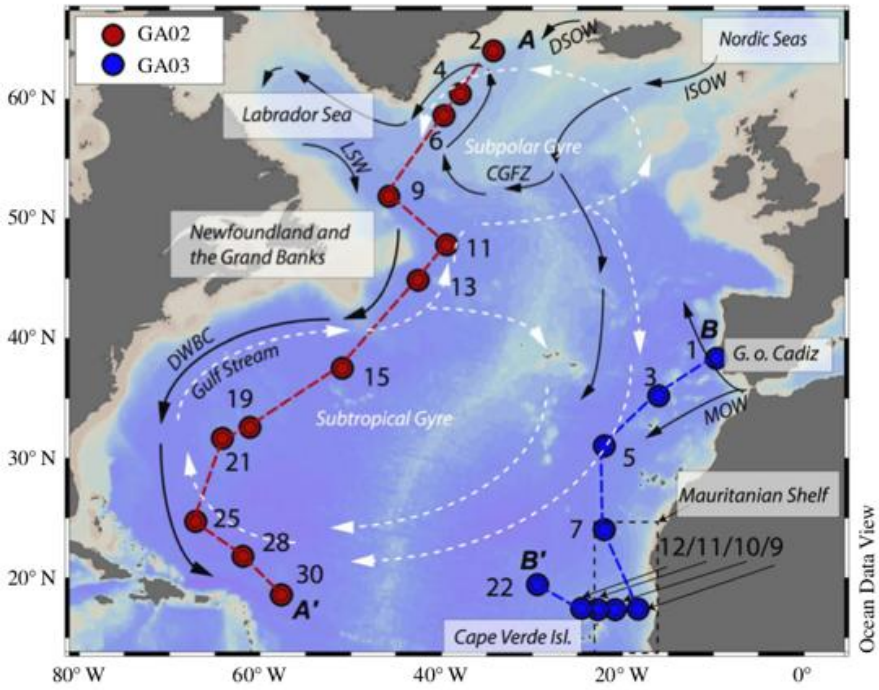

Figure 5. Stations analysed for Nd isotopic compositions and concentrations from Dutch GEOTRACES section GA02 (red) and US GEOTRACES section GA03 (blue), as well as geographical and hydrographic features in the North Atlantic. The main pathways of surface (white dashed arrows) and deep (black solid arrows) water masses are shown schematically. CGFZ, Charlie–Gibbs fracture zone; DSOW, Denmark Strait Overflow Water; DWBC, Deep Western Boundary Current; ISOW , Iceland–Scotland Overflow Water; LSW, upper and classical Labrador Sea Water; MOW, Mediterranean Outflow Water. Dashed lines labelled A to A′ and B to B′ illustrate the section lines of GA02 and GA03, respectively, shown in figures 6 and 9. Map visualized using the software Ocean Data View [101].

Fresher and cooler Atlantic equatorial water dominates the thermocline of the Mauritanian upwelling part of the eastern section [102].

Upper Labrador Sea Water (ULSW) and classical Labrador Sea Water (LSW) are formed in the southern Labrador Sea (figure 5) and exported southwards at intermediate depth, where they constitute the upper part of NADW. Higher chlorofluorocarbon (CFC) concentrations along the upper NADW flow path in the Deep Western Boundary Current (DWBC) highlight the more recently ventilated parts of the water column in the west compared with the east (figure 6). A distinct feature at similar water depths and latitudes south of approximately 35°N in the eastern Atlantic Ocean is the Mediterranean Outflow Water (MOW), which is distinguished by its high salinity and high potential temperature ($S = 36.4$, $\theta = 12°C$). Upon exit through the Straits of Gibraltar into the eastern Atlantic basin, MOW mixes with deeper Antarctic Intermediate Water (AAIW, approx. 800–1300 m), which, in turn, dominates the intermediate water column around the Mauritanian upwelling area ([102]; figure 6).

The deeper parts of NADW are comprised Iceland–Scotland Overflow Water (ISOW) and Denmark Strait Overflow Water (DSOW). Both these water masses are only present in rather dilute form in the North Atlantic, as they are modified from their source water compositions upon passing the sills separating the Nordic Seas from the open subpolar North Atlantic (figure 5), to form Northeast Atlantic Deep Water and Northwest Atlantic Bottom Water, respectively [103] (figure 6). While DSOW is detected in the northern stations along western section GA02, ISOW

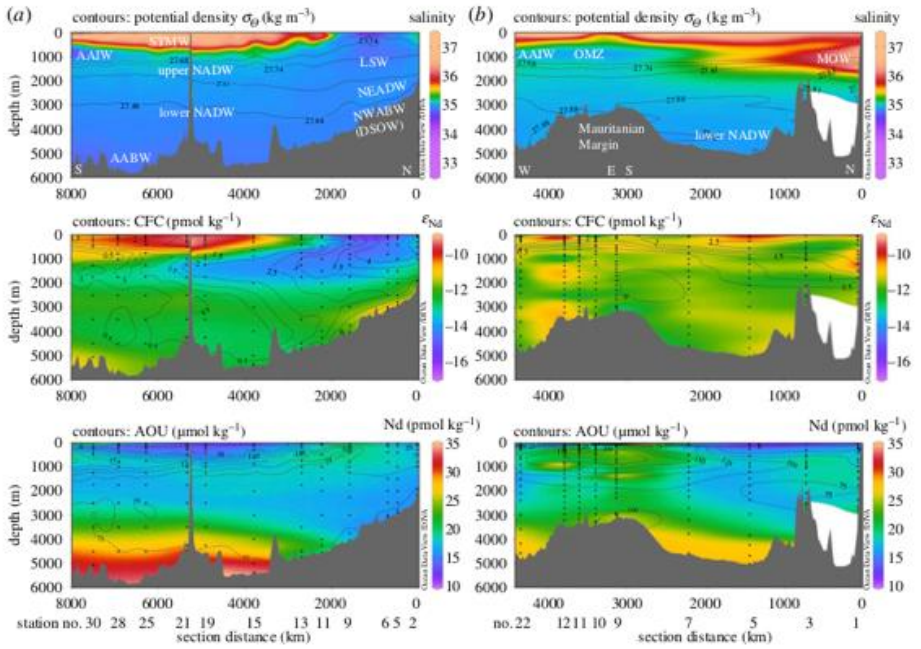

Figure 6. Hydrographic sections of (*a*) GA02 and (*b*) GA03 along A–A′ and B–B′, respectively (see figure 5 for section lines). Upper panel: salinity (coloured) with potential density anomaly relative to the surface isopycnals defining the main water masses; STMW, Subtropical Mode Water; (U)LSW = (upper) Labrador Sea Water; AAIW, Antarctic Intermediate Water; MOW , Mediterranean Outflow Water; NEADW, Northeast Atlantic Deep Water; NADW, North Atlantic Deep Water; NWABW, Northwest Atlantic Bottom Water; DSOW, Denmark Strait Overflow Water; and AABW, Antarctic Bottom Water. Middle panel: dissolved Nd isotopic compositions expressed as ε_{Nd} (coloured) with trichlorofluoromethane (CFC-11) isolines (CFC data from [45] and [102]). Bottom panel: dissolved Nd concentration (coloured) with apparent oxygen utilization (AOU) isolines. Numbers below the sections are station numbers. Data were visualized using the software Ocean Data View [101].

seems more significant for influencing deep water properties in the eastern basin [102]. In the subtropical deep Atlantic, both water masses are here combined and labelled as lower NADW (figure 6).

In the subtropical western and eastern North Atlantic, NADW flows southwards below AAIW and above AABW, two water masses formed in the Southern Ocean. Their northward export is more pronounced in the east, as traced by high concentrations of macronutrients, which stand out against nutrient-poor northern-sourced water masses (not shown).

In summary, the key differences between the western and eastern sections are (i) the strong flow associated with the DWBC in the western basin, and its associated strong export of LSW, (ii) the occurrence of MOW and an oxygen minimum zone (OMZ) off Mauritania in the eastern basin and (iii) the more pronounced influence of southern-sourced water in the east, and northern-sourced water in the west.

(c) Neodymium concentrations, isotopic compositions and nutrients

Neodymium concentrations range between 15 and 25 pmol kg^{-1} in most of the intermediate to deep waters in both sections (figure 6). Lower values are observed in the surface and subsurface waters in the subtropics, whereas higher values are observed in surface waters close to the Mauritanian shelf and west of the Cape Verde Islands, as well as below approximately 4000 m

water depth in both sections (figure 6). While maximum Nd concentrations in bottom waters in the eastern Atlantic are 28.5 pmol kg^{-1}, slightly higher values of up to 33.4 pmol kg^{-1} are observed in bottom waters along the deeper southern part of the western transect. With the exception of the subpolar area (GA02) and the pronounced OMZ off Mauritania (GA03), Nd concentrations below 2000–2500 m increase almost linearly with water depth in both eastern and western basins.

Neodymium isotopic compositions in both sections are largely described by ε_{Nd} values between −11 and −13 (figure 6). Higher values are observed in subtropical (sub)surface waters, and lower values are displayed in a well-defined tongue of LSW expanding southwards in the western basin ($\varepsilon_{Nd} = -13.7 \pm 0.9$) [45]. Overall, most stations along the eastern section reveal a rather homogeneous Nd isotopic composition with depth, whereas the profiles in the western section show pronounced patterns related to the prevailing water masses in the region of DWBC flow (i.e. outside the subpolar gyre). Notably, the typical composition of MOW ($\varepsilon_{Nd} = -9.4 \pm 0.6$) [47] is only hinted at in the northernmost station in the Gulf of Cadiz ($\varepsilon_{Nd} = -10.3$ to -10.8 between 657 and 1482 m water depth; station 1 in figure 5). For reference, table 1 summarizes our best estimates for the source compositions of key intermediate and deep water masses in the North Atlantic.

Overall, seawater Nd concentrations and isotopic compositions are partially decoupled (i.e. the Nd paradox; figure 7). Neodymium concentrations correlate well with nutrients in the upper water column, owing to the adsorption of Nd onto (organic) particles and subsequent release upon remineralization [45,46]. The exceptions are areas of surface Nd input around Grand Banks (GA02; Labrador Current) and the Mauritanian shelf (GA03; dust input; figure 6). Minimum Nd concentrations are observed over the depth of the mixed layer, below which they start to increase alongside phosphate concentrations, consistent with the fact that approximately 50% of the phosphate in the upper water column is regenerated, and with the hypothesis that scavenged Nd is released when organic matter is remineralized. Notably, the phosphate maximum and the coincident Nd concentration maximum are both more strongly expressed in the eastern basin than in the western basin (figure 7). Below that level, Nd concentrations decrease slightly with depth, are fairly constant between 1000 and 2500 m depth, and then increase towards the bottom. These features are observed throughout the subtropics, with zonally remarkably similar Nd concentrations, in contrast to distinct phosphate concentrations in both sections (figure 7*b*; cf. figure 7*d*). The similarity in the Nd concentration profiles also differs from the rather distinct shapes of the Nd isotope profiles between the sections (figure 7*b*; cf. figure 7*a*), suggesting at least partially different controls on these properties.

If Nd isotopes can be used as a tracer for ocean circulation, then ε_{Nd} values should delineate the main deep water masses in a similar way to the conservative water mass tracer phosphate star (PO_4^{3-*}; also called 'initial phosphate', P*; where $P^* = PO_4^{3-}{}_{observed} + (O_2/175) - 1.95$; [104]). Phosphate star expresses the preformed component of phosphate in the ocean, which behaves conservatively as long as the revised Redfield ratio of oxygen consumption to phosphate remineralization in the deep ocean is constant (175 : 1 [106,107]). In order to calculate the conservative tracer P*, nutrient data for the GA02 and GA03 cruises from the GEOTRACES intermediate data product (IDP2014) are used [105]. The east–west separation in phosphate concentrations is also visible for derived P* values (figure 7), indicating a greater contribution of southern-sourced water masses (higher P* values) in the middle and deep depths of the eastern basin compared with the western basin, consistent with hydrographic analyses [102].

Considering P*, ε_{Nd} and Nd concentration results from both sections for intermediate and deep water masses only, some interesting trends are observed (figure 8). First, a strong correlation is displayed for ε_{Nd} versus 1/Nd for all stations sampled in the subpolar gyre (GA02), and for intermediate depth stations in the subtropical gyre (GA02), describing a mixing line between LSW and DSOW (figure 8*a*). This strong correlation suggests conservative behaviour of both dissolved Nd isotopes and Nd concentrations in a significant fraction of the samples analysed from GA02. No such correlation can be observed for the GA03 data, mainly due to the absence of the distinct LSW and DSOW signature away from the DWBC. Second, both datasets describe

Table 1. Source water masses with hydrographic characteristics.

abbreviations	full name	salinity	pot. temp. Θ (°C)	O_2 (μmol kg^{-1})	silicate (μmol kg^{-1})	nitrate (μmol kg^{-1})	phosphate (μmol kg^{-1})	pot. dens. σ_θ (kg m^{-3})	ε_{Nd}	Nd (pmol kg^{-1})	P*
AAIW	Antarctic Intermediate Water	34.139 ± 0.250	3.26 ± 0.52	257.4 ± 85.6	15.6 ± 5.5	27.5 ± 3.3	1.9 ± 0.1	27.17 ± 0.25	−8.0 ± 0.3	11.1	1.4
ULSW	Upper Labrador Sea Water	34.896 ± 0.015	3.84 ± 0.32	265.6 ± 5.6	9.3 ± 0.1	16.8 ± 0.1	1.1 ± 0.0	27.72 ± 0.02	−14.34 ± 0.13	18.5 ± 0.2	0.7
LSW	Labrador Sea Water	34.906 ± 0.023	3.45 ± 0.40	268 ± 3.1	10.6 ± 1.9	17.0 ± 0.3	1.1 ± 0.0	27.77 ± 0.06	−14.15 ± 0.07	18.1 ± 0.0	0.7
MOW	Mediterranean Outflow Water	38.462 ± 0.021	13.06 ± 0.06	189.9 ± 0.2	8.3 ± 0.6	8.6 ± 0.2	0.4 ± 0.0		−9.4 ± 0.6	23.3 ± 4.2	−0.5
ISOW	Iceland–Scotland Overflow Water	34.899 ± 0.007	−0.49 ± 0.36	317.0 ± 12.8	10.2 ± 1.2	12.9 ± 0.7	1.0 ± 0.1	28.03 ± 0.08	−8.2 ± 1.8	19.9 ± 5.3	0.9
DSOW	Denmark Strait Overflow Water	34.890 ± 0.028	−0.43 ± 0.59	315.5 ± 0.4	9.8 ± 4.4	13.9 ± 1.1	1.0 ± 0.1	28.02	−8.3 ± 0.2	15.9 ± 3.5	0.9
AABW	Antarctic Bottom Water	34.657 ± 0.016	−0.47 ± 0.45	234.9 ± 17.4	124.4 ± 3.6	33.3 ± 0.6	2.3 ± 0.0	27.85 ± 0.01	−9.1 ± 0.7	26.5 ± 2.4	1.7

The Nd isotopic composition and concentrations were chosen as the best guess for the endmember, so the closest to the source area of the water mass (i.e. by nature, most of these values are not sampled in sections GA02 and GA03). Where possible, the hydrographic data were taken for the same sample as the Nd data (e.g. AABW, AAIW, LSW and ULSW). Where the hydrographic data were not available for a corresponding Nd sample, they were taken from the following database: http://ocean.ices.dk/HydChem/HydChem.aspx?plot=yes and were chosen in order to match as closely as possible the salinity (and/or any other hydrographic data available) of the Nd sample.

The errors represent two sigma standard deviations.

AAIW: Neodymium and hydrographic data are from [86]: one sample from station 244 (200 m depth) and one from station 250 (500 m depth). The concentration was available for the sample from station 250 only. The samples were filtered, and collected between February and April 2008.

ULSW: Neodymium and hydrographic data are from the GA02 cruise [45]: two samples from station 9 (800 and 1000 m depth). Samples were filtered, and collected in May 2010.

LSW: Neodymium and hydrographic data are from the GA02 cruise [45]: two samples from station 9 (1250 and 1735 m depth). Samples were filtered, and collected in May 2010.

MOW: Neodymium data from [47]: two samples from station MED-15 (150/250 m and 400/500 m). Samples were filtered, and no collection data were available. Hydrographic data: ICES Data Centre, cruise 35JC, station 8, $n = 5$. Collected in October 1981.

ISOW: Neodymium data are from [49]: three samples from station SGN 23 (between 600 and 1000 m depth). Station 23 is situated above the sill of the Faroe Scotland gap and represents 'proto ISOW' (i.e. before the entrainment of LSW and modified North Atlantic water). The samples were not filtered, and concentrations reported are as if filtered (i.e. considering that 5% of Nd is present in particulate form). Samples collected in August 1999. Hydrographic data: ICES Data Centre, cruise 74SC, station 326, $n = 3$. Collected in September 1999.

DSOW: Neodymium data are from [50]: one sample from station SGN 55 (610 m depth). The Nd isotopic composition was measured on a filtered sample. However, because the concentration was not available for that sample, it was taken from an unfiltered sample collected at the same depth, and was calculated as if filtered (i.e. considering that 5% of Nd is present in particulate form). Sample collected in August 1999. Hydrographic data: ICES Data Centre, cruise 64BS, station 5422, $n = 2$. Collected in September 1999.

AABW: Neodymium and hydrographic data are from [86]: three samples from station 161 (between 2400 and 4400 m depth) and three samples from station 193 (between 2200 and 4800 m depth). The samples were filtered, and collected between February and April 2008. Note that the samples were collected in the Atlantic sector of the Southern Ocean, and they therefore represent Weddell Sea deep or bottom water. The Nd isotope characteristics are different for AABW from the Pacific or Australian/Indian sectors of the Southern Ocean.

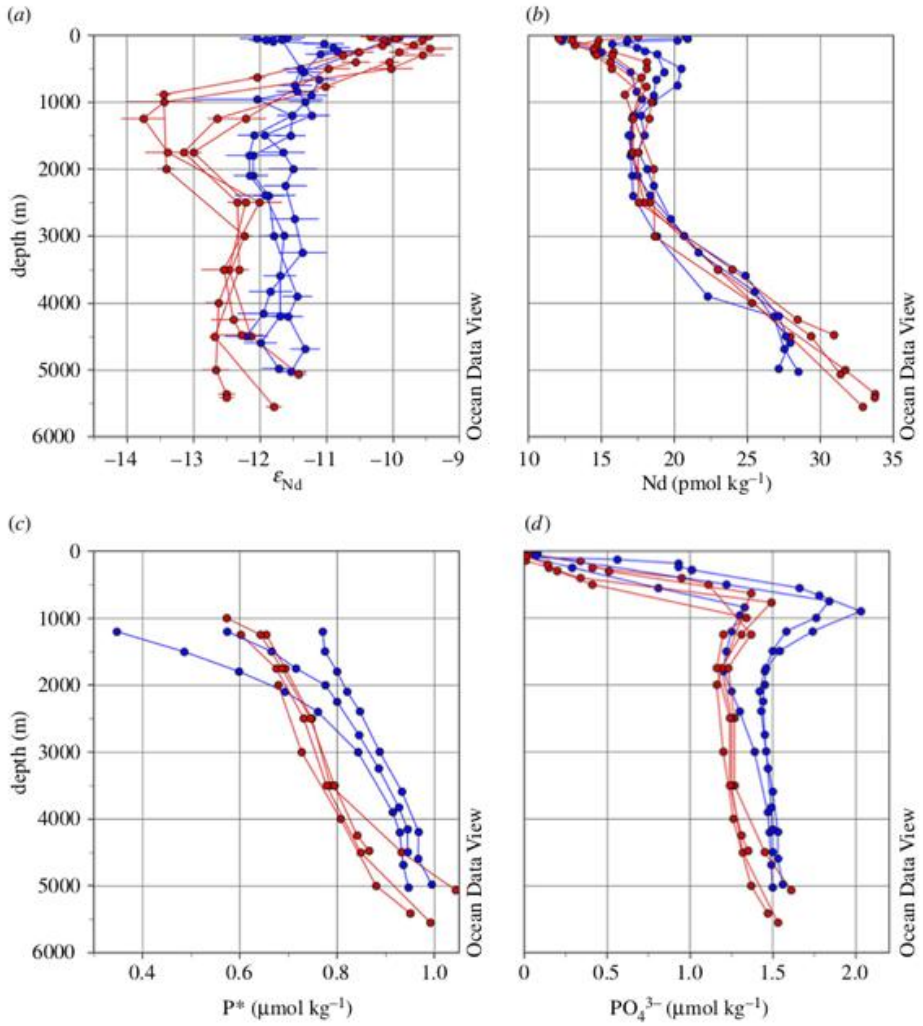

Figure 7. Selected depth profiles from sections GA02 (stations 15, 21, 25 and 30; red) and GA03 (stations 5, 7 and 22; blue) within the subtropical gyre, away from land masses: vertical distribution of seawater (*a*) Nd isotopic composition, (*b*) Nd concentration, (*c*) calculated phosphate star (P*) concentration below 1000 m and (*d*) phosphate concentration. Phosphate star is calculated after [104] using $P^* = PO_4^{3-}{}_{observed} + (O_2/175) - 1.95$. Oxygen and phosphate values for GA02 and GA03 were taken from the GEOTRACES IDP2014 [105]. Plots were generated using the software Ocean Data View [101].

rather horizontal trends in ε_{Nd} versus 1/Nd space due to an increase of Nd concentrations with depth, common to the entire subtropical Atlantic Ocean (figure 6). Deviations from this trend are due to the influence of Antarctic waters (both sections, but more pronounced in the east) and Mediterranean waters (eastern GA03 section only) with more radiogenic Nd isotopic compositions (figure 8*a*). The apparently contrasting behaviour of Nd isotopes between the two sections is further highlighted in a cross plot with phosphate star (figure 8*b*). The GA03 data are described by rather confined ε_{Nd} and P* values, with the exception of a trend towards the distinct MOW endmember at intermediate depths (i.e. negative P* and more radiogenic ε_{Nd} values; table 1), making it difficult to use either of the two proxies to depict individual water

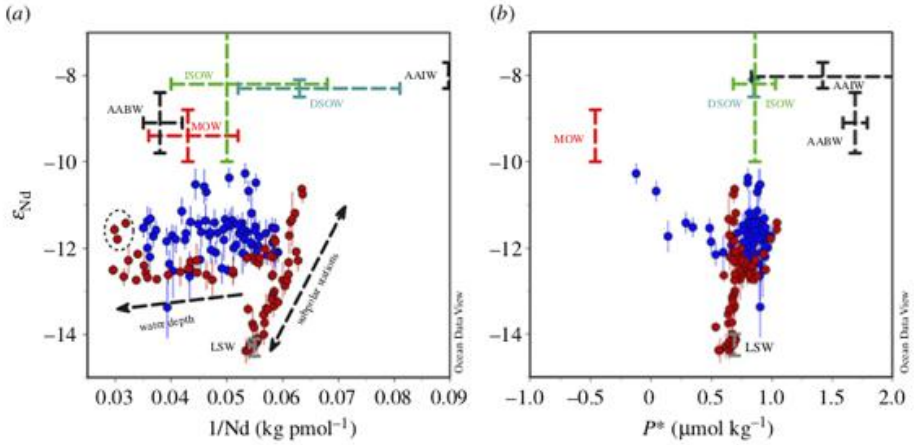

Figure 8. Neodymium isotopic composition as a function of (*a*) 1/Nd and (*b*) phosphate star (P*) for samples deeper than $\sigma_0 = 27.68$ kg m^{-3} (i.e. ULSW and below) from sections GA02 (red symbols) and GA03 (blue symbols). The approximate endmember compositions of the discussed water masses are also illustrated (table 1). For abbreviations of water masses, see figure 6. A detailed description of the near-vertical and near-horizontal trends indicated in panel A is provided in the main text. The three circled points in that plot represent the samples most strongly influenced by AABW. Note that P* is not a good tracer to distinguish between the two different North Atlantic Deep Water source regions (i.e. LSW versus Nordic Seas overflows), whereas Nd isotopes do allow this distinction. In contrast, neodymium isotopes are not very different between overflow waters (i.e. DSOW and ISOW), MOW and Antarctic water masses, whereas the P* values of those water masses are distinct. Plots were generated using the software Ocean Data View [101].

masses in the eastern basin. Even so, the generally higher P* values (figures 7*c* and 8*b*) do indicate a more pronounced admixture of southern-derived water masses (mainly AAIW [46,102]). In contrast, the GA02 data show well-defined trends between LSW, DSOW and AABW, consistent with stronger export of NADW and its precursor water masses along the DWBC and excellent water mass tracing by Nd isotopes [45].

In summary, intermediate and deep water Nd isotopic compositions along section GA02 in the western basin trace water masses (figure 6). The dominant feature along the western section is the very unradiogenic signature of LSW, which is strongly advected southwards in the Deep Western Boundary Current (figure 6). The relative homogeneity of seawater Nd isotopic compositions along section GA03 in the eastern basin is probably the result of less pronounced lateral admixture of water masses (i.e. more sluggish circulation, as indicated by low CFC-11 inventories [108]), as well as the absence of clear Nd isotope gradients between the water masses. The only water mass in the eastern Atlantic with the potential to create a tongue of distinct Nd isotopic compositions is MOW, which however does not show a strong fingerprint away from the Gulf of Cadiz (figure 6; see also §4). Similar Nd concentration profiles on both sides of the North Atlantic (figure 7*b*) argue against a stronger vertical supply of Nd in the east. The tracer P* is superior to Nd isotopes in depicting contributions of Southern Ocean waters, whereas Nd isotopes are the better tracer to distinguish between northwest and northeast Atlantic water sources.

4. Western and eastern North Atlantic GEOTRACES sections GA02 and GA03: insights from comparing Nd concentrations and isotopic compositions with Al concentrations

The GEOTRACES programme is providing a wealth of data from equivalent samples for a large number of elements and isotope systems, beyond traditional measurements on hydrography and

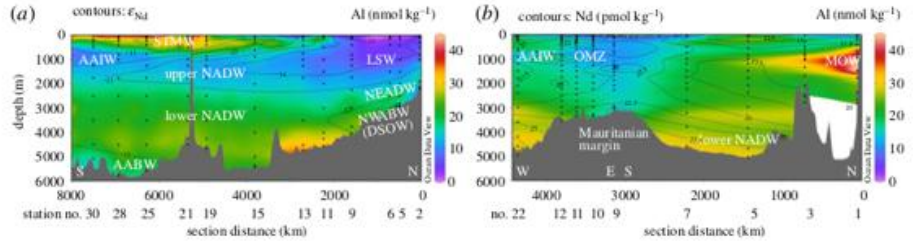

Figure 9. Aluminium concentrations along (*a*) section GA02 (line A–A′ in figure 5) contoured with Nd isotopic compositions and (*b*) section GA03 (line B–B′ in figure 5) contoured with Nd concentrations. For abbreviations of water masses, see figure 6. Numbers below the sections are station numbers. Data were visualized using the software Ocean Data View [101].

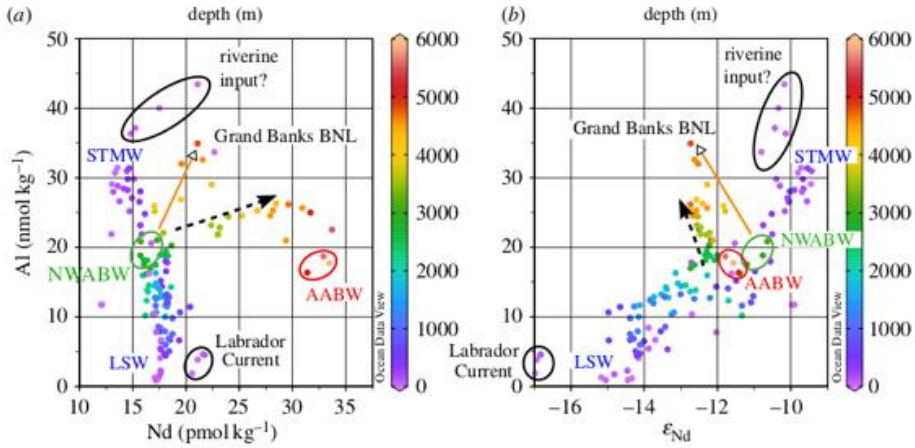

Figure 10. Aluminium concentrations versus (*a*) Nd concentrations and (*b*) Nd isotopic compositions for the western Atlantic section GA02. Colours represent water depth of sample collection. The main water masses are annotated and deviations from simple correlations are indicated by arrows or circles (see text for detailed description). Neodymium data are from [45] and Al data are from [109]. Plots were generated using the software Ocean Data View [101].

nutrients. Exploiting the potential for evaluation of trace metal cycling in 'tracer–tracer' space is, however, still in its infancy. In this section, we take a first step towards a tracer–tracer evaluation by carrying out a regional comparison of Nd isotopes and concentrations [45,46] with another lithogenic tracer, aluminium (Al). Aluminium data were collected on the same section cruises (GA02 and GA03), recently published by Middag *et al.* [109] and Measures *et al.* [110], and were extracted from the GEOTRACES IDP2014 [105]. There are many more Al concentration data for these sections than there are equivalent Nd concentration and isotope data, and only Al data for which equivalent Nd data points exist are included in the merged dataset. An offset of approximately 20% has been reported for the two Al datasets at the crossover station close to Bermuda (Bermuda Atlantic time series station, BATS), which remains to be explained, and prevents quantitative interpretations and illustration of Nd and Al data from the two sections (GA02 and GA03) on the same figures (figures 9–11).

As one of the first reactive trace elements to be reliably analysed in seawater, Al has a long history in oceanographic research [109–118]. However, despite many studies, both observational and modelling [119–121], the controls on oceanic Al distributions remain controversial. In the late 1990s to early 2000s, Al was thought of as the classic, short residence time, 'scavenged'-type element, with high concentrations close to sources (predominantly atmospheric and benthic)

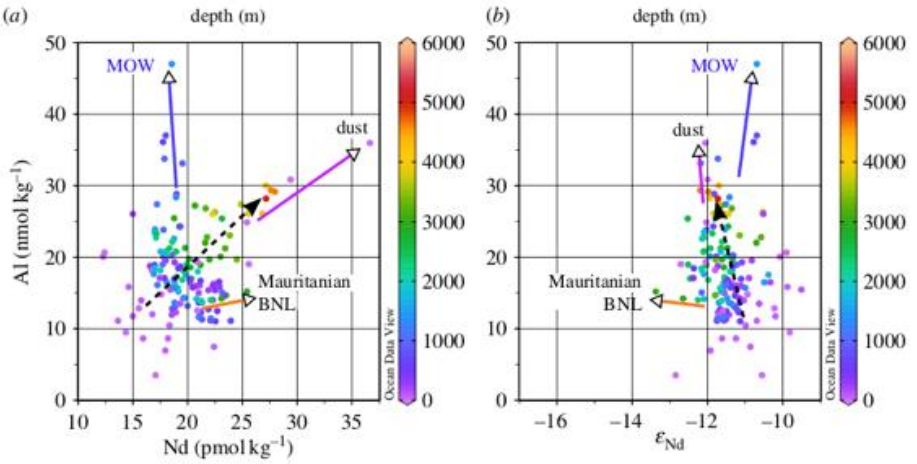

Figure 11. Aluminium concentrations versus (*a*) Nd concentrations and (*b*) Nd isotopic compositions for the eastern Atlantic section GA03. Colours represent water depth of sample collection. The only water mass that can be easily depicted in the area is MOW. Other arrows point towards the signature of dust influx and the Mauritanian benthic nepheloid layer (BNL). The dashed arrow indicates the trend of increasing Nd and Al concentrations with water depth. Neodymium data are from [46] and Al data are from [110]. Plots were generated using the software Ocean Data View [101].

and removal via particle scavenging [122]. Subsequent debate has focused on the relative roles of physical mixing versus internal cycling, and, in the latter case, passive scavenging versus active biological uptake. The arguments evolved around observations of Si–Al covariation (or its breakdown) and, in GEOTRACES data, the possibility of release (i.e. remineralization) of Al associated with high apparent oxygen utilization (AOU) in OMZs, as well as sedimentary (benthic) sources of Al. The possible importance of hydrothermal or hydrothermally related resuspension inputs of Al to the deep Atlantic has also been revisited [110].

(a) Reversible scavenging versus water mass mixing

A major question for understanding the distribution of dissolved Al in the ocean is the extent to which internal cycling (i.e. scavenging and desorption or uptake and remineralization) is required to explain the observed distributions, or whether physical mixing of water masses is the main control [109,110]. Below the thermocline, both Nd and Al concentrations classically increase rather linearly with depth. Indeed, away from external sources (i.e. MOW), dust supply at the surface and the pronounced OMZ (i.e. Mauritanian margin), increases in Nd and Al concentrations with depth are observed on both sides of the Atlantic Ocean (figures 6 and 9). Reversible scavenging has been invoked as a mechanism for both elements, based on observational and modelling studies [38,39,119–121].

Models of reversible scavenging are based on the landmark study of Bacon & Anderson [123], which described the process for tracers with a radioactive decay source throughout the water column (e.g. ^{230}Th). In the simpler case, for tracers without a radioactive decay source in the water column (e.g. Nd, Cu, Al), reversible scavenging models operate on the assumption that a single source of the tracer from the surface is balanced through removal by scavenging onto particles, according to an equilibrium scavenging coefficient, K,

$$K = \frac{C_p}{C_d \times R}, \tag{4.1}$$

where C_d is the dissolved concentration of tracer per kg of seawater, C_p is the particulate-associated concentration of tracer per kg of seawater and R is the concentration of

particulate material (and is dimensionless, being defined as the ratio of the mass of particles per cubic metre to the density of seawater). The equilibrium coefficient (K) is assumed to be constant with depth, and particles are assumed to have a constant sinking velocity. At steady state, the particulate-associated concentration of tracer (C_p) must also remain constant with depth (i.e. what comes in at the surface goes out on particles). Rearranging equation (4.1),

$$C_d = \frac{C_p}{K \times R}, \tag{4.2}$$

it becomes clear that, in order for C_p to remain constant as particles sink and dissolve or remineralize (i.e. while R decreases), the remaining particulate material must end up with a respectively *higher* concentration of adsorbed tracer (per kg of particle) and the dissolved concentration of tracer in seawater (C_d) must increase. In addition, in this model, the slope of this dissolved concentration increase is dependent upon the specific particle dissolution profiles that are imposed. Note that if dust is the principal scavenger, and dust is assumed not to dissolve on sinking, a profile of constant C_d is also possible. This simple model does not account for the case of addition/formation of particles elsewhere in the water column, e.g., Fe or Mn oxides, which may also act as efficient scavengers.

(b) Aluminium concentrations and neodymium isotopes in the western North Atlantic: physical circulation control?

Qualitatively, Al concentrations and Nd isotopic compositions in the western North Atlantic section share many features, which are evident in a section of Al concentrations with superimposed Nd isotope isolines (figure 9*a*). The distribution of Al in the western basin is strongly influenced by the distribution of the major water masses [109]. The radiogenic water mass in the subtropical thermocline (i.e. STMW) exhibits high Al concentrations due to a significant dust input to this region, whereas northern-sourced water masses of the subpolar gyre (ULSW and LSW) show much lower Al concentrations and an unradiogenic Nd isotope signature. These features of LSW reflect negligible Al input to the northwestern Atlantic surface waters, coupled with an Nd isotopic provenance signature acquired from the old continental crust surrounding this source region. In contrast, the source regions of the Southern Ocean-derived water masses (AAIW and AABW) are also regions of low Al input, but have much more radiogenic Nd isotope signatures, both of which are reflected in the resultant water mass compositions in section GA02. Finally, the striking distinction between upper NADW and lower NADW, documented for the first time in detail for Nd isotopes by Lambelet *et al.* [45], is equally well defined in Al concentrations, which are significantly elevated in lower NADW compared with upper NADW (figure 9*a*).

The elevated Al in lower NADW may in part be supplied directly from the overflow areas (e.g. DSOW) and increasing 'ingrowth' of Al concentrations from benthic sources along its flow path [109], but could also be linked to locally pronounced particle resuspension (and dissolution) associated with the BNL around Grand Banks (figure 9*a*). The peak in bottom water Al concentrations (at stations 11 and 13, approx. 45°N) is associated with a parallel shift towards the less radiogenic Nd isotope signature of lower NADW compared with its source components such as DSOW, suggesting active boundary exchange in this area.

These observations are also resolvable on cross plots of Al concentrations with Nd isotopes for the northwest Atlantic meridional section (figure 10*b*). Aluminium concentrations and Nd isotopic compositions in the upper approximately 2500 m of the water column show a strong positive correlation (purple to dark green colours in figure 10*b*). The most extreme compositions along this array are (i) northern-sourced ULSW/LSW, with low Al concentrations (less than 5 nmol kg^{-1} [109]) and unradiogenic Nd isotopic compositions ($\varepsilon_{Nd} = -14.3 \pm 0.3$ and -13.7 ± 0.9 [45]) and (ii) STMW, with high Al concentrations (greater than 25 nmol kg^{-1} [109]) and more radiogenic Nd isotopic compositions ($\varepsilon_{Nd} = -9.6 \pm 0.2$ [45]). Notably, both endmembers are upper ocean water masses, with ULSW/LSW being formed by seasonal convection in the Labrador Sea before being exported at mid-depths as upper NADW.

Two locations in the surface ocean show deviations from the above-described trend (figure 10). The first region, comprising the most southerly stations 25, 28 and 30, has elevated Al concentrations in surface waters, associated with slightly less radiogenic Nd isotopic compositions and higher Nd concentrations than typically observed for STMW (circled black, figure 10). The principal source of both Al and Nd to the surface ocean in the subtropical Atlantic Ocean is dust, whereas Lambelet *et al*. [45] noted a drop in salinity in these particular samples and suggested the Caribbean rivers could provide an additional input source in this area. The second region showing deviation from the LSW–STMW correlation comprises the surface samples around Grand Banks (circled black, figure 10), indicating inflow of very unradiogenic Nd via the Labrador Current [45]. Neodymium concentrations are slightly elevated, but Al concentrations are very low (less than 5 nmol dm^{-3}) in these waters (figure 10*a*,*b*), confirming that continental supply of Nd from old North American source terrains, via dissolved and/or particulate riverine material, does not seem to be a significant source for Al.

Additional groupings and trends between Al and Nd concentrations or isotopes can be observed in deeper waters (i.e. below 3000 m; light green to yellow-orange and red colours in figure 10). Northwest Atlantic Bottom Water (circled green, figure 10*b*), derived from its low Al and radiogenic Nd DSOW precursor, can be identified deep in the Irminger Basin (stations 2–6) and just to the north of Grand Banks (station 9) and lies on the LSW–STMW trend. However, its composition is modified on encountering the Grand Banks BNL, evolving towards somewhat less radiogenic ε_{Nd} values and highly enriched Al (and Nd) concentrations (orange arrows, figure 10). In the deep (depths below 3000 m) subtropical part of the section (stations 15–30), Nd and Al concentrations increase with water depth, whereas Nd isotopic compositions remain relatively unchanged. This trend could be interpreted either as upward diffusion of Nd and Al from a benthic source or as downward supply through reversible scavenging. The southernmost stations 25–30 encounter AABW, which is characterized by low Al concentrations, high Nd concentrations and a more radiogenic Nd isotopic composition (circled red, figure 10).

In summary, relatively simple mixing relationships can be distinguished between Al and Nd isotopes in the western North Atlantic (figures 9 and 10), suggesting that, away from source regions, Al behaves rather conservatively in the subsurface western North Atlantic. This observation does not rule out a minor role for internal processes, such as reversible scavenging or even limited scavenging loss of Al in deep waters, as proposed by Middag *et al*. [109].

(c) Aluminium and neodymium concentrations and neodymium isotopic compositions in the eastern North Atlantic: disentangling physical mixing and internal cycling

In the eastern North Atlantic, the relationship of Nd isotopic compositions with water mass distribution is less well defined than in the western basin [46] (see §3). Aluminium concentrations in the eastern basin are strongly influenced by the presence of MOW, which is a very Al-enriched source [110]. Mediterranean Outflow Water is also identifiable by its more radiogenic Nd isotopic signature and can be clearly depicted on cross plots of Al concentrations with Nd isotopic compositions and Nd concentrations (figure 11), despite its Nd concentration being indistinct from surrounding water masses. It is interesting to note that the southward penetration of MOW is better resolved in the Al data (figure 9) than in Nd isotopic compositions (figure 6), whereas the opposite was observed for northwest Atlantic bottom water (NWABW) (i.e. DSOW). This observation may in part reflect the highly distinct Al signature of MOW (see also P*; figure 8*b*), but could also suggest that, under certain conditions, Al concentrations might even behave more conservatively than Nd isotopic compositions. Indeed, Measures *et al*. [110] showed convincingly that, for densities between 27.5 and 27.9 kg m^{-3}, dissolved Al concentrations and salinity describe a mixing line between highly saline MOW and relatively fresh AAIW, indicating conservative behaviour of Al in this density layer.

However, there is also clear evidence that dissolved Al concentrations are influenced by internal cycling, in particular in the (sub)surface layer and near the continental margins. Both

Al and Nd exhibit concentration minima associated with the chlorophyll maximum (in both the eastern and western Atlantic sections), interpreted to reflect scavenging on organic particles. Aluminium is also incorporated directly into diatom frustules [124–127], which would bolster this signature, although evidence for the significance of incorporation versus scavenging is inconclusive [120]. Below the chlorophyll maximum, Nd concentrations increase in step with AOU, indicating desorption associated with particle remineralization [46], a signature that is more pronounced in the stronger OMZ of the eastern basin compared with the western Atlantic [45] (figure 6). Paradoxically, a similar process was proposed for Al in the western Atlantic [109], but discounted in the eastern basin [110]. Whereas Nd concentrations are elevated in a broad plume within the eastern OMZ, Al concentrations do not display this pattern (figure 9), indicating that any source of Al from remineralization associated with OMZs must be minor and restricted to a second-order role in controlling the Al distribution. Instead, close to the Mauritanian upwelling region, Al concentrations are low throughout the water column, pointing towards persistent removal through scavenging.

One further interesting observation in the eastern section is the behaviour of Al in the Mauritanian BNL. As described in §4*b*, a significant benthic source of Al is associated with the permanent BNL at Grand Banks, concomitant with a minor source of Nd and a notable shift in Nd isotopic compositions (figure 10). A BNL was also identified at the Mauritanian margin at station 9, and is associated with an increase in Nd concentrations and a shift towards less radiogenic Nd isotopic compositions [46]. There is, however, no clearly resolvable impact on local dissolved Al concentrations (figure 11). This difference in the behaviour of Al in BNLs has been noted previously [109,110,116,117], and has been attributed to varying Si concentrations in ambient deep waters. High Si concentrations, for example associated with AABW, are believed to inhibit the re-dissolution of Al from suspended sediment [120,128], which could explain the lack of a dissolved Al signature in the Mauritanian BNL. This effect has also been invoked to explain why the strong Al source around Grand Banks (§4*b*) occurs at a water depth of approximately 5000 m (45°N), and slightly to the north of the densest nepheloid layer (depths below 5500 m, 40°N), because the latter location exhibits slightly elevated Si concentrations due to the greater presence of AABW [109]. More generally, the observation that the presence of a BNL is not always associated with an Al source calls into question the utility of deep- and bottom water Al concentrations as a tracer of boundary exchange processes for other elements. More work is needed to fully understand the control of BNLs on both elements, Al and Nd.

In summary, the Al distribution in the eastern section is more complex to interpret, in part because the seawater Nd isotope signal does not allow for simple water mass depiction, complicating a coupled evaluation of the two tracers. There remains ample evidence that Al may behave largely conservatively, particularly in the case of the invasion of MOW at thermocline depths [110]. However, scavenging of Al (and Nd) occurs in association with the subsurface peak in biological productivity, and the covarying (increasing) concentrations of Nd and Al in the deep eastern basin (figure 11*a*, dashed arrow) may yet hint at a role for reversible scavenging (or other internal cycling processes) in deep and bottom waters. Measures *et al.* [110] proposed a hydrothermal origin for the high Al concentrations in the deep eastern basin, but no such hydrothermal source can be invoked to explain high concentrations of Nd in the area [40,129,130].

5. Implications from GEOTRACES observations for palaeoceanographic applications

A better understanding of the processes influencing the cycling of Nd in the modern ocean offers the potential to improve the application of Nd isotopes for understanding past ocean changes. In this section, we discuss the implications from GEOTRACES observations for palaeoceanographic studies, focusing on the North Atlantic region and on the topics of water mass endmember compositions, boundary exchange and internal cycling.

(a) North Atlantic water mass endmember compositions

Many palaeoceanographic studies assume a working model for the Atlantic Ocean that involves mixing between an unradiogenic NADW endmember with $\varepsilon_{Nd} \sim -13.5$ and southern-sourced AABW and AAIW with more radiogenic values of $\varepsilon_{Nd} \sim -7$ to -9 [8,9]. In this simplified view, northern values are set by weathering inputs from the old continental terrains surrounding the North Atlantic, and southern values are derived from admixture of more radiogenic Pacific waters into the Southern Ocean [8,9].

In detail, however, the northwest and northeast Atlantic source waters that contribute to NADW are distinct in their Nd isotopic composition [48]. Table 1 provides an update on the characteristics of the main intermediate to deep waters in the Atlantic Ocean. Labrador Sea Water is the most unradiogenic water mass in the North Atlantic ($\varepsilon_{Nd}(ULSW) = -14.34 \pm 0.13$ and $\varepsilon_{Nd}(LSW) = -14.15 \pm 0.13$), but its density is not high enough for it to sink beyond intermediate water depths (upper NADW). On the other hand, overflows from the Nordic Seas ($\varepsilon_{Nd}(ISOW) = -8.2 \pm 1.8$ and $\varepsilon_{Nd}(DSOW) = -8.3 \pm 0.2$; table 1) are sourced from more radiogenic surface waters (figure 2), and are furthermore influenced by exchange with young volcanic material in the area [49,50]. Upon export from the subpolar region, the overflows form the middle and lower layers of NADW, sometimes combined as lower NADW [45]. Data from GA02 have revealed that upper and lower NADW in the subtropical North Atlantic maintain an isotopic difference (upper NADW, $\varepsilon_{Nd} = -13.2 \pm 1.0$; lower NADW, $\varepsilon_{Nd} = -12.4 \pm 0.4$ [45]; figure 6).

Even small differences in the Nd isotopic compositions of NADW source waters may become more critical going back in time. In the past oceans, there is significant uncertainty in where exactly deep waters formed in the North Atlantic, including a debate over the presence and activity of LSW and overflows from the Nordic Seas (i.e. ISOW, DSOW) during the last glacial period. It has been suggested that LSW formation was reduced during glacial periods and probably absent at the Last Glacial Maximum (LGM) [131], whereas past activity of the Nordic Seas overflows is controversial, with arguments for continued but episodic overflow activity during the glacial period [132,133] or a complete switch to open ocean convection south of Greenland [134]. Changes in the location of convection and/or mixing proportions of source waters during past climate events may have resulted in a different Nd isotopic composition for NADW or its glacial equivalent, Glacial North Atlantic Intermediate Water (GNAIW), and some existing records point in this direction. For example, Nd isotope values at approximately 4500 m depth on the Bermuda Rise (figure 12) were more extreme than any values in the modern deep Atlantic both during the Early Holocene ($\varepsilon_{Nd} = -16.5$) [13] and during interstadials of the last glacial period ($\varepsilon_{Nd} = -15$ to -18) [15]. The only feasible source regions for such negative values (i.e. old source rocks) are the continents and shelf areas around the Labrador Sea [24]. Consequently, Bohm *et al.* [15] interpreted such values to represent a larger proportion of LSW in exported NADW during warm times. However, this scenario is only feasible if LSW significantly deepened compared to today, requiring rearrangement of the density structure in the North Atlantic [22]. In contrast, during the coldest times of the LGM, it has been suggested that GNAIW may have had a more radiogenic Nd isotopic composition than modern NADW as a result of reduced LSW contributions [136].

Rather than viewing such complexity as a challenge for using Nd isotopes, it appears that a better spatial sampling of the glacial ocean could provide improved constraints on the changing locations of deep water convection and the activity of LSW and overflows from the Nordic Seas, particularly if partnered with other proxies such as oxygen isotopes, carbon isotopes, Pa/Th ratios or radiocarbon.

(b) Boundary exchange

Boundary exchange describes particulate–seawater exchange occurring by a variety of processes, typically (but not exclusively) in marginal settings, and has been proposed as a major source of Nd to seawater [23,30,137]. If sediment–seawater interaction leads to the supply of Nd and/or

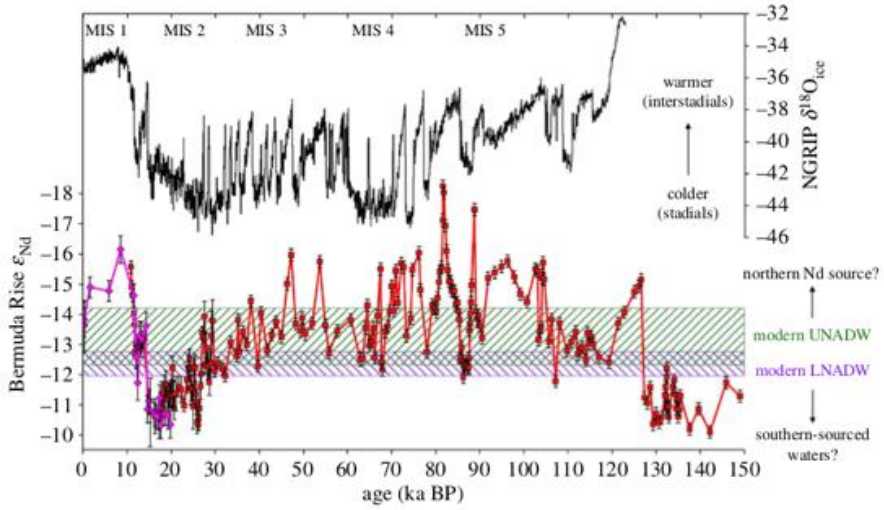

Figure 12. Time series of Nd isotope reconstructions through the last glacial cycle from Bermuda Rise cores OCE326-GGC6 [13] (pink) and ODP 1063 [15] (red) recovered from approximately 4500 m water depth. Also plotted (black) is the oxygen isotope record from Greenland ice core NGRIP [135], together with marine isotope stage (MIS) numbers. Modern-day Nd isotope endmembers are shown by hatched bars [45]. More radiogenic values during glacial maxima are widely linked to increased contributions from southern-sourced waters, whereas the origin of the highly unradiogenic values during warm periods is discussed in the text (see also [22]).

isotopic exchange close to water mass source regions, then it can be considered as a mechanism for imprinting water masses with their Nd isotopic signatures [48], but it would not affect the ability of Nd isotopes to monitor water mass mixing further downstream, as indicated by modelling studies [31,100]. However, if benthic supply [36,37] and/or remineralization of particulate Nd along the flow path of a water mass are included [40,109], then those processes may provide a non-conservative influence that alters the Nd isotopic composition of bottom waters and hence the record obtained from sediment cores. Such processes would limit (but not remove) the potential of using Nd isotopes to reconstruct (past) ocean circulation.

The new GEOTRACES data discussed in §3 contribute to this debate by clarifying the extent and geographical locations of boundary exchange in the North Atlantic. In the modern ocean, there is evidence for active boundary exchange in the deep Irminger Sea near Greenland, and on the Grand Banks near Newfoundland, confirming previous suggestions that boundary exchange in these regions contributes to the generation of the NADW endmember composition [48]. For example, NWABW changes by 1.1 ε_{Nd} units over a distance of approximately 650 km in the Irminger Sea [45]. In contrast, there is a change of less than 1 ε_{Nd} unit over approximately 5500 km between stations 9 and 30 following the downstream flow of NADW in the western Atlantic basin (GA02 section), restricting boundary exchange to a relatively minor influence. However, it should be noted that AABW entrainment south of 45°N leads to a loss of contact of lower NADW with the seafloor [109]. Overall, water mass advection clearly dominates the Nd isotope signature in intermediate to deep waters in the western North Atlantic, and Nd isotope distributions conform well to those of conservative water mass tracers such as salinity, CFCs (figure 6) or neutral density [45]. Similarly, in the eastern Atlantic section (GA03), an imprint of boundary exchange on dissolved Nd isotopes was only implicated in two locations [46]: station 9 on the Mauritanian margin, where the BNL represents a net source of Nd, and station 12 near the Cape Verde Islands, where there is no accompanying change in Nd concentrations.

While previous studies have emphasized the role of continental shelves and ocean margins as major boundary sources, the examples above highlight the significance of localized benthic sources. In modelling studies, boundary exchange is typically parametrized by a function that is at its maximum in the surface layer and decreases exponentially with depth to zero below 3000 m [30,31,138]. With the exception of a slightly higher spatial variability in Nd isotopes in the (sub)surface layer of the global oceans (figure 3), no obvious depth dependence of boundary exchange has emerged as yet from GEOTRACES data. If such an observation proves to be robust across multiple settings, then this particular model assumption should probably be revised (see also §4). In addition, the mechanisms and processes involved in boundary exchange need further exploration, and particularly BNLs may act as an as yet understudied source (or sink) of trace metals in the ocean (see also [37]).

(c) Internal cycling

Adsorption of Nd onto the surfaces of sinking particles and desorption upon decomposition may, in places, make dissolved Nd profiles in the upper ocean resemble those of biologically used elements (figure 7), albeit reflecting a rather different process [45,46]. Deeper in the water column, Nd concentrations at the depth levels of LSW (upper NADW), MOW and AAIW show remarkably conservative behaviour, an observation that has also been made for dissolved Al concentrations (see §4). In a recent study, Zheng *et al.* [40] used a multiparameter model to deconvolve the relative importance of water mass mixing and vertical cycling on seawater Nd concentrations along a section at 12°S in the Atlantic Ocean. They found that more than 75% of the REE concentrations (including Nd) are controlled by preformed concentrations, through physical transport and water mass mixing, and hence behave conservatively. However, away from water mass formation areas in the subpolar North Atlantic, Nd concentrations in excess of simple water mass mixing are observed in deeper waters and particularly in bottom waters (§§3 and 4), which may be tentatively attributed to reversible scavenging. Vertical transport by a reversible scavenging process may also play an important role in generating the homogeneous Nd isotopic distribution in the eastern Atlantic [46], where advection is more sluggish.

Excess Nd, observed in deep and bottom waters of the South Atlantic, has been attributed to either *in situ* remineralization or the accumulation of Nd along the flow path of southern-sourced bottom waters [40]. Based on the data from section GA02, where similar Nd concentrations in bottom waters are observed over approximately 4000 km of longitudinal transport, we would argue that along-flow accumulation is not widely occurring, and that *in situ* processes, such as the regeneration of Nd related to local calcite dissolution, are probably a more likely candidate. However, there is a gradient of increasing Nd concentrations along GA02 outside the subpolar gyre at the neutral density level of NWABW (i.e. lower NADW; approx. 3500–4500 m water depth) which does hint at the addition of Nd along the flow path of this particular water mass (see fig. 7 in [45]). Internal cycling, where it occurs, may potentially contribute to some downward smoothing of vertical Nd isotope structure, in comparison with a conservative tracer such as salinity, but from the GA02 and GA03 data, it does not appear to leave a clear Nd isotope fingerprint in this region. Future studies will need to tackle modern vertical Nd cycling in more detail before speculations on the nature of internal cycling in the past oceans can be made.

6. Concluding remarks

Our comparison of the recent GEOTRACES data published from the North Atlantic sections GA02 and GA03 [45,46] highlights similarities as well as differences in Nd cycling between the eastern and western Atlantic basins. Physical mixing seems to dominate the patterns observed in both Nd isotopes and concentrations in strongly advective areas, whereas deviations from mixing are observed in localized areas of non-conservative boundary exchange in both sections. Another feature common to both sections is the increase in Nd concentrations with water depth, generating rather similar concentration profiles for deep and bottom waters throughout the subtropical area.

Along the western North Atlantic section, Al concentrations and Nd isotopes show strikingly similar behaviours, further supporting the notion that both tracers are excellent water mass indicators in this area. Interestingly, continental inputs from North America and Greenland, which dominate the fingerprint of LSW for Nd isotopes (and concentrations), are not significant sources of Al. Furthermore, in detail, Nd and Al concentration profiles reflect a variety of different processes superimposed on the first-order control of water mass mixing, including passive cycling of Nd with nutrients in the upper water column, benthic sources of both Nd and Al, and the potential for (reversible) scavenging to play a role in their distributions.

One clear implication of the modern GEOTRACES data is that a spatial context is important for palaeoceanographic studies, which is nicely illustrated in studies on sediment core material from the Holocene western Pacific [139] and the Holocene and glacial western Indian Ocean [140]. However, at present, the palaeo data generally do not have the spatial resolution (both in location and especially in water depth) of the new GEOTRACES data, and significantly more progress is warranted in that respect. Obtaining a depth perspective from the past oceans will require the integration of multiple archives, such as shallow-dwelling corals in the surface and subsurface oceans [141], deep-sea corals in intermediate depths [142,143], foraminifera [51,144,145] or sediment leachates [11,146] from mid-depth sites, and fish teeth [147,148] from abyssal settings. For this combined approach to be successful, datasets measured on different types of archives in different laboratories worldwide need to be reliable and comparable. That has been a challenging task, particularly in the case of sediment leachates, but considerable progress has been made [145,146,149–152].

More generally, the GEOTRACES data demonstrate that potential changes in endmember compositions, boundary exchange or internal cycling challenge quantitative interpretations of authigenic Nd isotopes as a circulation tracer. However, the qualitative information on water mass provenance and mixing gained from palaeo Nd isotope datasets can be significantly enhanced by: (i) studying analogue modern-day scenarios; (ii) taking multi-proxy approaches; (iii) increasing the regional and vertical coverage of records; and (iv) using modelling approaches to invert palaeo data.

Data accessibility. The new global database on dissolved Nd isotopes, Nd concentrations and hydrography is available through the GEOTRACES International Data Assembly Centre, hosted at the British Oceanographic Data Centre (http://www.bodc.ac.uk/geotraces/data/historical/).

Authors' contributions. T.v.d.F. designed the paper. The global database was assembled by M.L. and A.M.G. Sections 3–5 and associated figures were drafted by T.S., S.H.L. and D.J.W. and table 1 was compiled by M.L. All authors worked together on developing the final manuscript.

Competing interests. We have no competing interests.

Funding. We acknowledge funding from the NERC (NE/J021636/1; NE/N001141/1; DTP 'Science and Solutions for a Changing Planet') and the Leverhulme Trust (RPG-398 and ECF-2014-615).

Acknowledgements. All authors thank the organizers of the Royal Society meeting on 'Biological and climatic impacts of ocean trace element chemistry' for a stimulating event.

References

1. Jacobsen SB, Wasserburg GJ. 1980 Sm–Nd isotopic evolution of chondrites. *Earth Planet. Sci. Lett.* **50**, 139–155. (doi:10.1016/0012-821X(80)90125-9)
2. Huang SC, Jacobsen SB, Mukhopadhyay S. 2013 $^{147}Sm/^{143}Nd$ systematics of Earth are inconsistent with a superchondritic Sm/Nd ratio. *Proc. Natl Acad. Sci. USA* **110**, 4929–4934. (doi:10.1073/pnas.1222252110)
3. Piepgras DJ, Wasserburg GJ. 1980 Neodymium isotopic variations in seawater. *Earth Planet. Sci. Lett.* **50**, 128–138. (doi:10.1016/0012-821X(80)90124-7)
4. Piepgras DJ, Wasserburg GJ, Dasch EJ. 1979 The isotopic composition of Nd in different ocean masses. *Earth Planet. Sci. Lett.* **45**, 223–236. (doi:10.1016/0012-821X(79)90125-0)
5. O'Nions RK, Carter SR, Cohen RS, Evensen NM, Hamilton PJ. 1978 Pb, Nd and Sr isotopes in oceanic ferromanganese deposits and ocean floor basalts. *Nature* **273**, 435–438. (doi:10.1038/273435a0)

6. Goldstein SL, O'Nions RK. 1981 Nd and Sr isotopic relationships in pelagic clays and ferromanganese deposits. *Nature* **292**, 324–327. (doi:10.1038/292324a0)
7. Albarede F, Goldstein SL. 1992 World map of Nd isotopes in sea-floor ferromanganese deposits. *Geology* **20**, 761–763. (doi:10.1130/0091-7613(1992)020<0761:WMONII>2.3.CO;2)
8. von Blanckenburg F. 1999 Perspectives: paleoceanography — tracing past ocean circulation? *Science* **286**, 1862–1863. (doi:10.1126/science.286.5446.1862b)
9. Goldstein SL, Hemming SR. 2003 Long-lived isotopic tracers in oceanography, paleoceanography and ice sheet dynamics. In *The oceans and marine geochemistry* (ed. H Elderfield), pp. 453–489. Oxford, UK: Elsevier-Pergamon.
10. Frank M. 2002 Radiogenic isotopes: tracers of past ocean circulation and erosional input. *Rev. Geophys.* **40**, 1001. (doi:10.1029/2000rg000094)
11. Rutberg RL, Hemming SR, Goldstein SL. 2000 Reduced North Atlantic deep water flux to the glacial Southern Ocean inferred from neodymium isotope ratios. *Nature* **405**, 935–938. (doi:10.1038/35016049)
12. Piotrowski AM, Goldstein SL, Hemming SR, Fairbanks RG. 2005 Temporal relationships of carbon cycling and ocean circulation at glacial boundaries. *Science* **307**, 1933–1938. (doi:10.1126/science.1104883)
13. Roberts NL, Piotrowski AM, McManus JF, Keigwin LD. 2010 Synchronous deglacial overturning and water mass source changes. *Science* **327**, 75–78. (doi:10.1126/science.1178068)
14. Skinner LC, Scrivner AE, Vance D, Barker S, Fallon S, Waelbroeck C. 2013 North Atlantic versus Southern Ocean contributions to a deglacial surge in deep ocean ventilation. *Geology* **41**, 667–670. (doi:10.1130/g34133.1)
15. Bohm E *et al.* 2015 Strong and deep Atlantic meridional overturning circulation during the last glacial cycle. *Nature* **517**, 73–76. (doi:10.1038/nature14059)
16. Wei R, Abouchami W, Zahn R, Masque P. 2016 Deep circulation changes in the South Atlantic since the last glacial maximum from Nd isotope and multi-proxy records. *Earth Planet. Sci. Lett.* **434**, 18–29. (doi:10.1016/j.epsl.2015.11.001)
17. Xie RFC, Marcantonio F, Schmidt MW. 2014 Reconstruction of intermediate water circulation in the tropical North Atlantic during the past 22,000 years. *Geochim. Cosmochim. Acta* **140**, 455–467. (doi:10.1016/j.gca.2014.05.041)
18. Jonkers L, Zahn R, Thomas A, Henderson G, Abouchami W, François R, Masque P, Hall IR, Bickert T. 2015 Deep circulation changes in the central South Atlantic during the past 145 kyrs reflected in a combined $^{231}Pa/^{230}Th$, neodymium isotope and benthic $\delta^{13}C$ record. *Earth Planet. Sci. Lett.* **419**, 14–21. (doi:10.1016/j.epsl.2015.03.004)
19. Howe JNW, Piotrowski AM, Noble TL, Mulitza S, Chiessi CM, Bayon G. 2016 North Atlantic deep water production during the last glacial maximum. *Nat. Commun.* **7**, 11765. (doi:10.1038/ncomms11765)
20. Wilson DJ, Crocket KC, van de Flierdt T, Robinson LF, Adkins JF. 2014 Dynamic intermediate ocean circulation in the North Atlantic during Heinrich Stadial 1: a radiocarbon and neodymium isotope perspective. *Paleoceanography* **29**, 1072–1093. (doi:10.1002/2014PA002674)
21. Roberts NL, Piotrowski AM. 2015 Radiogenic Nd isotope labeling of the northern NE Atlantic during MIS 2. *Earth Planet. Sci. Lett.* **423**, 125–133. (doi:10.1016/j.epsl.2015.05.011)
22. Deaney EL, Barker S, van de Flierdt T. In press. Late recovery of the AMOC explains larger CO_2 change across the penultimate deglaciation. *Nat. Commun.*
23. Lacan F, Jeandel C. 2005 Neodymium isotopes as a new tool for quantifying exchange fluxes at the continent–ocean interface. *Earth Planet. Sci. Lett.* **232**, 245–257. (doi:10.1016/j.epsl.2005.01.004)
24. Jeandel C, Arsouze T, Lacan F, Techine P, Dutay JC. 2007 Isotopic Nd compositions and concentrations of the lithogenic inputs into the ocean: a compilation, with an emphasis on the margins. *Chem. Geol.* **239**, 156–164. (doi:10.1016/j.chemgeo.2006.11.013)
25. Goldstein SL, O'Nions RK, Hamilton PJ. 1984 A Sm–Nd isotopic study of atmospheric dusts and particulates from major river systems. *Earth Planet. Sci. Lett.* **70**, 221–236. (doi:10.1016/0012-821X(84)90007-4)
26. Goldstein SJ, Jacobsen SB. 1987 The Nd and Sr isotopic systematics of river-water dissolved material: implications for the sources of Nd and Sr in seawater. *Chem. Geol.* **66**, 245–272. (doi:10.1016/0168-9622(87)90045-5)

27. Bertram CJ, Elderfield H. 1993 The geochemical balance of the rare-earth elements and neodymium isotopes in the oceans. *Geochim. Cosmochim. Acta* **57**, 1957–1986. (doi:10.1016/0016-7037(93)90087-D)
28. Jeandel C, Bishop JK, Zindler A. 1995 Exchange of neodymium and its isotopes between seawater and small and large particles in the Sargasso Sea. *Geochim. Cosmochim. Acta* **59**, 535–547. (doi:10.1016/0016-7037(94)00367-U)
29. van de Flierdt T, Frank M, Lee DC, Halliday AN, Reynolds BC, Hein JR. 2004 New constraints on the sources and behavior of neodymium and hafnium in seawater from Pacific Ocean ferromanganese crusts. *Geochim. Cosmochim. Acta* **68**, 3827–3843. (doi:10.1016/j.gca.2004.03.009)
30. Arsouze T, Dutay JC, Lacan F, Jeandel C. 2009 Reconstructing the Nd oceanic cycle using a coupled dynamical–biogeochemical model. *Biogeosciences* **6**, 2829–2846. (doi:10.5194/bg-6-2829-2009)
31. Rempfer J, Stocker TF, Joos F, Dutay JC, Siddall M. 2011 Modelling Nd-isotopes with a coarse resolution ocean circulation model: sensitivities to model parameters and source/sink distributions. *Geochim. Cosmochim. Acta* **75**, 5927–5950. (doi:10.1016/j.gca.2011.07.044)
32. Tachikawa K, Athias V, Jeandel C. 2003 Neodymium budget in the modern ocean and paleo-oceanographic implications. *J. Geophys. Res. – Oceans* **108**, 3254. (doi:10.1029/1999JC000285)
33. Jeandel C, Oelkers EH. 2015 The influence of terrigenous particulate material dissolution on ocean chemistry and global element cycles. *Chem. Geol.* **395**, 50–66. (doi:10.1016/j.chemgeo.2014.12.001)
34. Rousseau TCC, Sonke JE, Chmeleff J, van Beek P, Souhaut M, Boaventura G, Seyler P, Jeandel C. 2015 Rapid neodymium release to marine waters from lithogenic sediments in the Amazon estuary. *Nat. Commun.* **6**, 7592. (doi:10.1038/ncomms8592)
35. Johannesson KH, Burdige DJ. 2007 Balancing the global oceanic neodymium budget: evaluating the role of groundwater. *Earth Planet. Sci. Lett.* **253**, 129–142. (doi:10.1016/j.epsl.2006.10.021)
36. Abbott AN, Haley BA, McManus J. 2015 Bottoms up: sedimentary control of the deep North Pacific Ocean's Nd signature. *Geology* **43**, 1035–1038. (doi:10.1130/g37114.1)
37. Abbott AN, Haley BA, McManus J. 2016 The impact of sedimentary coatings on the diagenetic Nd flux. *Earth Planet. Sci. Lett.* **449**, 217–227. (doi:10.1016/j.epsl.2016.06.001)
38. Nozaki Y, Alibo DS. 2003 Importance of vertical geochemical processes in controlling the oceanic profiles of dissolved rare earth elements in the northeastern Indian Ocean. *Earth Planet. Sci. Lett.* **205**, 155–172. (doi:10.1016/S0012-821X(02)01027-0)
39. Siddall M, Khatiwala S, van de Flierdt T, Jones K, Goldstein SL, Hemming S, Anderson RF. 2008 Towards explaining the Nd paradox using reversible scavenging in an ocean general circulation model. *Earth Planet. Sci. Lett.* **274**, 448–461. (doi:10.1016/j.epsl.2008.07.044)
40. Zheng X-Y, Plancherel Y, Saito MA, Scott PM, Henderson GM. 2016 Rare earth elements (REEs) in the tropical South Atlantic and quantitative deconvolution of their non-conservative behavior. *Geochim. Cosmochim. Acta* **177**, 217–237. (doi:10.1016/j.gca.2016.01.018)
41. Henderson GM *et al.* 2007 GEOTRACES – an international study of the global marine biogeochemical cycles of trace elements and their isotopes. *Chem. Erde – Geochem.* **67**, 85–131. (doi:10.1016/j.chemer.2007.02.001)
42. Lacan F, Tachikawa K, Jeandel C. 2012 Neodymium isotopic composition of the oceans: a compilation of seawater data. *Chem. Geol.* **300**, 177–184. (doi:10.1016/j.chemgeo.2012.01.019)
43. Pahnke K, van de Flierdt T, Jones KM, Lambelet M, Hemming SR, Goldstein SL. 2012 GEOTRACES intercalibration of neodymium isotopes and rare earth element concentrations in seawater and suspended particles. Part 2: Systematic tests and baseline profiles. *Limnol. Oceanogr. Methods* **10**, 252–269. (doi:10.4319/lom.2012.10.252)
44. Grasse P, Stichel T, Stumpf R, Stramma L, Frank M. 2012 The distribution of neodymium isotopes and concentrations in the eastern equatorial Pacific: water mass advection versus particle exchange. *Earth Planet. Sci. Lett.* **353**, 198–207. (doi:10.1016/j.epsl.2012.07.044)
45. Lambelet M *et al.* 2016 Neodymium isotopic composition and concentration in the western North Atlantic Ocean: results from the GEOTRACES GA02 section. *Geochim. Cosmochim. Acta* **177**, 1–29. (doi:10.1016/j.gca.2015.12.019)

46. Stichel T, Hartman AE, Duggan B, Goldstein SL, Scher H, Pahnke K. 2015 Separating biogeochemical cycling of neodymium from water mass mixing in the eastern North Atlantic. *Earth Planet. Sci. Lett.* **412**, 245–260. (doi:10.1016/j.epsl.2014.12.008)
47. Spivack AJ, Wasserburg GJ. 1988 Neodymium isotopic composition of the Mediterranean outflow and the eastern North Atlantic. *Geochim. Cosmochim. Acta* **52**, 2767–2773. (doi:10.1016/0016-7037(88)90144-5)
48. Lacan F, Jeandel C. 2005 Acquisition of the neodymium isotopic composition of the North Atlantic deep water. *Geochem. Geophys. Geosyst.* **6**, Q12008. (doi:10.1029/2005gc000956)
49. Lacan F, Jeandel C. 2004 Neodymium isotopic composition and rare earth element concentrations in the deep and intermediate Nordic Seas: constraints on the Iceland Scotland overflow water signature. *Geochem. Geophys. Geosyst.* **5**, Q11006. (doi:10.1029/2004gc000742)
50. Lacan F, Jeandel C. 2004 Denmark Strait water circulation traced by heterogeneity in neodymium isotopic compositions. *Deep-Sea Res. Part I Oceanogr. Res. Pap.* **51**, 71–82. (doi:10.1016/j.dsr.2003.09.006)
51. Vance D, Scrivner AE, Beney P, Staubwasser M, Henderson GM, Slowey NC. 2004 The use of foraminifera as a record of the past neodymium isotope composition of seawater. *Paleoceanography* **19**, PA2009. (doi:10.1029/2003PA000957)
52. Amakawa H, Alibo DS, Nozaki Y. 2000 Nd isotopic composition and REE pattern in the surface waters of the eastern Indian Ocean and its adjacent seas. *Geochim. Cosmochim. Acta* **64**, 1715–1727. (doi:10.1016/S0016-7037(00)00333-1)
53. Amakawa H, Alibo DS, Nozaki Y. 2004 Nd concentration and isotopic composition distributions in surface waters of northwest Pacific Ocean and its adjacent seas. *Geochem. J.* **38**, 493–504. (doi:10.2343/geochemj.38.493)
54. Amakawa H, Nozaki Y, Alibo DS, Zhang J, Fukugawa K, Nagai H. 2004 Neodymium isotopic variations in northwest Pacific waters. *Geochim. Cosmochim. Acta* **68**, 715–727. (doi:10.1016/s0016-7037(03)00501-5)
55. Amakawa H, Sasaki K, Ebihara M. 2009 Nd isotopic composition in the central North Pacific. *Geochim. Cosmochim. Acta* **73**, 4705–4719. (doi:10.1016/j.gca.2009.05.058)
56. Amakawa H, Tazoe H, Obata H, Gamo T, Sano Y, Shen CC. 2013 Neodymium isotopic composition and concentration in the southwest Pacific Ocean. *Geochem. J.* **47**, 409–422. (doi:10.2343/geochemj.2.0260)
57. Andersson PS, Porcelli D, Frank M, Bjork G, Dahlqvist R, Gustafsson O. 2008 Neodymium isotopes in seawater from the Barents Sea and Fram Strait Arctic–Atlantic gateways. *Geochim. Cosmochim. Acta* **72**, 2854–2867. (doi:10.1016/j.gca.2008.04.008)
58. Basak C, Pahnke K, Frank M, Lamy F, Gersonde R. 2015 Neodymium isotopic characterization of Ross Sea bottom water and its advection through the southern South Pacific. *Earth Planet. Sci. Lett.* **419**, 211–221. (doi:10.1016/j.eps1.2015.03.011)
59. Carter P, Vance D, Hillenbrand CD, Smith JA, Shoosmith DR. 2012 The neodymium isotopic composition of waters masses in the eastern Pacific sector of the Southern Ocean. *Geochim. Cosmochim. Acta* **79**, 41–59. (doi:10.1016/j.gca.2011.11.034)
60. Chen TY, Stumpf R, Frank M, Beldowski J, Staubwasser M. 2013 Contrasting geochemical cycling of hafnium and neodymium in the central Baltic Sea. *Geochim. Cosmochim. Acta* **123**, 166–180. (doi:10.1016/j.gca.2013.09.011)
61. Copard K, Colin C, Frank N, Jeandel C, Montero-Serrano JC, Reverdin G, Ferron B. 2011 Nd isotopic composition of water masses and dilution of the Mediterranean outflow along the southwest European margin. *Geochem. Geophys. Geosyst.* **12**, Q06020. (doi:10.1029/2011gc003529)
62. Dahlqvist R, Andersson PS, Ingri J. 2005 The concentration and isotopic composition of diffusible Nd in fresh and marine waters. *Earth Planet. Sci. Lett.* **233**, 9–16. (doi:10.1016/j.epsl.2005.02.021)
63. Garcia-Solsona E, Jeandel C, Labatut M, Lacan F, Vance D, Chavagnac V, Pradoux C. 2014 Rare earth elements and Nd isotopes tracing water mass mixing and particle–seawater interactions in the SE Atlantic. *Geochim. Cosmochim. Acta* **125**, 351–372. (doi:10.1016/j.gca.2013.10.009)
64. Godfrey LV, Zimmermann B, Lee DC, King RL, Vervoort JD, Sherrell RM, Halliday AN. 2009 Hafnium and neodymium isotope variations in NE Atlantic seawater. *Geochem. Geophys. Geosyst.* **10**, 13. (doi:10.1029/2009GC002508)

65. Goswami V, Singh SK, Bhushan R. 2014 Impact of water mass mixing and dust deposition on Nd concentration and ε_{Nd} of the Arabian Sea water column. *Geochim. Cosmochim. Acta* **145**, 30–49. (doi:10.1016/j.gca.2014.09.006)
66. Grenier M, Jeandel C, Lacan F, Vance D, Venchiarutti C, Cros A, Cravatte S. 2013 From the subtropics to the central equatorial Pacific Ocean: neodymium isotopic composition and rare earth element concentration variations. *J. Geophys. Res. – Oceans* **118**, 592–618. (doi:10.1029/2012jc008239)
67. Haley BA, Frank M, Hathorne E, Pisias N. 2014 Biogeochemical implications from dissolved rare earth element and Nd isotope distributions in the Gulf of Alaska. *Geochim. Cosmochim. Acta* **126**, 455–474. (doi:10.1016/j.gca.2013.11.012)
68. Henry F, Jeandel C, Dupre B, Minster JF. 1994 Particulate and dissolved Nd in the western Mediterranean sea: sources, fate and budget. *Mar. Chem.* **45**, 283–305. (doi:10.1016/0304-4203(94)90075-2)
69. Jeandel C. 1993 Concentration and isotopic composition of Nd in the South Atlantic Ocean. *Earth Planet. Sci. Lett.* **117**, 581–591. (doi:10.1016/0012-821X(93)90104-H)
70. Jeandel C, Delattre H, Grenier M, Pradoux C, Lacan F. 2013 Rare earth element concentrations and Nd isotopes in the southeast Pacific Ocean. *Geochem. Geophys. Geosyst.* **14**, 328–341. (doi:10.1029/2012gc004309)
71. Jeandel C, Thouron D, Fieux M. 1998 Concentrations and isotopic compositions of neodymium in the eastern Indian Ocean and Indonesian straits. *Geochim. Cosmochim. Acta* **62**, 2597–2607. (doi:10.1016/S0016-7037(98)00169-0)
72. Lacan F. 2002 Masses d'eau des Mers Nordiques et de l'Atlantique Subarctique tracées par les isotopes du néodyme. PhD thesis, Toulouse III University, France. See http://tel.archives-ouvertes.fr/tel-00118162.
73. Lacan F, Jeandel C. 2001 Tracing Papua New Guinea imprint on the central equatorial Pacific Ocean using neodymium isotopic compositions and rare earth element patterns. *Earth Planet. Sci. Lett.* **186**, 497–512. (doi:10.1016/S0012-821X(01)00263-1)
74. Lacan F, Jeandel C. 2004 Subpolar mode water formation traced by neodymium isotopic composition. *Geophys. Res. Lett.* **31**, L14306. (doi:10.1029/2004gl019747)
75. Molina-Kescher M, Frank M, Hathorne E. 2014 South Pacific dissolved Nd isotope compositions and rare earth element distributions: water mass mixing versus biogeochemical cycling. *Geochim. Cosmochim. Acta* **127**, 171–189. (doi:10.1016/j.gca.2013.11.038)
76. Osborne AH, Haley BA, Hathorne EC, Flogel S, Frank M. 2014 Neodymium isotopes and concentrations in Caribbean seawater: tracing water mass mixing and continental input in a semi-enclosed ocean basin. *Earth Planet. Sci. Lett.* **406**, 174–186. (doi:10.1016/j.epsl.2014.09.011)
77. Piepgras DJ, Jacobsen SB. 1988 The isotopic composition of neodymium in the North Pacific. *Geochim. Cosmochim. Acta* **52**, 1373–1381. (doi:10.1016/0016-7037(88)90208-6)
78. Piepgras DJ, Wasserburg GJ. 1982 Isotopic composition of neodymium in waters from the Drake Passage. *Science* **217**, 207–214. (doi:10.1126/science.217.4556.207)
79. Piepgras DJ, Wasserburg GJ. 1983 Influence of the Mediterranean outflow on the isotopic composition of neodymium in waters of the North Atlantic. *J. Geophys. Res. – Oceans Atmos.* **88**, 5997–6006. (doi:10.1029/JC088iC10p05997)
80. Piepgras DJ, Wasserburg GJ. 1987 Rare earth element transport in the western North Atlantic inferred from Nd isotopic observations. *Geochim. Cosmochim. Acta* **51**, 1257–1271. (doi:10.1016/0016-7037(87)90217-1)
81. Rickli J, Frank M, Baker AR, Aciego S, de Souza G, Georg RB, Halliday AN. 2010 Hafnium and neodymium isotopes in surface waters of the eastern Atlantic Ocean: implications for sources and inputs of trace metals to the ocean. *Geochim. Cosmochim. Acta* **74**, 540–557. (doi:10.1016/j.gca.2009.10.006)
82. Rickli J, Frank M, Halliday AN. 2009 The hafnium–neodymium isotopic composition of Atlantic seawater. *Earth Planet. Sci. Lett.* **280**, 118–127. (doi:10.1016/j.epsl.2009.01.026)
83. Rickli J, Gutjahr M, Vance D, Fischer-Goedde M, Hillenbrand CD, Kuhn G. 2014 Neodymium and hafnium boundary contributions to seawater along the West Antarctic continental margin. *Earth Planet. Sci. Lett.* **394**, 99–110. (doi:10.1016/j.eps1.2014.03.008)

84. Shimizu H, Tachikawa K, Masuda A, Nozaki Y. 1994 Cerium and neodymium isotope ratios and REE patterns in seawater from the North Pacific Ocean. *Geochim. Cosmochim. Acta* **58**, 323–333. (doi:10.1016/0016-7037(94)90467-7)
85. Singh SP, Singh SK, Goswami V, Bhushan R, Rai VK. 2012 Spatial distribution of dissolved neodymium and ε_{Nd} in the Bay of Bengal: role of particulate matter and mixing of water masses. *Geochim. Cosmochim. Acta* **94**, 38–56. (doi:10.1016/j.gca.2012.07.017)
86. Stichel T, Frank M, Rickli J, Haley BA. 2012 The hafnium and neodymium isotope composition of seawater in the Atlantic sector of the Southern Ocean. *Earth Planet. Sci. Lett.* **317**, 282–294. (doi:10.1016/j.epsl.2011.11.025)
87. Stichel T, Frank M, Rickli J, Hathorne EC, Haley BA, Jeandel C, Pradoux C. 2012 Sources and input mechanisms of hafnium and neodymium in surface waters of the Atlantic sector of the Southern Ocean. *Geochim. Cosmochim. Acta* **94**, 22–37. (doi:10.1016/j.gca.2012.07.005)
88. Stordal MC, Wasserburg GJ. 1986 Neodymium isotopic study of Baffin Bay water: sources of REE from very old terranes. *Earth Planet. Sci. Lett.* **77**, 259–272. (doi:10.1016/0012-821x(86)90138-x)
89. Tachikawa K, Jeandel C, Roy-Barman M. 1999 A new approach to the Nd residence time in the ocean: the role of atmospheric inputs. *Earth Planet. Sci. Lett.* **170**, 433–446. (doi:10.1016/S0012-821X(99)00127-2)
90. Tachikawa K, Roy-Barman M, Michard A, Thouron D, Yeghicheyan D, Jeandel C. 2004 Neodymium isotopes in the Mediterranean sea: comparison between seawater and sediment signals. *Geochim. Cosmochim. Acta* **68**, 3095–3106. (doi:10.1016/j.gca.2004.01.024)
91. Tazoe H, Obata H, Amakawa H, Nozaki Y, Gamo T. 2007 Precise determination of the cerium isotopic compositions of surface seawater in the northwest Pacific Ocean and Tokyo Bay. *Mar. Chem.* **103**, 1–14. (doi:10.1016/j.marchem.2006.05.008)
92. Tazoe H, Obata H, Gamo T. 2007 Determination of cerium isotope ratios in geochemical samples using oxidative extraction technique with chelating resin. *J. Anal. Atom. Spectrom.* **22**, 616–622. (doi:10.1039/b617285g)
93. Tazoe H, Obata H, Gamo T. 2011 Coupled isotopic systematics of surface cerium and neodymium in the Pacific Ocean. *Geochem. Geophys. Geosyst.* **12**, 14. (doi:10.1029/2010gc003342)
94. Wu Q, Colin C, Liu ZF, Thil F, Dubois-Dauphin Q, Frank N, Tachikawa K, Bordier L, Douville E. 2015 Neodymium isotopic composition in foraminifera and authigenic phases of the South China Sea sediments: implications for the hydrology of the North Pacific Ocean over the past 25 kyr. *Geochem. Geophys. Geosyst.* **16**, 3883–3904. (doi:10.1002/2015gc005871)
95. Zimmermann B, Porcelli D, Frank M, Andersson PS, Baskaran M, Lee DC, Halliday AN. 2009 Hafnium isotopes in Arctic Ocean water. *Geochim. Cosmochim. Acta* **73**, 3218–3233. (doi:10.1016/j.gca.2009.02.028)
96. Zimmermann B, Porcelli D, Frank M, Rickli J, Lee DC, Halliday AN. 2009 The hafnium isotope composition of Pacific Ocean water. *Geochim. Cosmochim. Acta* **73**, 91–101. (doi:10.1016/j.gca.2008.09.033)
97. van de Flierdt T *et al.* 2012 GEOTRACES intercalibration of neodymium isotopes and rare earth element concentrations in seawater and suspended particles. Part 1: Reproducibility of results for the international intercomparison. *Limnol. Oceanogr. Methods* **10**, 234–251. (doi:10.4319/lom.2012.10.234)
98. Sholkovitz ER, Landing WM, Lewis BL. 1994 Ocean particle chemistry: the fractionation of rare earth elements between suspended particles and seawater. *Geochim. Cosmochim. Acta* **58**, 1567–1579. (doi:10.1016/0016-7037(94)90559-2)
99. Alibo DS, Nozaki Y. 1999 Rare earth elements in seawater: particle association, shale-normalization, and Ce oxidation. *Geochim. Cosmochim. Acta* **63**, 363–372. (doi:10.1016/S0016-7037(98)00279-8)
100. Jones KM, Khatiwala SP, Goldstein SL, Hemming SR, van de Flierdt T. 2008 Modeling the distribution of Nd isotopes in the oceans using an ocean general circulation model. *Earth Planet. Sci. Lett.* **272**, 610–619. (doi:10.1016/j.epsl.2008.05.027)
101. Schlitzer R. 2015 Ocean Data View. odv.awi.de.
102. Jenkins WJ, Smethie WM, Boyle EA, Cutter GA. 2015 Water mass analysis for the US GEOTRACES (GA03) North Atlantic sections. *Deep-Sea Res. Part II Top. Stud. Oceanogr.* **116**, 6–20. (doi:10.1016/j.dsr2.2014.11.018)

103. Dickson RR, Brown J. 1994 The production of North Atlantic deep water: sources, rates, and pathways. *J. Geophys. Res. – Oceans* **99**, 12 319–12 341. (doi:10.1029/94jc00530)
104. Broecker WS, Blanton S, Smethie WMJ, Ostlund G. 1991 Radiocarbon decay and oxygen utilization in the deep Atlantic Ocean. *Glob. Biogeochem. Cycles* **5**, 87–117. (doi:10.1029/90gb02279)
105. Mawji E *et al*. 2015 The GEOTRACES intermediate data product 2014. *Mar. Chem.* **177**(Part 1), 1–8. (doi:10.1016/j.marchem.2015.04.005)
106. Anderson LA, Sarmiento JL. 1994 Redfield ratios of remineralization determined by nutrient data analysis. *Glob. Biogeochem. Cycles* **8**, 65–80. (doi:10.1029/93gb03318)
107. Broecker WS, Takahashi T, Takahashi T. 1985 Sources and flow patterns of deep-ocean waters as deduced from potential temperature, salinity, and initial phosphate concentration. *J. Geophys. Res. – Oceans* **90**, 6925–6939. (doi:10.1029/JC090iC04p06925)
108. Smethie WM, Lebel DA, Fine RA, Rhein M, Kieke D. 2013 Strength and variability of the deep limb of the North Atlantic meridional overturning circulation from chlorofluorocarbon inventories. In *Ocean circulation: mechanisms and impacts—past and future changes of meridional overturning*, pp. 119–130. Washington, DC: American Geophysical Union.
109. Middag R, van Hulten MMP, Van Aken HM, Rijkenberg MJA, Gerringa LJA, Laan P, de Baar HJW. 2015 Dissolved aluminium in the ocean conveyor of the west Atlantic Ocean: effects of the biological cycle, scavenging, sediment resuspension and hydrography. *Mar. Chem.* **177**, 69–86. (doi:10.1016/j.marchem.2015.02.015)
110. Measures C, Hatta M, Fitzsimmons J, Morton P. 2015 Dissolved Al in the zonal N Atlantic section of the US GEOTRACES 2010/2011 cruises and the importance of hydrothermal inputs. *Deep-Sea Res. Part II Top. Stud. Oceanogr.* **116**, 176–186. (doi:10.1016/j.dsr2.2014.07.006)
111. Hydes DJ. 1979 Aluminum in seawater: control by inorganic processes. *Science* **205**, 1260–1262. (doi:10.1126/science.205.4412.1260)
112. Hydes DJ, Liss PS. 1976 Fluorimetric method for determination of low concentrations of dissolved aluminum in natural waters. *Analyst* **101**, 922–931. (doi:10.1039/an9760100922)
113. Measures CI. 1995 The distribution of Al in the IOC stations of the eastern Atlantic between 30 °S and 34 °N. *Mar. Chem.* **49**, 267–281. (doi:10.1016/0304-4203(95)00017-l)
114. Orians KJ, Bruland KW. 1985 Dissolved aluminum in the central North Pacific. *Nature* **316**, 427–429. (doi:10.1038/316427a0)
115. Orians KJ, Bruland KW. 1986 The biogeochemistry of aluminum in the Pacific Ocean. *Earth Planet. Sci. Lett.* **78**, 397–410. (doi:10.1016/0012-821x(86)90006-3)
116. Middag R, de Baar HJW, Laan P, Bakker K. 2009 Dissolved aluminium and the silicon cycle in the Arctic Ocean. *Mar. Chem.* **115**, 176–195. (doi:10.1016/j.marchem.2009.08.002)
117. Middag R, van Slooten C, de Baar HJW, Laan P. 2011 Dissolved aluminium in the Southern Ocean. *Deep-Sea Res. Part II Top. Stud. Oceanogr.* **58**, 2647–2660. (doi:10.1016/j.dsr2.2011.03.001)
118. Ohnemus DC, Lam PJ. 2015 Cycling of lithogenic marine particles in the US GEOTRACES North Atlantic transect. *Deep-Sea Res. Part II Top. Stud. Oceanogr.* **116**, 283–302. (doi:10.1016/j.dsr2.2014.11.019)
119. Moran SB, Moore RM. 1992 Kinetics of the removal of dissolved aluminum by diatoms in seawater: a comparison with thorium. *Geochim. Cosmochim. Acta* **56**, 3365–3374. (doi:10.1016/0016-7037(92)90384-u)
120. van Hulten MMP, Sterl A, Middag R, de Baar HJW, Gehlen M, Dutay JC, Tagliabue A. 2014 On the effects of circulation, sediment resuspension and biological incorporation by diatoms in an ocean model of aluminium. *Biogeosciences* **11**, 3757–3779. (doi:10.5194/bg-11-3757-2014)
121. van Hulten MMP, Sterl A, Tagliabue A, Dutay JC, Gehlen M, de Baar HJW, Middag R. 2013 Aluminium in an ocean general circulation model compared with the west Atlantic GEOTRACES cruises. *J. Mar. Syst.* **126**, 3–23. (doi:10.1016/j.jmarsys.2012.05.005)
122. Bruland KW, Lohan MC. 2003 Controls of trace metals in seawater. In *The oceans and marine geochemistry* (ed. H Elderfield), pp. 23–47. Oxford, UK: Elsevier-Pergamon.
123. Bacon MP, Anderson RF. 1982 Distribution of thorium isotopes between dissolved and particulate forms in the deep sea. *J. Geophys. Res. – Oceans Atmos.* **87**, 2045–2056. (doi:10.1029/JC087iC03p02045)

124. Hydes DJ, Delange GJ, Debaar HJW. 1988 Dissolved aluminum in the Mediterranean. *Geochim. Cosmochim. Acta* **52**, 2107–2114. (doi:10.1016/0016-7037(88)90190-1)
125. Koning E, Gehlen M, Flank AM, Calas G, Epping E. 2007 Rapid post-mortem incorporation of aluminum in diatom frustules: evidence from chemical and structural analyses. *Mar. Chem.* **106**, 208–222. (doi:10.1016/j.marchem.2006.06.009)
126. Stoffyn M. 1979 Biological control of dissolved aluminum in seawater: experimental evidence. *Science* **203**, 651–653. (doi:10.1126/science.203.4381.651)
127. Van Beusekom JEE, Weber A. 1992 Decreasing diatom abundance in the North Sea: the possible significance of aluminum. In *Marine eutrophication and population dynamics* (eds G Colombo, I Ferrari, VU Ceccherelli, R Rossi), pp. 121–127. Fredensborg, Denmark: Olsen & Olsen.
128. Mackin JE, Aller RC. 1986 The effects of clay mineral reactions on dissolved Al distributions in sediments and waters of the Amazon continental shelf. *Cont. Shelf Res.* **6**, 245–262. (doi:10.1016/0278-4343(86)90063-4)
129. German CR, Klinkhammer GP, Edmond JM, Mitra A, Elderfield H. 1990 Hydrothermal scavenging of rare-earth elements in the ocean. *Nature* **345**, 516–518. (doi:10.1038/345516a0)
130. Stichel T, Pahnke K, Goldstein S, Hartman A, Scher H. 2014 The geochemistry of seawater neodymium isotopes in the TAG hydrothermal plume at the mid Atlantic ridge. Presented at *Ocean Sciences Meeting*, Honolulu, HI, 23–28 February.
131. Hillaire-Marcel C, de Vernal A, Bilodeau G, Weaver AJ. 2001 Absence of deep-water formation in the Labrador Sea during the last interglacial period. *Nature* **410**, 1073–1077. (doi:10.1038/35074059)
132. Dokken TM, Jansen E. 1999 Rapid changes in the mechanism of ocean convection during the last glacial period. *Nature* **401**, 458–461. (doi:10.1038/46753)
133. Crocket KC, Vance D, Gutjahr M, Foster GL, Richards DA. 2011 Persistent Nordic deep-water overflow to the glacial North Atlantic. *Geology* **39**, 515–518. (doi:10.1130/g31677.1)
134. Labeyrie LD, Duplessy JC, Duprat J, Juillet-Leclerc A, Moyes J, Michel E, Kallel N, Shackleton NJ. 1992 Changes in the vertical structure of the North Atlantic Ocean between glacial and modern times. *Quat. Sci. Rev.* **11**, 401–413. (doi:10.1016/0277-3791(92)90022-z)
135. NGRIP. 2004 High-resolution record of Northern Hemisphere climate extending into the last interglacial period. *Nature* **431**, 147–151. (doi:10.1038/nature02805)
136. Gutjahr M, Frank M, Stirling CH, Keigwin LD, Halliday AN. 2008 Tracing the Nd isotope evolution of North Atlantic deep and intermediate waters in the western North Atlantic since the last glacial maximum from Blake Ridge sediments. *Earth Planet. Sci. Lett.* **266**, 61–77. (doi:10.1016/j.epsl.2007.10.037)
137. Pearce CR, Jones MT, Oelkers EH, Pradoux C, Jeandel C. 2013 The effect of particulate dissolution on the neodymium (Nd) isotope and rare earth element (REE) composition of seawater. *Earth Planet. Sci. Lett.* **369**, 138–147. (doi:10.1016/j.epsl.2013.03.023)
138. Friedrich T, Timmermann A, Stichel T, Pahnke K. 2014 Ocean circulation reconstructions from ε_{Nd}: a model-based feasibility study. *Paleoceanography* **29**, 1003–1023. (doi:10.1002/2014pa002658)
139. Horikawa K, Martin EE, Asahara Y, Sagawa T. 2011 Limits on conservative behavior of Nd isotopes in seawater assessed from analysis of fish teeth from Pacific core tops. *Earth Planet. Sci. Lett.* **310**, 119–130. (doi:10.1016/j.epsl.2011.07.018)
140. Wilson DJ, Piotrowski AM, Galy A, McCave IN. 2012 A boundary exchange influence on deglacial neodymium isotope records from the deep western Indian Ocean. *Earth Planet. Sci. Lett.* **341**, 35–47. (doi:10.1016/j.epsl.2012.06.009)
141. Lopez Correa M *et al.* 2012 Preboreal onset of cold-water coral growth beyond the Arctic Circle revealed by coupled radiocarbon and U-series dating and neodymium isotopes. *Quat. Sci. Rev.* **34**, 24–43. (doi:10.1016/j.quascirev.2011.12.005)
142. van de Flierdt T, Robinson LF, Adkins JF. 2010 Deep-sea coral aragonite as a recorder for the neodymium isotopic composition of seawater. *Geochim. Cosmochim. Acta* **74**, 6014–6032. (doi:10.1016/j.gca.2010.08.001)
143. Copard K, Colin C, Douville E, Freiwald A, Gudmundsson G, De Mol B, Frank N. 2010 Nd isotopes in deep-sea corals in the north-eastern Atlantic. *Quat. Sci. Rev.* **29**, 2499–2508. (doi:10.1016/j.quascirev.2010.05.025)

144. Palmer MR, Elderfield H. 1985 Variations in the Nd isotopic composition of foraminifera from Atlantic Ocean sediments. *Earth Planet. Sci. Lett.* **73**, 299–305. (doi:10.1016/0012-821X(85)90078-0)
145. Roberts NL, Piotrowski AM, Elderfield H, Eglinton TI, Lomas MW. 2012 Rare earth element association with foraminifera. *Geochim. Cosmochim. Acta* **94**, 57–71. (doi:10.1016/j.gca.2012.07.009)
146. Gutjahr M, Frank M, Stirling CH, Klemm V, van de Flierdt T, Halliday AN. 2007 Reliable extraction of a deepwater trace metal isotope signal from Fe–Mn oxyhydroxide coatings of marine sediments. *Chem. Geol.* **242**, 351–370. (doi:10.1016/j.chemgeo.2007.03.021)
147. Staudigel H, Doyle P, Zindler A. 1985 Sr and Nd isotope systematics in fish teeth. *Earth Planet. Sci. Lett.* **76**, 45–56. (doi:10.1016/0012-821X(85)90147-5)
148. Martin EE, Haley BA. 2000 Fossil fish teeth as proxies for seawater Sr and Nd isotopes. *Geochim. Cosmochim. Acta* **64**, 835–847. (doi:10.1016/S0016-7037(99)00376-2)
149. Wilson DJ, Piotrowski AM, Galy A, Clegg JA. 2013 Reactivity of neodymium carriers in deep sea sediments: implications for boundary exchange and paleoceanography. *Geochim. Cosmochim. Acta* **109**, 197–221. (doi:10.1016/j.gca.2013.01.042)
150. Martin EE, Blair SW, Kamenov GD, Scher HD, Bourbon E, Basak C, Newkirk DN. 2010 Extraction of Nd isotopes from bulk deep sea sediments for paleoceanographic studies on Cenozoic time scales. *Chem. Geol.* **269**, 414–431. (doi:10.1016/j.chemgeo.2009.10.016)
151. Tachikawa K, Piotrowski AM, Bayon G. 2014 Neodymium associated with foraminiferal carbonate as a recorder of seawater isotopic signatures. *Quat. Sci. Rev.* **88**, 1–13. (doi:10.1016/j.quascirev.2013.12.027)
152. Blaser P, Lippold J, Gutjahr M, Frank N, Link JM, Frank M. 2016 Extracting foraminiferal seawater Nd isotope signatures from bulk deep sea sediment by chemical leaching. *Chem. Geol.* **439**, 189–204. (doi:10.1016/j.chemgeo.2016.06.024)